The Diffuse Soft X-ray Background

The Local and the eROSITA Bubbles

Michael Chun Hei Yeung

München 2025

The Diffuse Soft X-ray Background

The Local and the eROSITA Bubbles

Michael Chun Hei Yeung

Dissertation
der Fakultät für Physik
der Ludwig-Maximilians-Universität
München

vorgelegt von
Michael Chun Hei Yeung
aus Hongkong

München, den 8 September 2025

Erstgutachter: Prof. Dr. Werner Becker
Zweitgutachter: Prof. Dr. Klaus Dolag
Tag der mündlichen Prüfung: 20 Oktober 2025

天其運乎？地其處乎？日月其爭於所乎？孰主張是？孰維綱是？

《莊子．天運》（戰國）

Excerpt from ***The Revolution of Heaven, Chuang Tzu***
Warring States Period, 369–286 BC

How (ceaselessly) heaven revolves! How (constantly) earth abides at rest! And do the sun and moon contend about their (respective) places? Who presides over and directs these (things)? Who binds and connects them together?

— Translation by James Legge (1891)

Contents

List of Figures

List of Tables

Zusammenfassung

Der diffuse weiche Röntgenhintergrund (SXRB) enthält wichtige Informationen über astrophysikalische Prozesse in einer Entfernung von wenigen Astronomische Einheiten (AE) bis zu kpc um uns herum. In dieser Arbeit gehe ich von der Wechselwirkung des Sonnenwinds mit dem einströmenden interstellaren Medium (ISM) auf Skalen von AE über die Local Hot Bubble (LHB) in der Grössenordnung von 100 pc und schließlich zu der möglicherweise $\gtrsim 10$ kpc großen Röntgenstruktur, die aus dem inneren Teil der Galaxie stammt und als eROSITA Bubbles (eRObub) bezeichnet wird, wobei ich die Daten der eROSITA All-Sky Surveys (eRASSs) verwende.

Die Sonne befindet sich in der LHB, einer Region mit geringer Dichte, die $\sim 10^6$ K Gas enthält und thermisch im weichen Röntgenbereich emittiert. Die Bestimmung der Eigenschaften des heißen Gases der LHB ist jedoch oft unklar, da es eine variable Vordergrundstrahlung gibt, die durch den Ladungsaustauschprozess zwischen den Ionen des Sonnenwinds und dem einströmenden neutralen ISM (SWCX) verursacht wird. Ich gehe dieses Problem an, indem ich Sichtlinien zu riesigen Molekülwolken auf der Oberfläche der LHB wähle, die den Vordergrund isolieren und Kalibrierungspunkte für die Dichte der LHB liefern. Durch die wiederholten Untersuchungen zeigt die Spektralanalyse einen monoton ansteigenden SWCX-Beitrag, der mit der Sonnenaktivität korreliert, sowie die Abhängigkeit des SWCX von den ekliptikalen Breiten, wie sie aufgrund der Ionisierung des Sonnenwinds zu erwarten ist. Andererseits scheint die LHB eine Temperaturschwankung in der Größenordnung von 0.02 keV aufzuweisen. Die projizierte Dichte der LHB scheint mit einer Konstante von $n_e \sim 4 \times 10^{-3}\,\mathrm{cm}^{-3}$ übereinzustimmen, was für ein Szenario sprechen würde, in dem sich das heiße Gas tatsächlich bis zur lokalen Blasenwand erstreckt.

Über isolierte Sichtlinien hinausgehend zerlege ich die gesamte westliche galaktische Hemisphäre räumlich und spektral in konventionelle SXRB-Komponenten und konzentriere mich auf den LHB-Aspekt. Ich finde eine offensichtliche Temperaturdichotomie zwischen der nördlichen und südlichen Hemisphäre bei $|b| > 30°$, die durch die jüngsten Supernova-Explosionen im LHB verursacht worden sein könnte. Das LHB-Emissionsmaß (EM) nimmt im Allgemeinen in Richtung der galaktischen Pole zu, was ein Hinweis auf eine größere Ausdehnung der LHB außerhalb der galaktischen Ebene ist, da dort weniger Druck der Expansion entgegenwirkt. Der Vergleich mit lokalen Staubkarten zeigt eine deutliche Antikorrelation zwischen N_H und EM, was ein Szenario stützt, in dem das heiße Gas Hohlräume in der lokalen Blase ausfüllt. Ich verifiziere einen bekannten und entdecke einen neuen Tunnel aus heißem Gas, der möglicherweise die LHB mit der nahe gelegenen Superblase verbindet. Vor diesem Hintergrund diskutiere ich die Möglichkeit eines größeren, miteinander verbundenen Netzwerks von heißem ISM in der gesamten Milchstraße. Die resultierende LHB EM-Karte wird verwendet, um ein neues 3D-LHB-Modell zu erstellen, das durch die Kombination bekannter Superblasen aus der Literatur einen aktuellen Überblick über die heiße Sonnenumgebung liefert.

Das letzte Projekt untersucht die Morphologie und das Spektrum der eRObub als Folge ihrer kürzlichen Entdeckung. Die 3D-Morphologie der eRObub wird anhand eines geometrischen Modells einer Druckwelle untersucht, die sich in einem idealen galaktischen Halo vom galaktischen Zentrum aus ausbreitet. Dies deutet auf eine horizontale Ausdehnung der eRObub von ~ 6 kpc hin und zeigt die große Entartung, die sich aus den Projektionseffekten ergibt, die aufgrund unserer Position auf der galaktischen Ebene auftreten. Die Spektralanalyse von eRObub zeigt ein anomales Verhältnis der Fe XVII $3d/3s$-Linien, das am besten durch zwei Temperaturkomponenten

bei $kT = 0.25 \pm 0.03$ und $0.56^{+0.04}_{-0.02}$ keV erklärt werden kann. Wir weisen auf die Existenz einer hellen Hülle hin, die die nördliche Blase umgibt, die kühler ist und kein Zwei-Temperatur-Modell erfordert, um zu passen. Wir schließen eine Nichtgleichgewichtsionisation als mögliche Erklärung aus und diskutieren die Möglichkeit, dass die kühle Hülle eine Vordergrundstruktur ist. Die eROobub-Spektren zeigen eine geringe Metallizität ($Z \sim 0.2\,Z_{\odot}$), was mit einer Stoßerwärmung des galaktischen Halos ohne signifikante Metallanreicherung übereinstimmt. Der Nordpolsporn scheint eine deutlich höhere Metallizität ($Z > 0.5\,Z_{\odot}$) aufzuweisen als die eROobub, was für einen mit der Sternentstehung zusammenhängenden und von den eROobub getrennten Ursprung spricht.

Abstract

The diffuse soft X-ray background (SXRB) holds important information about astrophysical processes from a few AU to kpc around us. In this thesis, I go from the solar wind's interaction with the inflowing interstellar medium (ISM) at AU scales, to the local hot bubble (LHB) in 100 pc scales, and eventually arrive at the possibly $\gtrsim 10$ kpc giant X-ray structure stemming from the inner part of the Galaxy, called the eROSITA bubbles (eRObub), using the eROSITA All-Sky Survey data (eRASS).

The Sun dwells in the LHB which is a low-density region containing $\sim 10^6$ K gas and emits thermally in the soft X-rays. The determination of the LHB hot gas properties, however, is often ambiguous because of a variable foreground caused by the charge exchange process between the solar wind ions and the inflowing neutral ISM (SWCX). I tackle this problem by choosing sight lines towards giant molecular clouds on the LHB surface, which isolate the foreground and provide calibration points for the LHB density. By the repeating surveys, the spectral analysis reveals a monotonically increasing SWCX contribution that correlates with solar activity, and the SWCX's dependence on ecliptic latitudes, expected from the ionisation properties of the solar wind. On the other hand, the LHB seems to exhibit a temperature variation in the order of 20 eV. The LHB projected density appears to be consistent with a constant of $n_e \sim 4 \times 10^{-3}\,\mathrm{cm}^{-3}$, which would argue for a scenario where the hot gas indeed extends to the local bubble wall.

Moving beyond isolated sight lines, I spatially and spectrally decompose the whole western Galactic hemisphere into conventional SXRB components and focus on the LHB aspect. I observe an apparent temperature dichotomy between the northern and southern hemispheres at $|b| > 30^\circ$, which could be set up by the most recent supernova explosions in the LHB. The LHB emission measure (EM) generally increases towards the Galactic poles, which is evidence of a larger LHB extent away from the Galactic plane due to less pressure resisting expansion. Comparison with local dust maps shows clear anti-correlation between N_H and EM, supporting a scenario where the hot gas fills cavities in the local bubble. I verify a known and discover a new tunnel of hot gas, potentially linking the LHB to the nearby superbubbles. In this light, I discuss the possibility of a wider interconnected network of hot ISM throughout the Milky Way. The resulting LHB EM map is used to produce a new 3D LHB model to create a latest view of the hot solar neighbourhood by combining known superbubbles in the literature.

The last project explores the morphology and the spectrum of the eRObub as a follow-up to their recent discovery. The 3D morphology of the eRObub is explored using a geometrical model of a blast wave propagating in an ideal Galactic halo from the Galactic centre, which indicates a eRObub horizontal extent of ~ 6 kpc and demonstrates the large degeneracy revolving the vertical extent due to projection effects inherent in our location on the Galactic plane. The spectral analysis of the eRObub reveals an anomalous Fe XVII $3d/3s$ line ratio, which is best explained by two temperature components at $kT = 0.25 \pm 0.03$ and $0.56^{+0.04}_{-0.02}$ keV. We point out the existence of a bright shell surrounding the northern bubble, which is cooler and does not require a two-temperature model to fit. We rule out non-equilibrium ionisation as a possible explanation and discuss the possibility of the cool shell being a foreground structure. The eRObub spectra show a low abundance ($Z \sim 0.2\,Z_\odot$) which is consistent with shock-heating of the Galactic halo without significant metal enrichment. The North Polar Spur appears to be significantly higher in metallicity ($Z > 0.5\,Z_\odot$) than the eRObub, lending support for a star-formation-related and a separate origin from the eRObub.

Preface

Where do we stand in the Universe? — a fundamental curiosity that has intrigued humans for millennia. The answer naturally depends on the spatial scale of interest: a being on the surface of the Earth, or a planet orbiting the Sun, or in the Solar System travelling through the Milky Way, or in the Milky Way Galaxy in the Local Group, etc., and the list goes on. The ambition of this thesis is conservative: it is set out to explore this curiosity in our immediate neighbourhood, at a scale of $\sim$100 pc – a volume often called the local cavity or local (hot) bubble (LHB), coined for its low density. In this pursuit, however, one would constantly find oneself in situations where processes in both smaller and larger physical scales could not simply be neglected, as is the reality for many other fields or disciplines. In addition to the original goal, much of this thesis will be devoted to decomposing physical components of various scales at X-ray energies where the hot gas within the local bubble volume emits.

The all-sky surveys conducted by the X-ray telescope SRG/eROSITA are the backbone of the results presented in this thesis. Despite the primary science goal of eROSITA being the detection of approximately a million galaxy clusters to constrain cosmological parameters, its all-sky surveys are bound to detect and reveal the properties of any hot gas around us. The photons from the foreground diffuse hot gas dominate the total photon budget ($\sim$70%). The tremendous improvements in both effective area and spectral resolution compared to its predecessor ROSAT, unsurprisingly, delivered discoveries, headlined by the discovery of the pair of giant bubbles which now bears the name of the telescope, seemingly risen from the central regions of the Galaxy. The spatial and spectral properties of the eROSITA bubbles will be explored in Chapter 4.

Much of the physics of hot gas and its emission mechanisms can be used to understand structures that span a wide physical scale, from the LHB ($\sim$100 pc) to the eROSITA bubbles (possibly $\sim$10 kpc). Chapter 1 aims to set the scene, introducing the primary constituents of the soft X-ray background, their history and their respective emission processes. An overview of the eROSITA telescope and its relevant technical details regarding observations of the X-ray background is also included in Chapter 1. The following two chapters focus on the properties of the LHB: Chapter 2 presents my work that uses giant molecular cloud sight lines, which efficiently attenuate the X-ray background originating from farther out, to constrain the properties of the foreground LHB and the solar wind charge exchange (SWCX) emission; Chapter 3 builds upon the molecular cloud shadowing work, but extends the measurements of the LHB to the whole western Galactic hemisphere. In this chapter, I also attempt to put the LHB in context with measurements in other wavebands and nearby hot bubbles and structures. Chapter 4 moves beyond the solar neighbourhood and investigates the spatial and spectral properties of the eROSITA bubbles. Lastly, in Chapter 5, I summarise the new findings but also highlight the limitations from the aforementioned works, in light of the future missions that will hopefully materialise in a decade or two.

Publications

This cumulative thesis is based on the following three first-author articles.

1. *SRG/eROSITA X-ray shadowing study of giant molecular clouds*
   Michael C. H. Yeung, Michael J. Freyberg, Gabriele Ponti, Konrad Dennerl, Manami Sasaki and Andy Strong
   Astronomy & Astrophysics, 676, A3 (2023) Chapter 2

2. *The SRG/eROSITA diffuse soft X-ray background I. The local hot bubble in the western Galactic hemisphere*
   Michael C. H. Yeung, Gabriele Ponti, Michael J. Freyberg, Konrad Dennerl, Teng Liu, Nicola Locatelli, Martin G. F. Mayer, Jeremy S. Sanders, Manami Sasaki, Andy Strong, Yi Zhang, Xueying Zheng and Efrain Gatuzz
   Astronomy & Astrophysics, 690, A399 (2024) Chapter 3

3. *The SRG/eROSITA diffuse soft X-ray background II. Morphology and spectra of the eROSITA bubbles*
   Michael C. H. Yeung, Martin G. F. Mayer, Andy Strong, Michael J. Freyberg, Gabriele Ponti, Konrad Dennerl, Xueying Zheng, Manami Sasaki, Jeremy S. Sanders, Junjie Mao, Jiejia Liu, Liyi Gu, Werner Becker, Frank Haberl and Teng Liu
   To be submitted to Astronomy & Astrophysics Chapter 4

All the articles are the original work of Michael C. H. Yeung, except for the section on the morphological analysis and the related interpretation of the eROSITA bubbles in Paper 3 (Chapter 4), which was done by Martin G. F. Mayer.

Glossary of acronyms

AGN Active galactic nuclei. 1, 11, 13, 136, 141, 142

CalPV Calibration and Performance Verification. 24–27, 36, 49, 52, 53

CGM Circum-galactic medium. In this thesis, it refers most of the time to the Milky Way's CGM. It is synonymous with the Galactic halo. 2, 3, 11, 16, 20, 34–37, 45, 46, 60, 61, 63–65, 67–69, 73, 79, 84–87, 98, 110–112, 114, 119, 120, 122, 123, 125–128, 136, 137, 139, 141–144, 154, 156, 157

CIE Collisional ionisation equilibrium. 3, 8, 11, 13, 16–19, 65, 67, 69, 101, 102, 119, 120, 126, 128, 131, 135–137, 143, 144, 151, 156, 157

COR The 0.7 keV Galactic corona component. 2, 11, 37, 64, 65, 119, 120, 122, 125, 126

CX Charge exchange. ix, 6–10, 20, 21, 151, 153, 157

CXB Cosmic X-ray background. 2, 11, 34–37, 45, 61–69, 94–98, 100, 101, 111, 119, 122, 125–127, 129, 156, 159

eFEDS eROSITA Final Equatorial-Depth Survey. 11, 36–38, 45, 46, 64, 67, 94

EM Emission measure. xv, xvii, 3, 4, 6, 10, 13, 35, 37, 43–46, 55, 65, 96, 119–123, 125, 126, 128, 131, 132, 135, 136, 138, 143, 144, 154–157

eRASS eROSITA All-Sky Survey. eRASS:n means the first to n^{th} survey. xv, xvii, 8, 11–13, 22, 24, 25, 29, 31, 35–38, 42, 46–50, 52, 53, 55, 59–64, 68, 69, 90, 98, 101, 109–113, 122, 123, 128, 143–146, 155, 156

eRObub eROSITA bubbles. xi, xv–xvii, 2, 12, 13, 16, 64, 65, 109–112, 114–116, 119–144, 146–148, 151, 153–159

eROSITA extended ROentgen Survey with an Imaging Telescope Array. It is the primary instrument on board SRG. It has seven telescope modules sensitive to the soft X-ray band and has completed four all-sky surveys. ix, xv, xvii, xix, 1, 2, 7, 8, 11–13, 22–26, 29–31, 33–37, 43, 45–49, 52, 55, 59–65, 68–71, 73, 78, 79, 82, 84, 85, 90–92, 95–100, 109–111, 113, 120, 121, 124, 125, 133, 135, 136, 142–144, 150, 151, 153, 155, 157, 158

FB Fermi bubbles. 12, 13, 109–111, 119–124, 136, 141–143, 156

FoV Field of view. ix, 23–26, 60, 157

FWC Filter-wheel closed. It represents data taken when the filter wheel was rotated to the closed position. ix, 2, 26–28, 49–54, 64, 67, 97, 125, 155, 159

GC Galactic centre. 1, 12, 13, 110, 112–114, 117, 142, 143

ISM Interstellar medium. ix, xv, xvii, 3, 5–8, 13–15, 30, 34, 35, 44, 60, 65, 70, 74, 81, 82, 91, 100, 123, 125, 128, 151, 156

LB Local bubble. 3, 4, 60, 73, 80–82, 91–93, 156, 157

LC Local cavity. 3, 4, 60, 92

LHB The ∼100 pc region the Solar System is currently situated. It has a low density of 10^{-3}–$10^{-2}\,\mathrm{cm}^{-3}$, and the gas within has a temperature around 1 MK, emitting in the soft X-ray band. ix, xv, xvii, xix, 2–6, 11, 16, 20, 22, 29–31, 34, 35, 37, 38, 42–46, 48, 55, 58–66, 68–74, 76–87, 90–93, 96–98, 100–104, 110–112, 119, 125, 126, 136, 138–140, 144, 155–157

LICs Local interstellar clouds. 4, 5, 90, 91

NEI Non-equilibrium ionisation. xiii, 17, 65, 101, 102, 110, 137, 142, 144, 156, 157

NPS North Polar Spur. 12, 13, 109–111, 114, 118, 119, 121–124, 132, 133, 135, 137, 138, 143, 144, 147, 151, 153, 154, 156, 157

PSPC Position Sensitive Proportional Counter. 3–6, 24, 30, 59, 63, 101

RASS ROSAT All-Sky Survey. 3, 4, 22, 30, 78, 79

ROSAT Röntgensatellit. Predecessor of eROSITA, which had completed an all-sky survey in 1990. xix, 3, 4, 6, 13, 15, 22, 24, 29–31, 43, 45, 59, 63, 65, 68, 73–75, 78, 79, 84, 85, 88, 89, 91, 101, 112, 119, 120, 125

RRC Radiative recombination continuum. 11, 20, 21

S/N Signal-to-noise ratio. 24, 61, 62, 66–68, 72, 101, 103, 107–109, 119, 121, 122, 125, 132, 133, 136, 143

SNR Supernova remnant. 3, 8, 12, 17, 112–114, 125, 136, 137, 144, 146, 147, 151

SRG Spectrum-Roentgen-Gamma observatory. This satellite hosts both eROSITA and ART-XC X-ray telescopes.. xix, 1, 7, 12, 22, 25, 29, 34, 35, 47, 52, 55, 59, 60, 90, 100, 101, 109, 110, 143

SWCX Solar wind charge exchange. xv, xvii, xix, 2, 4–8, 22, 29–31, 34–36, 38, 42, 43, 46–49, 55, 60, 61, 64, 68, 78, 79, 84, 85, 90, 91, 98, 155

SXRB Soft X-ray background. ix, xv, xvii, 1–4, 8, 10, 11, 15, 22, 25, 27, 28, 59–62, 67, 79, 100, 122, 128, 143, 155–157

TM Telescope module. ix, 23, 24, 26–28, 31, 33, 34, 38, 49, 51, 52, 61, 67, 68, 125

XRB X-ray background. 1, 2

Chapter 1

Introduction

The introduction is ordered in an observation-inclined way, as it is the order in which most components in the diffuse X-ray background were identified, where observation precedes the prediction or interpretation. The reverse is rare, but it is usually synonymous with great scientific triumphs; one may think of the discovery of Neptune after the prediction from John Couch Adams and Urbain Le Verrier as a prime example. For this thesis, I am content with the less glamorous way. I begin the chapter by introducing the X-ray background, highlighting that Galactic structures dominate the soft X-ray part. A brief description of the physical mechanisms responsible for the X-ray emissions from the background components then follows. Lastly, the introduction is concluded by summarising the SRG/eROSITA mission, the primary instrument enabling much of the work and results presented in this thesis.

1.1 Soft X-ray background (SXRB)

The discovery of the first extra-solar source, Sco X-1, is commonly recognised as the birth of X-ray astronomy (Giacconi et al., 1962). On the same sounding rocket mission, with Geiger counters sensitive to X-rays between 2–8 Å (1.5–6 keV), Giacconi et al. (1962) also observed a non-zero background level away from the Moon and Sco X-1, which is now referred to as the X-ray background (XRB). It is now understood, from X-ray deep fields, that the hard X-ray background (XRB) between ∼1–10 keV is dominated by accretions onto supermassive black holes across cosmic times, namely active galactic nuclei (AGN), and the hard XRB can be resolved, virtually completely, into discrete sources (e.g. Matilsky et al., 1973; Giacconi et al., 1979; Piccinotti et al., 1982; Hasinger et al., 1998; Giacconi et al., 2002; Lumb et al., 2002; Alexander et al., 2003; Revnivtsev et al., 2003; De Luca & Molendi, 2004; Hasinger, 2004; Hickox & Markevitch, 2006; Cappelluti et al., 2017). Due to the extragalactic nature of the hard XRB, it appears isotropic in the sky.

Not long after the discovery of the XRB, Bowyer et al. (1968) reported an anisotropy in the soft X-ray background (SXRB) at longer wavelengths between 44–70 Å (0.18–0.28 keV) and immediately concluded the existence of a Galactic contribution. However, the puzzle was the drastic decrease in intensity by a factor of 10 from the Galactic pole to the plane. Despite the drop in intensity following the direction of Galactic absorption qualitatively, for a simple model consisting of a $kT = 10^6$ K spherical emitting cloud centred at the Galactic centre to reproduce the observed intensity, one would also predict a gas pressure that exceeds the expectation by ∼20 times. The puzzle is largely resolved by the 'displacement model' after a decade (Tanaka & Bleeker, 1977; Sanders et al., 1977), where the main ideas remain largely accurate in the face of modern measurements. A more in-depth introduction is given in Sect. 1.2. The displacement model proposes that the emitting hot gas is local instead of at the Galactic Centre (GC), displacing the cold gas in the closest neighbourhood. The sight line through the hot emitting gas on the Galactic plane is short because the cold gas there is close and dense, and it is the reverse near the Galactic poles. The net effect is a higher SXRB intensity at high Galactic latitudes because

of a longer integrated line-of-sight filled by hot gas. The vertical position of the Solar System $\sim$ 20–30 pc above the Galactic disk (Bland-Hawthorn & Gerhard, 2016, and references therein) and the local $N_{\rm H}$ distribution would also have an effect on the SXRB asymmetry.

The discussion on the anisotropy SXRB above is valid only at the softest X-ray energies. One observes a summation of multiple components at slightly higher energies between 0.3–1.0 keV. The definition of the SXRB has been used loosely so far, as is the case in literature, understandably so, as soft and hard are relative concepts, and different authors apply them differently based on practical considerations. However, for this thesis, the SXRB is the XRB between 0.1–1 keV, although a broader or narrower spectral energy range will be used for spectral analysis, the emissions from the objects of interest, the local hot bubble (LHB) and the eROSITA bubbles (eRObub), emit primarily within this energy range.

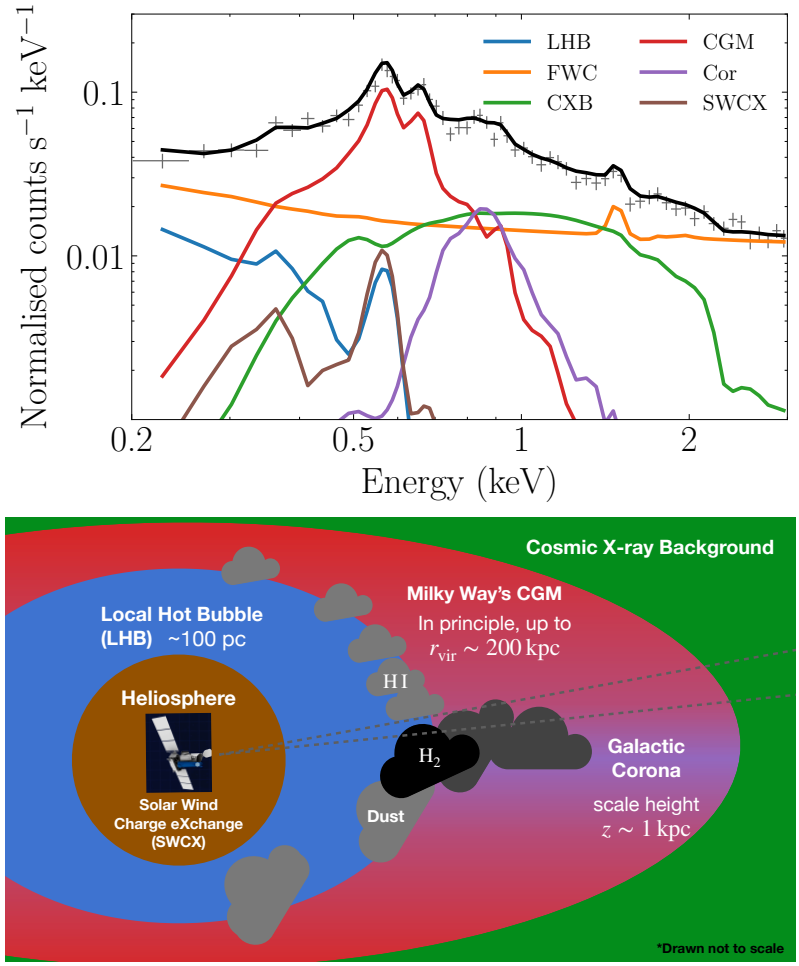

Figure 1.1: Illustration of the SXRB components. (Top) Example eROSITA spectrum of the SXRB taken from Yeung et al. (2023). SWCX: solar wind charge exchange (Sect. 1.3); LHB: local hot bubble (Sect. 1.2); CGM: Milky Way's circum-Galactic medium (Sect. 1.4); COR: Galactic corona (Sect. 1.4); CXB: cosmic X-ray background (Sect. 1.5); FWC: Filter-wheel closed background (Sect. 1.9.3). (Bottom) Illustration of the locations of the components with matching colours in the spectrum. The FWC component does not have a correspondence in the bottom panel, as it represents the instrumental background.

The components of the SXRB will be introduced in the following Sections. Figure 1.1 illustrates the energies and locations of the main components that contribute to the SXRB in matching

colours. This figure summarises the basis of the spectral analysis that will be used in all three projects of this thesis.

1.2 Local hot bubble (LHB)

The local hot bubble is also known as the local bubble (LB) or local cavity (LC). The other names are more popular outside X-ray astronomy and refer to the local interstellar medium (ISM) being a low-density region. Currently, the most popular scenario attributes the formation of the LHB to a series of supernova explosions in the last 10–20 Myr, which heated the ISM to $\sim 10^6$ K in the interior and swept up the colder ISM in a dense shell (e.g. Zucker et al., 2022; Schulreich et al., 2023).

The realisation of the Sun being embedded in a hot, low-density volume dates back to Sanders et al. (1977) and Tanaka & Bleeker (1977). Sanders et al. (1977) noticed the anti-correlation of the Wisconsin B (0.13–0.188 keV) and C (0.16–0.284 keV) bands with the Galactic H I cannot be explained by an absorption effect, but rather by a displacement effect. Photoelectric absorption affects the B band significantly more than the C band at fixed $N_{\rm H}$ because of the former's softer bandpass (Sect. 1.7). Both B and C bands count rates stayed roughly constant even in regions up to $4 \times 10^{20}\,{\rm cm}^{-2}$ (corresponds to $\sim$2 optical depths at the C band) is convincing evidence that much of the hot gas is located close to us, in front of most of the cold ISM that is observed in H I.

The structure of the neutral ISM can be probed using H I 21 cm measurements on the Galactic scale and stellar absorption to stars of known distances on a more local scale. One powerful way to deduce the column density of the neutral ISM around the 1980s–90s was to use UV absorption lines in stellar spectra. A shell-like structure on the Galactic disk could be seen from a compilation of these measurements, albeit with an opening towards Galactic longitude of $l = 270^\circ$ (Frisch & York, 1983; Paresce, 1984). This presence of the LC wall has since been further established from multiple tracers, including in reddening $E(B-V)$ from the *Hipparcos* catalogue (Perryman et al., 1997), Na I (Sfeir et al., 1999; Lallement et al., 2003) and optical polarisation (Leroy, 1999). Snowden et al. (1990a) pointed out, on the zeroth order, assuming a constant hot gas density in the displacement model, the B and C band count rates could reproduce the shape of the LHB reasonably well, especially at high Galactic latitudes. However, including a distant, absorbed component, now commonly referred to as the Galactic halo or the Milky Way's circum-galactic medium (CGM), would help to reconcile the observations at low latitudes.

A local, young supernova explosion or stellar winds are natural explanations to create a cavity displaced by hot gas (McKee & Ostriker, 1977; Cox & Anderson, 1982). Innes & Hartquist (1984) subsequently proposed that the LHB could be a superbubble, which is the result of multiple supernova explosions that excavated the LC about 4 Myr ago. This scenario remains the leading theory today, although the detailed numbers have been revised due to new multi-wavelength measurements.

A significant observational leap towards the SXRB and LHB measurement in the X-rays was delivered by ROSAT, whose great legacy was its X-ray All-Sky Survey (RASS) completed over six months in 1990 (Snowden & Schmitt, 1990). The spatial resolution and statistical significance improvement in the SXRB were two orders of magnitude compared to previous X-ray surveys (angular resolution from 2° to $1\farcm5$). The ROSAT/PSPC (Pfeffermann et al., 1987) broadband maps were the standard and leading dataset for SXRB studies in the following three decades (Snowden et al., 1997, 1998). The RASS consolidated the idea that SXRB has three main components: the unabsorbed LHB, the absorbed Milky Way halo or CGM and an isotropic extragalactic component, modulo prominent structures such as well-known supernova remnants (SNR), superbubbles and galaxy clusters. Using the R1 (0.11–0.284 keV) and R2 (0.14–0.284 keV) band count rates and their ratios, and under the assumption of collisional ionisation equilibrium (CIE), Snowden et al. (1998) constrained the LHB gas to a temperature centred at 1.2 MK (0.10 keV) with a $\sim$10% variation, with emission measure (EM) varying with a factor of 3–4 over the sky, between $(2–6)\times10^{-3}\,{\rm cm}^{-6}\,{\rm pc}$.

The RASS delivered the most accurate measurement of the LHB at the time. However, un-

expectedly, it also revealed a new foreground SXRB component: the solar wind charge exchange (SWCX) component originated within the Solar System. We defer the introduction of SWCX in Sect. 1.3. For the introduction of the LHB here, it suffices to note that the SWCX spectrum closely resembles a LHB spectrum (line-dominated spectrum at $\sim 10^6$ K) at PSPC and even CCD resolution, and SWCX emission is similarly unabsorbed due to its origin from within the heliosphere. Therefore, the precise LHB contribution of the ROSAT R1 and R2 count rates received significant uncertainties. The question of how much R1 and R2 fluxes genuinely originate from the LHB became the main research area in the following decade or so. Via careful selection of sight lines and observing times (since SWCX is highly correlated with solar activity and solar wind conditions), the emerging consensus is that despite the total EM originating from the LHB observed in ROSAT had to be adjusted down, a local volume filled with 10^6 K gas was still needed to fully explain the X-ray observations (e.g. Henley et al., 2007; Koutroumpa et al., 2009b). Experimentally, this problem was also tackled by a sounding rocket mission, DXL (Galeazzi et al., 2011), launched similarly near solar maximum as ROSAT, designed to imitate the scan geometry of ROSAT and observe towards a region of the highest expected SWCX intensity (helium focusing cone). They estimated ~40% of the flux in the ROSAT R1 and R2 bands originated from the SWCX process (Galeazzi et al., 2014). Liu et al. (2017) provides a revised temperature and geometry of the LHB using RASS data after taking into account the SWCX estimation from DXL and reiterates the accuracy of the displacement model on the zeroth order by showing the LHB wall inferred from X-ray closely matches the LC wall, at least in the Galactic plane (Fig. 1.2).

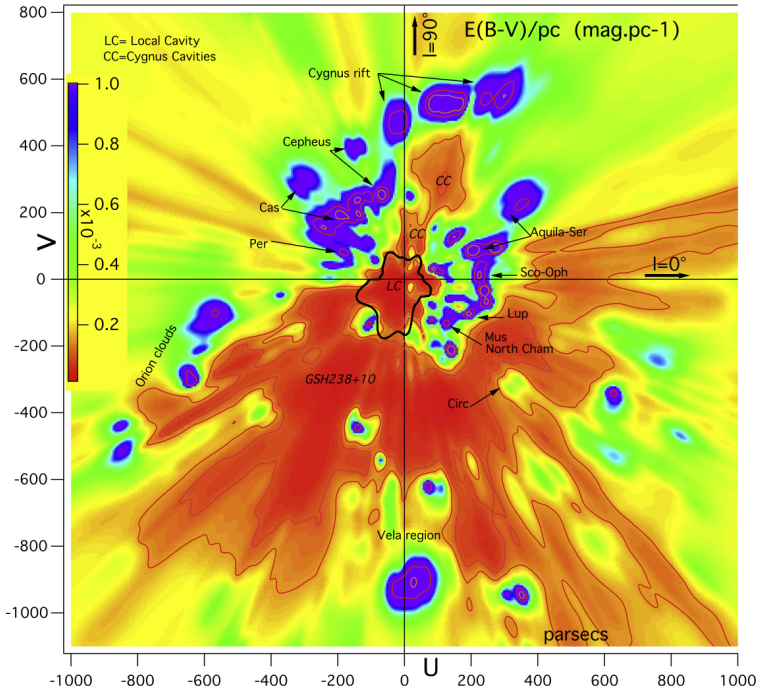

Figure 1.2: Differential $E(B-V)$ colour excess map in the solar neighbourhood from Lallement et al. (2014) overlaid with LHB geometry on the Galactic plane (Liu et al., 2017). Figure courtesy of Liu et al. (2017).

1.2.1 Pressure balance with the local interstellar clouds

Beyond the zeroth order approximation of a hot plasma filling the LB, there exists a cluster of local interstellar clouds (LICs) located within 10 pc of the Sun (see a review by Frisch et al., 2011). Their mean column density the LICs is rather low ($N_{\rm H\,I} = 17.91 \pm 0.18\,{\rm cm}^{-2}$; Wood et al., 2005)

and the LICs consist mainly of warm ISM (Redfield & Linsky, 2004). Due to their low column densities, the LICs are primarily studied through absorption lines in stellar spectra. While many aspects of the LICs can be and have been studied, the most relevant aspect to the LHB hot gas is the pressure balance between the LHB and the LICs. The mean thermal pressure of these clouds is $P/k = 2\,280 \pm 520\,\mathrm{K\,cm^{-3}}$ and the additional turbulent pressure contributes only ∼10% of the thermal pressure (Redfield & Linsky, 2004). On the other hand, the LHB hot gas amounts to $P/k \sim 15\,000\,\mathrm{K\,cm^{-3}}$ before SWCX subtraction (Snowden et al., 1997; Galeazzi et al., 2007), substantially above that of the LICs . This discrepancy was a well-known problem for two decades (see a review by Jenkins, 2009). The realisation and quantification of the SWCX foreground mitigated a large part of the issue. In addition, *Voyager I* measurement of the magnetic field beyond the heliosphere (Burlaga & Ness, 2014) put new constraints on the magnetic pressure in the LICs ($\sim 7\,500\,\mathrm{K\,cm^{-3}}$; Snowden et al., 2014). With these two new pieces of information, both the LHB thermal pressure and the LICs' total (thermal + turbulence + magnetic) pressure were then adjusted to $\sim 10\,000\,\mathrm{K\,cm^{-3}}$, hence largely resolving the issue of substantial pressure imbalance.

1.2.2 Origin of the LHB

If the origin of the LHB is indeed a superbubble, then one should be able to identify the stellar clusters that hosted the exploded massive stars. Maíz-Apellániz (2001) and Berghöfer & Breitschwerdt (2002) pioneered this work by back-tracing the trajectories of the stellar groups in the Sco-Cen OB stellar associations and found that at a realistic timescale of ∼ 10 Myr ago, they were inside the LHB. Hence, their most massive stars were likely responsible for creating the LHB. Fuchs et al. (2006) undertook a search for all blue stars within 400 pc that could be responsible for the LHB, from the time reversal of current trajectories of the selected stars and extrapolation of their initial mass function, they suggested these stars were within the LHB region 10–15 Myr ago and 14–20 supernovae have exploded since. This supernova rate was sufficient to excavate the LHB to its current size. On a similar note, the star-forming complexes on the wall of the LHB have motions consistent with an outward expansion from the LHB (Zucker et al., 2022). Modelling their motion with a realistic supernova input would also put the birth of the LHB to approximately 15 Myr ago, after which about a dozen supernovae exploded to sustain its expansion. The dense shell that the LHB have swept up has now fragmented and created the most active star-forming regions near us. In a broader context, the active star-forming regions on the wall of the LHB are the closest example of supernova-driven star formation (Zucker et al., 2022).

In addition to looking up to find more evidence for past supernova explosions, the other line of evidence is, interestingly, by looking down on the Earth. Long-lived (half-life ∼Myr) supernova-produced radioisotopes such as ^{60}Fe could be found in deep ocean sediments to constrain the times and sites of past supernovae (Ellis et al., 1996; Korschinek et al., 1996). Breitschwerdt et al. (2016) and Schulreich et al. (2017, 2023) carried out detailed numerical simulations to model the transport of the radioisotopes in the LHB and found that realistic supernova explosion sites and energies could produce the peaks of measured radioactive-to-stable element ratios in time. Interestingly, combining their simulations with radiometric measurements, they deduced that the Sun entered the LHB about 4–5 Myr ago, possibly coming from another superbubble, the Orion-Eridanus superbubble. This scenario could explain both the ^{60}Fe/Fe ratio 6–7 Myr ago and the Sun's motion with respect to other nearby stars.

1.3 Solar wind charge exchange (SWCX)

The astrophysical importance of the charge exchange process began to be recognised in 1996, which was triggered by the observation of the Comet C/Hyakutake 1996 B2 (Lisse et al., 1996). The comet's X-ray spectrum could reasonably be fitted by a significant absorbed hot plasma in PSPC resolution. However, a comet is not expected to possess hot plasma on the surface and absorption is also not expected to be significant for a nearby object, so it was a great surprise that

Comet Hyakutake shone brightly in X-rays, with the emission geometry apparently facing the Sun. Cravens (1997) pointed out that this emission was likely created by highly charged ions from the solar wind interacting with the cometary neutrals, which we now know to be correct. Dennerl et al. (1997) further established that comets are a new class of X-ray emitting objects with SWCX being the dominant emitting process. The discovery of the SWCX process also helps to understand a few other phenomena which were not completely understood at the time. This includes the long-term enhancements observed in the PSPC data, which had already been shown to be correlated to geomagnetic storms and solar wind variations at the time (Freyberg, 1994). Freyberg (1998) proposed that the Earth also acts like a giant comet, which serves as a reservoir of neutrals to interact with the solar wind ions. As ROSAT was orbiting in a low-Earth orbit, its observations would necessarily intersect with the charge exchange region, resulting in additional background in the ROSAT data in the form of the long-term enhancements. In addition, the non-illuminated side of the Moon was known to emit X-rays about 10 times brighter than the background level of ROSAT/PSPC (Schmitt et al., 1991). This can now be understood as the integrated SWCX emission from the Earth's exosphere to the lunar surface. The SWCX emission originated from the Earth's neutrals interacting with the solar wind is referred to as the geocoronal or magnetospheric SWCX, which is one of the two main regimes of SWCX that affects X-ray observations. The other regime is known as the heliospheric SWCX, which was first suggested by Cox (1998), who proposed that the inflowing neutral ISM into the Solar System could be another source of neutrals interacting with the solar wind.

1.3.1 Charge exchange process

Charge exchange (CX) occurs when a charge is transferred from a neutral atom or molecule B to an ion A during a close encounter. It can be described as

$$A^{q+} + B \rightarrow A^{*+q-1} + B^{+1}. \tag{1.1}$$

After the charge transfer, ion A remains in an excited state (denoted by the superscript $*$) and can subsequently decay radiatively to give a photon, which is usually in the extreme UV (EUV) or X-ray energies, that is:

$$A^{*+q-1} \rightarrow A^{+q-1} + \nu. \tag{1.2}$$

The CX surface brigtness (in unit of photons $\mathrm{cm}^{-2}\,\mathrm{s}^{-1}\,\mathrm{sr}^{-1}$) for a particular transition j due to the CX between a neutral species k and ion species s in charge state q can be written as

$$F_j = \int_0^\infty n_k n_{sq} \sigma_{sqk}(v_{\mathrm{rel}}) b_{sqk} d\Omega dl / 4\pi, \tag{1.3}$$

where n_k and n_{sq} denote the neutral and solar wind ion densities, $\sigma(v_{\mathrm{rel}})$ is the (relative) velocity-dependent cross-section of the CX process, and b_{sqk} is the branching ratio in transition j after the CX. The resulting CX signal is simply a line-of-sight integral of all the SWCX transitions from the telescope to infinity. The form of the equation is, in essence, similar to any collision emission process, like a collisionally ionised plasma; the intensity is a product of two densities and a cross-section. However, the CX cross-sections are 2–4 orders of magnitude larger than the collisional excitation cross-section ($\sim 10^{-15}\,\mathrm{cm}^2$ versus 10^{-19}–$10^{-17}\,\mathrm{cm}^2$). This explains how a short SWCX integration length within the heliosphere can already give comparable emissions to the LHB, which extends up to 100–200 pc [1].

The SWCX intensity is a strong function of solar wind density and ionisation. The r^{-2} radial dependence of the solar wind density dictates that the heliospheric SWCX would be contributed

[1] An order-of-magnitude comparison: The LHB size is about $\sim 10^5$ times larger than the heliosphere, but the LHB n^2 is $\sim 10^3$ times smaller than that of the heliosphere, meaning the LHB EM ($n^2 L$) is about $\sim 10^2$ larger than that of the heliosphere. Therefore, an approximately two orders of magnitude larger CX cross-section than the collisional cross-section could achieve emission comparable to that of the LHB.

more by regions close to the Sun. The ionisation states, a strong function of solar activity, also greatly affect the SWCX emission detectable in the X-ray band. For example, the O^{7+} ion abundance in the solar wind correlates positively with the solar cycle; therefore, the O VII line (from CX of O^{7+} ions capturing an electron from a neutral to form O^{6+}) is expected to be stronger towards solar maximum. The time evolution of the (heliospheric) SWCX is one of the main topics of Chapter 2.

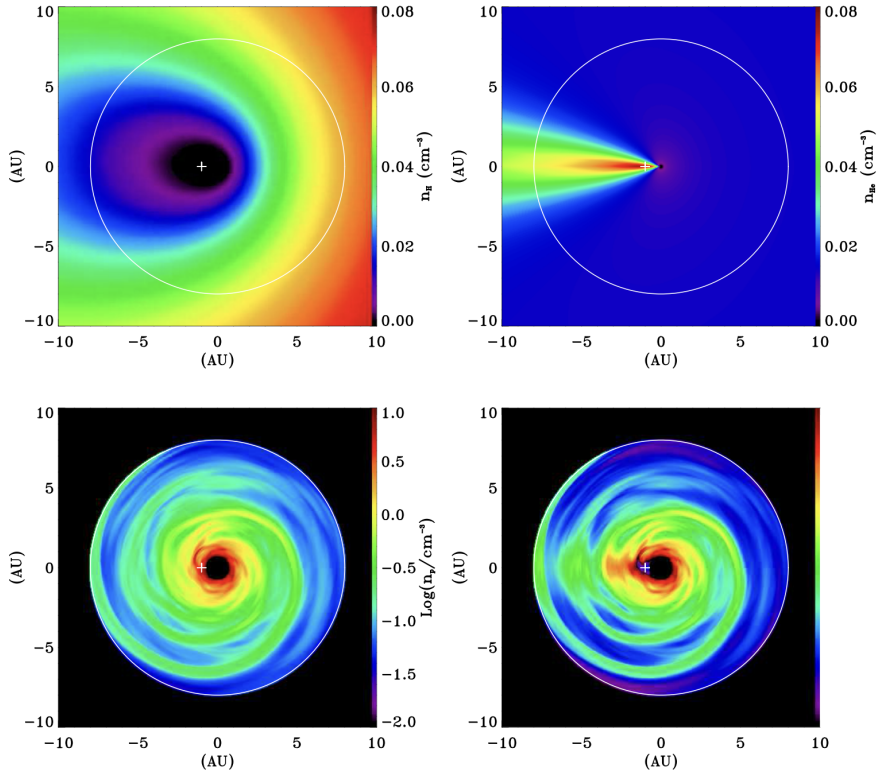

Figure 1.3: Densities of neutrals (H and He), solar wind proton and the prediction on the heliospheric solar wind charge exchange intensity. Each panel is centred on the Sun, and a white plus sign shows the Earth's location on 7 December. Direction to the right is the upwind direction of the Solar System with respect to the inflowing neutral ISM. (Top left) Neutral hydrogen density. It forms a cavity because neutral hydrogen can be ionised by the Sun's radiation and then be diverted by the magnetic field. (Top right) Neutral helium density. Unlike hydrogen, helium has a higher ionisation energy and cannot be ionised by the Sun. Therefore, it is only gravitationally deflected by the Sun to form the 'helium focusing cone' towards the downwind direction. (Bottom left) Proton density of the solar wind as a proxy for the heavy ion density. Due to the Sun's rotation, the solar wind forms a spiral structure known as the Parker spiral. It is worth noting that the density also drops radially ($\propto r^{-2}$). (Bottom right) The predicted SWCX emissivity calculated from $n_p v_{\rm rel}(\sigma_{\rm H} n_{\rm H} + \sigma_{\rm He} n_{\rm He})$. Figure courtesy of Kuntz (2019).

Heliospheric SWCX is the regime where this thesis will mainly focus on, as SRG/eROSITA carried out all-sky surveys outside of the Earth's exosphere, orbiting the Sun-Earth Lagrangian point L2, hence unaffected by geocoronal SWCX. Figure 1.3 shows an example of a calculation of the SWCX emissivity, with H and He neutral densities and solar wind proton density as input. Neutral H and neutral He have completely different density profiles because of the difference in their ionisation energy. Neutral H has a cavity in the inner Solar System because the Sun's radiation can ionise it. In contrast, He has a higher ionisation energy and cannot be efficiently ionised by the Sun, so the trajectory of He is deflected gravitationally by the Sun. The overall

effect is that it forms a feature called the 'helium focusing cone', where He has the highest density towards the downwind direction with respect to the inflowing neutral ISM (Weller & Meier, 1974). The SWCX emissivity also depends on the distribution of the heavy ions released from the Sun in a spiral pattern due to solar rotation known as the Parker spiral (Parker, 1958). Therefore, the resulting SWCX emissivity spatial profile is mainly dictated by the product of the two (Neutral H+He density profile × solar wind density profile), with additional scaling from the cross-sections and relative ion-neutral collision velocities (eq. 1.2). A simulated SWCX emissivity profile is shown in the bottom right panel of Fig. 1.3.

SWCX is the only SXRB component that is time-variable within the timescale of a few years because of the variability of the solar wind and solar activity. Its variability makes the repeating nature of eROSITA All-Sky Surveys (eRASSs), which surveyed the full sky every six months, a big advantage in isolating the SWCX contributions from the SXRB (see Sect. 1.9 details about eROSITA and eRASSs).

1.3.2 Spectral diagnostics of charge exchange

One of the most important line diagnostics for CX is from the He-like ions triplets, which includes the prominent O VII line at ∼0.57 keV. Gabriel & Jordan (1969) first proposed that the triplet line ratios can be used to probe plasma temperature or density (see also a review by Porquet et al., 2010). After the discovery of SWCX, it has been progressively shown that the triplet line ratio in CX spectra would be remarkably different from a CIE plasma (e.g. Beiersdorfer et al., 2003; Brown et al., 2009, and see Fig. 1.4).

The level scheme and the definition of the resonance (w), intercombination (x+y) and forbidden (z) lines are shown in Fig. 1.4. A useful diagnostic is called the G-ratio, defined as

$$G = \frac{z + (x + y)}{w}. \tag{1.4}$$

For CX, the forbidden (z) line is the brightest of the three, followed by the intercombination (x+y) line. The reason for this is that three-quarters of CX electron captures occur in the triplet states ($S = 1$), which can then radiatively cascade by allowed transitions into the ^3P states and the $^3S_1$ metastable level (Porquet et al., 2010). Additional decays from the ^3P states into the $^3S_1$ state can also occur (partly for $^3P_{1,2}$ and totally for $^3P_0$). The overall result is to boost the G-ratio compared to a CIE plasma. In contrast, for a CIE plasma where the excitation process is by electron collisions, the singlet $^1P_1$ level (resonance line) is preferred. This is because the change of spin (required to be excited to the $^3P_{0,1,2}$ or $^3S_1$ states from the $^1S_0$ ground state) is only possible by the exchange of the projectile electron with one of the two target electrons, but such 'exchange' process is disfavoured compared to the direct collision process at high projectile energies (high temperature). Indeed, enhanced forbidden line (high G-ratio) has been found in X-ray SWCX emissions of comets and planets, for instance from Mars's halo (Dennerl et al., 2006), Jupiter's aurorae (Branduardi-Raymont et al., 2007) and Comet C/2000 WM1 (Gu et al., 2016a). It has also been used to argue for the presence of CX in extra-solar objects, such as SNR (e.g. Rasmussen et al., 2001; Uchida et al., 2019; Tanaka et al., 2022; Gu et al., 2025), novae (Mitrani et al., 2024) and nearby galaxies (e.g. Liu et al., 2011; Yang et al., 2020). The power of the G-ratio for CX is that even with CCD-type spectral resolution where the O VII triplet is not resolved, the (redward) shift of the O VII blend peak energy allows one to infer the presence of CX (e.g. Liu et al., 2011; Roberts & Wang, 2015; Ponti et al., 2023b).

In some cases, only relying on enhanced G-ratio as evidence of CX may lead to a wrong conclusion, as other processes can lead to enhanced G-ratio, including recombination-dominated or photoionised plasma, resonance scattering and non-equilibrium plasma at the initial stage of heating (Porquet et al., 2010). However, misidentification of CX can be avoided if enhanced transitions from higher Rydberg states are identified in parallel to an enhanced G-ratio, such as Lyγ,δ of O VIII, because for most ions the CX process tends to capture electrons at an energy level

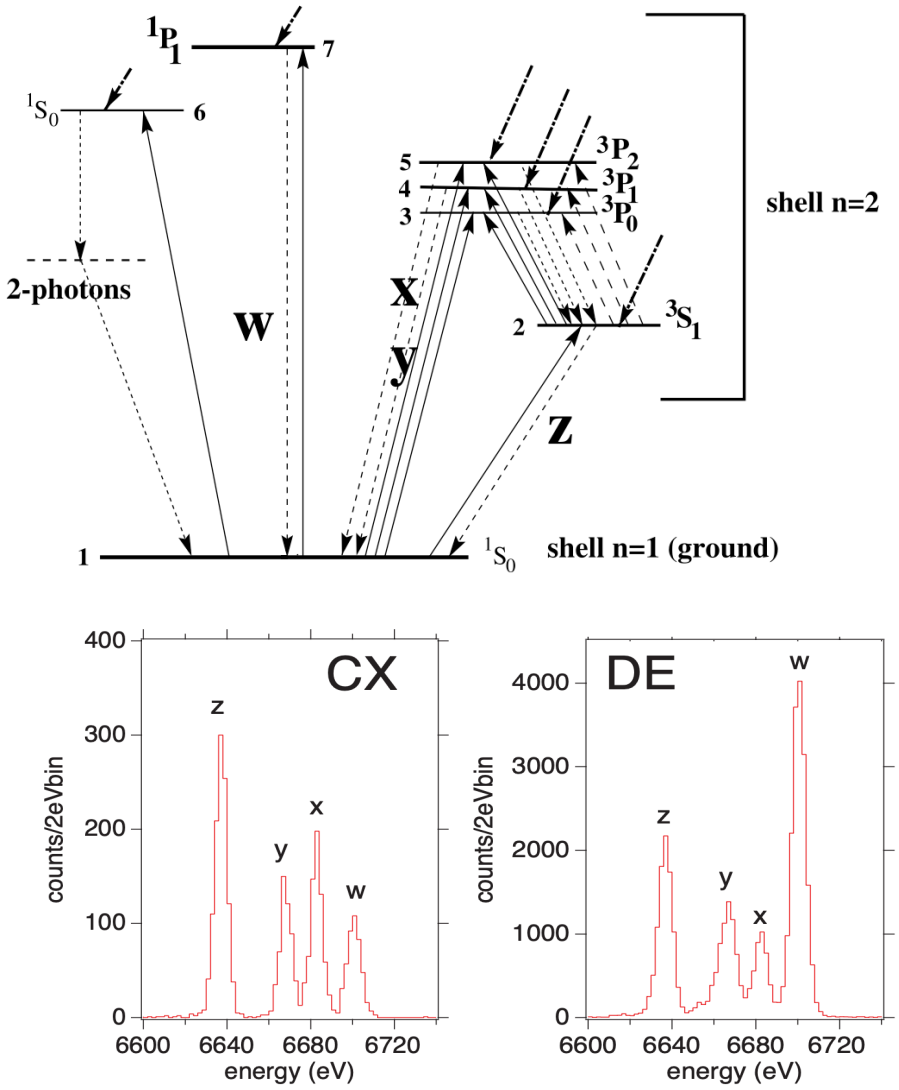

Figure 1.4: Simplified level scheme for He-like ions and a spectral comparison of CX versus collisional excitation process. (Top) Level scheme of a He-like ion. The resonance, intercombination and forbidden transitions are denoted by w, $x+y$ and z, respectively. Figure courtesy of Porquet & Dubau (2000). (Bottom) Spectra of He-like Fe (Fe XXVI) obtained from laboratory measurement, with the labelled transitions. The left panel shows the CX spectrum, and the right panel shows the spectrum resulting from direct electron impact excitation (DE). Figure courtesy of Brown et al. (2009).

$n > 1$. The most populated energy level after CX is described by

$$n_{\mathrm{p}} = \sqrt{\frac{I_{\mathrm{H}}}{2I_{\mathrm{t}}}q}\left(1+\frac{q-1}{\sqrt{2q}}\right)^{-1/2}, \tag{1.5}$$

where I_{H} and I_{t} are the ionisation potentials of H and the target atom, and q stands for the ion charge (Janev & Winter, 1985). Figure 1.5 demonstrates that CX preferentially captures electrons at energy level n_{p} and forms a peak around it. This means the radiative decay from $n \sim n_{\mathrm{p}}$ states would be enhanced, an unambiguous signature of CX. However, obtaining spectra of sufficient

quality (spectral resolution and signal-to-noise) would be expensive, and was only possible in bright objects in isolated cases (e.g. Rasmussen et al., 2001; Mitrani et al., 2024).

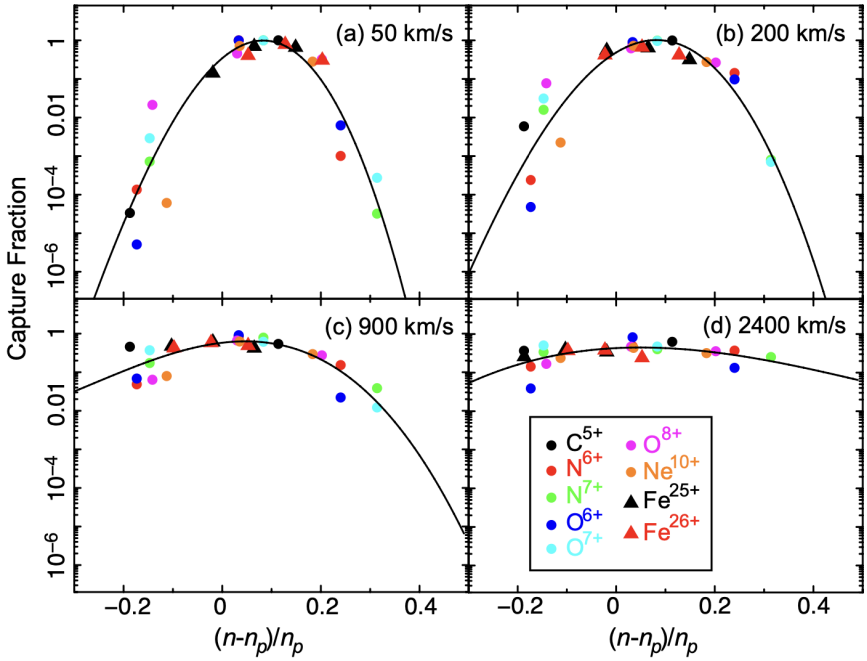

Figure 1.5: Fractions of electrons captured into n shell at different collision velocities. n_p represents the most populated level after CX (eq. 1.5), which is larger than 1 for most ions. This shows that the CX process preferentially populates energy states around $n_{\rm p}$ and forms a peak around it. Therefore, one would observe enhanced lines from $n > 1$ states if CX is present. Figure courtesy of Gu et al. (2016a).

1.4 Milky Way's circum-Galactic medium (CGM)

The Milky Way's hot halo or its circum-Galactic medium (CGM) is thought to possess a large portion of its baryonic content (see a review by Putman et al., 2012). Classically, it is believed to be heated to near its virial temperature by shock-heating during the accretion of the intergalactic medium and can extend up to the virial radius (e.g. White & Frenk, 1991). It can also trace the feedback mechanisms of the Galaxy. Observationally, this hot ($\sim 10^6$ K) phase can be probed by X-ray emission or absorption and pulsar dispersion measures, which can constrain the column of free electrons along the line-of-sight. In general, X-ray emission is biased towards the denser hot gas as EM scales as $\propto n^2$, while X-ray absorption studies making use of bright quasars' sightlines scale only with $\propto n$, are hence more sensitive to the outer halo, but suffer in terms of spatial coverage limited by the quasar sample. However, due to the tenuous nature of the hot halo (expected to be $n \sim 10^{-5}$–$10^{-4}\,{\rm cm}^{-3}$), its properties, such as its chemical abundance of this phase, are difficult to constrain.

From the perspective of the SXRB, a Galactic scale emitting component has always been suspected since the earliest days after its discovery (e.g. Bowyer et al., 1968), and has gradually been established as a necessary (but not the only) component in the SXRB (e.g. Wang & McCray, 1993; Snowden et al., 1998; Kuntz & Snowden, 2000; Yoshino et al., 2009; Henley & Shelton, 2013; Miller & Bregman, 2013; Ponti et al., 2023b). From the X-ray emission, the typical measured temperature of this component is ∼0.15–0.2 keV, consistent with the Milky Way's virial temperature. This aligns with the expectation of the hot, tenuous gas at $\sim 10^6$ K in the halo, as insufficient

time has elapsed after the heating by accretion shocks according to the cooling function (Miller & Bregman, 2013). Alternatively, this could also be the signature of higher-density gas being heated by stellar feedback, at a lower galactocentric distance.

A pilot study using the eROSITA Final Equatorial-Depth Survey (eFEDS), which has an exposure depth equivalent of eRASS:8, shows that with an excellent signal-to-noise (S/N) spectrum, the metal abundance of the CGM component in emission is low, as low as $Z = 0.1\,Z_{\odot}$ (Ponti et al., 2023b). This is lower than the conventional fiducial value of $Z = 0.3\,Z_{\odot}$ found in nearby galaxy clusters. A concern for such measurement using medium spectral resolution from CCDs is that the continuum level, hence the line strengths that determine the metal abundance, could be difficult to constrain for the line-dominated 0.2 keV plasma. On the other hand, bremsstrahlung is not the dominant continuum process for CIE plasma at this temperature, but the radiative recombination continuum is (RRC; Sect. 1.8.6). RRC of oxygen dominates the continuum at this range; it could therefore be reasonable that just the overall shape of CCD spectra, instead of a precise decomposition of lines and continuum, has the power to constrain the metal abundance.

Another finding from the eFEDS spectrum is that an additional hot component ($\sim$0.7 keV) is necessary to explain the residual about 0.7–1.0 keV (Ponti et al., 2023b). In this thesis, I follow the nomenclature of Ponti et al. (2023b) to call this the Galactic corona (COR; see Fig. 1.1). This 0.7 keV component is consistent with findings from absorption (Das et al., 2019) and pointed emission spectra (Gupta et al., 2021). The necessity of this 0.7 keV component seems to be more widespread, as shown by Halosat observations (Bluem et al., 2022). In the half-sky decomposition of the SXRB detailed in Chapter 3, despite the focus being on the LHB, an essential ingredient is the COR component, in which I was able to extract its spatial profile. An emerging result is that the COR spatial profile correlates excellently with the projected Milky Way stellar mass profile, with a luminosity per stellar mass agreeing well with the 10 pc volume-complete sample of low-mass stars. This suggests the 0.7 keV component is likely to be dominated by the coronal emissions from low-mass stars in the Galaxy instead of being a truly diffuse, 'super-virial' temperature component of the CGM. Currently, this result has been submitted to the journal Astronomy and Astrophysics, with me being the second author (Ponti et al., 2025). Based on this parallel development, in Chapter 4, a 'stars' component, made up of the stacked spectrum of the 10 pc volume-complete samples of low-mass stars and scaled by the three-dimensional stellar mass distribution of the Milky Way, will be used instead of the COR component in the modelling of the eROSITA bubbles' spectra.

1.5 Extragalactic cosmic X-ray background (CXB)

The SXRB spectrum above $\sim$1 keV is dominated by an extragalactic and isotropic background (Fig. 1.1), which I will refer to as the cosmic X-ray background (CXB) throughout this thesis. As mentioned at the beginning of this chapter, deep fields with high angular resolution telescopes like *Chandra* have shown that the hard X-ray background can virtually be fully resolved into discrete sources, mainly made of AGN. This is arguably a bigger topic than the Galactic part of SXRB, as the integrated emission from AGN across redshifts encodes the formation history of these supermassive black holes, their immediate environment, as well as their host galaxies. My treatment of the CXB is simple, nevertheless, in line with previous work on the subject of the SXRB. The CXB is well-known to follow a power-law spectrum between 1–10 keV (e.g. Gilli et al., 2007), and according to CXB synthesis models, some indication of steepening that might come from hot gas in galaxies and galaxy clusters below 1 keV. Observationally, the steepening is poorly constrained. Therefore, in my SXRB analyses, some freedom is given to this part: simple, broken and even double-broken power law models will be tested and compared (Chapter 3). While the slope at energies below 1 keV is poorly constrained, the slope above 1 keV is between 1.4–1.5 and its normalisation is about 8.2 photons $\mathrm{s^{-1}\,cm^{-2}\,sr^{-1}}$ at 1 keV (Gilli et al., 2007). This will be a fiducial value to compare with our eROSITA CXB measurement. Naturally, this value implicitly assumes a negligible contribution from Galactic sources and no masking of detected point sources, including the AGN.

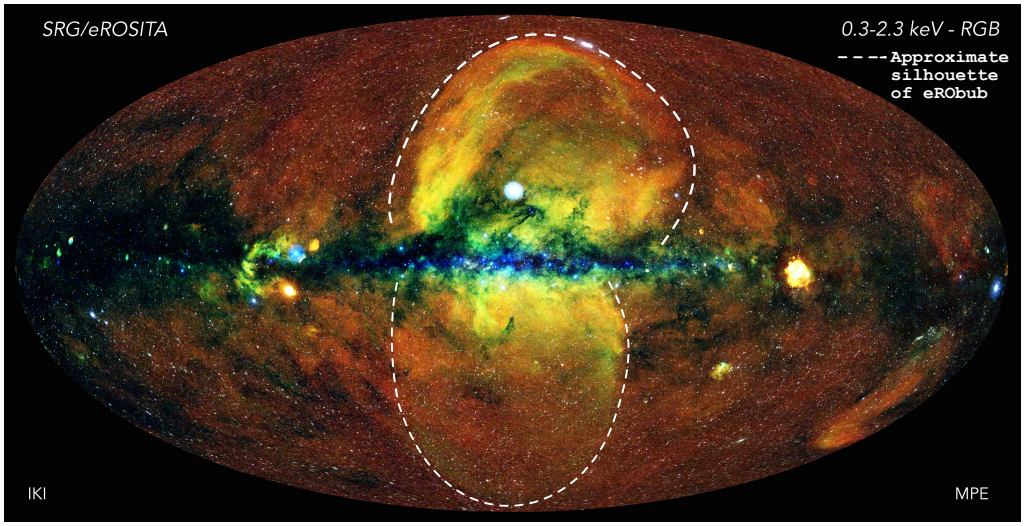

Figure 1.6: eRASS1 false-colour all-sky map (red: 0.3–0.6 keV; green: 0.6–1.0 keV; blue: 1.0–2.3 keV). The white dashed line indicates the approximate silhouette of the eRObub. Image Credit: Jeremy Sanders, Hermann Brunner and the eSASS team (MPE); Eugene Churazov, Marat Gilfanov (on behalf of IKI)

1.6 eROSITA bubbles (eRObub)

The eROSITA bubbles (eRObub) were one of the headline discoveries of the SRG/eROSITA mission (Predehl et al., 2020). The eRObub refer to the pair of bubble-like structures that stem apparently from the inner galaxy, each subtends about $80^\circ \times 80^\circ$ above and below the Galactic plane as shown by the eRASS1 false colour map (red: 0.3–0.6 keV; green: 0.6–1.0 keV; blue: 1.0–2.3 keV) in Fig. 1.6. Their emissions are the brightest in the 0.6–1.0 keV band. The structures of the northern bubbles are already well-known, and the bright eastern edge that extends towards the east is known as the North Polar Spur (NPS) (Egger & Aschenbach, 1995). The key that makes this a discovery is the clear signal of a counterpart in the southern Galactic hemisphere, which shows signs of brightened limbs. It is worth mentioning that in the same year, Nakahira et al. (2020) had already suggested the existence of the southern bubble with the MAXI 0.7–1.0 keV all-sky map, albeit with much less significance. The combined argument that the eRObub is approximately symmetric about the Galactic disk and the known existence of the Fermi bubbles (FB) in γ-rays (Su et al., 2010; Ackermann et al., 2014) seems to suggest that the eRObub is a Galactic-scale structure. Assuming a spherical geometry for each bubble and putting them above the GC region to match the projected emission, they correspond to structures that extend ~ 14 kpc vertically. Interestingly, the eRObub are larger than the FB, roughly twice in terms of radius.

One of the key uncertainties regarding the eRObub is their physical size. In fact, the discussion started way before we knew about the eRObub, at the time when all-sky radio surveys became available. Multiple giant radio loops were found to stem from the Galactic plane (e.g. Hanbury Brown et al., 1960; Berkhuijsen et al., 1971; Berkhuijsen, 1972; Haslam et al., 1974, 1982). The most prominent one, Loop I, which is co-spatial with the NPS in X-ray, was immediately proposed to be a SNR which has compressed magnetic fields at the shock front to emit synchrotron radiation (Hanbury Brown et al., 1960). In addition, for Loop I to venture as high as 80° in latitude, it should be fairly close (< 100 pc). On the other hand, an alternative scenario involving an explosion from the GC or nuclear starburst was proposed by Sofue (e.g. 1973, 1977, 1994, 2000). Obviously, the two scenarios differ by orders of magnitude in terms of energetics (SNR $\sim 10^{51}$ erg versus Galactic $\sim 10^{56}$–10^{57} erg), but could be remarkably similar in terms of surface brightness. This is one of the largest reasons why there has been little consensus on the nature of the Loop I/NPS/eRObub for decades. Egger & Aschenbach (1995) proposed that the NPS is created by the shock heating inside

a neighbouring superbubble, called the Loop I superbubble, $\sim$ 100–200 pc from us. This idea has been popular since the ROSAT era, since a ring of denser H I gas can be found around 100 pc from us in that direction, consistent with the predictions from numerical simulations of two old merging bubbles. The discovery of the FB motivated systematic studies of the X-ray emission across the FB (Kataoka et al., 2013, 2015). Using Suzaku data, Kataoka et al. (2013, 2015) demonstrated that if they assume a CIE component to model the X-rays from the 'FB', its EM drops sharply with latitudes, but its temperature would agree with a constant at $\sim$ 0.3 keV. Relying on a series of XMM-Newton observations of the southern NPS terminus and three-dimensional dust maps, Lallement et al. (2016) was able to set a conservative lower limit of 300 pc to the base of the NPS. More recently, Zhang et al. (2024) provides more evidence supporting the non-local origin of the eRObub by comparing the radio polarisation intensity maps and the expected depolarisation level at different frequencies. Combining X-ray shadowing and polarised features in radio maps, Liu et al. (2024) also suggests the eRObub are of non-local origin.

There have been many proposals for the Fermi/eROSITA bubbles, either as causally separate or connected structures. Lallement (2023) and Sarkar (2024) provide comprehensive reviews on the topic. The proposals can be primarily separated into two classes, AGN-driven or star-formation driven. Although AGN-driven scenarios are all related to the supermassive black hole at the GC, models differ regarding the energy injection time-scales. In an AGN burst scenario, which could be created from jets or tidal disruption events, most models that describe the morphology and spectrum of the FB well would produce an eRObub temperature that is higher than what is observed in the eRObub ($\sim$ 0.3 keV). It is also unclear whether the FB and the eRObub result from a single burst or two bursts. On the other hand, a more continuous mode of energy injection in the past $\sim$ 30 Myr, such as an enhanced (factor of a few) star-forming activity, likely from the central molecular zone ($\sim$ 200 pc from the GC) or in larger scale star-forming regions 3–5 kpc from the GC, is needed to explain the energetics.

Chapter 4 investigates the hot gas properties and the three-dimensional geometry of the eRObub using eRASS1 data, arguably the best dataset for the purpose, at least in terms of spatial coverage.

1.7 Interstellar absorption

At energies below 2.5 keV, photoionisation is the dominant process for absorption in X-rays in the ISM, above which Compton scattering becomes important (Draine, 2011). The photoionisation cross-section of hydrogen and hydrogenic ions can be solved analytically (Bethe & Salpeter, 1957). The frequency-dependent cross-section is given by eq. 13.1 in Draine (2011) (see also eq. 71.7 of Bethe & Salpeter, 1957):

$$\sigma_{\rm pi}(\nu) = \sigma_0 \left(\frac{Z^2 I_{\rm H}}{h\nu}\right)^4 \frac{e^{4-(4\arctan x)/x}}{1-e^{-2\pi/x}}, \tag{1.6}$$

where

$$x \equiv \sqrt{\frac{h\nu}{Z^2 I_{\rm H}} - 1} \tag{1.7}$$

$$\sigma_0 \equiv \frac{2^9\pi}{3e^4} Z^{-2} \alpha \pi a_0^2 = 6.304 \times 10^{-18} Z^{-2}\,{\rm cm}^2. \tag{1.8}$$

Z is the nuclear charge, $I_{\rm H} = 13.6$ eV is the hydrogen ionisation potential, $\alpha = e^2/\hbar c$ is the fine-structure constant and $a_0 = \hbar/m_e c\alpha$ is the bohr radius. The cross-section reaches the maximum at $h\nu = Z^2 I_{\rm H}$. Usually, power-law approximations to the asymptotic behaviour at energies above the peak are used. Between $Z^2 I_{\rm H} < h\nu < 100 Z^2 I_{\rm H}$, an approximation of

$$\sigma_{\rm pi} \approx \sigma_0 \left(\frac{h\nu}{Z^2 I_{\rm H}}\right)^{-3} \tag{1.9}$$

is common. For $h\nu \gg Z^2 I_{\rm H}$,

$$\sigma_{\rm pi} \rightarrow \frac{\sigma_o e^4}{2\pi} \left(\frac{h\nu}{Z^2 I_{\rm H}} \right)^{-3.5} . \tag{1.10}$$

For multi-electron atoms, the energy-dependent cross-section is complex, as the resulting ion has multiple possible states. Despite the complexity, the cross-sections of multi-electron atoms follow approximately the $\sigma \propto \nu^{-3}$ asymptote, with jumps at energies of the ionisation energy of the $n = 1, 2, 3, \ldots$ levels known as absorption edges. Figure 1.7 shows the cross-sections of abundant elements in the ISM (Cruddace et al., 1974). Many absorption edges in the soft X-ray energies are K-shell absorption edges, corresponding to the photoionisation of an electron from the $n = 1$ level. It is clear from Fig. 1.7 that the cross-section of heavy elements at X-ray energies (1–100 Å) is about four orders of magnitude higher than that of a hydrogen atom. This entails that, despite the abundance of metals being about a thousand times lower than that of hydrogen, metals in the ISM dominate the X-ray absorption above their respective K-edges.

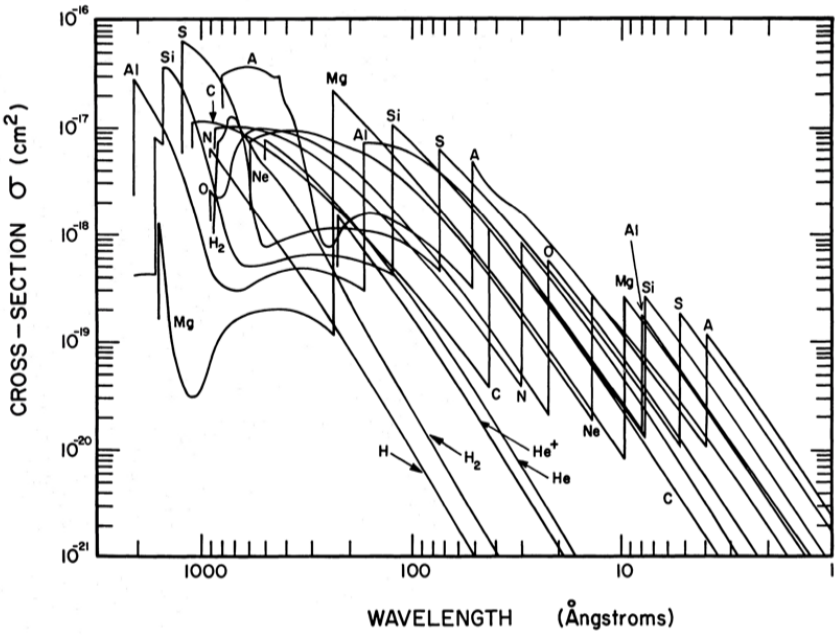

Figure 1.7: Photoabsorption cross-section of abundant elements in the ISM as a function of wavelength. Figure courtesy of Cruddace et al. (1974).

For practical purposes, photoionisation cross-sections are commonly fitted by analytical functions (Verner & Yakovlev, 1995; Verner et al., 1996). For simplicity, only ISM in the gas phase is considered here, that is $\sigma_{\rm ISM} = \sigma_{\rm gas}$. A more complete treatment, which considers both molecules (mostly H_2) and dust grains, can be found in Wilms et al. (2000). For the gas phase ISM, it is convenient to weight the cross-section of each element using their abundance with respect to hydrogen (e.g. Anders & Grevesse, 1989; Wilms et al., 2000; Lodders, 2003). The total energy-dependent cross-section of the ISM is given by

$$\sigma_{\rm ISM} = \sum_{Z,i} \frac{N(Z)}{N_{\rm H}} a_{Z,i} \sigma_{Z,i}(E), \tag{1.11}$$

where $N(Z)/N_{\rm H}$ denotes the number fraction of element Z with respect to H, $a_{Z,i}$ is the fraction of element Z in ionisation state i and $\sigma_{Z,i}$ is the cross-section of the atom or ion of element Z at ionisation state i. Finally, the observed X-ray spectrum after the attenuation of the ISM is related

to the source spectrum I_0 by

$$I_{\rm obs}(E) = I_0(E) \exp\left[-N_{\rm H}\sigma_{\rm ISM}(E)\right]. \tag{1.12}$$

Figure 1.8 shows the photoelectric cross-section of the ISM as a function of energy after considering the ISM metal abundance and the metals' respective cross-sections. It is worth noting that the ISM cross-section decreases roughly as E^{-3}, modified by the absorption edges from different elements. This is the reason why photoelectric absorption affects the softest X-rays the strongest. The ISM is opaque to photons as this energy with a column density as low as $N_{\rm H} \sim 10^{20}\,{\rm cm}^{-2}$, which is easily reached within 100–200 pc. Therefore, in the context of the SXRB, the fact that significant counts were measured from the Wisconsin B, C bands and ROSAT R1, R2 bands (∼0.1–0.3 keV) all sky is strong evidence to suggest that the source is of local origin.

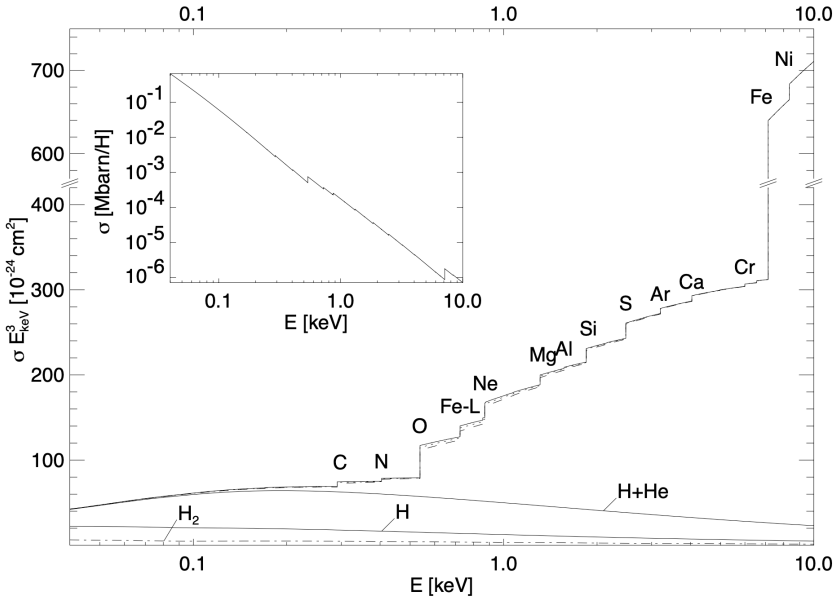

Figure 1.8: ISM photoelectric cross-section as a function of energy (Wilms et al., 2000). Notice that the y-axis of the main panel has been multiplied by E^3 to flatten the curve with respect to the asymptotic behaviour of the H cross-section. The inset shows the cross-section without the extra scaling. The dashed and dotted lines illustrate the effect of molecular hydrogen and metals being locked in dust grains of different sizes. Their effects are generally subdominant. Figure courtesy of Wilms et al. (2000).

1.8 Plasma emission processes

1.8.1 The coronal model and collisional ionisation equilibrium (CIE)

The coronal model is the standard set of assumptions commonly used to predict X-ray emission spectra. Mewe (1999) summarised the assumptions as follows.

1. The plasma is optically thin. This implies photoionisation is unimportant.
2. The gas density is low such that the excited state populations are negligible compared to the ground state population.
3. Radiation losses are balanced by non-radiative heating.

4. The plasma electrons and ions follow Maxwellian distributions with a common temperature controlled by external processes.

5. The gas is in a steady state of statistical equilibrium, both for the bound atomic states and ionisation balance.

A simple description of a plasma that obeys the above assumptions is called a plasma in collisional ionisation equilibrium (CIE). CIE refers to a stationary state of the plasma, where there is a balance between collisional ionisation (direct ionisation + excitation-auto-ionisation) and recombination (radiative + dielectronic). CIE plasma is used extensively to model the X-ray emissions of many components of the X-ray background in this thesis, such as the LHB, Milky Way's CGM and the eRObub.

For each ion in ionisation state i of element Z, the rate of change of the its volume density ($n_{Z,i}$; in cm^{-3}) at electron temperature T_e follows

$$\frac{dn_{Z,i}}{dt} = n_e\{\alpha_{Z,i+1}(T_e)n_{Z,i+1} + S_{Z,i-1}(T_e)n_{Z,i-1} - n_{Z,i}[S_{Z,i}(T_e) + \alpha_{Z,i}(T_e)]\}, \tag{1.13}$$

where $\alpha_{Z,i}$ and $S_{Z,i}$ denotes the total recombination and total ionisation rate coefficients ($\mathrm{cm}^3\,\mathrm{s}^{-1}$) of ion Z^{+i}. The first term on the right represents the increase in ion density due to recombination from a more ionised ion, and the second term describes the gain in ion density from ionisation from a less-ionised ion or atom. The last term on the right denotes the loss of ion density due to both ionisation to a higher ionisation state and recombination to a lower ionisation state. In general, since there are $Z+1$ ionisation states for a given atom, eq. 1.13 is a system of $Z+1$ differential equations. In CIE, which is a steady-state equilibrium, $\frac{dn_{Z,i}}{dt} = 0$. Since $i = 0$ refers to a neutral atom, there is no ionisation level below it, eq. 1.13 in CIE reduces to

$$n_{Z,1} = n_{Z,0}\frac{S_{Z,0}}{\alpha_{Z,1}}. \tag{1.14}$$

This result can be applied to solve $n_{Z,2}$ and so on. The density ratio of two adjacent ionisation stages is given by

$$\frac{n_{Z,i+1}}{n_{Z,i}} = \frac{S_{Z,i}(T_e)}{\alpha_{Z,i+1}(T_e)}. \tag{1.15}$$

A more convenient quantity to use is the fraction of element Z on ionisation stage i, $\frac{n_{Z,i}}{n_Z}$, such that $n_Z = \sum_{i=0}^{Z} n_{Z,i}$, where n_Z is determined by the total gas density and chemical abundances. A more in-depth review can be found in Kaastra et al. (2008).

1.8.2 Non-equilibrium ionisation (NEI)

In general, the system of equations described in eq. 1.13 can be solved numerically, if we know or assume T_e as a function of time, hence specifying $\alpha_{Z,i}(t)$ and $S_{Z,i}(t)$. The solution then represents the time evolution of the density of each ion population. One can express eq. 1.13 in matrix form,

$$\frac{1}{n_e}\frac{d\vec{F}}{dt} = -\mathbf{A}(Z, T_e(t)) \cdot \vec{F}(t), \tag{1.16}$$

where

$$\mathbf{A} = -\begin{pmatrix} -S_0 & \alpha_1 & 0 & 0 & \cdots & & & & \\ S_0 & -S_1-\alpha_1 & \alpha_2 & 0 & \cdots & & & & \\ 0 & S_1 & -S_2-\alpha_2 & \alpha_3 & \cdots & & & & \\ \vdots & \vdots & \vdots & \vdots & \ddots & & & & \\ & & & & & S_{Z-3} & -S_{Z-2}-\alpha_{Z-2} & \alpha_{Z-1} & 0 \\ & & & & & 0 & S_{Z-2} & -S_{Z-1}-\alpha_{Z-1} & \alpha_Z \\ & & & & & 0 & 0 & S_{Z-1} & -\alpha_Z \end{pmatrix}, \tag{1.17}$$

and

$$\vec{F} \equiv (n_{Z,0}, n_{Z,1}, \ldots, n_{Z,Z})/n_Z, \tag{1.18}$$

such that $\vec{F}$ is a normalised vector representing all the ionisation fractions of element Z and $|\vec{F}| = 1$. Solving this numerically is computationally expensive, especially when used for spectral fitting. A much faster way was proposed by Hughes & Helfand (1985) (see also Kaastra & Jansen, 1993; Smith & Hughes, 2010), which is to decouple the system of equations by pre-computing the eigenvalues and eigenvectors of $\mathbf{A}$ and solving independent ordinary differential equations instead. A caveat is that the electron temperature must be assumed constant after the sudden jump, which is generally sufficient to describe transient plasma in SNR. A useful transformation is to define $\vec{G} \equiv \vec{F} - \vec{F_{\rm eq}}$, where $\vec{F_{\rm eq}}$ corresponds to the CIE solution, such that $\lim_{t\to\infty} \vec{G} = 0$. The constant term $\mathbf{A} \cdot \vec{F_{\rm eq}}$ can be dropped after the substitution, so that

$$\frac{d\vec{G}}{dt} = -n_e \mathbf{A} \cdot \vec{G}. \tag{1.19}$$

One can compute eigenvalues $\vec{\lambda}$ and form a matrix of eigenvectors $\mathbf{V}$ from $\mathbf{A}$. Because the temperature is assumed constant, $\mathbf{V}$ is not a function of t. The coupled system of equation can be decoupled by setting $\vec{G'} \equiv \mathbf{V}^{-1}\vec{G}$ and $\mathbf{\Lambda} \equiv \vec{\lambda}\mathbf{I}$ to give

$$\frac{d\vec{G'}}{dt} = -n_e(\mathbf{AV})(\mathbf{V}^{-1}\vec{G}) = -n_e \mathbf{\Lambda}\vec{G'}, \tag{1.20}$$

which has a simple solution of

$$\vec{G'}(t) = \vec{c}\exp(-n_e\vec{\lambda}t), \tag{1.21}$$

where $\vec{c}$ is the integration constant dependent on the initial conditions. We can recover the original difference in ionic fraction from CIE by transforming $\vec{G} = \mathbf{V}G' = \mathbf{V}\mathbf{V}^{-1}\vec{G}$. The property $\lim_{t\to\infty} \vec{G} = 0$ also means all elements of $\vec{\lambda}$ are greater than 0, so that the ionic fractions will exponentially approach the steady-state solution. From the exponent in the solution, one can see that the parameter that dictates the ionic evolution of transient plasma is $n_e t$, called the ionisation timescale. Intuitively, the electron density enters the dependence because the ionisation process is controlled by collisions, in addition to time. Figure 1.9 shows two relevant ionisation timescales towards equilibrium for some astrophysically important elements, computed using the method described above with input of ionisation and recombination rates from Mazzotta et al. (1998).

1.8.3 Collisional ionisation

The last two Sections described how to compute the ion population at a given temperature (and ionisation timescale; for NEI), but did not explicitly mention the form of the ionisation and recombination coefficients except for their temperature dependence. Here, we begin with collisional ionisation. Collisional ionisation is the sum of two contributions: direct ionisation and excitation-autoionisation.

Direct ionisation refers to the case where a free electron with energy larger than the ionisation energy of the bound electron excites the bound electron to a free state.

$$Z^{+i} + e^- \rightarrow Z^{+(i+1)} + 2e^- \tag{1.22}$$

A commonly used formula for the cross-section of this process is the empirical Lotz formula (Lotz, 1967):

$$\sigma_{\rm DI} = \pi a_0^2 \sum_{k=m}^{N} C_k \xi_k \left\{1 - b_m \exp\left[1 - c_m\left(\frac{E}{\chi_k} - 1\right)\right]\right\} \left(\frac{E_{\rm H}}{\chi_m}\right)^2 \frac{\ln(E/\chi_m)}{E/\chi_m}. \tag{1.23}$$

In the equation, m stands for the subshell of the bound electron such that χ_m is the ionisation energy of subshell m. ξ_k is the number of electrons in subshell k. b_m and c_m are fitted coefficients

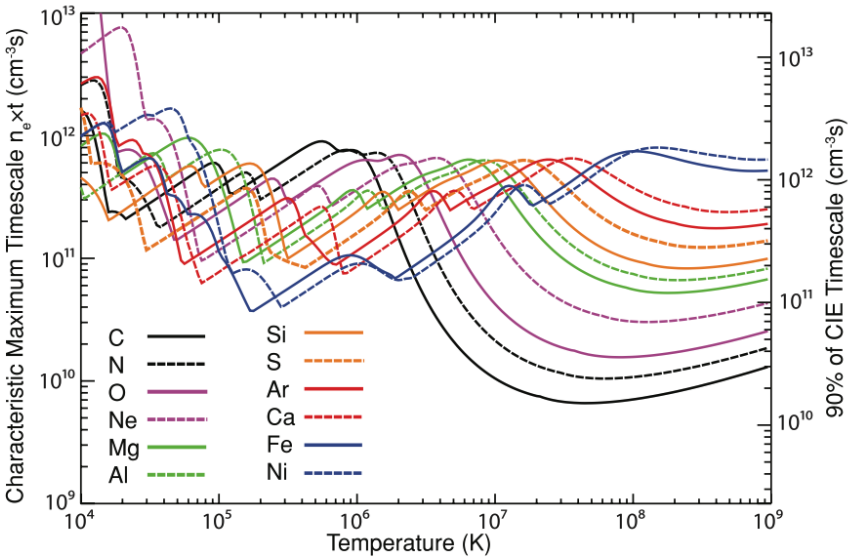

Figure 1.9: Ionisation timescales of astrophysically abundant elements as a function of temperature in a constant temperature plasma. Two criteria are shown. The left vertical axis represents the maximum characteristic ionisation timescale for an element of interest to reach a fraction of $1/e$ towards CIE. 'Maximum' here refers to the ionisation level that takes the longest time. The right vertical axis indicates the time for all ionisation levels of an element to be within 10% of the equilibrium value. Figure courtesy of Smith & Hughes (2010).

listed in Lotz (1967). The bracketed term approximates the behaviour near the threshold energy, which is only significant for low-charge ions at low temperatures. This term reduces to 1 for multiply ionised atoms (>4) and $C_k = 2.76$ (Lotz, 1968). The direct ionisation rate coefficient can then be found by an integration over a Maxwellian distribution, yielding

$$S_{\rm DI} \approx 1.5 \times 10^{-10} \left(\frac{\chi_m}{1\,{\rm keV}}\right)^{-2} \left(\frac{T}{10^7\,K}\right)^{1/2} \exp\left(-\frac{\chi_m}{kT_e}\right)\ {\rm cm}^3\,{\rm s}. \tag{1.24}$$

The other contribution of collisional ionisation comes from excitation-autoionisation, which is most important for atoms with a large number of inner shell electrons compared to the outermost shell. Excitation-autoionisation refers to an electron impact excitation of a bound electron from the ground state to a level above the first ionisation energy (minimum energy to ionise a bound electron), and subsequently followed by autoionisation. The process can be summarised as

$$Z^{+i} + e^- \rightarrow (Z^{+i})^* + e^- \rightarrow Z^{+(i+1)} + 2e^-. \tag{1.25}$$

A common description of excitation-autoionisation coefficients relies on parametrised models with parameters recorded in tables compiled from analytical fits of laboratory data. This is adopted by two of the most popular X-ray spectral fitting codes SPEX (Kaastra et al., 1996) and Xspec (Arnaud, 1996). For example, Arnaud & Raymond (1992) approximates the excitation-autoionisation rate coefficient using

$$S_{\rm EA}(T) = 2.28 \times 10^{-8} \left(\frac{T}{10^7}\right)^{-1/2} e^{-x} F(x)\,{\rm cm}^3\,{\rm s}^{-1}, \tag{1.26}$$

where $x = E_{\rm EA}/kT$ and $E_{\rm EA}$ is a free excitation energy fitted to the laboratory measured cross-sections. $F(x)$ is a complicated function that contains another four parameters, again, fitted to reproduce the measured cross-sections.

1.8.4 Radiative recombination

The reverse process of ionisation is recombination. In CIE, the ionisation rate is balanced by the recombination rate. The latter mainly consists of two processes: radiative recombination and dielectric recombination. Radiative recombination refers to the process

$$Z^{+(i+1)} + e^- \rightarrow Z^{+i} + h\nu. \tag{1.27}$$

A single photon with energy $h\nu$ is released in radiative recombination.

This is the inverse process of photoionisation. Milne (1924) utilised the principle of detailed balance in thermodynamic equilibrium to derive the relation between the photoionisation cross-section and the radiative recombination cross-section, now known as the Milne relation,

$$\frac{\sigma_{\rm RR}}{\sigma_{\rm PI}} = \frac{(h\nu)^2}{2Em_ec^2}\frac{g_i}{g_{i+1}}. \tag{1.28}$$

Here, E is the energy of the free electron, while $h\nu$ is the energy of the emitted photon. g stands for the statistical weight of the two ionisation levels. Although the Milne relation was calculated under the assumption of thermodynamic equilibrium, it still holds outside of such an assumption because the cross-sections are fundamentally atomic properties.

For hydrogenic ions of atomic number Z, the photoionisation cross-section from principal quantum number n is given by the Kramers-Gaunt formula (Gaunt, 1930):

$$\begin{cases} \sigma_{{\rm PI},n}(\nu) = 7.9\times10^{-18} n Z^{-2} f_1 \left(\frac{\nu_n}{\nu}\right)^3 \ {\rm cm}^2 & \text{for} \quad \nu \geqslant \nu_n \\ \sigma_{{\rm PI},n}(\nu) = 0 & \text{for} \quad \nu < \nu_n \end{cases}, \tag{1.29}$$

where f_1 is the Gaunt factor (in the order of unity). One needs to integrate the electron energy over a Maxwellian electron distribution $\int v\sigma_{\rm RR}dv$ and sum over all the principal quantum numbers n to yield the total radiative recombination coefficient (α; in ${\rm cm}^3\,{\rm s}^{-1}$). A popular formula to use for the total recombination coefficient is from Seaton (1959)

$$\alpha = 5.197\times10^{-14} Z\lambda^{1/2}[0.4288 + 0.5\ln\lambda + 0.469\lambda^{-1/3}], \tag{1.30}$$

where $\lambda = 157890Z^2/(T/{\rm K})$.

1.8.5 Dielectric recombination

Dielectric recombination is a multi-step process where two electrons are in play, analogous to excitation-autoionisation but in the reverse direction. The first step is the capture of a free electron. Instead of releasing a photon as in radiative recombination, the kinetic energy is used to excite an inner shell electron to a doubly excited state (above the first ionisation limit):

$$Z^{+(i+1)} + e^- \rightarrow (Z^{+i})^{**}. \tag{1.31}$$

The inner shell excited electron now has two pathways: autoionising again or decaying by spontaneous radiative transition to a state below the first ionisation limit. No recombination occurs in the first case, which is called the Auger effect. The second case is called dielectric recombination:

$$(Z^{+i})^{**} \rightarrow (Z^{+i})^{*} + h\nu, \tag{1.32}$$

and photon energy $h\nu$ corresponds to a dielectric satellite line. The satellite line is so named because its energy is shifted slightly to a slightly longer wavelength because of the electrostatic shielding provided by the captured electron on an excited level. In fact, the satellite line is the only observable effect of dielectric recombination. Dielectric recombination becomes favourable over autoionisation for large Z atoms, especially highly ionised ones. Lastly, the electron from the singly excited state also decays to the ground state by a cascade:

$$(Z^{+i})^{*} \rightarrow Z^{+i} + h\nu' + h\nu'' + \cdots. \tag{1.33}$$

The dielectric recombination coefficient can be approximated by

$$\alpha_{\rm DR} \approx 6.55 \times 10^{-27} \left(\frac{T}{10^7\,{\rm K}}\right)^{-3/2} \sum_s B_s \exp\left(-E_s/kT\right), \tag{1.34}$$

with $B_s \equiv \frac{w_S A^a_S S^r_S}{w_1(A^a_S + \sum A^r_S)}$, where $A^{a,r}$ stand for spontaneous autoionisation or radiative decay rates in $\rm s^{-1}$ and $w_s = 2l(l+1)$ is the statistical weight of excited state S (e.g. Bely-Dubau et al., 1979).

1.8.6 Radiative recombination continuum

A free electron recombines with the release of a photon of energy $\chi + \frac{1}{2}mv^2$, where χ is the ionisation energy of the recombined level. Radiative recombination, in addition to line emissions from the radiative cascade, is a continuum emission process as the free electrons have a continuous energy distribution. The emissivity of radiative recombination continuum (RRC) can be derived from the Milne relation again (eq. 1.28), connecting with the photonionisation cross-section (eq. 1.29), with the integration over a Maxwellian distribution for the energy of the free electrons. The resulting emissivity is given by (e.g., eq. 207 in Kahn 2005 or eq. 10.25 in Draine 2011)

$$\epsilon(T,\nu) = n_e n_{Z,i} \frac{g_{Z,i}}{g_{Z,i+1}} \frac{2h^4\nu^3}{(2\pi m_e kT)^{3/2}c^2} \sigma_{\rm PI}(\nu) e^{(\chi-h\nu)/kT}. \tag{1.35}$$

A few aspects of the equation are interesting:

1. It is 0 below the threshold energy because the photoionisation cross-section is 0 below the threshold.
2. When $h\nu \gtrsim kT$, the emissivity has a shape of exponential cut-off with energy.
3. The width of the RRC is dictated by the electron temperature, due to the factor $e^{-h\nu/kT}$. The RRC is wide, sometimes indistinguishable from bremsstrahlung, if the temperature is high; conversely, the RRC can appear line-like if the electron temperature is low. In fact, the width of the RRC is a diagnostic of electron temperature (Liedahl, 1999).

RRC is relatively important for 'cool plasma' ($\sim$0.1 keV) where bremsstrahlung is weak. Such cool plasmas could be found, for instance, in the LHB, from RRC of $O^{6+,7+}$ ions. This also means that the elemental abundance can affect the continuum level. Model RRC spectra of three different temperatures are shown in Fig. 1.10, which illustrates the cut-off below the ionisation energy as well as the positive correlation of the electron temperature with the width of the RRC. For hot gas at temperatures of 100–200 eV, which can be found in the LHB and CGM, the RRC would be even wider and difficult to isolate from the bremsstrahlung continuum (Sect. 1.8.7).

An excellent example of RRC in astrophysical spectrum is from the classical nova YZ Ret (Mitrani et al., 2024). Figure 1.11 shows the XMM-Newton/RGS spectrum of it. An exponential decay blueward of the ionisation energy of C^{4+} can clearly be seen in the spectrum. In the spectrum, the RRC is narrow, hence identifiable. The width suggests an electron temperature of 1.96 ± 0.04 eV. In contrast to the model RRC spectrum in Fig. 1.10, there is no cut-off below the ionisation energy of C^{4+} because of the unusually high population of the high-n levels of the same ion. The authors suggest this is very strong evidence for CX of C^{5+} ion with neutral H, resulting in a population of C^{4+} ions at high-n levels (Sect. 1.3.2). This is the first unambiguous evidence of CX in an extrasolar object.

1.8.7 Thermal bremsstrahlung

Bremsstrahlung is the German word for 'braking radiation'. As the word entails, it is a process where a charged particle undergoes emission because of the acceleration it experiences in the Coulomb field of another charged particle. The dominant bremsstrahlung process in a plasma is

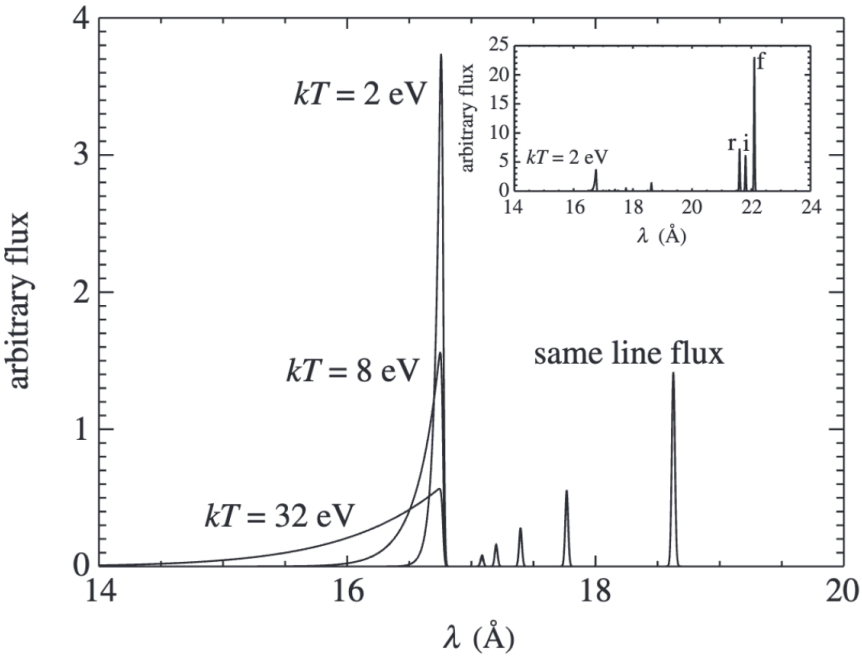

Figure 1.10: Model radiative recombination continuum spectra from recombining into He-like oxygen at three different electron temperatures. It demonstrates that the RRC width depends on the electron temperature and illustrates the sharp cut-off below the ionisation energy of He-like oxygen. Figure courtesy of Kahn et al. (2002).

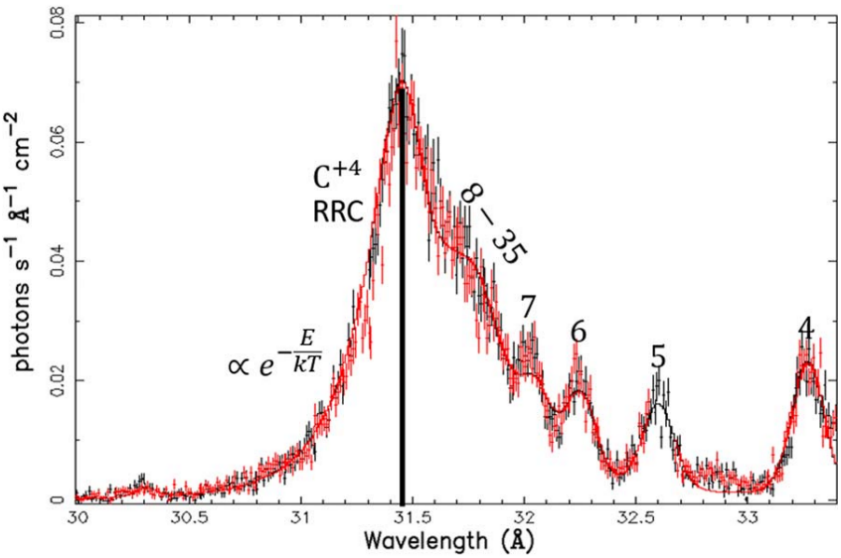

Figure 1.11: XMM-Newton/RGS observation of the radiative recombination continuum of C^{4+} ion in classical nova YZ Ret (Mitrani et al., 2024). The RRC has a narrow profile, which suggests an electron temperature that is low ($\approx 2\,\mathrm{eV}$). The spectrum distinguishes itself from a pure RRC spectrum (Fig. 1.10) because it does not exhibit a cut-off at the ionisation energy (black line). The cut-off is erased by a high occupancy of the high-n levels, which is a signature of CX. Figure courtesy of Mitrani et al. (2024).

the encounter of the free electrons with ions. An example of a detailed derivation of bremsstrahlung emissivity can be found in Longair (1999). Here, I quote the result relevant for the soft X-ray, where the electrons are non-relativistic and their velocities can be estimated by the Maxwellian distribution, hence the prefix 'thermal'. The bremsstrahlung emissivity follows

$$\epsilon(T_e, \nu) = 6.8 \times 10^{-38} T_e^{-1/2} e^{-h\nu/kT_e} \sum_i n_e n_i Z_i^2 g(\nu, T_e) \,\mathrm{erg\,cm^{-3}\,s^{-1}\,Hz^{-1}}, \tag{1.36}$$

where $g(\nu, T_e)$ is the Gaunt factor that takes into account the quantum mechanical effect of the interaction, which is only weakly varying with frequency. The summation over i refers to the sum of all ion species. The key feature of a bremsstrahlung continuum is that it drops as $\sqrt{T_e}$ and exhibits a cut-off above $h\nu = kT_e$. Thermal bremsstrahlung is especially important for hot plasma ($\gtrsim 2\,\mathrm{keV}$), while for plasma at lower temperatures, which the SXRB is mainly composed of, line emissions contribute significantly. This makes the continuum level from bremsstrahlung difficult to determine, particularly with CCD spectral resolution.

1.8.8 Two-photon continuum

As the name suggests, two-photon emission is the radiative decay process by emission of two photons. It is of great importance to H- and He-like ions because of the presence of the metastable excited level $2s$ (H: $^2S_{1/2}$; He: $^1S_0$). By the selection rules, allowed transitions should have $\Delta l = \pm 1$; therefore, the decay from the excited level $2s$ to $1s$ is forbidden. Given that the density is low, such that the collisional excitation from the $2s$ to the $2p$ orbital is infrequent, the electron on the metastable level could decay spontaneously with the emission of two photons. This is a continuum process, and the spectrum of the two-photon process is symmetric about the peak at $\frac{1}{2}E_0$, and spans E=0 to E_0, where E_0 is the excitation energy of the $2s$ level.

1.9 eROSITA

Observations from the eROSITA telescope serve as the foundation of this thesis. eROSITA (Predehl et al., 2021) is the primary instrument on board the Spectrum-Röntgen-Gamma (SRG; Sunyaev et al., 2021) spacecraft, which is a German-Russian collaborative mission. The fundamental advantage of eROSITA in the study of the SXRB lies with its all-sky surveys (eRASS). As we live inside the LHB and within the MW halo, all-sky surveys allow us to study their spatial (at least projected) properties in a continuous manner (Chapter 3). The repeating nature of the eRASSs also enables the decomposition of the time-variable SWCX emissions from the background emissions beyond the Solar System (Chapter 2). A lot of the current knowledge of the SXRB was advanced by the last generation of X-ray all-sky survey, RASS, using ROSAT. A fundamental improvement of eRASSs is that the soft X-ray (0.3–2.3 keV) sensitivity has improved by 25 times compared to ROSAT and moderate energy resolution provided by charge-coupled device (CCD) allows for spectral fitting, as opposed to broadband ratios to probe plasma conditions. The drastic increase in sensitivity directly contributed to the discovery of the eROSITA bubbles (Predehl et al., 2020). A detailed spectral and morphological analysis of the eROSITA bubbles will be presented in Chapter 4.

eROSITA data are proprietary and are shared between the German and Russian consortia. The German consortium has the right to exploit and publish the data on the western Galactic hemisphere ($\approx 180^\circ < l < 360^\circ$; the precise division is at the location of Sgr A*), and vice versa for the Russian consortium on the eastern hemisphere. As a member of the German consortium, all the content in this thesis related to eRASSs is from the western Galactic hemisphere. The public data release of the first eRASS (eRASS1) of the western Galactic hemisphere occurred on 31 January 2024.

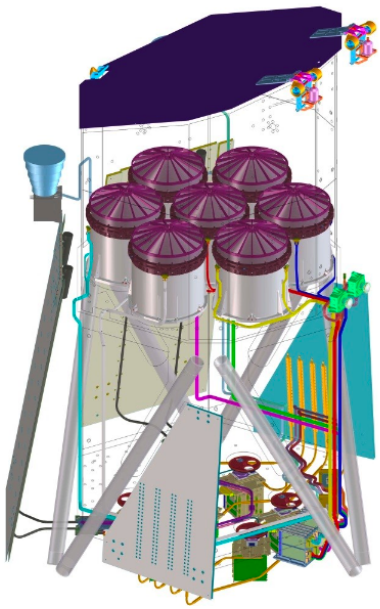

Figure 1.12: Schematic view of eROSITA. From top to bottom: The front cover (top; deep blue) is flipped open during operation. The seven mirror assemblies of the seven TMs (purple: baffle, brown: electron deflector, silver: mirror shells) are put 1.6 m above the pnCCD cameras. The camera assemblies (brown: filter wheel, yellow: pnCCD camera, green: electronics box) are located at the bottom of the telescope. The telescope is surrounded by four large radiators to dissipate the heat from the cameras and their electronics. Figure courtesy of Predehl et al. (2021).

1.9.1 Instrument

eROSITA is made up of 7 telescope modules (TMs), each comes with its own mirror module (Friedrich et al., 2008; Arcangeli et al., 2017) and pnCCD camera (Meidinger et al., 2014). A schematic view of eROSITA is shown in Fig. 1.12. The eROSITA mirrors implement the Wolter-I geometry, where incoming X-ray photons are first reflected by a hyperbolic surface, then by a parabolic surface to converge at the focus (Wolter, 1952). Each mirror module consists of 54 hyperboloid/paraboloid gold-coated nickel mirror shells, which can achieve a field-of-view-averaged (FoV-averaged) half-energy width of $\approx 26''$. The X-ray baffle installed on top of the mirror shells is to suppress single reflections on the hyperboloid from photons outside the FoV. Single reflections would contribute to additional X-ray background, or worse, in the event of a bright source out of the FoV, contribute to a bright ring on the image plane.

The focal length of the mirror shells is 1 600 mm. The relatively short focal length of eROSITA (e.g. XMM-Newton has a focal length of 7 500 mm), combined with the CCD area of $28.8 \times 28.8\,\mathrm{mm}^2$, means the FoV of eROSITA is $\approx 1^\circ$. The large FoV is designed to increase the survey efficiency. However, as a trade-off for the large FoV, the effective area at high energies is sacrificed. The eROSITA CCD has 384×384 pixels, corresponding to a plate scale of $9''.6$. The CCD is read out every 50 ms during survey mode. The eROSITA pnCCD is an updated version of the ones on XMM-Newton/EPIC-pn, whereby the charges from the image area can be shifted within 0.115 ms to the neighbouring shielded framestore area, which are subsequently read out in 9.18 ms. This dramatically suppresses the 'out-of-time' events, which are events recorded during readout. The spectral resolution of eROSITA increases from $\approx$ 60 eV at 0.28 keV (C-K line) to $\approx$ 80 eV at 1.49 keV (Al-K line), and is fairly constant across all TMs.

The aspect that distinguishes eROSITA from any past and current X-ray telescopes is its 'grasp', defined as the product of the effective area and FoV. Figure 1.13 shows eROSITA's grasp compared to other X-ray telescopes as a function of energy. This quantity is especially relevant

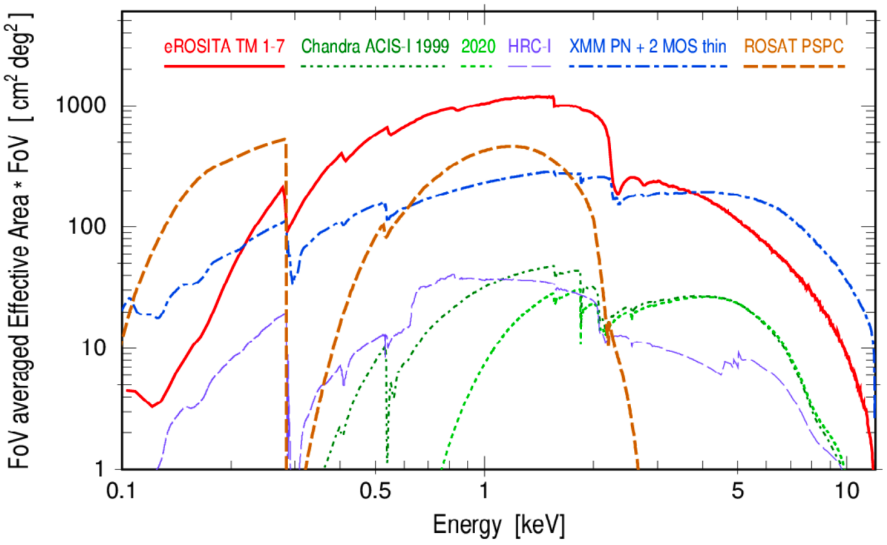

Figure 1.13: The grasp (effective area × FoV) of eROSITA compared to other X-ray telescopes as a function of energy. Figure courtesy of Predehl et al. (2021).

to the studies of diffuse emission, where the source signal really scales with the FoV. eROSITA's grasp exceeds any other missions between $\sim$ 0.3–2 keV, which approximately translates to the S/N increase in detecting large-scale diffuse X-ray emission. Below the carbon edge at 0.28 keV, ROSAT/PSPC has a higher grasp compared to eROSITA (despite the worse spectral resolution); therefore, the spectral analyses in the following Chapters often rely on simultaneous spectral fits of eROSITA and ROSAT/PSPC data. The drop in soft energy response of eROSITA is caused by the presence of optical blocking filters, whose presence helps suppress optical loading but attenuates soft X-rays. Optical loading refers to the effect that the accumulated energies from many optical photons (each in order of eV) in one readout (50 ms) are mistaken as one X-ray photon, as the CCD is sensitive to both. Two implementations of optical-blocking filters are used in eROSITA. Five of the seven TMs (TM1, 2, 3, 4, 6; collectively as TM8) have 200 nm aluminium coated on the CCDs, with an additional 200 nm polyimide filter in the `Filter` position of the filter wheel. TM5 and 7, collectively as TM9, were designed to give higher soft X-ray sensitivity. Therefore, they do not possess the aluminium on-chip filters; instead, an additional 100 nm of aluminium was coated on the same 200 nm polyimide filter, yielding 100 nm less aluminium in total thickness compared to TM8. Unfortunately, TM9 suffered from an optical light leak, discovered during the commissioning phase of eROSITA. The optical light leak means the optical photons (primarily from the Sun) could bypass the optics and the filter wheel and shine directly onto the CCDs. The heavy non-uniform optical loading and the solar angle dependence render TM9 data unusable for spectral analysis in the soft X-rays. They are therefore discarded from our analyses throughout this thesis. It is now understood that the path for the optical light to reach the CCD is through the openings in the housing of the CCD, whose main purpose is to allow the heat pipes to reach the CCD.

For completeness, each TM comes with its own filter wheel with four positions — `Filter`, `Open`, `Closed` and `CalClosed`. As described in the last paragraph, the `Filter` position is the nominal filter used for science and the eRASSs. `Open` is, as the name suggests, a position where no external filter was installed, and the main purpose is for optimal outgassing. It can have scientific value as it could boost the soft response. Indeed, it was used to observe the Comet C/2018 W2 during the Calibration and Performance Verification (CalPV) phase. Observations with TM8 using the `Open` filter are not completely naked because the on-chip filter gives at least some degree of optical suppression. The `Closed` filter is the same as the plate of the filter wheel, made up of 4 mm of

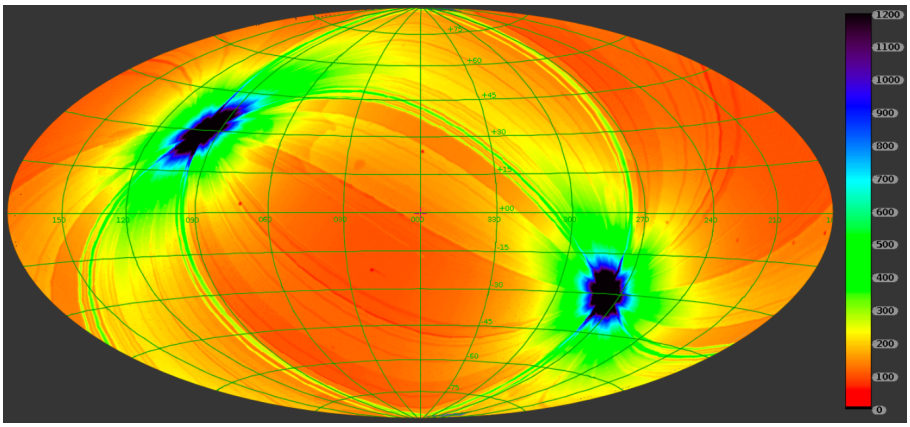

Figure 1.14: Vignetted exposure map of eRASS1 (in seconds) in 0.6–2.3 keV band. The map is in Aitoff projection in Galactic coordinates. The vignetting correction applied in this energy band is about a factor of 1.9 lower than the on-axis value. Figure courtesy of Predehl et al. (2021).

aluminium, which blocks all external X-rays up to 20 keV. The `CalClosed` position contains a radioactive ^{55}Fe source in a copper-nickel capsule (Freyberg et al., 2012), which has a half-life of 999 days. Its main use is to create an array of fluorescence lines for in-flight calibrations of, for instance, charge transfer inefficiency, energy resolution and energy scale.

1.9.2 Orbit and survey strategy

SRG was launched on 13 July 2019 from the Baikonur cosmodrome in Kazakhstan. It carried out all-sky surveys from a halo orbit around the Sun-Earth Lagrangian point L2. The halo orbit is not circular, but SRG generally maintains a distance in the order of 100 Earth radii from L2. Occasional active orbit corrections were needed to correct the trajectory of SRG to alleviate gaps in radio contact with Russian ground stations (Sunyaev et al., 2021). An overview of the SRG orbit (before Nov 2020) can be found in Freyberg et al. (2021) and Sunyaev et al. (2021).

After the CalPV phase following the arrival at the L2 halo orbit, eROSITA began its all-sky surveys starting from 12 December 2019. Every four hours, SRG rotates once about the axis towards the Sun, resulting in an approximate great circle scan ($\approx$1°wide because of the FoV) of the sky. Since the L2 point progresses with the Earth's orbit, the SRG rotation axis also shifts by $\approx 1^\circ$ per day. With this strategy, a complete sky coverage can be achieved in half a year. In addition, all the great circle scans converge at the ecliptic poles, yielding the highest exposure time there, but the least exposure on the ecliptic plane. Figure 1.14 shows the eRASS1 exposure map in the energy band 0.6–2.3 keV, which shows the high exposure at the ecliptic poles. The energy dependence comes from the vignetting correction (loss of effective area with increasing off-axis angle is a function of energy).

Thus far, eROSITA has completed 4.3 all-sky surveys out of the total of eight planned, named eRASS1–5, or their combination as eRASS:5. However, all observations with eROSITA have been halted since 26 February 2022, two days after Russia's invasion of Ukraine. eROSITA has since been put into safe mode and can resume science operation in principle.

1.9.3 Background

The determination of the background level is of great importance for the study of diffuse emissions, especially for the faint SXRB. One cannot simply define an aperture next to the source of interest to estimate the background level, as we would like to study the background itself. Freyberg et al. (2021) compiled a list of main background contributors for eROSITA, but also applies to other X-ray missions:

1. high-energy particles hitting the CCD directly, or indirectly by the creation of secondary particles or X-rays when hitting the camera;
2. soft protons focused by the mirrors;
3. low-energy electrons;
4. single reflections of X-ray from outside of the FoV;
5. optical light through the mirrors;
6. optical light leak not via the mirrors.

The contributions from the direct or indirect incidence of high-energy particles are usually referred to as the instrumental background. This part of the background is constrained by the filter-wheel closed (FWC) data, which is the calibration exposures taken when the filter wheel was rotated to the `Closed` position. During the surveys, FWC data of each TM were taken at different times to ensure continuous sky coverage. Most of the FWC data was collected during orbit corrections. Fig. 1.15 shows the cumulative FWC data exposure time: the near-vertical increases in exposure times often correspond to times of orbit corrections when all TMs had to be closed. Figure 1.16 shows a time-averaged FWC spectrum of TM8. It features a fairly flat continuum at high energies and a gradual increase at the softest end due to electronic noise. The cut-off at about 9.5 keV is caused by the rejection of events with amplitudes above 12288 adu (Freyberg et al., 2021).

An in-depth analysis of the time and CCD temperature dependence of the FWC data will be presented in Chapter 2. A summary is that the FWC data remain relatively stable at low energies above 0.2 eV, but its normalisation decreases as the solar activity increases from eRASS1 to 4. This was caused by the increased shielding of the cosmic rays into the inner Solar System, which was provided by the rising solar activity. Pommranz (2024), by using a realistic eROSITA mass model and particle input spectrum in *Geant4* simulations, shows that the dominating primary particle population of the FWC spectrum are protons. In addition, the fluorescence lines are thought to (due to uniformity of the CCD image at the fluorescence line energies) and confirmed by the simulation to originate mainly from the impurities in the graded Z shield or the beryllium layer that surrounds the CCD (if all the materials are pure, the graded Z shield and beryllium would absorb all the fluorescence lines and re-emit them below 0.2 keV).

Contaminations from soft protons can be suppressed by identifying flaring periods during the observations. All the events used for spectral analyses were taken from quiescent times by inspecting the light curves. The threshold is usually 1.5 times the FWC background level, above which the time periods were removed from the good-time intervals (GTI). We delay the specifics to the following Chapters. During the CalPV observation of the dark cloud Corona Australis, soft proton flares were short and showed quick time variability. Spectrally, soft proton exhibits a steeper spectral index compared to the FWC, making them quite noticeable. Perinati et al. (2024) shows that the FWC spectrum and the combined quiescent spectrum (same screening used in this thesis) of eRASS1 at the 5–7 keV band are consistent within 0.6%, hence leaving little room for residual soft proton contamination.

The contributions from (primary) low-energy electrons are minimised by the installation of an electron deflector between the baffle and X-ray mirrors of each TM. There have not been indications that a significant residual portion remains, which has thus been neglected in spectral analyses. On the other hand, the secondary electrons created within the telescope are modelled by the FWC data.

Single reflections of photons outside of the FoV are suppressed by the X-ray baffle, but not completely and can be seen as ring-like contaminations if a bright point source is right outside of the FoV. This would be a significant problem for studies on dedicated regions on the Galactic plane, where many bright sources lie, and would require dedicated masking or spatial modelling. However, it is less of a problem for the aim of this thesis, as I mostly focus on the extra-planar regions.

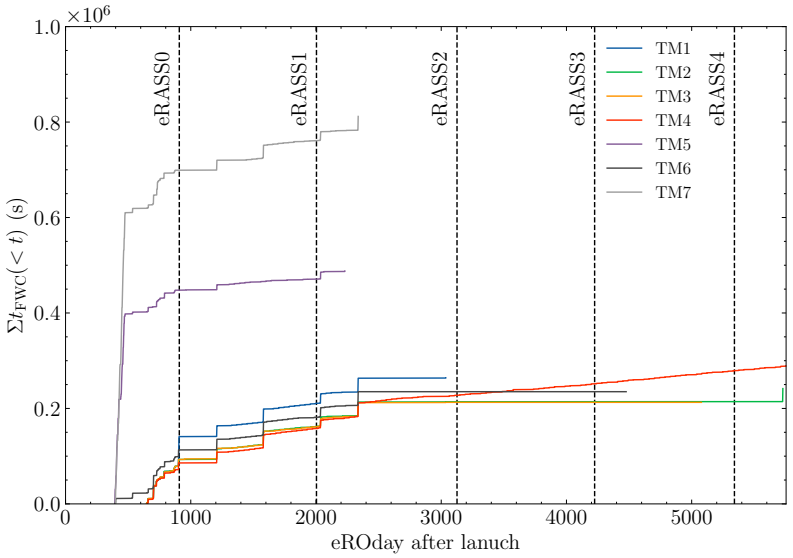

Figure 1.15: Cumulative FWC exposure time of each TM as a function of time. The unit of time is eROday (4 hours), which corresponds to the period of one great circle scan. The near-vertical increases in FWC exposure time are mainly from orbit corrections. Long exposures on TM5 and 7 were taken to investigate the optical light leak during the CalPV phase (eRASS0).

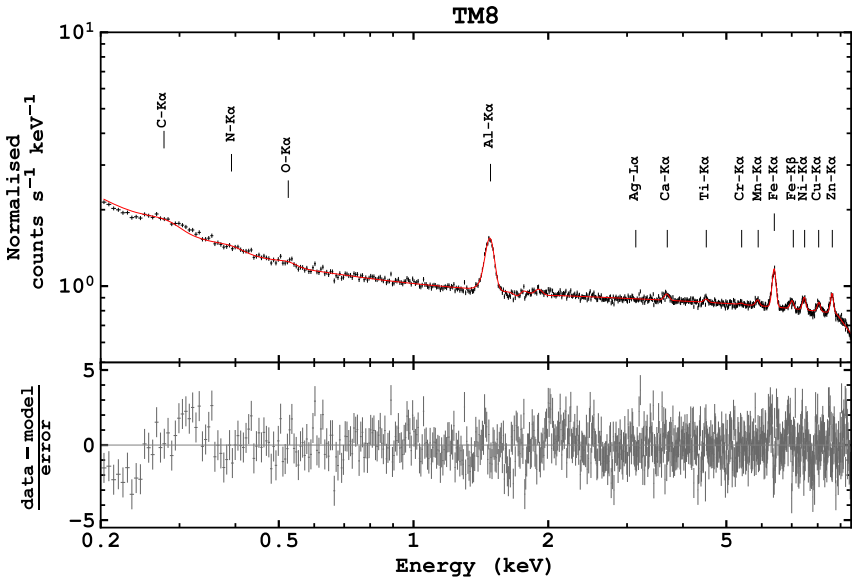

Figure 1.16: FWC spectrum of TM8 with fluorescence line labels. The red line shows the best-fit phenomenological model to the data that is used in spectral fitting of the SXRB.

A similar situation applies to optical loading, which is a concern for bright optical sources, which not only produces an excess at low energies but also shifts the energy scale of the X-ray spectrum. Luckily, only the positions of the optical sources are affected. Because bright X-ray sources (not necessarily optically bright, but often the case) are masked in the SXRB spectra, they also only produce a minimal effect on the SXRB spectra.

The optical light leak affects mostly TM5 and 7 because of the lack of an on-chip optical blocking filter. Despite the higher soft response, they have to be discarded from my analysis. Detector image of TM8 is uniform, which means the on-chip filters effectively block the light leak, and the TM-specific FWC models can be used to model the instrumental background. TM5 and 7 may be usable in the future since the source of the light leak into the CCD is now understood. If its solar angle dependence is fully characterised, one could select periods of absence or low light leak for X-ray analysis.

Chapter 2

Studying the X-ray foreground via molecular cloud sight lines

This chapter was published in an article titled 'SRG/eROSITA X-ray shadowing study of giant molecular clouds' in Astronomy & Astrophysics, Volume 676, A3 (Yeung et al., 2023). This article is reproduced with permission from the publisher, EDP Sciences.

2.1 Abstract

Context. SRG/eROSITA is situated in a halo orbit around L2, where the highly variable solar wind charge exchange (SWCX) emission from Earth's magnetosheath is expected to be negligible. The soft X-ray foreground emissions from the local hot bubble (LHB) and the remaining heliospheric SWCX emissions could be studied in unprecedented detail with eROSITA All-Sky Survey (eRASS) data in a 6-month cadence and better spectral resolution than ROSAT.
Aim. We aim to use eRASS data of the sight lines towards three giant molecular clouds away from the Galactic plane to isolate and study the soft X-ray diffuse foreground emission. These X-ray shadows will serve as calibration baselines for the future three-dimensional structural study of the LHB.
Methods. We conducted spectral analysis on the diffuse X-ray spectra of these clouds from the first four eRASSs to estimate and separate the heliospheric SWCX contribution from the LHB emission.
Results. We find the density of the LHB to be independent of the sight line with $n_e \sim 4 \times 10^{-3}\,\mathrm{cm}^{-3}$, but not the temperature. We report a lower temperature of $kT_{\mathrm{LHB}} = 0.084 \pm 0.004\,\mathrm{keV}$ towards Chamaeleon II & III (Cha II & III) than Ophiuchus (Oph) and Corona Australis (CrA), in which we measured 0.102 ± 0.006 and $0.112 \pm 0.009\,\mathrm{keV}$, respectively. We measured the emission measure of the LHB to be $\sim 2 \times 10^{-3}\,\mathrm{cm}^{-6}\,\mathrm{pc}$ at medium Galactic latitudes ($|b| \sim 20°$). A monotonic increase in the SWCX contribution has been observed since the start of 2020, coincidental with the beginning of solar cycle 25. For Oph, SWCX has dominated the LHB in the 0.3–0.7 keV band intensity since eRASS2. We observed lower SWCX contributions in Cha II & III and CrA, consistent with the expected decreasing solar wind ion density at high heliographic latitudes.

2.2 Introduction

The notion of the soft X-ray emitting local hot bubble (LHB) emerged after Wisconsin sounding-rocket data showed an anti-correlation between the soft X-ray intensity and neutral hydrogen column density (N_{H}) in the southern Galactic hemisphere (Sanders et al., 1977). In their concise yet seminal paper, Sanders et al. (1977) pointed out that the anti-correlation could not be accommodated by photoelectric absorption but by a displacement effect in which the local volume

is filled with an X-ray emitting gas bounded by a thick wall of cool neutral hydrogen gas. In this picture, a low $N_{\rm H}$ (thin) section of the wall is displaced by additional X-ray emitting gas, resulting in a higher X-ray intensity in low $N_{\rm H}$ regions. Independently, Tanaka & Bleeker (1977) reached the same conclusion and coined the term LHB. The existence of the LHB had henceforth become the standard conceptual picture of the local interstellar medium (ISM) — a low H I column density region ($N_{\rm H} \lesssim 10^{20}$ cm^{-2}) filled with hot plasma extending to 100–200 pc (e.g. see reviews by Bochkarev, 1987; McCammon & Sanders, 1990; Breitschwerdt, 1996). After the launch of ROSAT, shadowing experiments on Draco and MBM12 clouds firmly indicated the presence of a more distant soft X-ray background from the Galaxy in addition to the foreground LHB emission (e.g. Snowden et al., 1991, 1993).

However, ROSAT delivered arguably even more insights into the additional soft emission, which turned out to be foreground emission and led to the discovery of the solar wind charge exchange (SWCX) process. It began with the detection of long-term enhancements (LTEs) in the ROSAT All-Sky Survey (RASS) with durations ranging up to $\sim$ 8 hours, which were then found to be correlated with solar wind variations and geomagnetic storms (Freyberg, 1994). Later detection of an unexpectedly bright soft X-ray from the Comet C/Hyakutake 1996 B2 with an emission morphology facing the Sun but not the direction of motion strongly suggests that the Sun is the culprit (Lisse et al., 1996). Soon after, Cravens (1997) proposed that the charge exchange process between the cometary neutrals and heavy solar wind ions could explain the comet's soft X-ray emission. Dennerl et al. (1997) established comets as a class of X-ray sources by systematically searching the archival ROSAT data, and they pointed out that the charge exchange between highly charged solar wind ions and cometary neutrals is the dominant emission process. A LTE in the X-ray background was also detected near the outbursts of the comet, prompting Dennerl et al. (1997) and Freyberg (1998) to suggest the Earth could also act as a bright, soft X-ray source from the SWCX process. Concurrently, Cox (1998) pointed out that the flowing neutral ISM also provides a source of neutrals to interact with the solar wind. The SWCX emissions from these two sources of neutral atoms are usually referred to as magnetospheric and heliospheric SWCX, respectively (see review by Kuntz, 2019).

Distinguishing between the contributions of LHB and SWCX using ROSAT PSPC is challenging due to the reliance on broadband count rates. Many cross-sections of the heavy ions were unknown, further complicating the issue. Before the arrival of more SWCX-focussed missions such as the Diffuse X-rays from the Local Galaxy (DXL), simultaneous modelling of the LHB and SWCX have resulted in sometimes inconsistent results — from estimations of SWCX contributing to half to all of the $\frac{1}{4}$ keV emission in the galactic plane (Koutroumpa et al., 2009a; Robertson et al., 2009, and references therein). There was naturally a worry that LHB had become redundant and all the $\frac{1}{4}$ keV emission could be accounted for by SWCX, despite a consistent requirement of additional emission at high galactic latitudes also shown by these studies.

Galeazzi et al. (2014) mostly settled the situation by estimating the heliospheric SWCX contribution in ROSAT using the DXL sounding rocket mission and reported that the LHB still contributes to $\sim$ 60% of the emission in the galactic plane. Based on the estimated SWCX contribution from DXL (Galeazzi et al., 2011; Uprety et al., 2016), Liu et al. (2017) measured a LHB temperature of 0.097 ± 0.019 keV from the ROSAT R2/R1 band ratio map and mapped out the three-dimensional (3D) structure of the LHB assuming a constant electron density plasma. They show that the inferred boundary of the LHB agrees reasonably well with the onset of a higher absorbing column inferred from the local ISM density map (Lallement et al., 2014).

With energy-resolved imaging and repeated all-sky surveys every six months, eROSITA is providing an unprecedented view of the soft X-ray foreground in terms of the depth and differentiation of LHB from SWCX. Situated in a halo orbit around L2, eROSITA is expected to be free of the highly variable SWCX coming from the Earth's magnetosheath. The energy resolution of $\Delta E \simeq 58$ eV at the C-K line (0.277 keV) allows for spectral decomposition of the heliospheric SWCX and LHB components (Predehl et al., 2021), as well as measurements of the properties of the LHB and SWCX intensity in six-month cadence along the chosen sight lines.

In this paper, we study the emissions from three of the darkest X-ray shadows away from the Galactic plane in the German eROSITA sky (Galactic coordinates restricted to $180^\circ \leqslant l \leqslant 360^\circ$,

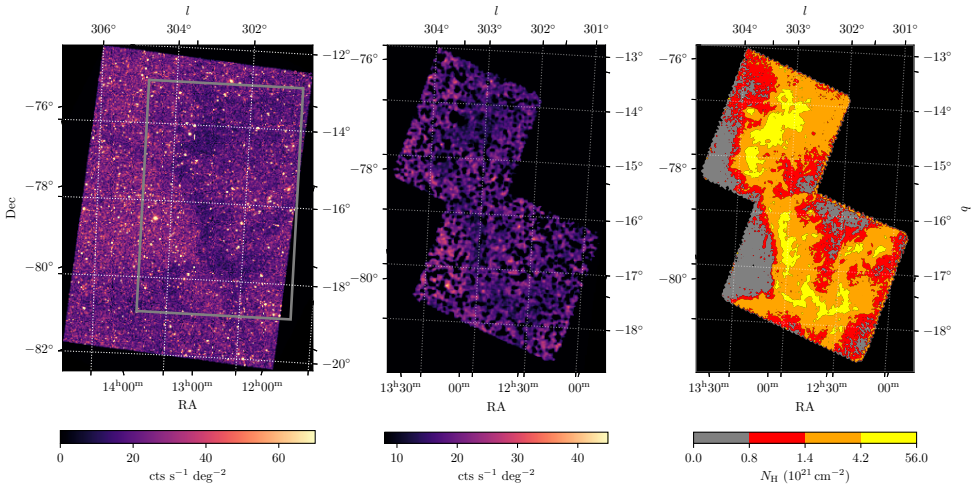

Figure 2.1: eROSITA 0.2–3 keV image of the shadow cast by Cha II & III. The left panel shows the eROSITA 0.2–3 keV band image of Cha II & III colour-coded with the vignetting-corrected count rate. The grey rectangular box indicates the region shown in the middle and right plots. The middle panel shows the point-source-free region where spectral analysis is carried out. The two rectangular mosaics represent the region covered by the *Herschel* column density map. The right panel shows the four column density bins that define the regions for spectral extraction. The dotted grid is in the Galactic coordinate system.

$-90^\circ \leqslant b \leqslant 90^\circ$) — Chamaeleon II & III (Cha II & III), Ophiuchus (Oph), and Corona Australis (CrA). They lie on the boundary of the LHB (Zucker et al., 2022) with accurate distances and are, therefore, ideal calibration points of the LHB properties, which could later be extended to infer the 3D structure of the LHB. Earlier observational work based on ROSAT found the LHB is well described by a single temperature and density plasma (e.g. Liu et al., 2017). We aim to subject this assumption to the tighter constraints set by eROSITA. These sight lines also enable us to infer the time evolution of the relative contribution between the LHB and heliospheric SWCX.

In Sect. 2.3, we describe the eROSITA observations of the clouds and the specific regions chosen for spectral extraction, as well as the XMM-Newton celestial calibration source as an independent monitoring of the SWCX variation. We lay out the constituents of our spectral model and our spectral fitting procedures in Sect. 2.4. We report our results and interpretations in Sect. 2.5. Finally, we deliver our concluding remarks in Sect. 2.6.

2.3 Data and calibration

We extracted data of Cha II & III, Oph and CrA from the first four eROSITA All-Sky Surveys (eRASSs). Only data from telescope modules (TM) with on-chip filters (TM 1–4 and 6) were extracted to avoid the light leak issue (Predehl et al., 2021). Four visits to each cloud enable an analysis of the variability over intervals of half a year. The data were processed with the 020 version of the eSASS pipeline (Brunner et al., 2022). Flares were removed using the standard eSASS task `flaregti`. After removing the flared time intervals, the total vignetting-corrected exposure times within the defined regions (right panel of Figs. 2.1, 2.2 and 2.3) in the first four eRASSs in the 0.2–3 keV band (our spectral-fitting range) are $\sim$ 760 s for Cha II & III, $\sim$ 330 s for Oph, and $\sim$ 250 s for CrA. The difference is mainly caused by their angular distance from the ecliptic poles, where all the great circles of the eROSITA scans merge to result in the maximum exposure time.

All valid event patterns were used because the low-energy electronic noise component (mostly

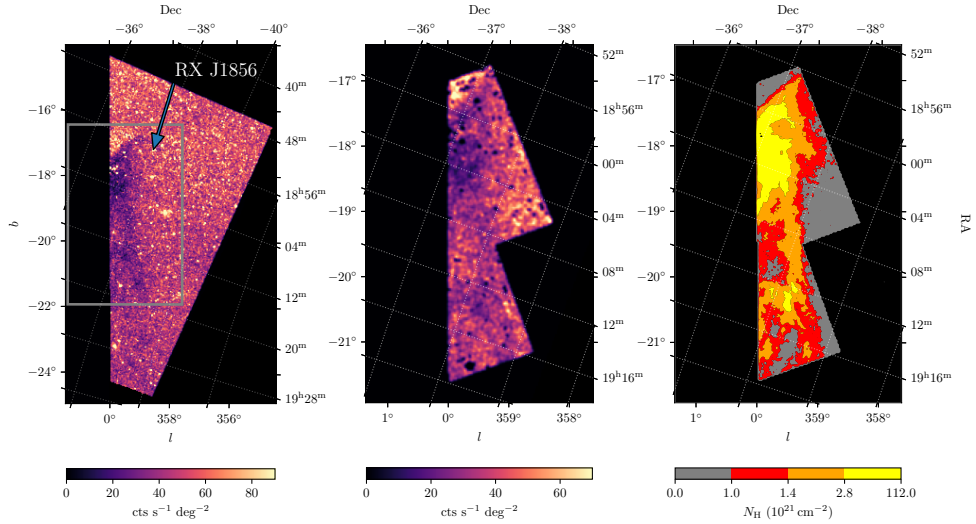

Figure 2.2: Same as Fig. 2.1, but for CrA. The dotted grid is in the equatorial coordinate system.

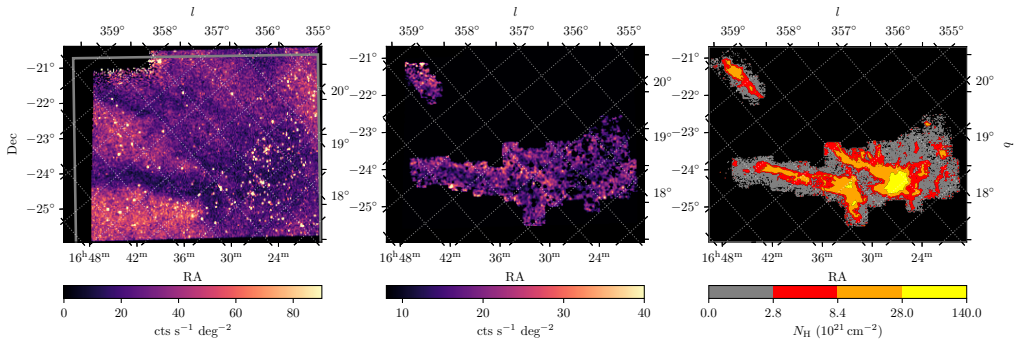

Figure 2.3: Same as Fig. 2.1, but for Oph. The dotted grid is in the Galactic coordinate system, with l increasing towards the top left and b increasing towards the top right.

Table 2.1: Summary of the exposure times and the extraction regions in each molecular cloud.

Cloud	Exposure Time (s)	Region	Area (deg^2)	N_H (10^{21} cm^{-2})		
				Herschel	*Planck R*	*Planck* τ_{353}
Cha II & III	762	1	1.69	$0.47^{+0.11}_{-0.12}$	$0.75^{+0.14}_{-0.15}$	$0.84^{+0.16}_{-0.19}$
		2	2.21	$0.80^{+0.14}_{-0.12}$	$1.01^{+0.11}_{-0.13}$	$1.31^{+0.22}_{-0.18}$
		3	4.14	$1.55^{+0.52}_{-0.33}$	$1.43^{+0.27}_{-0.17}$	$2.36^{+0.67}_{-0.39}$
		4	1.15	$4.10^{+1.02}_{-0.73}$	$2.34^{+0.38}_{-0.28}$	$4.86^{+1.19}_{-0.87}$
CrA	251	1	1.37	$0.55^{+0.10}_{-0.09}$	$0.60^{+0.11}_{-0.09}$	$0.60^{+0.21}_{-0.15}$
		2	1.40	$0.86^{+0.07}_{-0.08}$	$0.89^{+0.12}_{-0.11}$	$1.08^{+0.17}_{-0.19}$
		3	1.32	$1.25^{+0.24}_{-0.14}$	$1.17^{+0.26}_{-0.11}$	$1.64^{+0.34}_{-0.23}$
		4	0.60	$3.54^{+3.09}_{-1.01}$	$2.58^{+1.07}_{-0.55}$	$4.56^{+2.33}_{-1.10}$
Oph	330	1	3.77	$0.93^{+0.52}_{-0.37}$	$7.86^{+4.66}_{-3.61}$	$4.35^{+1.02}_{-0.77}$
		2	2.49	$3.24^{+1.12}_{-1.18}$	$8.69^{+4.41}_{-3.21}$	$5.73^{+1.33}_{-1.05}$
		3	1.40	$8.43^{+2.96}_{-1.90}$	$11.07^{+4.77}_{-3.68}$	$8.41^{+2.44}_{-1.22}$
		4	0.19	$27.89^{+6.56}_{-5.29}$	$38.90^{+20.16}_{-13.44}$	$17.91^{+3.01}_{-3.46}$

Notes. The exposure time is the average vignetting-corrected on-axis exposure time, assuming a nominal seven-TM effective area in the 0.2–3 keV band. The N_H values from *Herschel* and *Planck* are the 50^{th} percentile in each extraction region after convolving the maps to a common angular resolution of $5'$. with the lower and upper bounds showing the 25^{th} and 75^{th} percentiles respectively.

$\lesssim$ 0.3 keV) has been greatly reduced from the 946 (as used in the Early Data Release (Brunner et al., 2022)) to the 020 processing version. Thus, one could take advantage of more photons to constrain the spectral models at low energies and need not sacrifice higher-pattern events to suppress the electronic noise.

The 0.2–3 keV images of the clouds are shown in the left panels of Figs. 2.1, 2.2 and 2.3. One can observe a clear shadow between $301^\circ \lesssim l \lesssim 304^\circ$ and $13^\circ \lesssim b \lesssim 18^\circ$ cast by Cha II & III. The X-ray shadows are even more prominent in the case of CrA and Oph — a consequence of the two clouds being in front of and absorbing the emissions from the bright eROSITA bubbles (Predehl et al., 2020). Point sources were masked using the CheeseMask images produced by the standard eSASS detection chain, as shown in the middle panels.

In our spectral analysis, spectra of varying column density regions were extracted. The extraction regions are colour-coded on the right panels of Figs. 2.1, 2.2 and 2.3 by column density. The hydrogen column density information was obtained from the *Herschel* Gould Belt Survey Archive (André et al., 2010). The column density maps[1] were produced by fitting the SEDs formed by the 160, 250, 350 and 500 μm images in a $6''$grid at an angular resolution of $18\farcs2$ (Alves de Oliveira et al., 2014; Bresnahan et al., 2018; Ladjelate et al., 2020). We convolved the column density map to the approximate eROSITA angular resolution of $30''$, then defined four regions bound by the contour levels. Regions of Cha II & III and CrA are defined in this way. Table 2.1 lists the solid angles of the defined regions.

For Ophiuchus, the area coverage of *Herschel*'s column density map is limited to the cloud core. We extended the area with column density information by using the ^{13}CO 1–0 (110.201 GHz) map observed by the 14 m Five College Radio Astronomy Observatory (FCRAO) telescope (Ridge et al., 2006). This was done by deriving the mean ^{13}CO-to-N_H conversion factor from the overlap region of the *Herschel* and FCRAO maps while taking into account the difference in angular resolution and hence applying this factor to the additional area that the ^{13}CO map possesses. The result, in the form of the four regions' contours, is shown in the right panel of Fig. 2.3.

While the *Herschel* column density maps provide the exceptional angular resolution necessary for this work, similar to the *Planck* radiance map (R) that also adopts SED fitting to extract N_H information, they are likely to be affected by variations in the radiation field strength caused by increased attenuation of the interstellar radiation field and local heating photons in molecular

[1]The *Herschel* N_{H_2} maps were converted to N_H using $\frac{\mu_{\mathrm{H}_2}}{\mu_\mathrm{H}} = \frac{2.8}{1.37} \simeq 2$ (Roy et al., 2014)

clouds (Planck Collaboration et al., 2014). Planck Collaboration et al. (2014) suggests the dust opacity at 353 GHz (τ_{353}) is a better tracer of $N_{\rm H}$ in these regions. To estimate the possible range of $N_{\rm H}$ in each extraction region, we computed the $N_{\rm H}$ inferred from the aforementioned tracers and list the results in Table 2.1.

All the maps were convolved to the common angular resolution of 5′(resolution of the *Planck* maps) to ensure a fair comparison. The *Planck* maps were first converted to the corresponding $E(B-V)$ maps using the relations $E(B-V)/R = (5.40 \pm 0.09) \times 10^5$ and $E(B-V)/\tau_{353} = (1.49 \pm 0.03) \times 10^4$ using quasars in the diffuse ISM at high Galactic latitudes (Planck Collaboration et al., 2014). Subsequently, we adopted the scaling of $N_{\rm H}/E(B-V) = 4 \times 10^{21}\,{\rm cm}^{-2}\,{\rm mag}^{-1}$ to get $N_{\rm H}$ from the $E(B-V)$ maps. This scaling is representative of values derived from the detailed multiphase analysis conducted by Planck Collaboration et al. (2015) and is shown by Lallement et al. (2016) to match the fitted X-ray foreground absorption in 19 XMM-Newton sight lines towards the North Polar Spur.

We note the reasonable agreement between the three tracers, given that there is still a large scatter with each scaling relation we used to convert R and τ_{353} to $N_{\rm H}$. The variations of $N_{\rm H}$ inferred from different tracers inform the scale of systematic uncertainties in our derivation of $N_{\rm H}$, which is instructive to compare with the best-fit $N_{\rm H}$ values in Table 2.2 in Sect. 2.5. Interestingly, a direct comparison between our best-fit $N_{\rm H}$ and the values derived from the three tracers would suggest τ_{353} might be a better $N_{\rm H}$ tracer towards these high $N_{\rm H}$ regions, despite the fact that the region boundaries are drawn from the *Herschel* maps. An exception to the overall agreement is found in region 1 of Oph. The reason for this is likely to be the inaccurate extrapolation of the *Herschel* map using ^{13}CO map when the latter approaches the sensitivity limit in the lowest $N_{\rm H}$ region.

Background count rates in the 0.3–0.7 keV and 8-12 keV bands of the XMM-Newton routine calibration source RX J1856.5-3754 (RX J1856) were also extracted in order to compare and cross-check our findings on SWCX towards the direction of CrA. The position of RX J1856 relative to CrA is indicated on the left panel of Fig. 2.2. Sect. 2.8 describes the datasets and the results in more detail.

2.4 Spectral analysis

This section describes the various components that comprise the soft X-ray spectrum and our spectral fitting procedures. The spectral components are summarised in Fig. 2.4, which we subsequently elaborate on individually in the rest of the section.

We divide the physical components into two groups, foreground and background. The former includes the local hot bubble (LHB) and solar wind charge exchange (SWCX) emissions in front of the molecular clouds. The latter comprises the circum-galactic medium (CGM), cosmic X-ray background (CXB) and a Galactic corona (Cor) component (Ponti et al., 2023b). The background components, for simplicity, are assumed to be absorbed by the same column within the cloud. In addition, we assume there is no absorption between us and the cloud.

The instrumental background is fixed using the empirical models developed from the filter-wheel closed data accumulated since the launch of SRG. Because the instrumental background differs slightly between the 5 TMs, as shown in Sect. 2.9, the instrumental model used is TM-specific. In Sect. 2.9, we also demonstrate that the eROSITA instrumental background remained stable within the 0.2–9 keV, independent of time and CCD temperature.

2.4.1 Foreground components

Chamaeleon II & III are located at a distance of $\sim$ 190–200 pc (Voirin et al., 2018; Galli et al., 2021) which lie on the surface of the LHB (Zucker et al., 2022). In the simplified scenario, most, if not all, of the soft X-ray photons behind the cloud are absorbed, and one could isolate the foreground soft X-ray emissions due to the LHB and SWCX. As one would see later in Fig. 2.5 in Sect 2.5, this is only realised in two regions with the highest column densities, below $\sim$ 0.4 keV, where the two

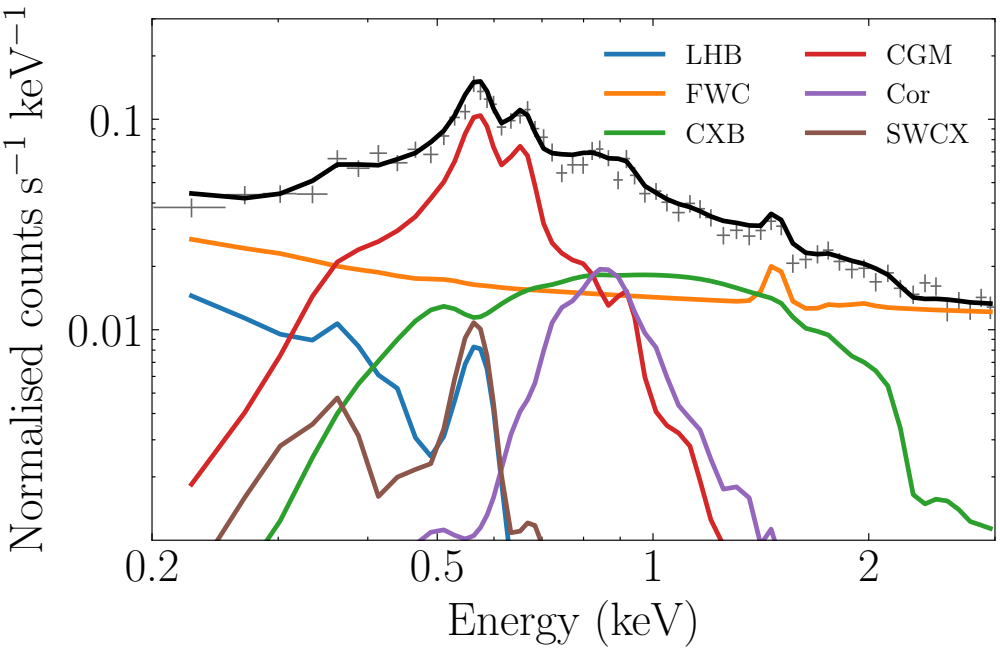

Figure 2.4: Illustration of all the spectral components taken from Cha II & III.

foreground components begin to emerge over the CGM emission. The limited energy range where the foreground components dominate but remain below the instrumental background component necessitates using regions (1 and 2) of lower column densities to estimate the contribution of other background components below ~ 0.4 keV.

We modelled the LHB as a plasma in collisional ionisation equilibrium (Liu et al., 2017), which is described by the `APEC` model (Smith et al., 2001). The LHB component is assumed to have solar abundance, given that the Sun is embedded within it. Therefore, the only free parameters of the LHB component are the plasma temperature and the emission measure (EM). We note that for each region, the normalisation of the LHB is scaled by the region area only and remains independent of time (eRASS). The latter reflects that the LHB does not vary on time scales from half a year to two years. As such, the LHB component is only scaled by one free EM parameter, despite different panels showing various combinations of region and eRASS as shown in Fig. 2.5. This single-parameter component normalisation applies to all other background components (CGM, corona and CXB), and the additional regions introduce no extra free parameter.

The other foreground component is SWCX, which would produce extra diffuse soft X-ray emission in the foreground. The primary source of SWCX in eROSITA is expected to be heliospheric. In heliospheric SWCX, the charge exchange between the neutral atoms in the ISM and ionised particles in the solar wind emits X-ray lines. For magnetospheric SWCX, the solar wind is shocked, compressed, and interacts with the much denser neutral exosphere. The magnetospheric SWCX is expected to vary on a shorter time scale ($\sim$ minutes to days). In eROSITA observations, the magnetospheric SWCX contribution is expected to be negligible (at least for high ecliptic latitude sources) since, being at L2, eROSITA observation geometry intersects only the most tenuous flanks of the magnetosheath. Another potential source of magnetospheric SWCX is the surface of the magnetotail. We believe this effect is minimal because, as shown in more detail in Sect. 2.10, SRG/eROSITA was mostly located outside the magnetosphere due to its halo orbit around L2 during our observations, and additionally, no excess emissions have been found from the frequent observations through the magnetotail of the south ecliptic pole.

The time scale of the heliospheric SWCX is generally longer than the magnetospheric SWCX because the SWCX flux received is integrated along the line of sight up to the edge of the helio-

sphere, averaging out shorter variations of the solar wind. This is likely true for Cha II & III and CrA that are located at higher ecliptic latitudes ($\beta \sim -62°$ and $-14°$) and are thus out of the plane of the Parker spiral (Parker, 1958). However, the situation is less clear for Oph ($\beta \sim -1°$) near the ecliptic plane. A shorter variation time scale in the order of hours to days is possible if the sight line is parallel to the pattern of the Parker spiral nearby and vice versa for the perpendicular case (Dennerl et al. in prep).

Ignoring the potential complication for Oph, a simple estimation using the distance to the heliopause ($\sim$ 120 AU) and the mean solar wind speed of 450 $\mathrm{km\,s^{-1}}$ yields a time scale of $\sim$ 460 days (Kuntz, 2019). However, the line-of-sight integration is heavily weighted by the r^{-2}-dependence of the solar-wind density away from the Sun, which, for reference, is $\sim$ 1% of its initial density at $r = 10\,\mathrm{AU}$ — a distance solar wind only takes $\sim$ 40 days to traverse. Therefore, the heliospheric SWCX likely varies from days to weeks. Recently, Qu et al. (2022) showed that the heliospheric SWCX is also correlated positively with the solar cycle using O VII and O VIII line fluxes measured by XMM-Newton for 10 years until 2010. Their study revealed a long-term variation in the heliospheric SWCX. However, it is not sensitive to shorter-term variations in the order of or less than half a year, as the width of the line flux bin was chosen to be half a year. SWCX variations on time scales of half a year between CalPV to eRASS3 have also been found by Ponti et al. (2023b). In addition, within the $\sim$ 4 days scanning time of the eFEDS field, no noticeable variation from SWCX was found (Ponti et al., 2023a). The two studies support the expectation that eROSITA is only subject to the heliospheric SWCX observing from L2.

In our spectral fitting, we modelled the SWCX component using the `ACX2` (v1.0.3) model (Smith et al., 2012; Foster et al., 2020). The `ACX2` model supersedes the older version `ACX` by including velocity-dependent effects and charge exchange cross-sections from the Kronos database (Mullen et al., 2016, 2017; Cumbee et al., 2018). We simplify the model by assuming all the solar wind ions have a single velocity at the mean solar wind speed (450 $\mathrm{km\,s^{-1}}$), the fraction of neutral Helium at the cosmic value 0.09 (default), solar abundance, recombination type to be single recombination and the `acxmodel` parameter to be 4. We found the choice of solar wind speed and the `acxmodel` parameter is not critical to the shape of the SWCX component by inspecting model `ACX2` spectra with eROSITA's spectral resolution, while for the other fixed parameters, we argue that they hold representative values.

The SWCX component is allowed to vary from cloud to cloud primarily because (1) the clouds were observed at different times during eRASSs, and (2) SWCX is expected to be spatially variable on large angular scales. The normalisation of the SWCX component is allowed to vary for each eRASS to account for variability. However, for different regions within the same eRASS, the SWCX normalisation is fixed by the corresponding region area without introducing extra degrees of freedom. Last but not least, we simplify the model on the freeze-in temperature T_{SWCX}. The freeze-in temperature sets the solar wind ion population by assuming the ion population was in collisional ionisation equilibrium with electrons at this temperature. We assume the freeze-in temperature would not change between eRASSs, and therefore, T_{SWCX} constitutes a single free parameter in the spectra fitting.

2.4.2 Background components

We model the non-instrumental X-ray background with three model components: CXB, CGM, and Galactic corona. These components are all modulated by the absorption of the molecular cloud, which we model using the `tbabs` model (Wilms et al., 2000). It is important to note that we leave N_{H} as a free parameter and do not impose priors on N_{H} in all extraction regions, given the systematic uncertainties from various tracers as shown in Table 2.1. The *Herschel* N_{H} information only defines the regions. For simplicity, we take the approximation that all absorptions occur within the cloud, hence the same column density for all background components within the same region.

The presence of the CXB was first observed by Giacconi et al. (1962). The CXB was subsequently found to be isotropic (e.g Schwartz, 1980), suggesting an extragalactic origin. Nowadays, it is known that a range of sources, including active galactic nuclei, galaxies, and galaxy clusters,

all contribute to the CXB (see Brandt & Yang, 2022, for a review). Cappelluti et al. (2017) found that 91% of the observed CXB can be resolved to detected X-ray sources and galaxies from the Chandra COSMOS-legacy field. The CXB spectrum can be modelled as a power law with $\Gamma \sim 1.4$–1.5 above ~ 1 keV (Vecchi et al., 1999; Kushino et al., 2002; Hickox & Markevitch, 2006; Cappelluti et al., 2017). Ponti et al. (2023b) also tested a double power law with $\Gamma_1 = 1.9$ below 0.4 keV, $\Gamma_2 = 1.6$ keV, and $\Gamma_3 = 1.45$ above 1.2 keV for the CXB component in light of the observational constraints on the CXB (Gilli et al., 2007). While the latter is likely more realistic, we justify using a simple power law with a fixed $\Gamma = 1.45$ as most of the CXB is absorbed by the column density of the molecular cloud or subdominant to the CGM component. This value of Γ is based on the measurement of Cappelluti et al. (2017), who found $\Gamma = 1.45 \pm 0.02$. Upon fixing the photon index, the only parameter allowed to vary is the normalisation of the CXB component.

We model the emissions from the Milky Way as a combination of the CGM and Galactic corona, following the treatment of Ponti et al. (2023b). The CGM is generally attributed to the hot gas halo of the Milky Way (e.g. Miller et al., 2016; Ponti et al., 2023b, and references therein), which could extend up to its virial radius of ~ 280 kpc or beyond (Bland-Hawthorn & Gerhard, 2016). This hot gas halo could be the shock-heated gas created by accretion onto Milky Way's dark matter halo (e.g. White & Frenk, 1991). In our model, the CGM is assumed to be in collisional ionisation equilibrium like the LHB, but with a much lower abundance of 0.1 $Z_\odot$ compared to the conventional value of $Z_{\rm CGM} = 0.3\,Z_\odot$. The low abundance is motivated by the finding of Ponti et al. (2023b) in the eFEDS field, who found $Z \simeq 0.06\,Z_\odot$ with an upper limit of $Z \sim 0.1\,Z_\odot$.

The Galactic corona component was detected in the eFEDS field as well and is hypothesised to originate from energetic activities such as supernova explosions with sufficient energies to break free from the Galactic disk and supply hot plasma and metals into the spaces above and below the disk (e.g. Fraternali et al., 2015; Ponti et al., 2023b). If one assumes the corona is in collisional ionisation equilibrium with solar abundance, Ponti et al. (2023b) inferred a temperature of $\simeq 0.7$ keV. Solar abundance is assumed because the source of the corona is believed to be from chimneys or outflows from the Galactic disk, which are expected to be chemically enriched.

There is a concern that the corona component could be confused with the coronal emission from M dwarfs, as suggested by Wulf et al. (2019). A recent eROSITA study by Magaudda et al. (2020) suggests 65% of the 687 detected M dwarfs have a temperature ~ 0.5 keV, similar to the corona component. It is unclear at the moment the significance M dwarfs play in the soft X-ray diffuse emission, whether they are negligible, partly or wholly responsible for the corona component. However, analysing the physical origin of this component is beyond the scope of our work.

With the aforementioned assumptions, only temperatures and their EMs are free to vary in the CGM and corona components. The solar abundances reference for all components modelled by `APEC` (LHB, CGM, COR) follows Anders & Grevesse (1989).

2.4.3 Fitting procedures

Spectral fitting was performed with the PyXspec software (Arnaud, 1996; Gordon & Arnaud, 2021). For each cloud, we carried out a simultaneous fit of 80 spectra (5 TMs $\times$ 4 regions $\times$ 4 eRASSs). The spectral fits began with minimising the C-statistic (Cash, 1979). The resulting covariant matrix would then be used to construct a Gaussian proposal distribution in the following Markov Chain Monte Carlo (MCMC) step. We ran three MCMC chains for each cloud using the Goodman-Weare method (Goodman & Weare, 2010), each with 100 walkers of 10000 steps. The initial positions of the walkers were randomised to avoid being trapped in local minima, and the first 1000 steps they sampled were discarded. As all the resulting corner plots (marginalised posterior distributions) from merging the three chains exhibit only a single peak without complicated profiles (see Sect. 2.11), we finally constructed the model spectra using the 50 percentile of each parameter (as in Figs. 2.5, 2.6 and 2.7).

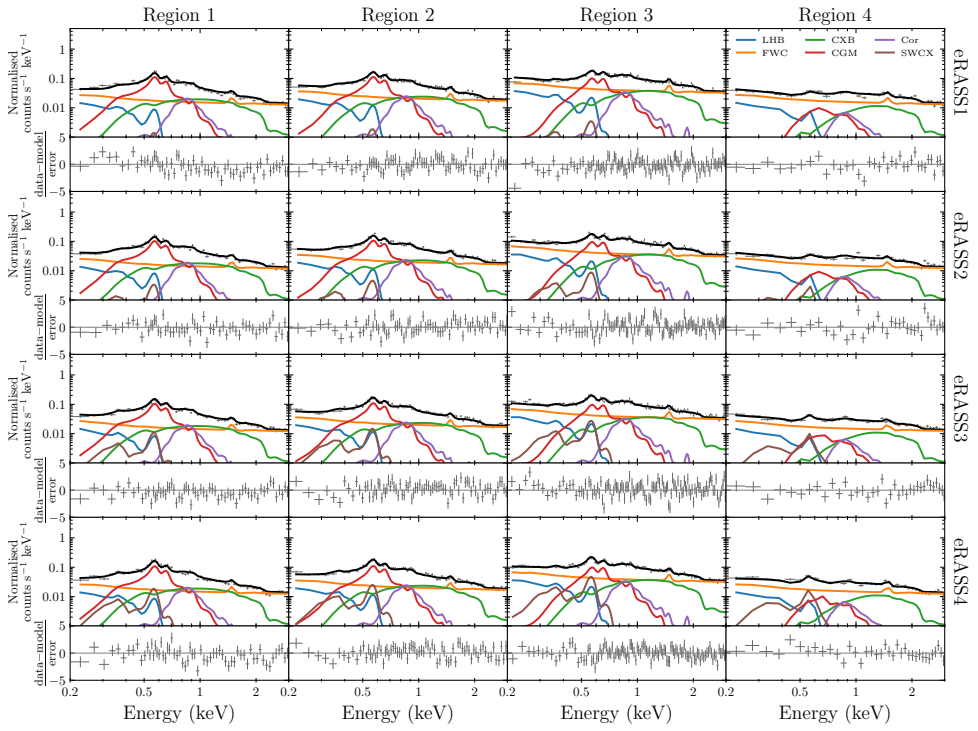

Figure 2.5: Spectral model of Cha II & III as functions of time in half-year intervals (from top to bottom row) and column density (from left to right column). Each panel shows the TM-averaged data in grey and the corresponding model in black. The constituents of the models are also shown (see the legend).

2.5 Results and discussions

The fit with the highest likelihood for each cloud is shown in Figs. 2.5, 2.6 and 2.7 with the corresponding parameters in Table 2.2. Figs. 2.5, 2.6 and 2.7 are arranged such that each row corresponds to the observation within the one eRASS, as indicated on the right axis. Each column corresponds to spectra extracted within the same region, as defined by the $N_{\rm H}$ maps as shown in the right panel of Figs. 2.1, 2.2 and 2.3. Column density increases from left to right. We present the spectral fit in this manner so that the difference between the rows reflects the variations from SWCX, and the difference between the columns shows the absorption of the background components. There are no strong correlations between the parameters, as evidenced by the two-dimensional projections of the posterior distributions shown in Sect. 2.11.

2.5.1 SWCX

For Cha II & III, one can immediately identify the monotonically increasing SWCX component from eRASS1 to eRASS4, in line with the observations in eFEDS and eRASSs (Ponti et al. 2023b, Dennerl et al. in prep.). The SWCX contribution is negligible in eRASS1, matches the O VII line from the LHB subsequently at eRASS3, then ultimately dominates the foreground O VII emission in eRASS4. This trend echoes the natural expectation and the findings by Qu et al. (2022), where the heliospheric SWCX is positively correlated with the solar cycle (solar cycle 25 began on December 2019, as well as eRASS1).

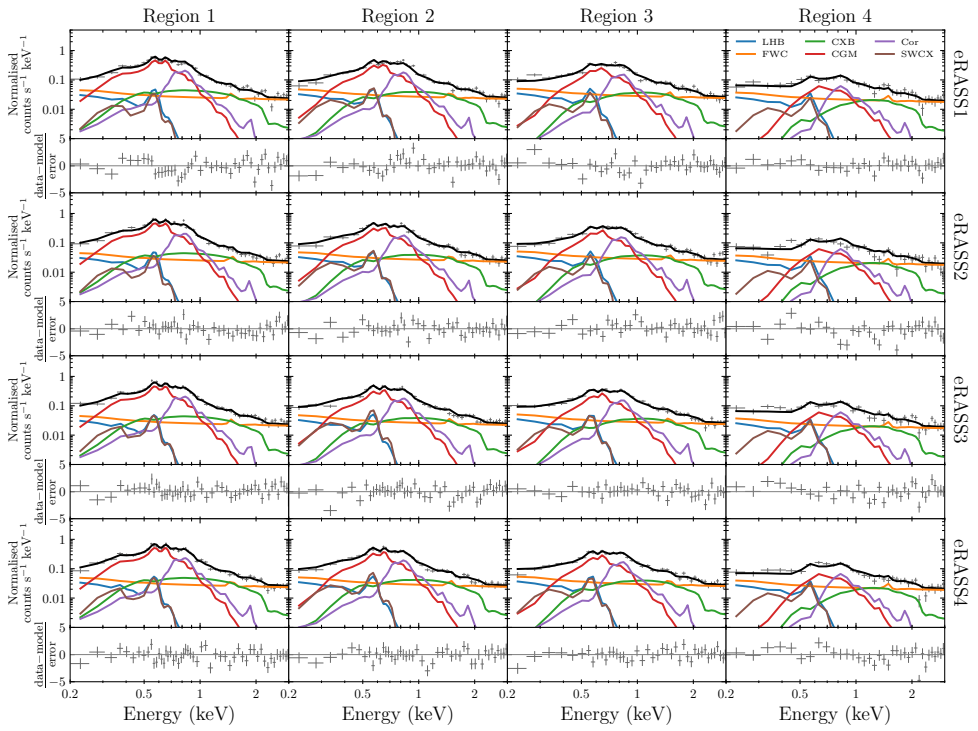

Figure 2.6: Same as Fig. 2.5, but for CrA.

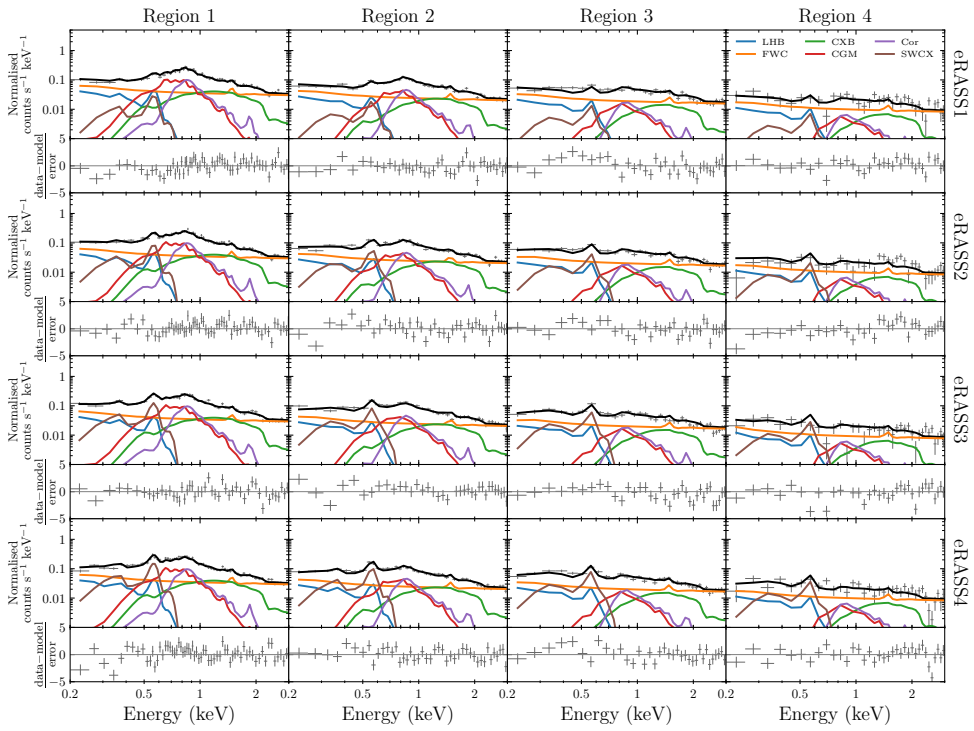

Figure 2.7: Same as Figs. 2.5 and 2.6, but for Oph.

Table 2.2: Fit parameters of the spectral fitting.

Cloud	Cha II & III	Oph	CrA
$kT_{\rm LHB}{}^{(a)}$	$0.084^{+0.004}_{-0.004}$	$0.102^{+0.006}_{-0.006}$	$0.115^{+0.012}_{-0.011}$
$\rm EM_{LHB}{}^{(b)}$	$2.563^{+0.356}_{-0.299}$	$2.062^{+0.237}_{-0.221}$	$1.913^{+0.369}_{-0.284}$
$kT_{\rm SWCX}{}^{(a)}$	$0.109^{+0.003}_{-0.004}$	$0.110^{+0.002}_{-0.002}$	$0.108^{+0.005}_{-0.006}$
$n_{\rm SWCX,e1}{}^{(c)}$	$0.192^{+0.217}_{-0.159}$	$1.687^{+0.511}_{-0.530}$	$3.215^{+1.297}_{-1.182}$
$n_{\rm SWCX,e2}{}^{(c)}$	$0.495^{+0.306}_{-0.230}$	$4.948^{+0.616}_{-0.617}$	$3.271^{+1.207}_{-1.177}$
$n_{\rm SWCX,e3}{}^{(c)}$	$1.544^{+0.428}_{-0.305}$	$7.214^{+0.783}_{-0.811}$	$4.200^{+1.235}_{-1.102}$
$n_{\rm SWCX,e4}{}^{(c)}$	$2.596^{+0.540}_{-0.426}$	$8.635^{+0.915}_{-0.834}$	$3.973^{+1.110}_{-1.232}$
$N_{\rm H,reg1}{}^{(d)}$	$1.106^{+0.062}_{-0.059}$	$2.618^{+0.191}_{-0.162}$	$0.641^{+0.050}_{-0.044}$
$N_{\rm H,reg2}{}^{(d)}$	$1.434^{+0.066}_{-0.054}$	$3.665^{+0.191}_{-0.177}$	$1.196^{+0.063}_{-0.052}$
$N_{\rm H,reg3}{}^{(d)}$	$2.313^{+0.070}_{-0.058}$	$5.566^{+0.215}_{-0.220}$	$1.673^{+0.067}_{-0.062}$
$N_{\rm H,reg4}{}^{(d)}$	$4.258^{+0.124}_{-0.085}$	$6.582^{+0.415}_{-0.370}$	$3.324^{+0.118}_{-0.113}$
$kT_{\rm CGM}{}^{(a)}$	$0.183^{+0.002}_{-0.002}$	$0.270^{+0.010}_{-0.011}$	$0.213^{+0.005}_{-0.005}$
$\rm EM_{CGM}{}^{(e)}$	$6.950^{+0.437}_{-0.478}$	$5.581^{+0.851}_{-0.745}$	$12.529^{+0.799}_{-0.673}$
$kT_{\rm Cor}{}^{(a)}$	$0.746^{+0.017}_{-0.014}$	$0.719^{+0.017}_{-0.018}$	$0.613^{+0.014}_{-0.015}$
$\rm EM_{Cor}{}^{(b)}$	$0.670^{+0.034}_{-0.039}$	$2.294^{+0.222}_{-0.226}$	$3.272^{+0.211}_{-0.226}$
$\rm norm_{CXB}{}^{(f)}$	$0.237^{+0.003}_{-0.003}$	$0.286^{+0.006}_{-0.007}$	$0.278^{+0.008}_{-0.008}$

Notes. The values reported are the 50 percentiles, with the lower and upper bounds showing the 16 and 84 percentiles of the Markov Chain Monte Carlo analysis result.
(*a*) $kT_{\rm LHB}$, $kT_{\rm SWCX}$, $kT_{\rm CGM}$ and $kT_{\rm Cor}$ are in units of keV.
(*b*) $\rm EM_{LHB}$ and $\rm EM_{Cor}$ are in units of $10^{-3}\,\rm cm^{-6}\,pc$.
(*c*) $n_{\rm SWCX}$ is in the unit of $10^{-2}\,\rm deg^{-2}$. The normalisation parameter of the `ACX2` model is dimensionless and is only intended for relative scaling (see the documentation of the `ACX` model). We normalised this factor by the sky area to give the unit $\rm deg^{-2}$.
(*d*) $N_{\rm H}$ values are in units of $10^{21}\,\rm cm^{-2}$.
(*e*) $\rm EM_{CGM}$ is in $10^{-2}\,\rm cm^{-6}\,pc$.
(*f*) $\rm norm_{CXB}$ has unit of $10^{-2}\,\rm photons\,keV^{-1}\,cm^{-2}\,s^{-1}\,deg^{-2}$ at 1 keV.

We found the best-fit $kT_{\rm SWCX} \sim 0.1$ keV for all three sight lines, a value consistent with solar wind data (von Steiger et al., 2000; Gloeckler & Geiss, 2007). Despite similar temperatures of the LHB and SWCX ($kT_{\rm LHB} \simeq kT_{\rm SWCX} \simeq 0.1$ keV), the spectral shapes of the SWCX and LHB are significantly different — SWCX has two prominent peaks, C VI at 0.37 keV and O VII at 0.57 keV, while the LHB has both of these prominent emission lines, an extra rising continuum towards the low energy from radiative recombination and bremsstrahlung is present. Combining such differences with the fact that only the SWCX component is allowed to vary between eRASSs, eliminates much of the degeneracy between the two components, given our SWCX spectral model is correct and our constant $kT_{\rm SWCX}$ assumption is valid. The (lack of) correlations between the LHB and SWCX parameters can be shown from the posterior distributions of the model parameters in Fig 2.14.

Fig. 2.8 summarises the SWCX variability to the directions of the three clouds. It shows the 0.3–0.7 keV band intensities from the models as a function of eRASS. This energy band includes most of the emissions from our SWCX component. Clear increasing trends are observed for all the clouds, showing the correlation with the solar activity, irrespective of the pointing direction. Interestingly, among the three clouds, we observe that the SWCX intensity is the highest towards Oph and the lowest towards Cha II & III. We argue this is likely the difference in the zero-level SWCX, caused by the difference in the solar wind density, which is a decreasing function of heliolatitude (e.g. see Fig. 18 of Porowski et al., 2022). Ignoring the minor difference between heliolatitude and ecliptic latitude (β)[2], one could see this argument matches, at least qualitatively, with the ecliptic latitude of the clouds — Cha II & III has the highest $\beta \sim -62°$, followed by CrA at $\beta \sim -14°$, and finally Oph at $\beta \sim -1°$. As a result, the LHB intensity dominates the SWCX emissions from Cha II & III in all eRASSs in this band, but SWCX overtook it towards Oph since eRASS2.

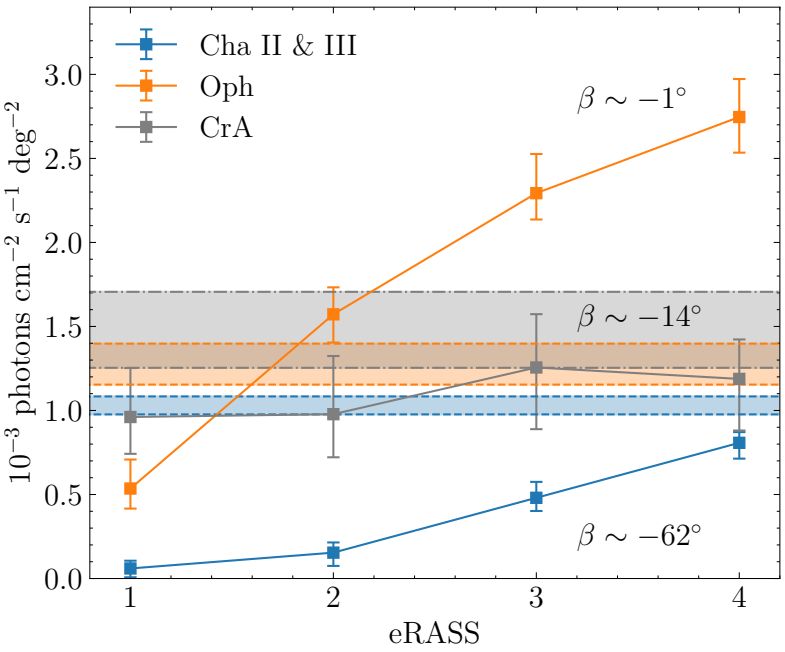

Figure 2.8: Variation of the model SWCX intensity in the 0.3–0.7 keV band in eRASS1–4. The LHB intensities within 1 σ confidence level in the same band are also shown by the shaded regions.

We notice that the rate of increase of SWCX intensity is not at all constant and differs from cloud to cloud. Explaining the precise trends is complex and is beyond the scope of this work. To

[2]The solar equatorial plane is inclined by $\sim 7\overset{\circ}{.}5$ with the ecliptic plane, with the line of nodes at ecliptic longitude of $\sim 76°$ (H.M. Nautical Almanac Office, 1961; Hapgood, 1992).

complicate the issue further, we point out that Fig. 2.8 contains a caveat where the observations of different clouds made within the same eRASS were not done simultaneously. Instead, they could differ up to $\sim$ 1.5 months in the case of CrA ($\lambda \sim 282°$) and Cha II & III ($\lambda \sim 246°$), because eROSITA's scanning approximately follows the ecliptic longitude (λ) with a progression of about 1°per day.

The background 0.3–0.7 keV count rate of RX J1856 located in the neighbourhood of CrA indicates a similar trend as CrA from eRASS1–3 (see Table 2.4). This comparison suggests our inferred SWCX contribution from spectral fitting is reliable, and indeed the increase in SWCX emission from CrA is less pronounced than the rest (see Sect. 2.8 for more discussion).

2.5.2 LHB

We found the temperature of the LHB to range from $0.084^{+0.004}_{-0.004}$–$0.115^{+0.012}_{-0.011}$ keV from the three sight lines. We also found $\mathrm{EM_{LHB}}$ to span a range from $1.91^{+0.37}_{-0.28}$ – $2.56^{+0.36}_{-0.30} \times 10^{-3}$ cm^{-6} pc. As mentioned in Bluem et al. (2022), a direct comparison of these values, which are derived from the `APEC` model in `AtomDB` version 3.0.9, with those measured by Liu et al. (2017) is no longer valid due to the updates introduced since its publication date. Therefore, we repeat the same spectral fitting using `AtomDB` version 3.0.3, released about half a year before the publication of Liu et al. (2017). This result is shown in more detail in Sect. 2.12. In summary, the LHB temperature we found is consistent with the SWCX-subtracted measurement from ROSAT by Liu et al. (2017), who found $kT_{\mathrm{LHB}} = 0.097 \pm 0.019$ keV averaging across the whole sky. In terms of EM, our measurement is in line with values inferred from the EM map of Liu et al. (2017). One could also compare our LHB measurement to McCammon et al. (2002), who observed the diffuse X-ray background using microcalorimeters with a high energy resolution of 5–12 eV on a sounding rocket. McCammon et al. (2002) reported a kT_{LHB} of 0.099 keV and an $\mathrm{EM_{LHB}}$ of 8.8×10^{-3} cm^{-6} pc — a similar temperature but a significantly different $\mathrm{EM_{LHB}}$. The main sources of the discrepancy are likely to be a higher Galactic latitude in their observations ($|\Delta b| \sim 40°$), a limited knowledge of SWCX at the time, which was not modelled, as well as a significantly fainter Galactic halo component ($\mathrm{EM_{CGM}} = 3.7 \times 10^{-3}$ cm^{-6} pc) in their spectral fits.

Using the Wisconsin B/C band intensity ratio, Snowden et al. (1990b) reported a dominantly longitudinal LHB temperature dipole, from $10^{5.9}$ K towards the Galactic anti-centre to $10^{6.2}$ K towards the Galactic centre. Later, the existence of the temperature dipole was further consolidated using X-ray shadows and their ROSAT R2/R1 band ratio by Snowden et al. (2000), which show a minimum temperature of $10^{6.04}$ K (0.09 keV) near the Galactic anti-centre and a maximum of $10^{6.13}$ K (0.11 keV) at the Galactic centre. We observe the same trend and systematic temperature variation in the three molecular clouds, which shows a decreasing temperature from $0.084^{+0.004}_{-0.004}$ keV at $l \sim 300°$ to $0.115^{+0.012}_{-0.011}$ keV at $l \sim 360°$, although the X-ray shadows in Snowden et al. (2000) are located at higher latitudes ($|b| \gtrsim 20°$). We would like to note that it is not clear whether this is a real temperature change, as incorrect modelling of the absorption could also result in an apparent temperature change in the LHB.

It is also interesting to test if the LHB is homogeneous in density with the known distances of the clouds in the literature. The distances to these clouds were mainly derived from *Gaia*-DR2 astrometry of young stars embedded within the cloud complexes. For instance, the distances to Cha II & III are known to a very high accuracy from *Gaia* parallax measurements — Cha II is $197.5^{+1.0}_{-0.9}$ pc away (Galli et al., 2021) and Cha III 199^{+20}_{-18} pc (Voirin et al., 2018). One could infer the electron density n_e of the LHB using

$$\mathrm{EM} \quad = \quad \int_0^L n_e(l) n_{\mathrm{H}}(l) dl, \tag{2.1}$$

where n_{H} is the hydrogen density and L is the distance to the molecular cloud concerned. We simplify the expression further by adopting a few assumptions — the LHB is completely volume-filling up to the clouds with a constant density and it is fully ionised with $n_{\mathrm{He}}/n_{\mathrm{H}} = 0.1$, so that the electron density is 1.2 times the hydrogen density n_{H} of the LHB plasma (Snowden et al.,

Table 2.3: Distances to the clouds and the estimation of the LHB electron density and thermal pressure along these sight lines.

Cloud	Distance (pc)	n_e (10^{-3} cm^{-3})	P_T/k (cm^{-3} K)	Distance references
Cha II & III	$197.5^{+1.0}_{-0.9}$ & 199^{+20}_{-18}	$3.94^{+0.26}_{-0.24}$	7380^{+860}_{-780}	1, 2
Oph	$141.2^{+8.4}_{-7.5}$	$4.19^{+0.23}_{-0.23}$	9520^{+1110}_{-1050}	3
CrA	$149.4^{+0.4}_{-0.4}$	$3.92^{+0.36}_{-0.30}$	10050^{+2070}_{-1660}	4

(1) Galli et al. (2021); (2) Voirin et al. (2018); (3) Cánovas et al. (2019); (4) Galli et al. (2020)
Notes. The uncertainties in the distance are relatively small compared to the EM uncertainties reported in Table 2.2. Therefore, they are ignored in the conversion to n_e.

2014). Therefore, we have

$$n_e = \sqrt{\frac{1.2\mathrm{EM}}{L}}. \tag{2.2}$$

We assume further that the distance to both cloud complexes is $L \simeq 198$ pc with negligible uncertainty compared to the EM, we infer $n_e = 3.94^{+0.26}_{-0.24} \times 10^{-3}$ cm^{-3}. This dwells on the low side, but is nonetheless consistent with the measurement of $n_e = (4.68 \pm 0.47) \times 10^{-3}\,\mathrm{cm}^{-3}$ by Snowden et al. (2014). Similarly, we estimate the electron density of CrA and Oph using the calculation above using their most recent distance measurements and present the results in Table 2.3.

With the conversion from EM to electron density, we present the posterior distributions of the LHB properties in Fig. 2.9. Despite the three lines of sight agreement on the LHB density at $\sim 4 \times 10^{-3}$ cm^{-3}, the LHB temperature inferred from Cha II & III is significantly colder than the rest. The LHB properties towards Oph and CrA agree at $1\,\sigma$ level but differ from those derived from Cha II & III at $\geqslant 3\,\sigma$ level. The variation in electron density of the three lines of sight is a constant within 10%.

We would like to highlight that the three chosen sight lines of significantly different distances (Cha II & III is $\sim$ 40% farther than the rest) corroborate a single LHB density within 10% is an interesting result. This result strongly indicates that the LHB extends up to the molecular clouds' distance unless the LHB density or the volume filling factor is much more variable than we assumed.

The presence of a temperature gradient is not completely surprising as magneto-hydrodynamic (MHD) simulations have already shown the turbulent temperature and density structures sustained by supernova explosions in the ISM (e.g. see Fig. 1 of Hill et al. 2012, de Avillez & Breitschwerdt 2005). It is reasonable to find varying temperature densities when integrating the emission in the turbulent LHB medium along different lines of sight. The fact that we inferred consistent LHB properties from Oph and CrA, which are separated by a significant angular separation of $\sim 35^\circ$, indicates the constant temperature and density assumption is a reasonable modelling simplification to the more complicated scenario presented by MHD simulations.

We estimate the thermal pressure inside the LHB along the three lines of sight following the treatment in Snowden et al. (2014) using

$$P_T/k = nT \simeq 1.92 n_e T, \tag{2.3}$$

where k is the Boltzmann constant and n is the total particle density. We found P_T/k to be in the range of 6600–12100 cm^{-3} K (see Table 2.3). The resulting pressures are consistent with a constant, unlike the plasma temperature, as a result of propagating the uncertainties of n_e and T. However, we note that there is a hint of pressure inhomogeneity between Cha II & III and the other two clouds ($\sim 1\,\sigma$), which could indicate a recent supernova or stellar wind expanding from within the LHB that has not yet attained pressure equilibrium with the ambient medium.

The LHB is more elongated in the direction perpendicular to than along the Galactic plane, most probably due to the higher pressure exerted by the ISM in the Galactic disk (Liu et al.,

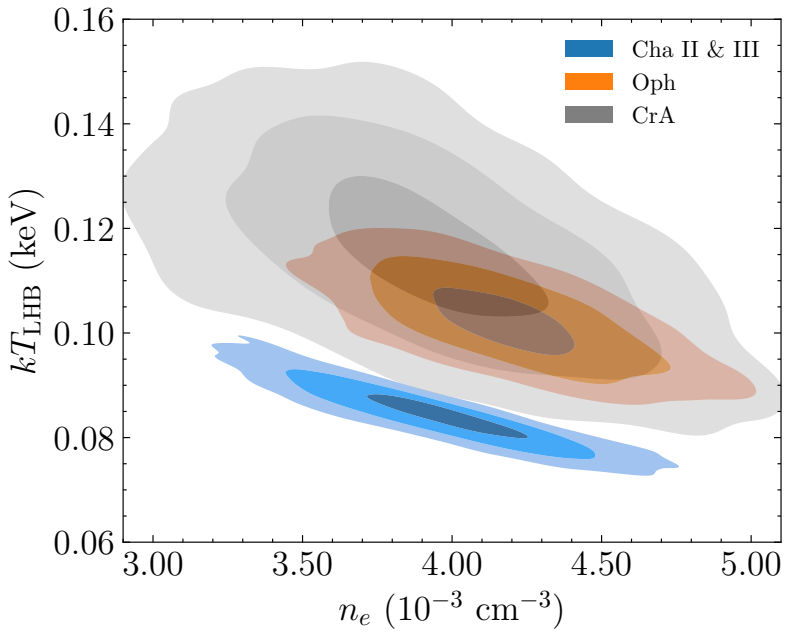

Figure 2.9: Posterior distributions of the temperature and electron density of the LHB. The contours indicate the 1, 2 and 3 σ confidence levels (enclose $\sim$39, 86 and 99% of the probability from the highest density).

2017). If the LHB is expanding adiabatically, we would expect a lower pressure also towards the Galactic poles. Unfortunately, our current samples cannot probe the Galactic-latitudinal dependence comprehensively as they are close to the Galactic plane and are only valid within $13^\circ \lesssim |b| \lesssim 22^\circ$.

2.5.3 Background components

As we are probing the regions with some of the highest column density away from the Galactic plane, naturally, our analysis is not the best suited to the analysis of the background components located beyond $\sim$ 200 pc from us. Nonetheless, even from the images (left panels of Figs. 2.1, 2.2 and 2.3), one could see the emissions from the eROSITA bubbles would bias our conclusion about the background components. Therefore, we begin our discussion with Cha II & III, the only cloud in our samples not located in front of the eROSITA bubbles, hopefully giving more reliable results.

It is instructive to begin by comparing the normalisation of the isotropic CXB component with literature values. With a single power-law with $\Gamma = 1.48$, Chen et al. (1997) found $\mathrm{norm_{CXB}} = 10.5\pm0.4$ photons cm^{-2} s^{-1} sr^{-1} at 1 keV, corresponding to $(3.2\pm0.2)\times10^{-3}$ photons cm^{-2} s^{-1} deg^{-2}, using a combination of ROSAT and ASCA. More recently, Cappelluti et al. (2017) found $\mathrm{norm_{CXB}} = (3.32 \pm 0.05) \times 10^{-3}$ photons cm^{-2} s^{-1} deg^{-1} at 1 keV from the much more sensitive 2.15 deg^2 Chandra COSMOS-legacy field data. Upon removing all the X-ray detected sources, they found $\mathrm{norm_{CXB}}$ drops to $(1.27 \pm 0.08) \times 10^{-3}$ photons cm^{-2} s^{-1} deg^{-1} at 1 keV, corresponding to a decrease of $\sim$ 2.5 times. Our measurement of $\mathrm{norm_{CXB}}$ for Cha II & III, but also the other two clouds, fall between the values of Cappelluti et al. (2017) before and after the X-ray detected source removal. This is expected as eROSITA is much less sensitive and has a lower angular resolution than Chandra's 4.6 Ms COSMOS-Legacy survey, naturally detecting much less detected X-ray sources to exclude in our analysis.

We found the CGM component to be similar in temperature and EM as the value inferred from the eFEDS field[3] (Ponti et al., 2023b), despite the completely different line-of-sight. The eFEDS

[3]Ponti et al. (2023b) provides several models. Here, we refer to their shift-LHB-CGM-Coro-CXB-SWCX model,

field and Cha II & III are separated by $\sim 85^\circ$ in different galactic hemispheres and latitudes so that it could be a glimpse of an approximately spherical Milky Way hot halo preferred by the analysis of Bregman et al. (2018), but it is certainly far from conclusive. Similarity can also be found in the temperature of the corona component (~ 0.7 keV) when compared with the thermal equilibrium model in Ponti et al. (2023b). However, we found a $\mathrm{EM_{Cor}}$ that is higher than the eFEDS field ($\mathrm{EM_{eFEDS}} = (0.385 \pm 0.025) \times 10^{-3}\,\mathrm{cm^{-6}\,pc}$). This is qualitatively consistent with the picture that the corona is more confined to the Galactic plane from outflows from supernovae or stellar winds since Cha II & III has a lower galactic latitude than the eFEDS field ($|b| \sim 30^\circ$).

A high galactic latitude ($|b| > 30^\circ$) HaloSat study by Bluem et al. (2022) also detected the corona component, which they call the hot component of the CGM, to have the same temperature $kT_{\mathrm{Cor}} \sim 0.7$ keV. They inferred the same temperature for the cooler CGM component ($kT_{\mathrm{CGM}} \sim 0.18$ keV) as our Cha II & III sight line. However, our assumptions of the abundances differ — both their cool and hot CGM components are assumed to have $Z = 0.3\,Z_\odot$. Regarding the EM, our values of both CGM and corona are significantly higher than those found by Bluem et al. (2022) in the closest sight lines (separated $\sim 15^\circ$ from Cha II & III along the galactic longitude). The reason for the discrepancy is not apparent except for the different assumed abundance of both components. One possible explanation could be that the corona component is flattened along the Galactic plane, so the path length through a flattened corona increases more significantly towards the Galactic plane, resulting in a steep increase in EM.

For Oph and CrA, which are situated in front of the eROSITA bubbles, one could easily observe that their spectra are much more enhanced around ~ 0.8–1 keV, where the Ne IX, Ne X and various Fe lines are. The enhancement is most certainly coming from the eROSITA bubbles, which causes the EM of the corona component to 3–5 times the value in Cha II & III. Naturally, the bubbles affect not only the fit to the corona component but also the CGM component, as their spectra largely overlap. The CGM is hotter towards Oph, while a much brighter but cooler CGM is preferred towards CrA. There are at least two possibilities that could contribute to the difference: (1) Oph has a higher column density in general, which could bias towards a higher CGM temperature because the temperature proxy O VIII/O VII line ratio could also be accommodated for by a higher column density; (2) the properties of the northern and southern eROSITA bubbles are different, where the northern bubble is likely hotter. The second possibility can be explored and constrained relatively tightly with large regions within the northern and southern eROSITA bubbles at much lower column densities, which would largely remove the ambiguity caused by significant opacity. Nevertheless, the eROSITA bubbles are not expected to affect the measured properties of the foreground components because of the high absorption.

2.6 Summary and conclusions

We performed X-ray shadowing experiments on three giant molecular clouds using the data from the first four eRASSs. eROSITA spectra of the clouds allow us to separate the heliospheric SWCX and LHB contributions in soft X-ray foreground emission. We observed a monotonic increase of SWCX since eRASS1, independent of the cloud, matching the expectation based on the solar cycle. An ecliptic latitudinal dependence is also observed, consistent with the expected decreasing solar wind ion density.

From the known distance to the clouds, we found a constant electron density of the LHB plasma towards all three clouds, with $n_e \sim 4 \times 10^{-3}$ cm^{-3}. However, we measured a lower LHB temperature towards Cha II & III ($kT_{\mathrm{LHB}} = 0.084^{+0.004}_{-0.004}$ keV) compared to Oph and CrA ($\simeq 0.1$ keV). Our results show for the first time that there is a possible galactic longitudinal, but not a latitudinal gradient in the LHB temperature after the subtraction of SWCX. We also found that the thermal pressure in the LHB is consistent with a constant, given the current measurement uncertainty.

which is the most similar to our model setup.

2.7 Acknowledgments

MY and MF acknowledge support from the Deutsche Forschungsgemeinschaft through the grant FR 1691/2-1. GP acknowledges funding from the European Research Council (ERC) under the European Union's Horizon 2020 research and innovation programme (grant agreement No 865637). MS acknowledges support from the Deutsche Forschungsgemeinschaft through the grants SA 2131/13-1, SA 2131/14-1, and SA 2131/15-1.

We would like to thank the anonymous referee for the constructive and in-depth comments. We thank Susanne Friedrich for sharing the results of the SEP orbital analysis prior to publication.

This work is based on data from eROSITA, the soft X-ray instrument aboard SRG, a joint Russian-German science mission supported by the Russian Space Agency (Roskosmos), in the interests of the Russian Academy of Sciences represented by its Space Research Institute (IKI), and the Deutsches Zentrum für Luft- und Raumfahrt (DLR). The SRG spacecraft was built by Lavochkin Association (NPOL) and its subcontractors, and is operated by NPOL with support from the Max Planck Institute for Extraterrestrial Physics (MPE).

The development and construction of the eROSITA X-ray instrument was led by MPE, with contributions from the Dr. Karl Remeis Observatory Bamberg & ECAP (FAU Erlangen-Nuernberg), the University of Hamburg Observatory, the Leibniz Institute for Astrophysics Potsdam (AIP), and the Institute for Astronomy and Astrophysics of the University of Tübingen, with the support of DLR and the Max Planck Society. The Argelander Institute for Astronomy of the University of Bonn and the Ludwig Maximilians Universität Munich also participated in the science preparation for eROSITA.

The eROSITA data shown here were processed using the eSASS/NRTA software system developed by the German eROSITA consortium.

2.8 Appendix A: Cross-checking the SWCX variation with XMM-Newton's routine calibration source RX J1856.5-3754

We would like to have an indicator of SWCX variability independent of our spectral analysis. Therefore, we used the EPIC-MOS2 data on board XMM-Newton of the routine calibration source RX J1856.5-3754 (hereafter RX J1856). RX J1856 is a neutron star revisited by XMM-Newton approximately every six months for calibration. For the four observations carried out during the eRASSs, each has an exposure time ranging from 71500–74600 s. These observations provide an independent constraint on the SWCX level because of its proximity to CrA, as indicated by the left panel of Fig. 2.2 with $(l,b) = (358\overset{\circ}{.}59962, -17\overset{\circ}{.}21311)$. Both eROSITA and XMM-Newton require the solar angle to stay within $90 \pm 20^{\circ}$, owing to operational considerations such as ensuring a sufficient power supply from the solar panels and thermal stability. Therefore, the close spatial proximity of two celestial sources would also entail a close temporal coverage by eROSITA and XMM-Newton.

To infer SWCX variation, we focus on the background region count rate during each visit instead of the neutron star itself. MOS2 is a natural choice; all six outer ring CCDs remained operational despite being configured to the small window mode. On the other hand, two of the outer ring CCDs of MOS1 were lost due to micrometeoroid impacts, decreasing the background area. EPIC-pn was configured to the small window mode; therefore, it does not provide sufficient background region for analysis.

We found the count rates were high at the beginning of all four visits due to the radiation belts. These periods were removed. We note that XMM-Newton observations are affected not just by heliospheric SWCX but also by magnetospheric SWCX. We attempt to minimise the contribution from the latter, at least the time-variable component (variable in a time scale of hours, see Kuntz (2019)) of it, by filtering flares in the softer band (0.3–0.7 keV) within the comparatively long ($\gtrsim$ 20 h) exposure time in each visit. We found no flares in the first two visits, and $\sim$ 8% of

Table 2.4: Background count rate of the field of RX J1856.5-3754 as observed by XMM-Newton/EPIC-MOS2 in a similar time period of eROSITA's coverage of CrA.

eROSITA Coverage	XMM-Newton Coverage	0.3–0.7 keV	8–12 keV
2020-Apr-10–2020-Apr-14	2020-Mar-31–2020-Apr-01	5.989 ± 0.045	2.244 ± 0.019
2020-Oct-13–2020-Oct-17	2020-Sep-15–2020-Sep-16	6.123 ± 0.048	2.286 ± 0.020
2021-Apr-08–2021-Apr-14	2021-Apr-01–2021-Apr-02	6.101 ± 0.046	2.270 ± 0.019
2021-Oct-12–2021-Oct-17	2021-Oct-11–2021-Oct-12	7.934 ± 0.062	2.976 ± 0.025

Notes. The count rates reported in the 0.3–0.7 keV band are calculated using the vignetting-corrected exposure time, while the 8–12 keV band count rate used the exposure time without vignetting correction, because the latter should be dominated by particles that did not go through the mirror module. They have units of counts $\mathrm{s}^{-1}\,\mathrm{deg}^{-2}$. The $1\,\sigma$ error bars are shown.

exposure times were discarded in the third visit from the filtering. Unfortunately, the fourth visit on 11 October 2021 suffered from an enhanced quiescent background which cannot be cleaned. Further investigation into the radiation levels from all the instruments on board XMM-Newton reveals that a coronal mass ejection likely caused this. eROSITA also suffered from an enhanced background during this period; however, we could identify and remove this period from the data because of the much more extended coverage. Moreover, CCD5 of MOS2 were in an anomalous state at least during the first and third visits, where the background below 1 keV was strongly enhanced (Kuntz & Snowden, 2008). To err on the safe side, we removed CCD5 in all visits from the analysis.

From the sight line of CrA, we found the least increase in SWCX from eRASS1–4. Models with a constant SWCX could also fit the eRASS1–4 data, considering the measurement uncertainties. Nonetheless, we calculate the background count rates from the RX J1856 datasets to inspect the match. We report count rates from two bands — 0.3–0.7 keV for variation in SWCX and 8–12 keV for instrumental and particle background monitoring. The count rates and the eROSITA and XMM-Newton coverage period are listed in Table 2.4.

The 0.3–0.7 keV count rates appear to be constant from the period corresponding to eRASS1–3. While the increase from eRASS1 to eRASS2 appears to be $\gtrsim 1\,\sigma$ significance at first glance, but coincidentally, the instrumental or particle background was also enhanced as evidenced by the 8–12 keV band, which could likely cause the enhancement. We cannot attribute any count rate increase in eRASS4 to SWCX because of the coronal mass ejection that raised the count rates significantly in both bands (see Sect. 2.3). In summary, the SWCX variation observed by XMM-Newton in approximately the same epoch as the first three eRASSs seems to agree with eROSITA, which was relatively constant in time towards CrA, despite the uncertainty in determining the magnetospheric SWCX level.

2.9 Appendix B: Filter wheel closed data in 020 processing version

To study low-intensity diffuse emission, one needs to separate the contribution of the eROSITA instrumental background of the total measured intensity. The most direct way to estimate the instrumental background is by measuring the background level when the filter wheel is rotated to the `CLOSED` position. For the study of the local hot bubble (LHB) assuming the canonical plasma temperature of 0.1 keV, the relevant energy range for spectral analysis is $\lesssim 0.6$ keV. The emission of the LHB is expected to dominate the overall X-ray background at an even lower energy (< 0.2 keV) so that spectral analysis in this range would permit more stringent constraints on the properties of the LHB plasma. However, the lack of effective area combined with the rapidly increasing instrumental background of eROSITA $\lesssim 0.2$ keV makes this impossible. Therefore, the useful spectral range to constrain the LHB is limited to $0.2 < E \lesssim 0.6\,\mathrm{keV}$. The main

sources of instrumental background at this energy range include electronic noise arising from the circuitry and secondary X-rays created by high-energy particles hitting the camera (Freyberg et al., 2021). The background induced by high-energy particles, commonly referred to as the particle background, does not dominate in the energy range concerned. The particle background dominates the spectrum at $E > 4$ keV in the case of eROSITA. Due to an update of the pipeline processing of eROSITA data since version 010 (also implemented in the newer version 020), which includes improvements to the pattern identification algorithms to suppress the electronic noise at the low energy end, the instrumental background also changes accordingly. In this section, we present the filter-wheel-closed (FWC) data in the latest 020 version at the time of writing and their extraction procedures.

The 020 processing version provides the broadest uniformly calibrated eROSITA dataset thus far, in the sense that all retrieved eROSITA event lists, from the CalPV phase to the completion of eRASS4 of all 7 TMs have been processed. Despite the pipeline processing improvements, its breadth supersedes the 010 version in terms of temporal coverage, where only the data prior to eRASS2 were processed. The temporal coverage in the even earlier 946 processing version was similar to 020. However, in contrast to 020, TM4 data were not processed after a micro-meteoroid hit the detector on 23 February 2020 (Freyberg et al., 2022). For this reason, we had fewer signals for spectral analysis when using the 946 dataset. Complete temporal coverage from eRASS1 to eRASS4 of all the TMs (only TM1–4 and 6 were used for analysis due to optical light leak in TM5 and 7 (Predehl et al., 2021)) allows us to have a better estimation of the contamination introduced by the time-variable SWCX component.

Filter-wheel-closed spectra are created by merging all the events when the filter wheel was in the `CLOSED` position. However, an artefact that plagues most TMs in varying degrees needs to be removed before merging the FWC events, namely the $\sim$ 10 min 'afterglow' following the rotation of the filter wheel. This afterglow was first seen in ground calibration but was no longer detected after interchanging the materials of the small wheel that drives the filter disc and the inner ring of the filter disc. Unfortunately, the afterglow reappeared after launch, which can be clearly seen in light curves of both FWC and `FILTER` exposures in all energies above $\sim$ 0.5 keV. The afterglow is apparent in an example light curve from TM1 in Figure 2.10 as sandwiched by the red and green dashed lines, where the red line indicates the time stamp when the filter wheel rotation ceased and stopped at the `CLOSED` position and the green line 10 min after it as reference. The time intervals affected by the afterglow were removed from the good time intervals (GTIs) when extracting the FWC spectra. On top of the afterglow filtering, all FWC observations that have mean count rate deviating from the 90–160 counts min^{-1} were removed in order to avoid inclusion of contaminated data[4]. Moreover, a basic flag-filtering was applied to the FWC data before creating the spectra. The flag selection parameter used in the eSASS task `evtool` is 0xE000F000, which primarily rejects events detected by bad pixels and in the out-of-the-field-of-view CCD area. We note that this choice of flag selection is identical to that applied to all science data processed in 020 to ensure the FWC data is representative of the instrumental background in the astrophysical observations. The resulting live times for all TMs are in the order of 100 ks. Table 2.5 lists the precise live times of each TM.

Figure 2.11 shows the FWC spectra combining all patterns overlaid with the best-fit models in red for TM1–4 and 6. All TMs possess an approximately flat spectrum between $\sim$ 1–9 keV, then a variable cut-off between 9–10 keV, depending on the TM. The variable cut-off is caused by the minimum ionisation particle threshold being defined on the raw event amplitudes instead of energy. Thus, the cut-off varies according to the gain of each TM (Freyberg et al., 2021). Fluorescence lines, including the most prominent Al Kα at 1.5 keV and Fe Kα at 6.4 keV, are clearly visible. The fluorescence lines are believed to originate within the cameras from the graded shield consisting primarily of Al, Be, plus some impurities including Fe in the Be layer (Predehl

[4]This filtering criterion also applies to light curves that have CHOPPER > 1. In these cases, the bin width increases dynamically to accommodate the changes in CHOPPER. CHOPPER refers to the read-out cadence of the CCD where only 1/CHOPPER$^{\mathrm{th}}$ of all frames would be read out, stored and transmitted back to Earth. CHOPPER > 1 is used to reduce telemetry when encountering bright sources. Otherwise, in most pointing directions, CHOPPER = 1.

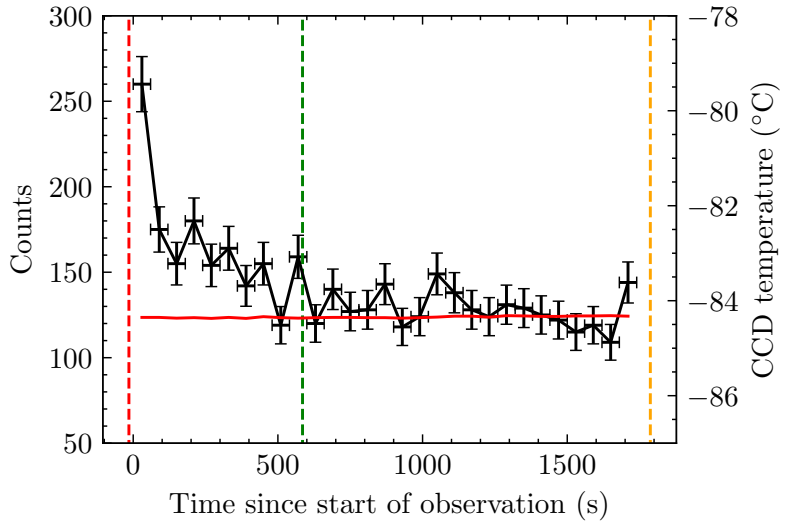

Figure 2.10: Example FWC light curve in eRASS1 at the $0.5 < E < 10$ keV band. The vertical red dashed line indicates when the filter wheel stopped rotating and stopped at the `CLOSED` position. The green dashed line indicates the reference cut-off time, which is 10 min after the red line. The orange line represents the time stamp when the filter wheel rotates again after the observation. Any events recorded between the red and green dashed lines are removed from the FWC dataset, and only events sandwiched between the green and orange dashed lines were considered. The width of the time bin is 60 s. The red horizontal line plots the CCD temperature in °C.

Table 2.5: FWC live times of the TM1–4 and 6.

TM	Live time (s)
1	138257
2	117327
3	88255
4	125169
6	106495

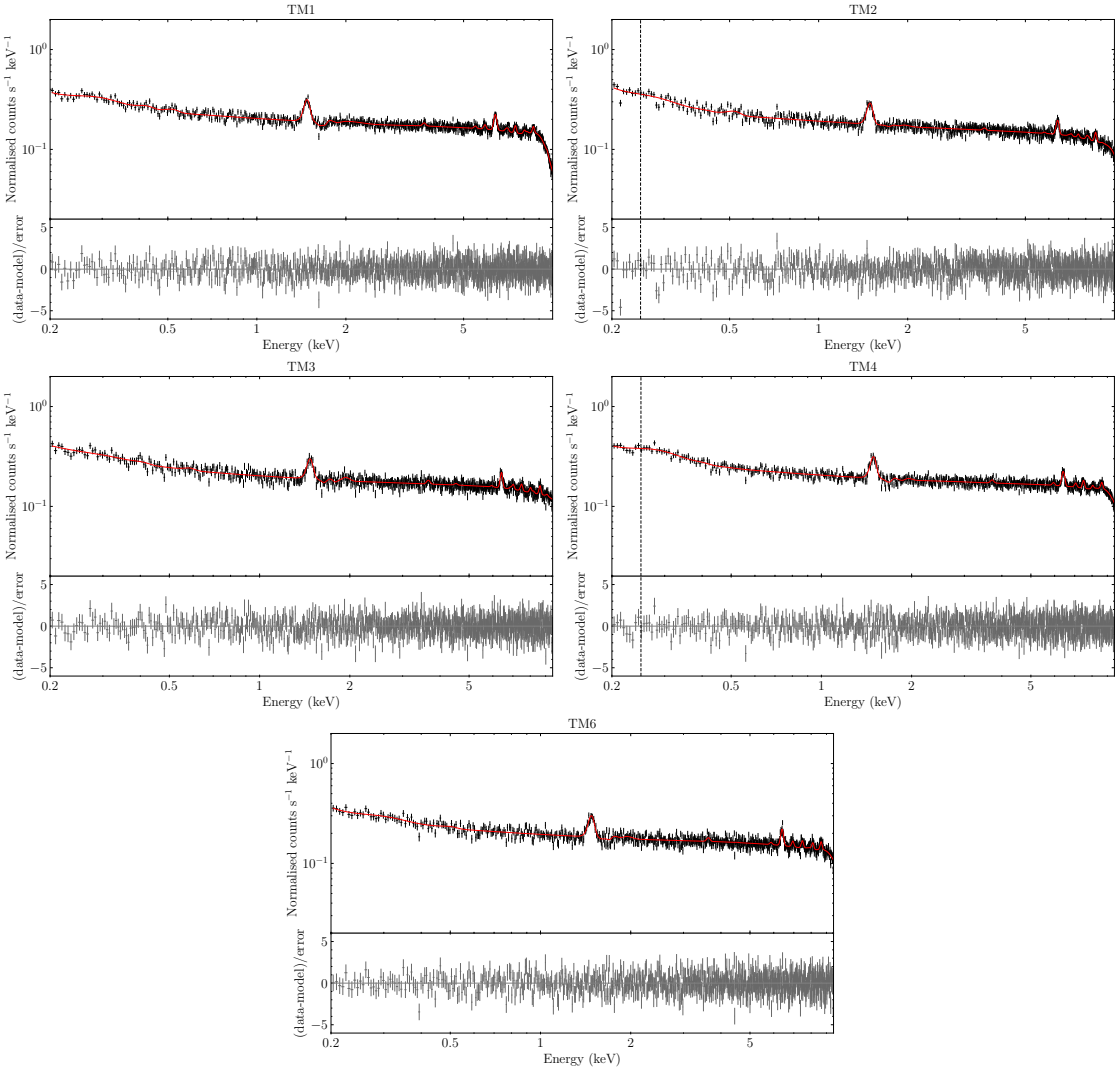

Figure 2.11: FWC spectra of all patterns for TM1–4 and 6. The best-fit FWC model is shown in red. The vertical dashed lines show the lowest energy the FWC model is employed due to variability considerations (Section 2.9.1).

et al., 2021). A gradual enhancement below 1 keV is mainly induced by electronic noise.

The FWC spectral models provide a convenient way to subtract the instrumental background from the spectra of extended sources or diffuse emissions. These models aim to reproduce the FWC data as closely as possible instead of being fully physically motivated. The main components include power-law models to trace the overall shape of the continuum with an exponentially decaying tail $\sim$ 9–10 keV to reproduce the cut-off. Fluorescence lines are reproduced by introducing Gaussians at the appropriate energies. In addition to the fluorescence lines, Gaussians are also introduced to modulate the model to accommodate small perturbations deviating from a perfectly smooth continuum.

There is an assumption that the FWC spectra do not change with time and are stable despite variations in CCD temperature to justify our use of a single FWC model for each TM. In Section 2.9.1, we demonstrate the variabilities of the FWC spectra regarding the time evolution and the CCD temperature.

2.9.1 Appendix B.1: Variability of FWC spectra

Figure 2.12 shows the integrated FWC spectra for each eRASS, where eRASS0 corresponds to times in the commissioning, calibration and performance verification (CalPV) programme which preceded eRASS1. FWC observations were conducted for all TMs in eRASS0–2, while only TM4 and TM2 had FWC observations in eRASS3 and 5, respectively. For TM1, 3, 4 and 6, no noticeable variability was observed across $0.2 < E < 9$ keV. For TM2, the spectrum in eRASS5 is more enhanced $\lesssim 0.3$ keV, and slightly below the spectra of earlier eRASSs between 2–9 keV. The lower particle background above 2 keV is expected due to the well-known anti-correlation of Galactic cosmic ray flux with solar activity (the Sun was approaching maximum activity from eRASS0 to 5), where the solar wind provides some degrees of shielding to Galactic cosmic rays (Neher & Anderson, 1962; Bulbul et al., 2020). Given that the FWC spectrum of TM2 is stable in the 0.25–2 keV range, the energy range for spectral analysis of eRASS3–4 data is limited to > 0.25 keV.

For all TMs at $E \lesssim 0.2$ keV, there is a clear trend of higher electronic noise for later eRASSs, despite the exact difference being dependent on the TM concerned. This could be the effect of CCD degradation caused by, for instance, radiation damage.

CCD temperature is expected to correlate with the electronic noise that contributes to the rising background at low energies. To investigate this effect, we extracted the CCD temperature records from the eROSITA housekeeping files to create GTIs which divide the FWC data into temperature bins of 1°C width. Figure 2.13 shows the FWC spectrum of each temperature bin. Similarly to time variability, no significant difference between spectra of each temperature is observed for TM1, 3 and 6 above 0.2 keV. For TM2 and 4, for temperature bins centred at or above −82°C, noticeable enhancements $\lesssim 0.25$ keV can be observed. While the shapes are similar, the cause of the enhancements is not necessarily identical. Further inspection reveals that all the events in the −81°C bin of TM2 are from eRASS5, which means one is essentially looking at the same spectrum shown in Fig. 2.12. Therefore, it is unclear whether the enhancement is a pure result of the degradation of the CCD or also involves genuine CCD temperature dependence. It is most likely that both effects are present. On the other hand, despite most of the events in the −81 and −80°C bins being recorded in eRASS3 in TM4, the eRASS3 spectrum of TM4 (Fig. 2.12) includes events also from lower CCD temperatures. The eRASS3 spectrum between 0.15 and 0.25 keV is slightly lower compared to the −80°C and −81°C spectra, suggesting the events recorded at lower temperatures have suppressed the enhancement in the eRASS3 spectrum. Hence, at least for TM4, one could see that both CCD degradation and temperature affect the electronic noise component $\lesssim 0.25$ keV.

For each TM, we have identified the lowest energy at which the FWC spectrum is stable, namely, 0.2 keV for TM1, 3 and 6, and 0.25 keV for TM2 and 4. These energies were plotted on Fig. 2.11, 2.12 and 2.13 as reference. Naturally, they serve as the lowest energies to which the corresponding FWC models should be applied. For our purpose, they also set the lowest energies for our spectral analysis.

2.10 Appendix C: Position and pointing of SRG/eROSITA with respect to the magnetosphere

We also checked the position of SRG/eROSITA with respect to the Sun-Earth-L2 line at the times of our shadowing observation periods. Table 2.6 gives the distances in geocentric solar ecliptic (GSE) coordinates, in units of Earth radii (R_E). In this right-handed system the $+X$ axis points towards the Sun, with the $+Z$ axis towards the North, $-Y$ in the ecliptic plane in the direction of planetary motion. $YZ = \sqrt{Y^2 + Z^2}$ is the distance from the Sun-Earth-L2 line, the larger the value, the more likely SRG/eROSITA is outside of the magnetosheath. The radius of the bow shock at L2 is usually assumed to be of order $100\,R_\mathrm{E}$ (for a review on Earth's magnetosphere, see, e.g. (Borovsky & Valdivia, 2018) and references therein). During the four eRASSs the values of YZ ranged between 44 and 139 R_E, while our targets were observed mostly at $YZ > 90\,R_\mathrm{E}$, which is outside the magnetosheath. Enhanced variable background was found more frequently

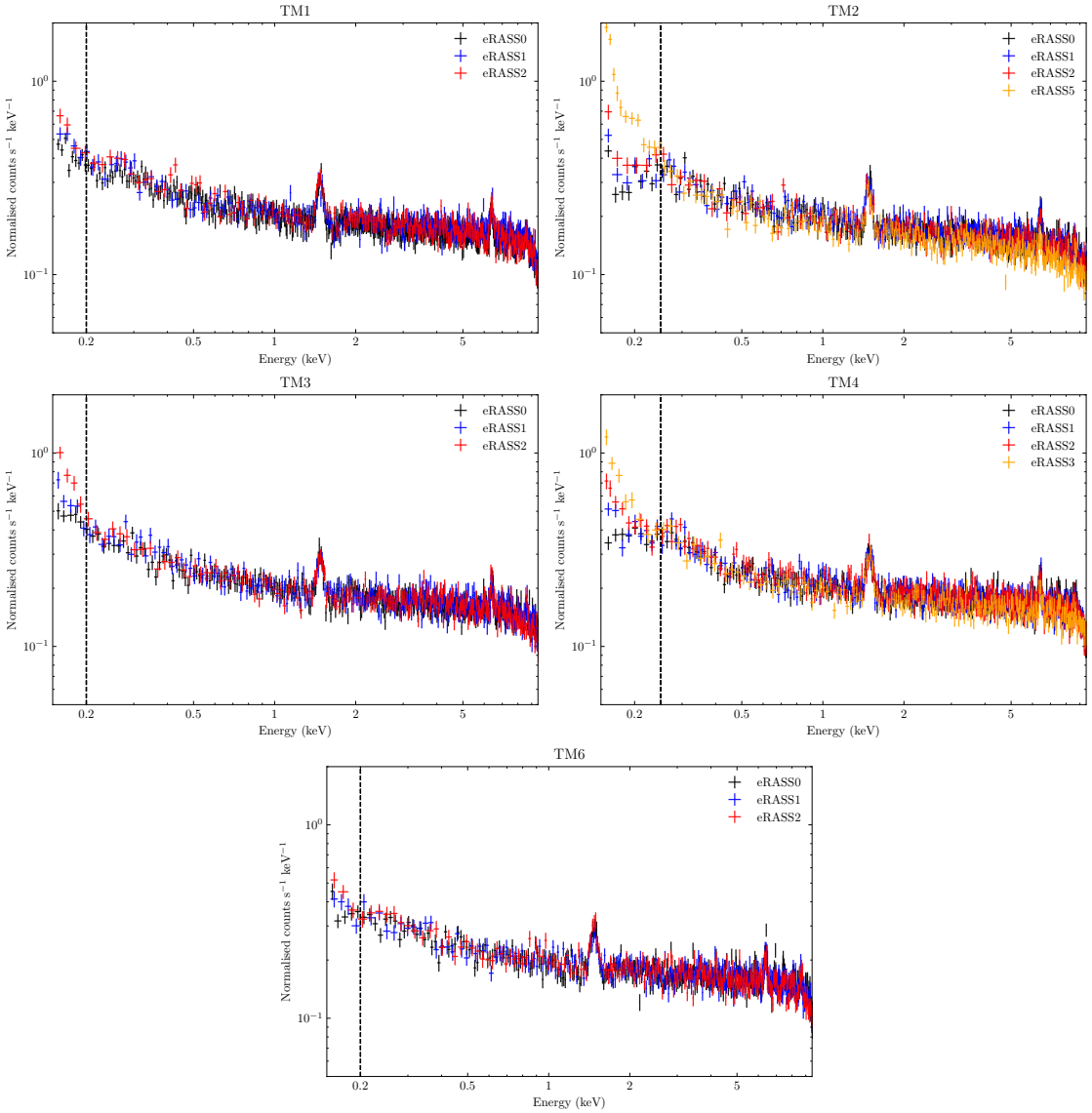

Figure 2.12: FWC Spectra of each eRASS including the CalPV phase. The vertical dashed lines indicate the energy below which variability sets in.

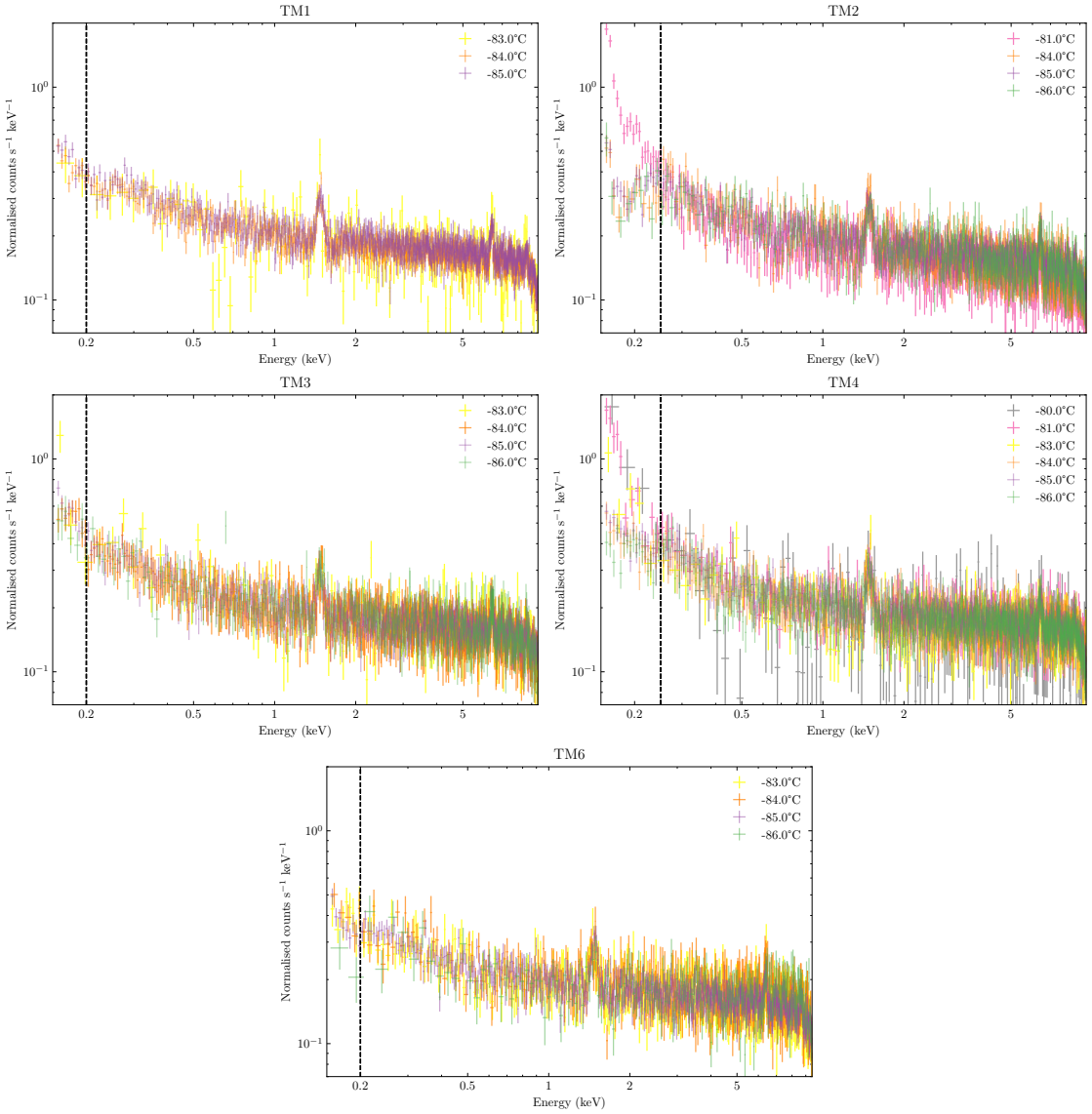

Figure 2.13: FWC Spectra of as a function of CCD temperature. Each temperature bin has a width of 1°C centring at the temperature indicated in the legend. The size of the error bars reflects the duration the detector was in the corresponding temperature when the FWC observations were taken. The vertical dashed lines indicate the energy below which variability sets in.

Table 2.6: Average position of SRG/eROSITA in geocentric solar ecliptic (GSE) coordinates with respect to the Sun-Earth-L2 line at the times of the X-ray shadowing observations (with ecliptic look direction indicated), in units of Earth radii. For details on the orbit, see Freyberg et al. (2021).

eROSITA target (λ, β)	eRASS	Dates	X	Y	Z	YZ
Cha II & III $(246^\circ, -61^\circ)$	1	2020-02-27 – 2020-03-13	-234.07	111.07	1.00	111.42
	2	2020-08-26 – 2020-09-12	-239.43	102.64	7.98	103.68
	3	2021-02-11 – 2021-03-10	-238.59	84.28	25.69	91.48
	4	2021-08-20 – 2021-09-06	-238.50	90.68	27.46	95.84
CrA $(284^\circ, -14^\circ)$	1	2020-04-10 – 2020-04-14	-185.07	91.22	-58.26	108.27
	2	2020-10-13 – 2020-10-17	-183.05	75.48	-67.20	101.11
	3	2021-04-08 – 2021-04-14	-185.93	66.78	-70.49	97.20
	4	2021-10-12 – 2021-10-17	-186.52	47.65	-72.95	87.26
Oph $(250^\circ, -1^\circ)$	1	2020-03-07 – 2020-03-15	-224.82	122.12	-11.05	122.70
	2	2020-09-06 – 2020-09-15	-228.70	114.73	-7.48	115.12
	3	2021-02-23 – 2021-03-12	-230.16	101.03	7.81	102.24
	4	2021-08-31 – 2021-09-10	-228.11	102.67	7.63	103.33

for lower values.

At the times of Oph observations, SRG/eROSITA was close to the ecliptic plane (low Z values) and looking almost in the ecliptic plane ($\beta \sim -1^\circ$). In March (eRASS1 and 3), eROSITA was thus looking through the magnetosphere, while in September (eRASS2 and 4), it was looking away when Ophiuchus was in the field of view. From observations of the South Ecliptic Pole, which was observed every four hours in Survey mode, we could not find any significant difference when being above or below the magnetosphere.

2.11 Appendix D: Posterior distributions of model parameters

We present the projected posterior distributions of the model parameters of Cha II & III in Fig. 2.14. No significant correlations between LHB and SWCX parameters are found. The results for CrA and Oph are similar; thus, they are not presented for the sake of brevity.

2.12 Appendix E: Comparison of LHB properties using `AtomDB` version 3.0.3

All the spectral fitting results reported in Sect. 2.5 are done using the latest `AtomDB` version 3.0.9. However, to ensure a direct comparison of LHB temperature and EM with the most recent and relevant measurement of the LHB by Liu et al. (2017), we repeat the spectral fitting using `AtomDB` version 3.0.3. While the `AtomDB` version adopted by Liu et al. (2017) is not specified in their work, version 3.0.3 appears to be a reasonable choice as it would be the latest version six months before its publication, taking into account the reviewing process.

We find marginally significant differences towards Cha II & III in the foreground components; otherwise, the background components are unaffected. Best-fit parameters of Oph and CrA are not affected by the change of `AtomDB` version (see Table 2.7). The increase of $kT_{\rm LHB}$ of Cha II & III from $0.084^{+0.004}_{-0.004}$ keV (v3.0.9) to $0.089^{+0.003}_{-0.005}$ keV (v3.0.3) would slightly impact the significance of the LHB temperature difference between the clouds we mentioned in Sect. 2.5. Using an older version of `AtomDB` appears to bring $kT_{\rm LHB}$ measured in Cha II & III closer to the other two clouds (Fig. 2.15) and the measurement of Liu et al. (2017) averaged across the whole sky. Nonetheless,

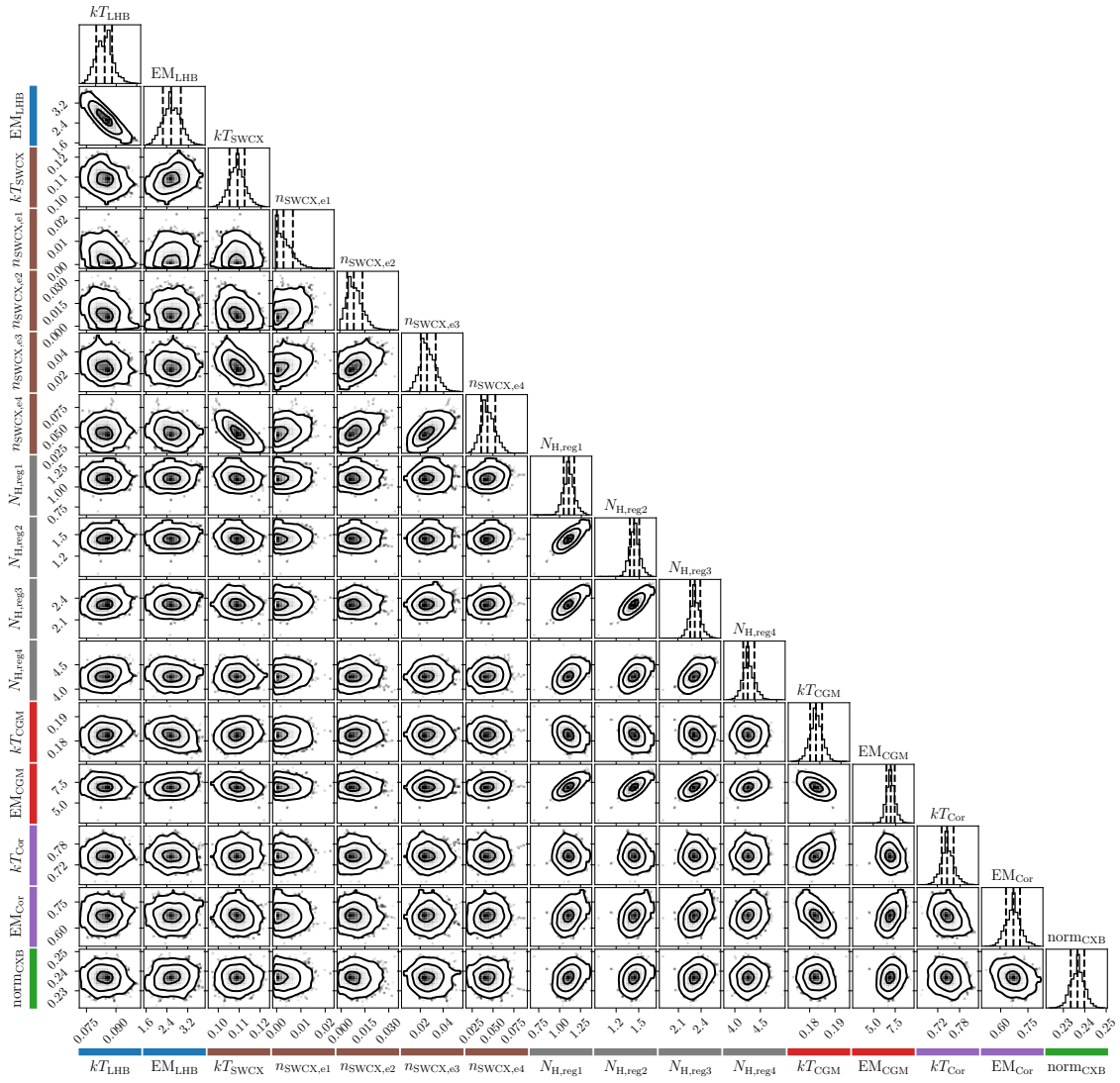

Figure 2.14: Two-dimensional projections of the posterior distributions of all the model parameters of Cha II & III. The contours represent 1, 2 and 3 σ confidence levels. The parameters are colour-coded using the same colours as in the spectra shown in Fig. 2.5, 2.6 and 2.7. The units are the same as in Table 2.2.

Table 2.7: Fit parameters of the spectral fitting using AtomDB version 3.0.3.

Cloud	Cha II & III	Oph	CrA
$kT_{\rm LHB}{}^{(a)}$	$0.089^{+0.003}_{-0.005}$	$0.100^{+0.007}_{-0.007}$	$0.109^{+0.010}_{-0.010}$
$\rm EM_{LHB}{}^{(b)}$	$2.304^{+0.291}_{-0.216}$	$2.138^{+0.324}_{-0.279}$	$1.740^{+0.343}_{-0.266}$
$kT_{\rm SWCX}{}^{(a)}$	$0.108^{+0.003}_{-0.004}$	$0.109^{+0.002}_{-0.002}$	$0.105^{+0.004}_{-0.003}$
$n_{\rm SWCX,e1}{}^{(c)}$	$0.225^{+0.274}_{-0.187}$	$1.684^{+0.516}_{-0.566}$	$4.026^{+1.200}_{-1.157}$
$n_{\rm SWCX,e2}{}^{(c)}$	$0.446^{+0.325}_{-0.273}$	$4.927^{+0.642}_{-0.629}$	$4.306^{+1.239}_{-1.116}$
$n_{\rm SWCX,e3}{}^{(c)}$	$1.566^{+0.437}_{-0.348}$	$7.277^{+0.782}_{-0.750}$	$5.623^{+1.239}_{-1.253}$
$n_{\rm SWCX,e4}{}^{(c)}$	$2.671^{+0.602}_{-0.477}$	$8.857^{+0.807}_{-0.805}$	$5.681^{+1.277}_{-1.305}$
$N_{\rm H,reg1}{}^{(d)}$	$1.154^{+0.069}_{-0.056}$	$2.410^{+0.196}_{-0.191}$	$0.644^{+0.042}_{-0.038}$
$N_{\rm H,reg2}{}^{(d)}$	$1.486^{+0.070}_{-0.064}$	$3.442^{+0.210}_{-0.204}$	$1.930^{+0.059}_{-0.044}$
$N_{\rm H,reg3}{}^{(d)}$	$2.376^{+0.079}_{-0.069}$	$5.327^{+0.256}_{-0.215}$	$1.623^{+0.057}_{-0.050}$
$N_{\rm H,reg4}{}^{(d)}$	$4.348^{+0.122}_{-0.116}$	$6.377^{+0.417}_{-0.442}$	$3.670^{+0.086}_{-0.081}$
$kT_{\rm CGM}{}^{(a)}$	$0.183^{+0.002}_{-0.002}$	$0.272^{+0.010}_{-0.011}$	$0.205^{+0.004}_{-0.003}$
$\rm EM_{CGM}{}^{(e)}$	$7.260^{+0.538}_{-0.487}$	$4.435^{+0.812}_{-0.656}$	$13.674^{+0.719}_{-0.732}$
$kT_{\rm Cor}{}^{(a)}$	$0.756^{+0.019}_{-0.020}$	$0.711^{+0.015}_{-0.014}$	$0.586^{+0.008}_{-0.008}$
$\rm EM_{Cor}{}^{(b)}$	$0.661^{+0.045}_{-0.040}$	$2.371^{+0.177}_{-0.157}$	$3.383^{+0.131}_{-0.134}$
$\rm norm_{CXB}{}^{(f)}$	$0.236^{+0.003}_{-0.003}$	$0.285^{+0.007}_{-0.006}$	$0.224^{+0.006}_{-0.006}$

Notes. The values reported are the 50 percentiles, with the lower and upper bounds showing the 16 and 84 percentiles of the Markov Chain Monte Carlo analysis result.
(*a*) $kT_{\rm LHB}$, $kT_{\rm SWCX}$, $kT_{\rm CGM}$ and $kT_{\rm Cor}$ are in units of keV.
(*b*) $\rm EM_{LHB}$ and $\rm EM_{Cor}$ are in units of $10^{-3}\,\rm cm^{-6}\,pc$.
(*c*) $n_{\rm SWCX}$ is in the unit of $10^{-2}\,\rm deg^{-2}$. The normalisation parameter of the ACX2 model is dimensionless and is only intended for relative scaling (see the documentation of the ACX model). We normalised this factor by the sky area to give the unit $\rm deg^{-2}$.
(*d*) $N_{\rm H}$ values are in units of $10^{21}\,\rm cm^{-2}$.
(*e*) $\rm EM_{CGM}$ is in $10^{-2}\,\rm cm^{-6}\,pc$.
(*f*) $\rm norm_{CXB}$ has unit of $10^{-2}\,\rm photons\,keV^{-1}\,cm^{-2}\,s^{-1}\,deg^{-2}$ at 1 keV.

the best-fit $kT_{\rm LHB}$ and $\rm EM_{LHB}$ values of both versions are consistent with the measurement of Liu et al. (2017).

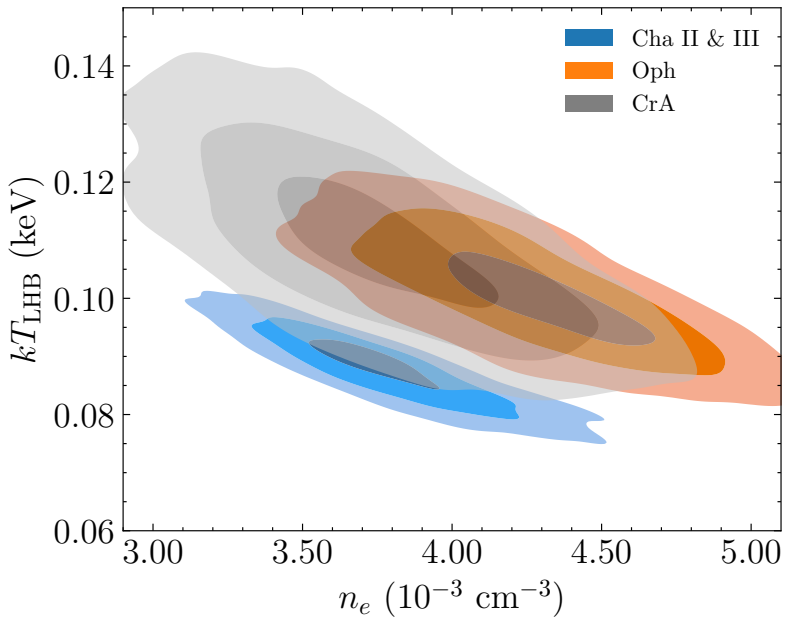

Figure 2.15: Posterior distributions of the temperature and electron density of the LHB using `AtomDB` version 3.0.3. The contours indicate the 1, 2 and 3 σ confidence levels (enclose $\sim$ 39, 86 and 99% of the probability from the highest density).

Chapter 3

Local hot bubble

This chapter on the local hot bubble is based on the published article, titled 'The SRG/eROSITA diffuse soft X-ray background I. The local hot bubble in the western Galactic hemisphere' in Astronomy & Astrophysics, Volume 690, A399 (Yeung et al., 2024). This article is reproduced with permission from the publisher, EDP Sciences.

3.1 Abstract

Context. SRG/eROSITA All-Sky Surveys (eRASSs), combining the advantage of complete sky coverage and energy resolution provided by charge-couple-device, provide the most holistic and detailed view of the diffuse soft X-ray background (SXRB) to date. The first eRASS (eRASS1) was completed at solar minimum when solar wind charge exchange emission was minimal, providing the clearest view of the SXRB.
Aim. We aim to extract spatial and spectral information from each constituent of the SXRB in the western Galactic hemisphere, focussing on the local hot bubble (LHB).
Methods. We extracted and analysed eRASS1 spectra from almost all directions in the western Galactic hemisphere by dividing the sky into equal signal-to-noise bins. We fitted all bins with fixed spectral templates of known background constituents.
Results. We found the temperature of the LHB to exhibit a North-South dichotomy at high latitudes ($|b| > 30°$), with the South being hotter with a mean temperature at $kT = 121.8 \pm 0.6$ eV and the North at $kT = 100.8 \pm 0.5$ keV. At low latitudes, the LHB temperature increases towards the Galactic plane, especially towards the inner Galaxy. The LHB emission measure ($\mathrm{EM_{LHB}}$) enhances approximately towards the Galactic poles. The $\mathrm{EM_{LHB}}$ map shows clear anti-correlation with the local dust column density. In particular, we found tunnels of dust cavities filled with hot plasma, potentially forming a wider network of hot interstellar medium. We also constructed a 3-dimensional LHB model from $\mathrm{EM_{LHB}}$, assuming constant density. The average thermal pressure of the LHB is $P_{\mathrm{thermal}}/k = 10100^{+1200}_{-1500}\,\mathrm{cm^{-3}\,K}$, a lower value than typical supernova remnants and wind-blown bubbles. This could be an indication of the LHB being open towards high Galactic latitudes.

3.2 Introduction

The diffuse soft X-ray background (SXRB) is known to be a superposition of emission components spanning from the length scale of AU to cosmic distances (e.g. McCammon & Sanders, 1990; Kuntz & Snowden, 2000). All-sky analyses of the SXRB have largely relied on ROSAT/PSPC broadband count rates and ratios (e.g. Snowden et al., 1997, 1998; Kuntz & Snowden, 2000), especially for studies on the local hot bubble (LHB) (e.g. Snowden et al., 2000; Liu et al., 2017) as background photons with energies $\lesssim 0.3$ keV (R1: 0.11–0.284 keV; R2: 0.14–0.284 keV) are readily absorbed by the wall of the local bubble and all R12 counts are effectively of local origin. The brightest soft

X-ray line feature in the SXRB is the O VII triplet at 0.57 keV. This is an important diagnostic, which encapsulates emissions from the LHB, as well as the background Galactic emission, including the Milky Way circum-galactic medium (MW CGM), and, depending on sight lines, intervening Galactic structures. Hence, extracting information for a particular component using broadband count rates and ratios alone becomes challenging and heavily dependent on the knowledge and the accurate subtraction of the rest. The discovery of the time-variable solar wind charge exchange (SWCX) component aggravated the issue even further (Lisse et al., 1996; Cravens, 1997; Dennerl et al., 1997).

X-ray observatories with charge-couple-device (CCD) cameras such as *XMM-Newton*/EPIC, *Chandra*/ACIS and *Suzaku*/XIS demonstrated the importance of spectral resolution to decompose the SXRB into their respective components (e.g. Lumb et al., 2002; Markevitch et al., 2003; Henley & Shelton, 2008; Yoshino et al., 2009), but restricted to limited 'pencil-beam' sight lines due to their relatively small field-of-view (FoV) and observing strategies. It was only since the last decade that a substantial number of pointings were accumulated to enable a more holistic view of the SXRB (Henley & Shelton, 2010, 2012, 2013; Nakashima et al., 2018; Gupta et al., 2023; Pan et al., 2024). A notable exception is Halosat, where a large portion of the sky is covered in 333 pointings by virtue of its large FoV ($\sim 10^\circ$), whilst achieving CCD-type energy resolution using non-imaging silicon drift detectors (Kaaret et al., 2019, 2020; Ringuette et al., 2021; Bluem et al., 2022).

High spectral resolution observation of the SXRB remains extremely difficult without telescopes of large grasp currently. However, successive sounding rocket launches of the X-ray Quantum Calorimeter (XQC) (McCammon et al., 2002; Crowder et al., 2012; Wulf et al., 2019) have shown promise of separating the SWCX contribution from the LHB emission beyond CCD energy resolution using C VI Ly-α, γ and the fine structure lines within the O VII triplet, despite their short exposure times.

The local interstellar medium is known to be a volume devoid of neutral gas, also known as the local cavity (LC) or the local bubble (LB) (e.g. see a review by Frisch et al., 2011). This cavity is instead filled by a ~ 0.1 keV ($\sim 10^6$ K) plasma (e.g. Snowden et al., 1990b, 1997; McCammon et al., 2002; Liu et al., 2017; Yeung et al., 2023). The electron density of this plasma is uncertain without the assumption of its line-of-sight density profile. However, shadowing studies of molecular clouds on the wall of the LC at different distances have consistently shown that a uniform electron density of $\sim 4 \times 10^{-3}\,\mathrm{cm}^{-3}$ is a reasonable assumption as probed by various sight lines (Snowden et al., 2014; Yeung et al., 2023). There is a growing number of studies supporting a formation scenario of dozens of supernova explosions creating and sustaining the LHB (e.g. Fuchs et al., 2006; Zucker et al., 2022; Schulreich et al., 2023), employing a combination of star clusters trace-back, numerical simulations and matching supernova-produced radioisotopes found in Earth's crust.

SWCX has long been the biggest source of uncertainty revolving around the X-ray measurements of the LHB, as its spectrum resembles that of the LHB despite being non-thermal in nature (see reviews by Dennerl, 2010; Kuntz, 2019, and references therein). SWCX can be broadly separated into two categories: magnetospheric and heliospheric. The former refers to the emission from solar wind ions interacting with neutrals in Earth's exosphere and the latter with the inflowing neutral interstellar medium (ISM) into the solar system. Observations conducted by most X-ray missions are prone to both kinds. An exception is eROSITA (Predehl et al., 2021) on board of the Spectrum-Roentgen-Gamma (SRG) (Sunyaev et al., 2021) observatory. It orbits around the Sun-Earth Lagrangian point L2. It was always pointed perpendicular to the Sun-Earth line during all-sky surveys (eRASSs). Hence, it never looked through the Earth's exosphere, avoiding the magnetospheric SWCX. No evidence of SWCX emission from the magnetotail has been found thus far (Yeung et al. 2023, Dennerl et al. in prep). Heliospheric SWCX indeed caused variations in the SXRB in eRASSs, and correlates with the solar cycle and ecliptic latitudes (Ponti et al., 2023b; Yeung et al., 2023). Studies using other soft X-ray instruments find the same correlation between solar cycles and heliospheric SWCX (Qu et al., 2022; Ueda et al., 2022; Pan et al., 2024). The first eRASS (eRASS1) was completed during solar minimum and is demonstrated to exhibit, on average, a low amount of heliospheric SWCX (Ponti et al., 2023b; Yeung et al., 2023). A parallel work (Dennerl et al. in prep) will rigorously present and discuss the SWCX contributions in eRASSs. In this work, we leverage this advantage and model the SXRB in eRASS1 without

the SWCX contribution, which became non-negligible in later eRASSs.

The hot phase of the CGM in a spiral galaxy is believed to trace gas from both feedback processes and shock-heated inter-galactic medium out to its virial radius (e.g. see Putman et al., 2012, for a review). The hot halo gas is also predicted to be at approximately the virial temperature (for the MW, $\sim 0.2\,\mathrm{keV}$) and holds a large fraction of its baryons. Numerous X-ray observations have confirmed the existence of this phase via both emission (e.g. Yoshino et al., 2009; Henley & Shelton, 2010, 2012, 2013; Miller & Bregman, 2015; Nakashima et al., 2018; Kaaret et al., 2020; Ponti et al., 2023b) and absorption studies (e.g. Bregman & Lloyd-Davies, 2007; Yao & Wang, 2007; Yao et al., 2008; Sakai et al., 2012; Miller & Bregman, 2013; Fang & Jiang, 2014; Fang et al., 2015). Recently, there have been growing reports of the presence of an additional thermal component in the CGM, at $\sim 0.7\,\mathrm{keV}$ (e.g. Das et al., 2019; Bluem et al., 2022; Ponti et al., 2023b), which could alternatively be attributed to coronal emission from M-dwarfs (Wulf et al., 2019). One of our spectral analysis's prime goals is the characterisation of the two CGM components. This warrants presenting the results and discussions in a separate Paper II (Ponti et al. in prep) of the series.

Our understanding of the cosmic X-ray background (CXB) at the low-energy end (0.5–2 keV) has taken a giant leap with *Chandra* and *XMM-Newton* surveys, resolving $\sim 80\%$ of the CXB sources (De Luca & Molendi, 2004; Luo et al., 2017; Cappelluti et al., 2017). The resolved sources are mostly identified as active galactic nuclei (AGNs). Still, contributions from galaxies, galaxy groups and clusters are expected to rise below 1 keV, steepening the slope at the softest end (Gilli et al., 2007). eROSITA is an instrument specialised in the soft X-ray band; as a result, we expect to be able to measure such a steepening and subsequently apply the result to refine our measurements on the Galactic components.

In this work, we report on the spectral analysis of the eRASS1 data in the western Galactic hemisphere, being as spatially continuous as possible, by extracting a large number (~ 2000 bins) of high signal-to-noise (S/N) spectra. This work is the first of a series focussing on the various components of the SXRB seen by eROSITA. In particular, this paper lays out the data extraction and the general methodology adopted in the spectral modelling in Sect. 3.3 and 3.4, which is the backbone for the series. Then, in Sect. 3.5, we report on the results mainly on, but not limited to, the LHB and the hot local interstellar medium, with intervening discussions and interpretations. The results on the CGM, the Galactic corona and the eROSITA bubbles will mainly be presented in other works in the series (Ponti et al. in prep; Yeung et al. in prep) and, hence, would only be mentioned in this work when they directly affect results on the LHB.

3.3 Data selection and spectral extraction

We study the diffuse soft X-ray background from the eRASS1 data of processing version `c020` of the western Galactic hemisphere ($180^\circ < l < 360^\circ$). We cleaned the data following a few criteria. First, we discarded the data from TM5 and TM7 due to optical light-leak (Predehl et al., 2021), and removed good-time-intervals (GTIs) with count rates $> 1.435\,\mathrm{counts\,s^{-1}\,deg^{-2}}$ in the 4–9 keV band to minimise contaminations by flares. The particle background dominates this band, and the threshold corresponds to 1.5 times the level of particle background in this band (Yeung et al., 2023). The eROSITA-DE consortium has also released a list of temperature-sensitive or bright pixels that occasionally produce artefacts but are not officially flagged as bad pixels. They are mostly from TM4, which suffered from a major micrometeoroid hit (Freyberg et al., 2022). We rejected these sensitive pixels in addition. Last but not least, we masked regions with overdense source detection (Merloni et al., 2024) and positions of known galaxy clusters with $R_{500} \gtrsim 3'$ as described in Bulbul et al. (2024, and references therein). The overdense source detection regions could be regions within or near extended sources, such as supernova remnants or artefacts caused by bright point sources, which triggered a high density of spurious source detections.

Subsequently, we defined our spatial binning of spectral extraction using the software `contbin` (Sanders, 2006), with the primary aim of dividing the western Galactic hemisphere into bins of approximately constant S/N in the diffuse soft X-ray emission, instead of imposing a regular grid

system such as the *skytile* system adopted by the standard products of eROSITA. For our analysis, `contbin` also has the advantage of defining bins with edges more closely following distinct features (for example, from superbubbles, supernova remnants etc.) and being computationally efficient compared to traditional Voronoi binning codes. The binning was done on the eRASS1 0.2–0.6 keV diffuse emission count map (all detected sources masked[1]) after subtracting the expected counts from the non-X-ray background measured from the filter-wheel-closed data (Yeung et al., 2023), as this band contains the bulk of the emissions from the LHB that eROSITA observes. This can be written explicitly as

$$S(\vec{r}) = C(\vec{r}) - B_{\rm nonvig}(\vec{r}) \tag{3.1}$$
$$= C(\vec{r}) - E_{\rm nonvig}(\vec{r}) \times R_{\rm FWC}(\vec{r}) \ , \tag{3.2}$$

where $\vec{r}$, S, C and $B_{\rm nonvig}$ denote the sky position, signal, total counts from diffuse emission, and non-X-ray or non-vignetted background counts, respectively. $B_{\rm nonvig}$ can be further written as a product of non-vignetted exposure time ($E_{\rm nonvig}$) and the count rate of the filter-wheel-closed background ($R_{\rm FWC}$). We estimate the corresponding noise map $N(\vec{r})$ for the S/N calculation using equation (4) of Sanders (2006) as adopted from Gehrels (1986), that is,

$$N(\vec{r}) = \sqrt{g[C(\vec{r})] + g[B_{\rm nonvig}(\vec{r})]} \ , \tag{3.3}$$

where

$$g(c) = \left(1 + \sqrt{c + \frac{3}{4}}\right)^2 \tag{3.4}$$

is an estimation of the upper limit of the squared uncertainty on c counts in Poissonian statistics. Before binning, the maps were projected into the zenithal equal area (ZEA) projection. Contour-binning yielded 2010 bins larger than 1 deg^2, which we consider valid bins for spectral analysis. 1 deg^2 is approximately the eROSITA field-of-view. This selection primarily removed areas near the south ecliptic pole and the Large Magellanic Cloud, where the exposure time is maximal due to the overlapping of the scanning loci in eRASSs, but are not representative of the general SXRB.

Figure 3.1 shows the contour-binned eRASS1 0.2–0.6 keV band surface brightness map of the valid bins. Large soft X-ray emitting structures such as the eROSITA bubbles (a pair of bubbles at $l \gtrsim 290^\circ$ in the north and $l \gtrsim 320^\circ$ in the south), Antlia supernova remnant $(l, b) \sim (275^\circ, 15^\circ)$, Monogem Ring $(l, b) \sim (200^\circ, 8^\circ)$ and Orion-Eridanus Superbubble $(l, b) \sim (205^\circ, -30^\circ)$, and the Galactic disc stand out in stark relief. The sky area distribution of the valid contour bins is shown in Fig. 3.2. The median bin size is ~ 7 deg^2. All bins with an area less than 1 deg^2 were removed. The distribution can be well approximated by a log-normal function, as shown by the red line.

Possible fluctuations contributed by bright X-ray sources should be removed from the analysis of diffuse emission. However, as is discussed in more detail in Sect. 3.4.2, removing sources alters the shape and normalisation of the cosmic X-ray background (CXB). Masking sources above a flux limit threshold substantially higher than the eRASS1 flux limit ($F_{\rm lim,0.5-2\,keV} \sim 10^{-14}$ erg s^{-1} cm^{-2}; Merloni et al., 2024) could avoid the problem of having an exposure-dependent CXB component in the spectra. In other words, if one were to mask all detected sources, the CXB resolve fraction would depend on the exposure depth, causing spatially correlated CXB normalisation and photon index variations. As such, we chose to mask only sources with fluxes $F_{0.5-2\,\rm keV} > 10^{-12}$ erg s^{-1} cm^{-2} and detection likelihood of `DET_LIKE_0` > 10 in the eRASS1 source catalogue (Merloni et al., 2024), using circular masks of radius four times their aperture photometry extraction radii ($4 \times$ `APE_RADIUS_1` $\simeq 2'$)[2] during spectral extraction. This choice minimises

[1] More precisely, the masking of 'all' detected sources is done by merging the `CheeseMask` images from the standard eSASS pipeline from all the skytiles and project them into a `HEALPix` map of Nside = 4096 (pixel size $\simeq 51''$) using nearest-neighbour interpolation. Contribution from the masked pixels is then removed from the final diffuse emission count map after downsampling the `HEALPix` map from Nside = 4096 to Nside = 256.

[2] The masking radius of four times `APE_RADIUS_1` is $\simeq 2'$ for most sources since `APE_RADIUS_1` relates directly to the encircled energy fraction (0.75) set during the source detection pipeline, which corresponds to $\simeq 0'.5$ for the point-spread-function of eROSITA.

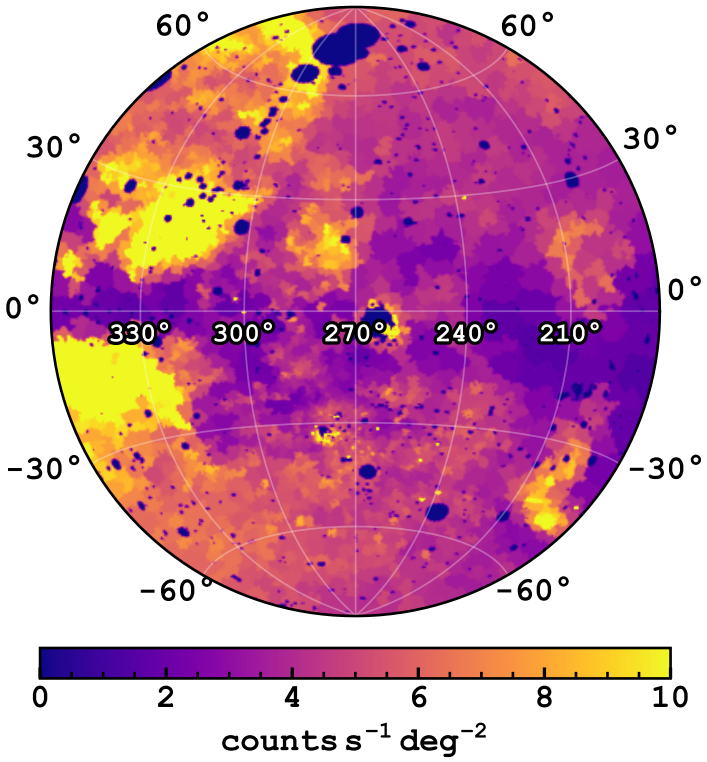

Figure 3.1: Contour-binned eRASS1 0.2–0.6 keV band surface brightness map in zenithal equal-area projection. Locations of big galaxy clusters, overdense regions in source detection, and bins with sky area less than 1 deg^2 were masked. Counts from the non-X-ray background and all eRASS1-catalogued sources (Merloni et al., 2024) were also removed from this image (but not in the spectra; see Sect. 3.3 for more details).

the spectral fluctuations introduced by bright sources while maintaining a largely uniform CXB component in all spectra. This masking was applied during spectral extraction and differs from the one used to create the diffuse emission map for contour-binning.

We extracted the spectrum and its auxiliary response file for events of all valid patterns (`pat=15`) of each contour bin by providing a point source cheesemask and a contour bin mask that demarcates the bin profile to the `eSASS` task `srctool`. They serve as the basis of all analyses in this work.

Last but not least, we also utilised publicly available ROSAT R1 and R2 diffuse background maps in our spectral fitting (Snowden et al., 1997). Despite ROSAT/PSPC's poor spectral resolution, it provides a larger grasp than eROSITA at energies $\lesssim 0.3$ keV (see Fig. 10 of Predehl et al., 2021). We found the addition of ROSAT data helps break the degeneracies between the LHB and the CGM components that arose in some low absorption regions (see Sect. 3.5.3).

The R1 and R2 band count rate and sigma maps were used to provide two more data points in each spectrum, with some manipulations. In detail, we began by binning the maps using the same set of contour bins, then we converted the map unit of count Ms^{-1} arcmin^{-2} to a flux unit of erg s^{-1} cm^{-2} by assuming a 0.1 keV `apec` spectral model and multiplication with the bin area. The use of a `apec` model (Smith et al., 2001) is motivated by the approximation that the contribution from the LHB dominates R1 and R2 counts. As the last step, we used the `ftflx2xsp` task in `FTOOLS` to create `Xspec`/`PyXspec`-ready spectra and diagonal response matrices to enable simultaneous fitting with the eROSITA spectra. The bin edges of the R1 and R2 maps were taken from (Snowden et al., 1994) where the band response drops to 10% of the peak values, namely,

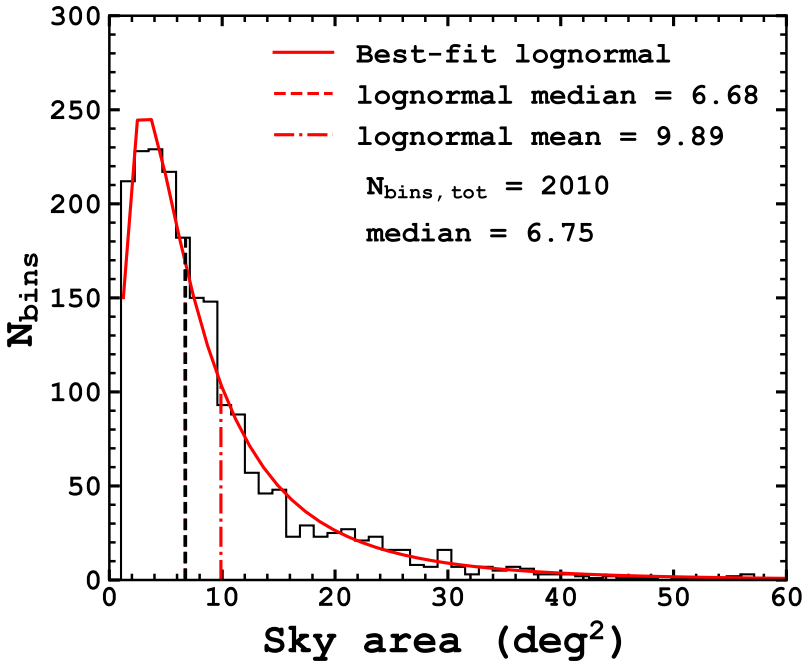

Figure 3.2: Sky area distribution of the contour bins. It can be approximated by a log-normal distribution, as shown with the red line.

0.11–0.284 keV for R1 and 0.14–0.284 keV for R2.

3.4 Spectral analysis

Attempting to decompose the diffuse emission from half the sky both spatially and spectrally is an ambitious task. As the first study to do so, we decided to employ a more conventional approach in the analysis, whereby treating the contour bins as independent during spectral fitting. Additionally, we adopted a fixed number of spectral components to fit the spectra from all contour bins. These components include four conventional X-ray background components (e.g. Gupta et al., 2021; Bluem et al., 2022; Ponti et al., 2023b; Yeung et al., 2023): (1) the local hot bubble (LHB), (2) the Milky Way's halo or (warm-hot) CGM, (3) the Galactic corona or the hot component of the CGM (COR) and (4) the cosmic X-ray background (CXB), and the non-X-ray background modelled by (5) the eROSITA filter-wheel-closed (FWC) background models (Yeung et al., 2023). The SWCX emission during eRASS1 was weak, as it was the time of solar minimum, as shown by Dennerl et al. (in prep.) in a detailed eRASS1–eRASS4 half-sky analysis, Ponti et al. (2023b) in the eFEDS field, and Yeung et al. (2023) in three giant molecular cloud sight lines. Therefore, we did not include an SWCX component in our spectral fits. In addition, we included an extra thermal component for contour bins overlapping with the eROSITA bubbles (eRObub) (Sect. 3.4.4).

3.4.1 Description of model components

Figure 3.3 shows two example spectra to illustrate our spectral templates, one outside the eROSITA bubbles and one inside. The discussion in the remainder of this Section deals with the detailed description of these model components.

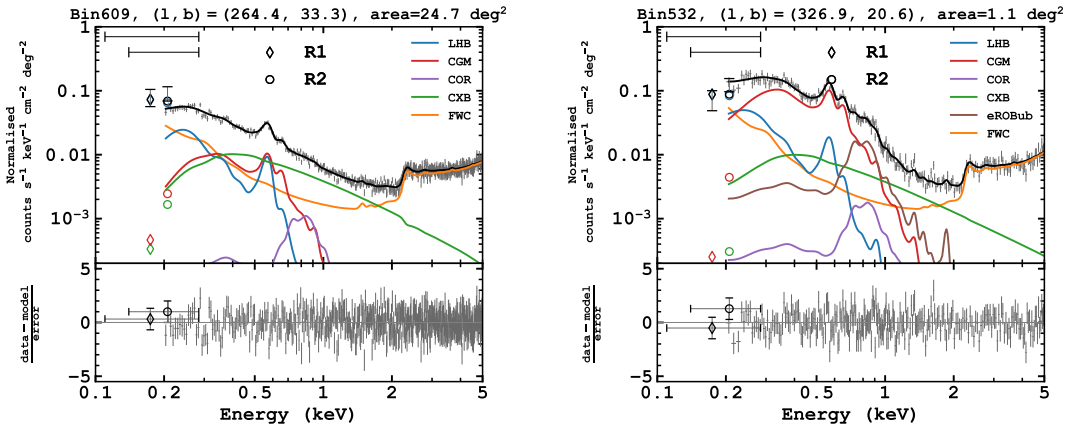

Figure 3.3: Example spectra outside (*left*) and inside (*right*) of the eROSITA bubbles, overlaid with the best-fit spectral models labelled in the legends. We modelled the eROSITA bubbles with an additional thermal component in brown. Both spectra have been divided by the effective area, aiming to bring the ROSAT R1 and R2 count rates into a reasonable range. This has the disadvantage of creating the fictitious jump of the instrumental background component above the gold absorption edge at $\sim 2\,\mathrm{keV}$. The horizontal error bars at the top left corners of the figures reflect the width of the ROSAT R1 and R2 bands.

Local hot bubble

The LHB is a foreground component and was thus modelled as an unabsorbed optically thin plasma in collisional ionisation equilibrium (CIE) using the `apec` model (Smith et al., 2001) using `AtomDB` version 3.0.9 (Foster et al., 2012). Its temperature is allowed to vary freely only below 0.15 keV, for contour bins that have $\log_{10}(N_\mathrm{H}/\mathrm{cm}^{-2}) < 20.5$, estimated from a combination of HI4PI and *Planck* dust radiance map (see Sect. 3.4.1). The introduction of this bound was to prevent the LHB component from 'switching' with the CGM component in low column density (N_H) regions. We refer the reader to Sect. 3.5.3 for a detailed discussion. While this effect was mitigated by introducing the ROSAT R1 and R2 bands into the spectral fitting, this degeneracy remained in some low N_H regions and necessitated the use of a hardbound. Its emission measure (EM) was left to vary in all locations. The abundance of the LHB is assumed to be solar.

In Sect. 3.9, we loosen our CIE prescription of LHB to see if there is evidence of non-equilibrium ionisation (NEI) in our data. In short, we did not find a clear indication of NEI despite it being the general expectation from simulations of the ISM (e.g. de Avillez & Breitschwerdt, 2012; Breitschwerdt & de Avillez, 2021). We attribute this to the insufficient spectral resolution to resolve the emission lines and their ratios, which are crucial diagnostics of NEI.

Absorption of background components

For the X-ray background components (CGM, COR, CXB and eRObub), we adopted the simplifying assumption that they are absorbed by the same N_H layer within each bin. In addition, their absorption was modelled by the `disnht` model (Locatelli et al., 2022), which behaves identically to `tbabs` (Wilms et al., 2000) but with a lognormal distribution with mean $\log N_\mathrm{H}$ and width $\sigma_{\log N_\mathrm{H}}$. We believe this treatment is more realistic than a single N_H as some of our bins cover a large sky area and a range of N_H within the field. While $\log N_\mathrm{H}$ is left to vary during the spectral fits, we fixed the value of $\sigma_{\log N_\mathrm{H}}$ in each contour bin according to the following estimation.

We estimated N_H independently from our X-ray spectral measurement assuming $N_\mathrm{H} = N_\mathrm{HI} + 2N_{\mathrm{H}_2}$. We adopted the N_HI information from 21 cm line measurement by HI4PI Collaboration

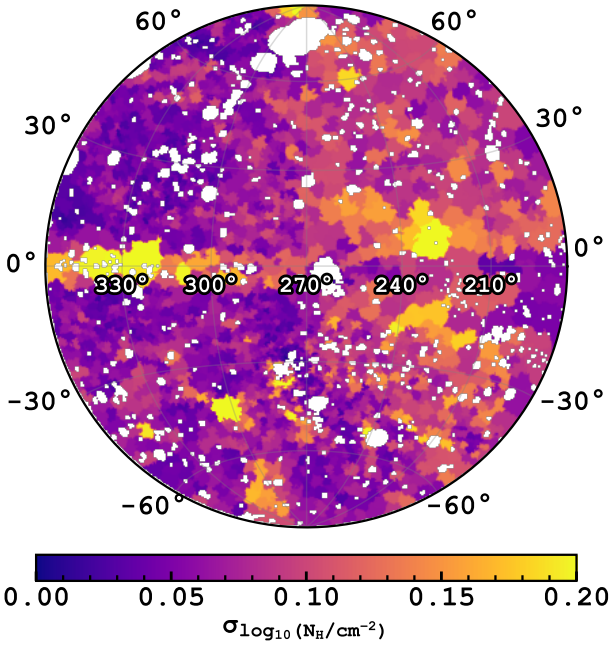

Figure 3.4: Values of $\sigma_{\log N_\mathrm{H}}$ used in our spectral fitting, considering only the spatial spread. They were computed using a combination of N_HI information from HI4PI and N_{H_2} information inferred from *Planck*. (See Sect. 3.4.1.)

et al. (2016), while N_{H_2} was estimated using the conversion given in Willingale et al. (2013):

$$N_{\mathrm{H}_2} = 7.2 \times 10^{20} \left[1 - \exp\left(-\frac{N_\mathrm{HI} E(B-V)}{3 \times 10^{20}\,\mathrm{cm}^{-2}} \right) \right]^{1.1} , \tag{3.5}$$

where $E(B-V)$ was taken from the conversion from the *Planck* dust radiance (R) map using $E(B-V)/R = 5.4 \times 10^5$ given in Planck Collaboration et al. (2014). We refer to this N_H estimation simply by HI4PI N_H hereafter for brevity. We then estimated $\sigma_{\log N_\mathrm{H}}$ as the standard deviation of HI4PI N_H within the area of each contour bin. In other words, our estimated value of $\sigma_{\log N_\mathrm{H}}$ accounts only for the spatial variation in the column density and can be treated as a lower limit to the 'genuine' variation, which should include the line-of-sight component.

We have indeed attempted to let $\sigma_{\log N_\mathrm{H}}$ freely vary in the fits. However, this choice brought about two unforeseen issues:
1) We found the fitted $\log N_\mathrm{H}$ to be higher than total HI4PI N_H by $\gtrsim 0.3$ dex, usually at high $\sigma_{\log N_\mathrm{H}}$ areas ($\gtrsim 0.6$ dex) near $(l,b) \sim (300^\circ, -20^\circ)$, and consequently, boosted the CXB above a level allowed by cosmic variance.
2) A significant number of contour bins resulted in a vanishing LHB component, which we considered unphysical, especially since their occurrences appear random.
On the other hand, these issues were not present when $\sigma_{\log N_\mathrm{H}}$ was fixed using the aforementioned method. Therefore, we kept $\sigma_{\log N_\mathrm{H}}$ fixed throughout our spectral analysis.

Fig. 3.4 shows the values of $\sigma_{\log N_\mathrm{H}}$ in all contour bins. A clear decreasing trend can be seen as a function of Galactic longitude. This is primarily caused by the larger contour bins away from the Galactic centre, capturing larger spatial spread in N_H. The scatter plot in Fig. 3.5 demonstrates this correlation. Of course, the areas of the contour bins are dictated by the S/N in the soft band, affected by both exposure time and soft band intensity in the sky, which happens to be lower between $250^\circ \lesssim l \lesssim 180^\circ$.

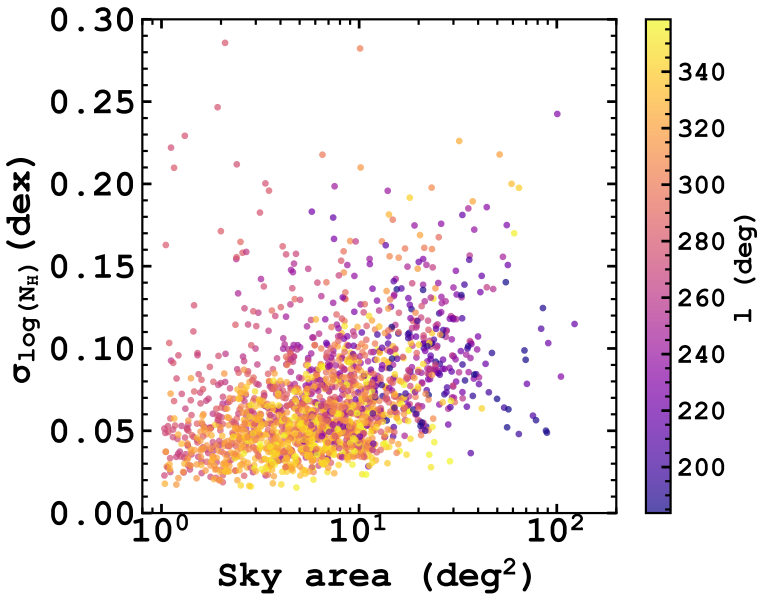

Figure 3.5: Scatter plot of $\sigma_{\log N_{\rm H}}$ against solid angle of contour bins. A positive correlation between $\sigma_{\log N_{\rm H}}$ and the contour bin area can be seen, as larger bins tend to capture a larger spread in $N_{\rm H}$. The points are coloured according to their Galactic longitudes.

Milky Way's circum-galactic medium

The CGM component was modelled using an `apec` model with the abundance fixed at $0.1\,Z_\odot$. The low abundance was found to be required by the eFEDS data (Ponti et al., 2023b) and is shown to be stable against the choice of the emission models of optically thin plasma in CIE (for example, `Raymond-Smith, Mekal`) in Paper II (Ponti et al., in prep). The main impact of assuming a different abundance is reflected primarily in the emission measure. The behaviour is fairly linear; for instance, the conventional choice of $Z = 0.3\,Z_\odot$ would lower the emission measure by about three times compared to $Z = 0.1\,Z_\odot$.

Several recent publications have found a Galactic corona or a hotter CGM component necessary to reproduce the spectra of the SXRB (e.g. Gupta et al., 2021; Bluem et al., 2022; Ponti et al., 2023b). We refer the reader to Paper II for an in-depth discussion. In this paper, it suffices to note that this component was necessary for reproducing the spectra. We modelled the Galactic corona component using an `apec` model with solar abundance. Our choice of S/N = 80 at the 0.2–0.6 keV band did not usually provide sufficient constraints on the Galactic corona component in the spectral fitting. Hence, throughout this paper, we kept its temperature fixed at $kT_{\rm COR} = 0.7$ keV.

Instrumental background

For the instrumental background, the spectrum for each TM was modelled by its own FWC model to account for any TM-specific features. The normalisation of the FWC model in the sky spectrum is related to that of the FWC spectrum by the ratio of their `BACKSCAL` header keywords and was fixed accordingly in the spectral fit. However, we noticed the Al-Kα fluorescence line at 1.49 keV in the CXB regions (see Fig. 3.6 and Sect. 3.4.2) is always weaker than that in the FWC data for all TMs, by ∼20%–60% depending on the TM. The precise cause of this phenomenon is unknown. Still, it is suspected to be linked to the extra Aluminium put above the CCD when the filter wheel was rotated to the `CLOSED` position compared to the `FILTER` position. However, this explanation cannot explain the relatively large spread in the deficit between the TMs. To compensate for the

Al-Kα line deficit in the sky spectra, we singled out this line and refitted its normalisation of all TMs as the first step of all our spectral fits. It was then frozen in the subsequent optimisation of the rest of the free parameters.

Summary of model parameters

We elaborate on the description of the CXB in Sect. 3.4.2. In summary, two parametrisations (single ($\Gamma = 1.7$) and broken power-law ($\Gamma_1 = 1.9$, $\Gamma_2 = 1.6$, $E_b = 1.2\,\mathrm{keV}$)) of the CXB component could reproduce the data equally well at high Galactic latitudes. Therefore, both were used in the spectral fits, and the differences between the two were considered to be systematic uncertainties.

There are a total of 7 or 9 free parameters in the spectral fits: kT_{LHB}, $\mathrm{EM}_{\mathrm{LHB}}$, kT_{CGM}, $\mathrm{EM}_{\mathrm{CGM}}$, $\mathrm{EM}_{\mathrm{COR}}$, $\mathrm{norm}_{\mathrm{CXB}}$ and $\log N_{\mathrm{H}}$ for contour bins outside the eROSITA bubbles; and an addition of kT_{eRObub} and $\mathrm{EM}_{\mathrm{eRObub}}$ for bins inside the eROSITA bubbles.

3.4.2 Treatment of the cosmic X-ray background

In our spectral analysis, detected sources with $F_{0.5-2\,\mathrm{keV}} > 10^{-12}\,\mathrm{erg\,s^{-1}\,cm^{-2}}$ as well as known clusters from X-ray cluster catalogues with $R_{500} \gtrsim 3'$ were masked (Liu et al., 2022; Merloni et al., 2024; Bulbul et al., 2024, and references therein). The choice of the flux threshold is more than an order of magnitude higher than the eRASS1 flux limit. With this limit, we can assume eROSITA is complete in detecting sources above this threshold in all look directions, and the corresponding resolved fraction across the western Galactic hemisphere is uniform. Masking of sources is expected to change the photon index of the cosmic X-ray background (CXB) from the canonical value of $\Gamma \sim 1.4$–1.5 (Vecchi et al., 1999; Kushino et al., 2002; Hickox & Markevitch, 2006; Cappelluti et al., 2017); however, the high flux threshold guarantees this change is not spatially dependent.

Figure 3.6 shows the regions we chose to determine the CXB model. These regions correspond to the spatial bins with centres located above $|b| > 30^\circ$, and are free of large-scale foreground structures upon binning the western Galactic hemisphere using `contbin` (Sanders, 2006) with a target S/N of 400. In addition to the CXB model we focus on, we fitted the spectrum of each region independently with freely varying LHB, CGM, Galactic corona and absorption column densities similar to the description in Sect. 3.4.1, with the omission of SWCX since the contribution of SWCX in eRASS1 is low (Dennerl et al., in prep).

From the spectral analysis of the regions shown in Fig. 3.6, we found that simple power-law and broken power-law models perform equally well in reproducing the data, but a double broken power-law was unnecessary. Therefore, both simple and broken power-laws were adopted as our CXB models. We delay the details of this CXB analysis to Sect. 3.5.8.

3.4.3 Fitting procedures

Spectral fitting was done in `PyXspec` version 2.1.0 (Arnaud, 1996; Gordon & Arnaud, 2021). Lodders (2003) was used as the reference for abundance, and absorption cross-sections from Verner et al. (1996) were assumed.

We repeated the following fitting procedure for all the 2010 contour bins. After determining the normalisation of the Al-Kα line (Sect. 3.4.1), we made a simultaneous fit of 5 eROSITA spectra (5 TMs) and 2 ROSAT band fluxes (R1 and R2) for each contour bin. The eROSITA spectra were fitted in the energy range 0.2–5 keV using Poissonian statistics (`cstat`) (Cash, 1979), and as the R1 and R2 data points were fluxes, χ^2-statistics was used. We minimised the total statistics using the Levenberg-Marquardt algorithm. Then, we ran a MCMC with 64 walkers, each with 1.6 ksteps, giving a total of 102.4 ksteps, using the Goodman-Weare method (Goodman & Weare, 2010). The walkers were initially distributed in a Gaussian distribution around the best fit from the minimisation. We found discarding the initial 80 ksteps, albeit aggressive, was a conservative and uniform way to ensure all parameters had moved past the burn-in phase and reached convergence in the vast majority of bins. In this paper, we report the median, 16^{th} and 84^{th} percentiles of the

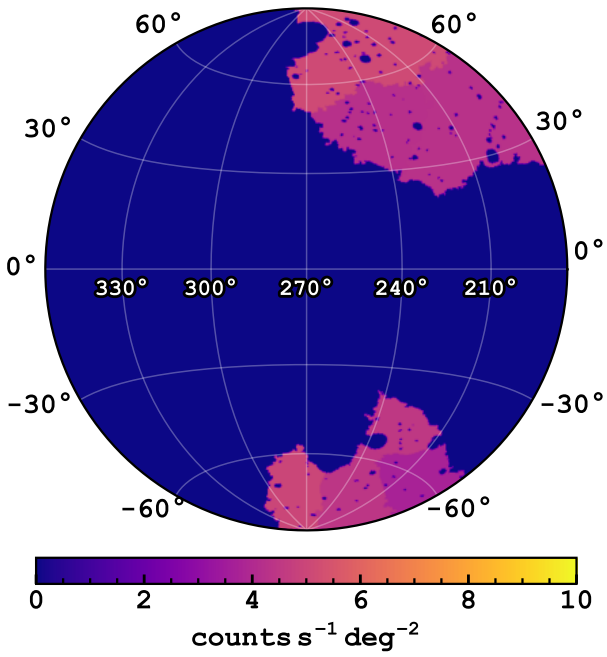

Figure 3.6: Similar to Fig. 3.1 but showing only regions selected to determine the spectral shape of the CXB.

posterior distribution as the most probable value, the lower and the upper errors, respectively. If the posterior distribution is Gaussian, these reduce to the mean and $\pm 1\,\sigma$ errors.

3.4.4 Treatment of the eROSITA bubbles

The enigmatic eROSITA bubbles (Predehl et al., 2020) emit thermally in the soft X-rays at ~ 0.3 keV, and we modelled it using the `apec` model at solar abundance[3]. Combining with the LHB and CGM, the multi-component spectral analysis in eRASS exposure depth and spectral resolution inescapably entails model degeneracies because of their similar spectral shapes (0.1, 0.2 and 0.3 keV plasma in CIE). As such, we implemented a two-step approach in fitting spectra within the eROSITA bubbles region, where some spectral parameters outside the eROSITA bubbles were passed in the form of Gaussian priors into spectral fits within the eROSITA bubbles.

We began by defining the demarcation of the eROSITA bubbles using the 0.6–1.0 keV intensity map, where the eROSITA bubbles are the most prominent. The turquoise line in Fig. 3.7 shows the demarcation. We fitted the spectra of the contour bins outside the eROSITA bubbles before those inside, following the procedure described in Sect. 3.4.3. Subsequently, we fitted the contour bins within the eROSITA bubbles by passing Galactic latitude-dependent priors based on the fit results. More precisely, for a given contour bin within the eROSITA bubbles centred at (l,b), we created a Gaussian prior for each relevant parameter based on fitting results of all the bins outside the eROSITA bubbles centred within the range of $b \pm 5°$. This implementation reflects our recurring observation with the eROSITA data that most spectral parameters are either constant (for example, the CXB) or exhibit primarily Galactic latitudinal dependence (for example, $kT_{\rm LHB}$, see Fig. 3.8). These priors were only applied to $kT_{\rm LHB}$, $kT_{\rm CGM}$, $\rm EM_{CGM}$, $\rm EM_{COR}$, $\rm norm_{CXB}$. We did not impose Galactic latitude-dependent priors on $\rm EM_{LHB}$, $kT_{\rm eROsub}$, $\rm EM_{eROsub}$ because in

[3]We assumed solar abundance for simplicity, following Lallement et al. (2016). Indeed, there are reports of sub-solar abundances both from observations (e.g. Miller et al., 2008; Kataoka et al., 2013; Gu et al., 2016a) and as expectations from simulations (e.g. Mou et al., 2023). We defer the abundance measurement in eROSITA to an ongoing work (Yeung et al., in prep).

this paper, we primarily focus on inferring the 3-dimensional (3D) structure of the LHB. The eROSITA bubbles will be the focus of a forthcoming paper in the series (Yeung et al., in prep; Chapter 4).

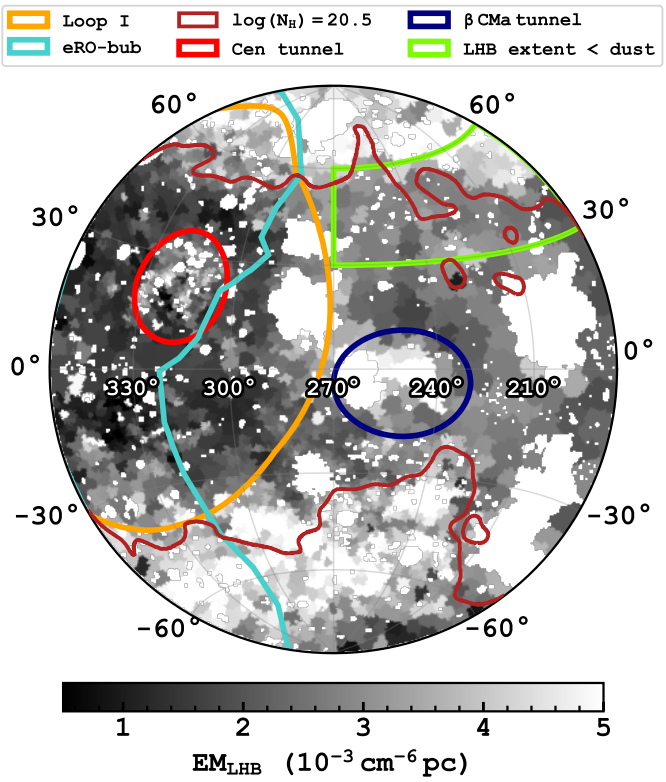

Figure 3.7: Finding chart for features discussed mainly in Sect. 3.4.4 and 3.5.2. The background image shows the emission measure of the LHB, which is a proxy of the extent of the LHB and is relevant for discussions (Sect. 3.5.2) on interstellar tunnels and anti-correlation with dust. The demarcation of the eROSITA bubbles is shown by the turquoise line, based on the 0.6–1.0 keV intensity map.

3.4.5 Limitations of the current method

At the end of this section, we would like to emphasise that the data obtained by eROSITA is rich, especially for diffuse emission. A weakness of our method is that the inference of spectral parameters was independent of locations. However, some parameters, such as the LHB temperature, are likely correlated for bins in proximity based on the intuitive consideration that the local ISM would preferentially be in similar conditions the closer they are in space. There exist some potential methods that could take this into account. For instance, one idea is to use Bayesian hierarchical modelling and treat the proximity of bins as a hyperprior. Another potentially interesting method is to utilise an algorithm called the generalised morphological components analysis (GMCA) or its variants (sGMCA, pGMCA) to decompose the spectral components with the help of each component's intrinsically unique spatial distribution, which has recently been demonstrated to disentangle spectral components remarkably well in extended X-ray sources (Bobin et al., 2015; Picquenot et al., 2019, 2021, 2023; Carloni Gertosio et al., 2023).

3.5 Results and discussion

The sheer number of spectra we analysed prevents us from discussing them individually. Therefore, we provide a webpage hosted on the eROSITA Data Release 1 server that provides all the relevant information, including visualisations and the fitting results organised in downloadable tables, for readers who are interested in the spectra, their associated model parameters, uncertainties or fit quality of any our contour bins (Sect. 3.7).

3.5.1 Evidence of a variable LHB temperature

Figure 3.8 shows the spatial distribution of $kT_{\rm LHB}$ in the high latitude regions, where the Galactic plane ($|b| < 30^\circ$) and regions overlapping with the Large Magellanic Cloud, known supernova remnants or superbubbles (Antlia, Orion-Eridanus, Monogem Ring, Vela; masked also in other parameter maps) and the recently discovered structure surrounding the LMC, dubbed the 'Goat Horn Complex' (Locatelli et al., 2024a), were ignored. In addition, regions with $1\,\sigma$ LHB temperature or emission measure fitting uncertainty $\sigma_{kT_{\rm LHB}} < 5 \times 10^{-3}$ keV or $\sigma_{\rm EM_{LHB}} < 5 \times 10^{-5}\,{\rm cm}^{-6}$ pc were removed. These criteria are possible indications of sub-optimal spectral fits; the former is to avoid regions with $kT_{\rm LHB}$ pegged at edges of the uniform prior, and the latter is useful for removing regions with $\rm EM_{LHB}$ pegged close to zero. A total of 788 valid bins remained following the screening (36 bins were screened out).

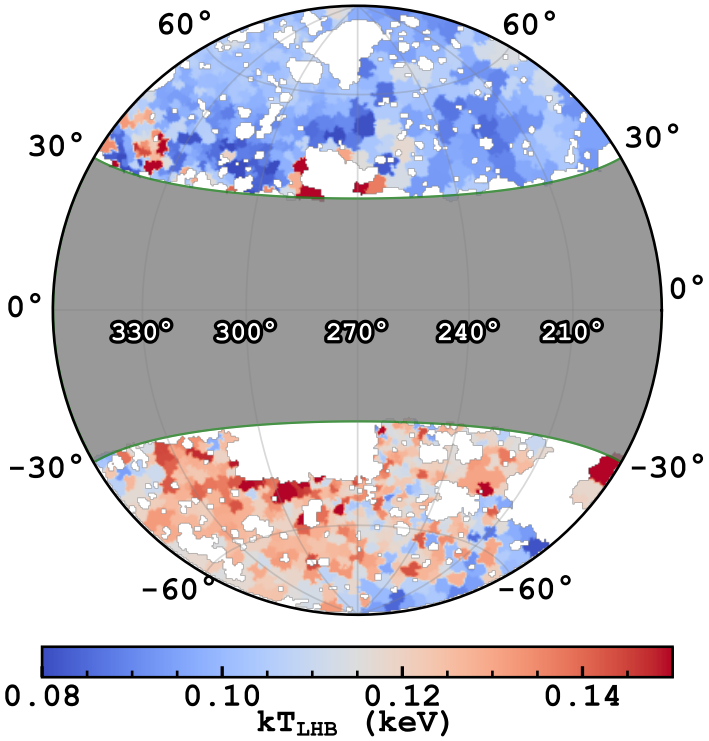

Figure 3.8: Spatial distribution of $kT_{\rm LHB}$ in the high latitude regions ($|b| > 30^\circ$).

The histogram of $kT_{\rm LHB}$ of all the valid bins is shown in the black line in Fig. 3.9. We report a median (and the 0.16 and 0.84 quantiles) $kT_{\rm LHB}$ of $0.111^{+0.018}_{-0.015}$ keV. The observation of the mean $1\,\sigma$ fitting uncertainty (0.010 keV), as shown in the black error bar, being significantly smaller than the σ of the distribution (0.018 keV) indicates a variable $kT_{\rm LHB}$. An inspection of Fig. 3.8 shows the primary origin of this variation is a large-scale temperature gradient, with the northern

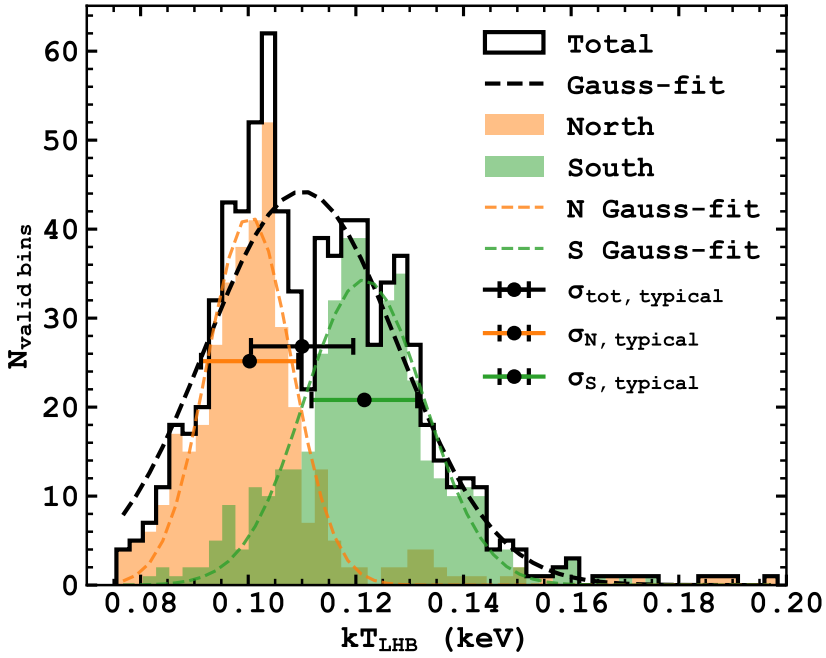

Figure 3.9: Distribution of $kT_{\rm LHB}$ in the high latitude regions ($|b| > 30°$). The unfilled histogram outlined in black displays the distribution of all the high latitude bins displayed in Fig. 3.8. The black dashed line shows the Gaussian best fit for the distribution. The black data point with error bars shows the typical (median) $1\,\sigma$ spectral fitting uncertainty, centred at the mean of the fitted Gaussian. It is plotted at a height of $\exp(-1/2)N_{\rm gauss,peak} = 0.606\,N_{\rm gauss,peak}$ for proper comparison between the spectral fitting uncertainty and the width of the distribution. The former (0.010 keV) is approximately half of the latter (0.018 keV), demonstrating a genuine variation in the LHB temperature. The sample is divided into the northern (orange) and the southern (green) Galactic hemispheres to demonstrate the primary source of variation is a large-scale gradient instead of small-scale fluctuations. The northern hemisphere is cooler (0.100 keV) than the south (0.122 keV), and comparing their distributions with the respective typical spectral fitting uncertainties shows that each hemisphere exhibits approximately constant LHB temperature.

Galactic hemisphere being cooler than the south by ~ 0.02 keV. This is further demonstrated by dividing the histogram in Fig. 3.9 into the north (orange) and south (green). The north-south temperature dichotomy is evident. By overlaying the typical spectral fitting uncertainties within each hemisphere on the figure, one can notice the width of the temperature distributions within both hemispheres could be attributed mainly to their respective spectral fitting uncertainties, especially in the north. Hence, the dominating factor of the spread in the LHB temperature is a large-scale temperature gradient, but not bin-to-bin fluctuations. To complement the systematic change in $kT_{\rm LHB}$ observed from the projected map and histogram, Sect. 3.12 highlights the spectral signature that determines the LHB temperature using high-S/N spectra from each hemisphere.

We tested if the northern and southern temperature distributions could be drawn from the same underlying distribution using the two-sample Kolmogorov-Smirnov test. The test returned a statistic of 0.693 and a p-value in the order of $10^{-102} \ll 0.01$. Thus, we can safely reject the null hypothesis that the temperature dichotomy occurs by chance.

To quantify the intrinsic temperature distributions in each hemisphere, we used a maximum likelihood approach to identify the mean and width of the Gaussian distributions, which

best reproduce the observed temperature measurements, including their statistical errors. We constrained the mean temperature in the northern and southern Galactic hemispheres to be $kT_{\rm N} = 100.8 \pm 0.5\,{\rm eV}$ and $kT_{\rm S} = 121.8 \pm 0.6\,{\rm eV}$, respectively. We also extracted the widths ($1\,\sigma$) of the intrinsic temperature distributions, which are $\sigma_{\rm N} = 2.9^{+1.0}_{-1.3}\,{\rm eV}$ in the north and $\sigma_{\rm S} = 8.5^{+0.7}_{-0.6}\,{\rm eV}$ in the south. This result reiterates the temperature dichotomy is highly significant, as is evident from the precision with which we can determine the mean temperature of each hemisphere. It is also clear that the southern hemisphere exhibits a larger intrinsic temperature scatter than the northern counterpart. We would like to emphasise that the statistical uncertainty of the means and the widths of the intrinsic temperature distributions should not be confused with the fitting uncertainty of each bin. The temperature dichotomy is highly significant because of the large number of bins that sampled each hemispheric distribution well despite the individual bin having a median fitting uncertainty ($\simeq 0.01\,{\rm keV}$; see Fig. 3.9) larger than the intrinsic widths of the distributions.

Having established a temperature dichotomy at high Galactic latitudes, it is natural to ask if a smooth transition across the Galactic plane connects them. We separated the discussion of high latitude regions since we believe our measurement there is relatively secure. Still, it is unclear how close to the Galactic plane one can venture before one is heavily biased by complexities such as multiple line-of-sight emitting and absorbing components. We relax the $|b| > 30^\circ$ limit and plot all the valid bins, including those on the Galactic plane in Fig. 3.10, using the same screening applied to Fig. 3.8. Fig. 3.10 shows a remarkable temperature enhancement towards the Galactic plane, especially at $l \gtrsim 270^\circ$. Inspection of the spectra and their posterior distributions suggests the spectra have significant constraining power on $kT_{\rm LHB}$ down to at least 10° of the Galactic plane, albeit a subjective choice. The column densities in these regions ($\gtrsim 10^{21}\,{\rm cm}^{-2}$; see Fig. 3.16 for $N_{\rm H}$ information) are adequate and peak strongly at the first wall of LB absorption ($\sim 100-200\,{\rm pc}$) (Lallement et al., 2022; Edenhofer et al., 2024), enabling us to differentiate between the unabsorbed LHB and the absorbed components, primarily the CGM. Therefore, we argue that the temperature enhancement towards the inner Galaxy is a real feature of the LHB.

First, we must address why earlier studies did not observe the north-south LHB temperature gradient using ROSAT data (see Sect. 3.5.1 for a deeper literature discussion). The R2/R1 band ratio is the main tracer of LHB temperature using ROSAT data, commonly assumed to be contributed only by the LHB emission. Fig. 3.11 shows the R2/R1 band ratio as a function of plasma temperature at solar abundance, using three common plasma models, `Raymond-Smith` (Raymond & Smith, 1977), `Mekal` (Mewe et al., 1985, 1986; Liedahl et al., 1995) and `apec` (Smith et al., 2001). The `Raymond-Smith` model was commonly used by studies before and around the millennium (e.g. Snowden et al., 1990b, 1997, 1998) to infer the temperature of the LHB. The calibration curve of the `Raymond-Smith` model in Fig. 3.11 shows that the R2/R1 ratio is insensitive to temperatures above 0.13 keV. This could be one of the reasons why the LHB temperature was not found to be $\sim 0.2\,{\rm keV}$ in earlier LHB temperature measurements using ROSAT.

Another possibly more important reason is the flawed assumption that only the LHB emission contributes to the R1 and R2 bands. To demonstrate this, we forward-modelled the same models used to extract Fig. 3.10, using the R1 and R2 band responses. The resulting R2/R1 band ratio map is shown in the left panel of Fig. 3.12. The eROSITA bubbles appear distinctly on the map, indicating that absorbed background structures can shine through and alter the R2/R1 ratio. The north-south LHB temperature dichotomy also disappears. It is fair to suggest the forward-modelled R2/R1 map does not capture the primary morphological features of the $kT_{\rm LHB}$ map, and conversely, $kT_{\rm LHB}$ directly inferred from R2/R1 without contributions from the background components could be biased. Furthermore, regions within the eROSITA bubbles in the forward-modelled map commonly show R2/R1 > 1.4, a limit according to the calibration curves in Fig. 3.11 that should not be crossed for an unabsorbed plasma. This is another evidence of the absorbed components contributing to the R1 and R2 bands, boosting the R2/R1 ratio. The right panel of Fig. 3.12 displays the binned R2/R1 ratio of the original ROSAT maps presented in Snowden et al. (1997), which can be directly compared to our forward-modelled map. Their resemblance reiterates that our $kT_{\rm LHB}$ measurement is not at odds with the ROSAT data, and including background components in the modelling is essential to extract information on the LHB.

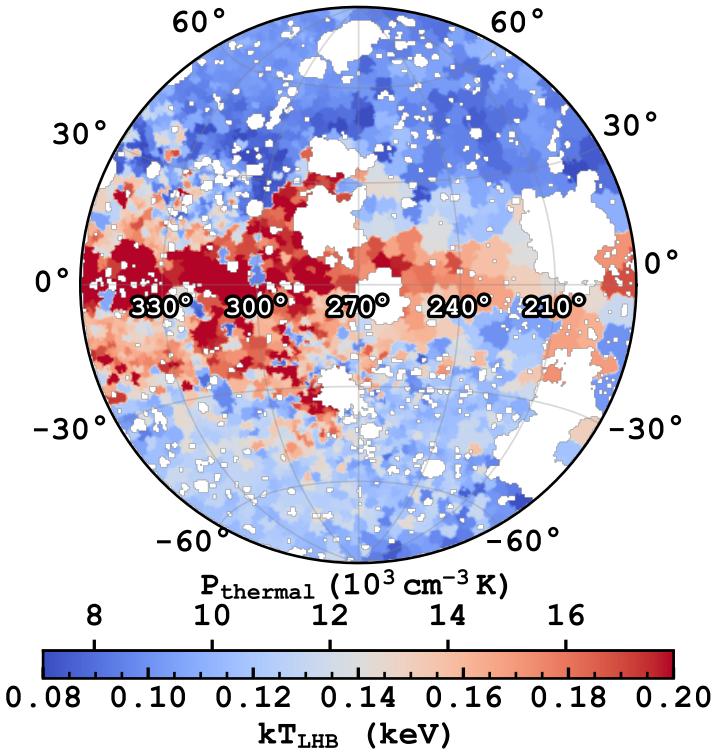

Figure 3.10: Map of $kT_{\rm LHB}$ including low latitude regions. We note that the colour bar is scaled differently from Fig. 3.8. The thermal pressure is also shown under the assumption of constant $n_e = 4 \times 10^{-3}\,{\rm cm}^{-3}$.

Merely showing our measurement is consistent with ROSAT does not necessarily mean it is robust, especially towards the inner Galaxy at low latitudes. We want to show that the LHB emission we measured at low latitudes must be local and not heavily contaminated by background ISM. Fig. 3.13 shows the corresponding $\mathrm{EM}_{\rm LHB}$ map. The details of it are discussed in Sect. 3.5.2, but for the current purpose, it suffices to note that the EM at low latitudes within the Loop I contour in Fig. 3.7 is one of the lowest in this hemisphere. Our LHB component is unlikely to capture extra emission from the background ISM and returns a lower EM. Figure 3.19 demonstrates the column density reaches $10^{20}\,{\rm cm}^{-2}$ at a very close distance ($\sim 100\,{\rm pc}$) and inspection of the local dust radial profiles suggests most of the total $N_{\rm H}$ is located within the first 250 pc, corroborating that very few background ISM photons can contaminate our LHB measurement. Indeed, because of the lower $\mathrm{EM}_{\rm LHB}$, the uncertainties of the $kT_{\rm LHB}$ is larger ($\sigma_{kT_{\rm LHB}} \sim 0.03\,{\rm keV}$), which is a well-known anti-correlation that can also be readily observed from their posterior distributions. These regions, excluding the ones that are exactly lying on the Galactic plane, do not show poorer fit statistics than the rest of the sky (see Sect. 3.5.9 and Fig. 3.30). Even if they do, they are mostly due to larger residuals above $\gtrsim 0.6\,{\rm keV}$, and not at energies where the LHB dominates. Therefore, we conservatively consider our inferred LHB temperature credible at $|b| > 10^\circ$ and characterise it using spherical harmonics in the next Section.

Spherical harmonic analysis

In Figs. 3.8 and 3.10, an apparent gradient or dichotomy in approximately the north-south direction and an enhancement towards the Galactic plane can be observed, respectively. One way to quantify a gradient in the sky is by fitting a combination of spherical harmonics to the data given the

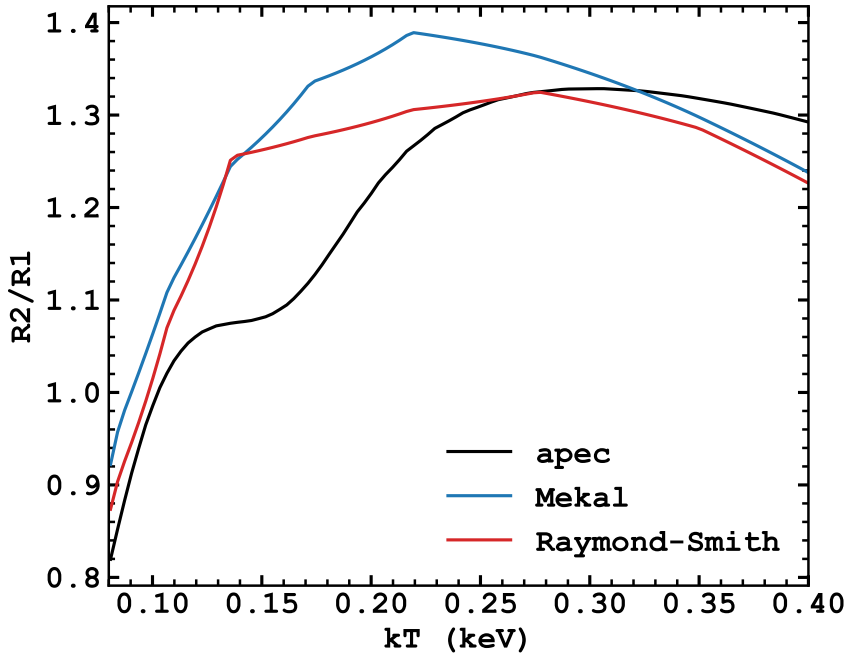

Figure 3.11: Calibration curves of R2/R1 band ratio of the `Raymond-Smith` (Raymond & Smith, 1977), `Mekal` (Mewe et al., 1985, 1986; Liedahl et al., 1995), and `apec` (Smith et al., 2001) models as a function of the temperature of an unabsorbed plasma at solar abundance.

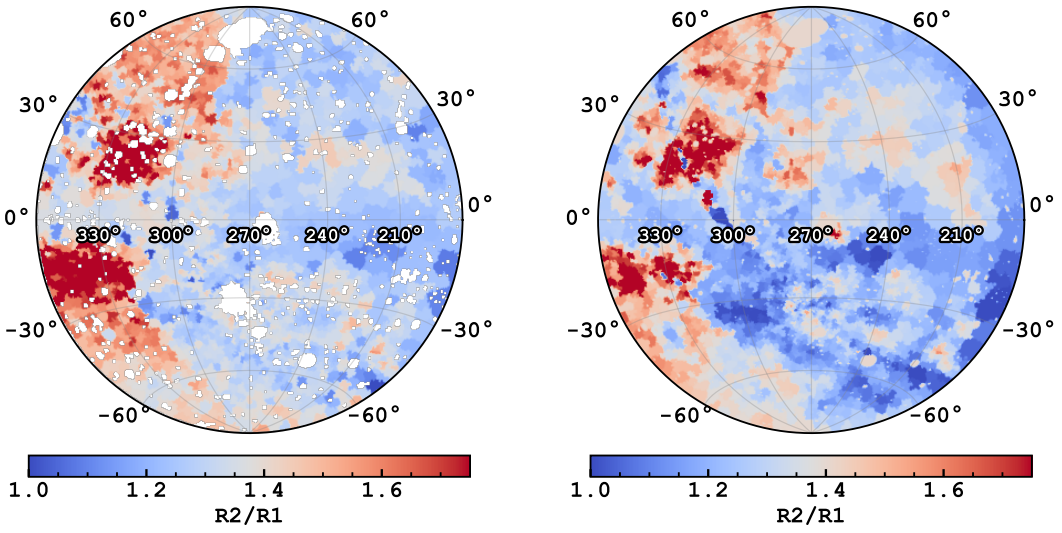

Figure 3.12: Comparison of our forward-modelled R2/R1 band ratio map with the observation. *Left*: R2/R1 band ratio map calculated by folding our best-fit (median) spectral models with the ROSAT R1 and R2 band responses. *Right*: R2/R1 data binned to the same contour-binning scheme (Snowden et al., 1997).

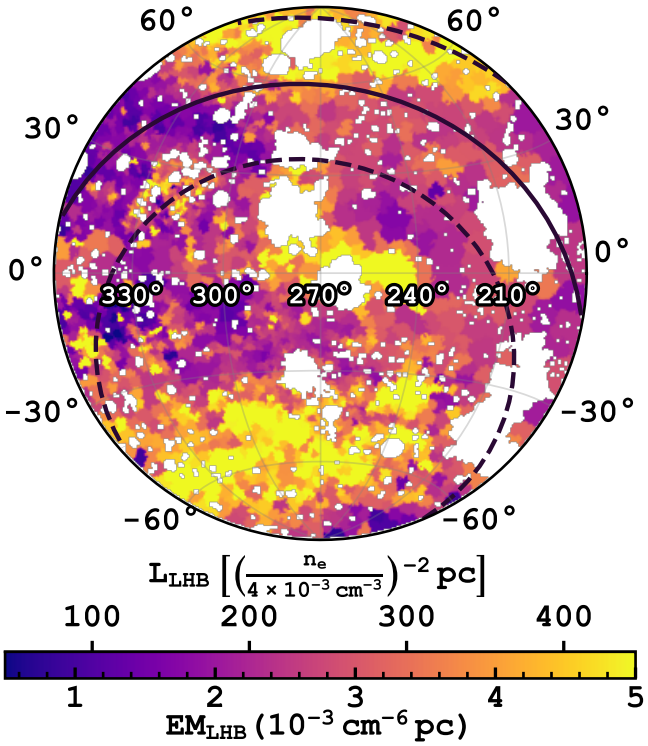

Figure 3.13: Spatial distribution of $\mathrm{EM_{LHB}}$. Regions with $\mathrm{EM_{LHB}}$ uncertainty $< 5\times10^{-5}\,\mathrm{cm^{-6}\,pc}$ were also masked. The solid black line indicates the position of the ecliptic, and the two dashed lines represent a range of $\pm25^\circ$ around it in ecliptic latitude where the solar wind density is expected to be high. The extent of the LHB under the assumption of $n_e = 4\times10^{-3}\,\mathrm{cm^{-3}}$ is also shown.

uncertainties, and the simplest case of a gradient is a dipole. We decided to separate the analysis of the high latitude regions ($|b| > 30^\circ$) from the 'full sample' down to $|b| > 10^\circ$, because we want to tackle two different issues: 1) quantify the significance of the (high latitude) north-south gradient as modelled by a dipole, and 2) produce an empirical multipole model that captures the main kT_{LHB} profile.

The significance of the high latitude north-south gradient can be evaluated by independently fitting a monopole and dipole model to the data. Then, the F-test could determine if the improvement of using a dipole is statistically significant over the null hypothesis of a uniform kT_{LHB} model (monopole).

The expansion of any well-behaved functions (in our case, the LHB temperature) on a sphere can be expanded into spherical harmonics Y_{lm} up to degree $l_{\max}$ by

$$kT_{\mathrm{LHB}}(\theta,\phi) = \sum_{l=0}^{l_{\max}} \sum_{m=-l}^{m=+l} a_{lm} Y_{lm}, \tag{3.6}$$

where a_{lm} is the complex coefficient associated with each Y_{lm}. The question is finding the set of a_{lm} that minimises the χ^2 between the observed data and spherical harmonic model $kT_{\mathrm{LHB}}(\theta,\phi)$, which can be written explicitly as

$$\chi^2 = \sum_i \left[\frac{d(\theta_i,\phi_i) - \sum_{l=0}^{l_{\max}} \sum_{m=-l}^{m=+l} a_{lm} Y_{lm}(\theta_i,\phi_i)}{\sigma(\theta_i,\phi_i)} \right]^2, \tag{3.7}$$

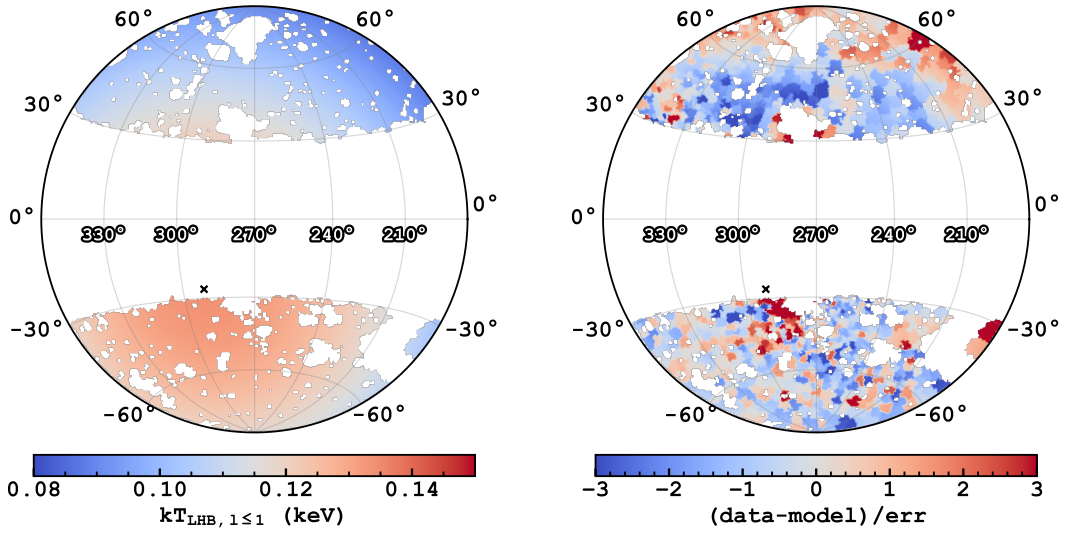

Figure 3.14: Dipole model and residual. *Left*: Dipole model of $kT_{\rm LHB}$. *Right*: Residual normalised by the $1\,\sigma$ fitting uncertainty of each valid bin. The black cross in both panels shows the direction of the dipole towards $(l, b) = (291^\circ, -26^\circ)$.

where $d(\theta_i, \phi_i)$ and $\sigma(\theta_i, \phi_i)$ represent the $i^{\rm th}$ data point and uncertainty associated with it. In our convention, $\phi_i = l_i$ and $\theta_i = 90 - b_i$, where l_i and b_i are the Galactic longitude and latitude. For real-valued functions, the conjugate property of spherical harmonics means that $a_{l(-m)} = (-1)^m a^*_{lm}$, where the $*$ denotes the complex conjugate. It follows that a_{l0} has no imaginary part, and the number of independent parameters required to describe each spherical harmonics of degree l is $2l + 1$ (each complex a_{lm} requires two).

The most probable a_{lm} coefficients and their associated uncertainties are found by running MCMC using the `emcee` package (Foreman-Mackey et al., 2013), with the walkers initialised (with a small spread) at the minimum χ^2 position found by the Levenberg-Marquardt algorithm implemented in `lmfit` (Newville et al., 2016).

We begin with evaluating the significance of the north-south gradient, using the same regions ($|b| > 30^\circ$) shown in Fig. 3.8.

We began by modelling $kT_{\rm LHB}$ as a constant (monopole) in the unmasked regions. We found a median $kT_{\rm LHB}$ of 0.1154 ± 0.0003 keV with $\chi^2/{\rm dof} = 6.36$ (915 dof), a unacceptable fit. Subsequently, we fitted the data with a dipole ($l_{\rm max} \leqslant 1$). The most probable model and the corresponding residual normalised by the bins' fitting uncertainty are shown in Fig. 3.14. The $\chi^2/{\rm dof}$ decreased to 4.01 (912 dof) compared to the monopole. Using the F-test and a significance level of 0.001, we deduced an F-statistic of $179.7 > {\rm F_{crit}} = 5.5$ with a p-value in the order of 10^{-16}. This suggests the dipole model is strongly preferred over the constant model, and the presence of a north-south gradient is statistically significant. However, one could still recognise systematic residuals in the northern hemisphere by inspecting the residual image, reflecting the north-south gradient is not simply a dipole.

Naturally, raising $l_{\rm max}$ can improve the fidelity of our spherical harmonics model to reproduce the data more closely. We included data as close as 10° from the Galactic plane for this empirical model. With multiple trials of different $l_{\rm max}$ values, we arrived at a $l_{\rm max} = 6$ model that captures the main large-scale features in the data reasonably well, presented in Fig. 3.15. It has a $\chi^2/{\rm dof}$ of 3.11 (1560 dof). We emphasise that we do not associate any physical interpretations with the multipoles. It merely serves as an empirical model for the LHB temperature profile. However, we speculate on the origin of the gradient in Sect. 3.5.1. The model parameters can be found in Sect. 3.10. Sect. 3.11 presents the latitudinal profiles of $kT_{\rm LHB}$, where both the uncertainties and

scatters of $kT_{\rm LHB}$ are shown to compare with the spherical harmonics models.

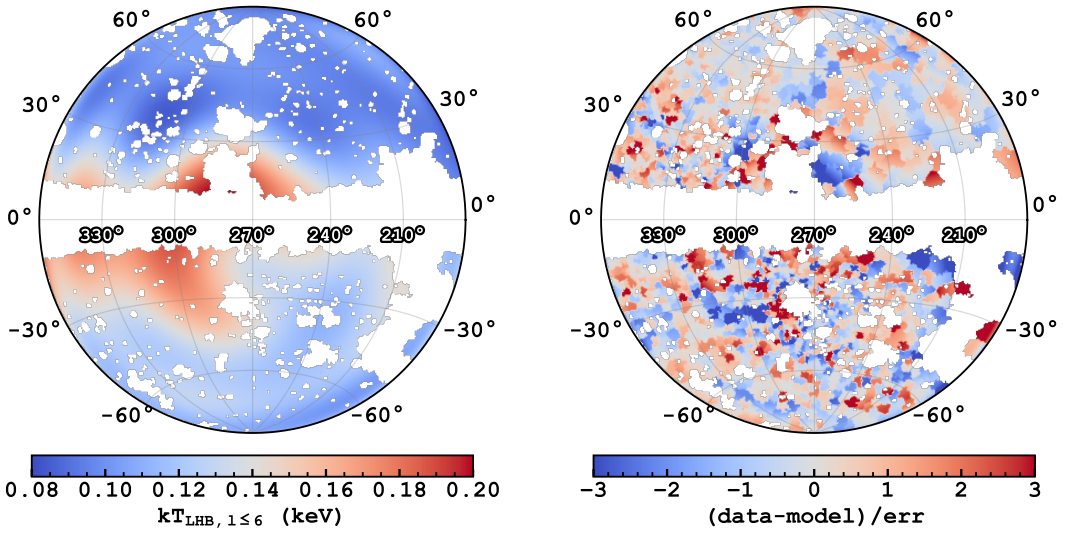

Figure 3.15: Similar to Fig. 3.14 but for the spherical harmonics model of $l_{\rm max} = 6$. The data were fitted down to 10° from the Galactic plane. We note that the colour bar of the left panel was scaled up to 0.2 keV, identical to Fig. 3.10 for comparison.

Comparison with past observations

The most relevant references on the large-scale temperature variations of the LHB are Snowden et al. (1990b), Snowden et al. (2000) and Liu et al. (2017). Snowden et al. (1990b) inferred a temperature gradient of the LHB for the first time using the Wisconsin B/C band intensity ratio. They reported a mean temperature of 0.097 keV ($10^{6.05}$ K), and a dipole gradient pointing towards (l,b) = (348.°7,−11.°2) going from 0.064 keV ($10^{5.87}$ K; near Galactic anti-centre) to 0.127 keV ($10^{6.17}$ K; near Galactic centre). With the advent of ROSAT All-Sky Survey data (RASS), Snowden et al. (2000) compiled a catalogue of X-ray shadows at high Galactic latitudes ($|b| > 20°$). With these X-ray shadows and taking the simplifying assumption similar to us, that all components except the LHB are absorbed by the total Galactic $N_{\rm H}$, they arrived at an LHB temperature dipole in a similar direction, but with the dipole spanning the range of 0.094($10^{6.04}$ K)–0.116 ($10^{6.13}$ K), only $\sim 1/3$ of that of Snowden et al. (1990b). We note that our dipole model has the dipole amplitude in between the two studies ($A_{\rm di} = 0.0133 \pm 0.0004$ keV[4]; Table 3.2). Liu et al. (2017) make use of both the RASS R2/R1 band ratio as well as the estimation of the SWCX contribution from the DXL sounding rocket (Galeazzi et al., 2011) mission to conclude that $kT_{\rm LHB}$ is fairly uniform over the sky at 0.097 ± 0.019 keV (Bluem et al. (2022) recently lower this estimate to 0.084 ± 0.019 keV using `AtomDB` version 3.0.9). Inspection of the $kT_{\rm LHB}$ map (left panel of their Fig. 6) from Liu et al. (2017) shows enhanced temperature in the Galactic south pole, but the enhancement appeared more localised than we observed using eROSITA, possibly caused by the unsubtracted eROSITA bubbles component.

Snowden et al. (1990b, 2000) and our work show markedly different dipole direction of the LHB temperature. While a quantitative comparison of Snowden et al. (1990b, 2000)'s dipole models with our dipole model is problematic because we found the LHB temperature profile not fully following a dipole, a qualitative comparison suggests our observed dipole axis is almost $\sim 60°$ away from Snowden et al. (1990b, 2000)'s. In contrast, despite being similar to Snowden et al. (1990b, 2000) in using band ratio as a proxy of LHB temperature, Liu et al. (2017) reports a

[4]The full temperature range spanned by the dipole model is $2A_{\rm di}$.

temperature map that resembles ours more closely. For Snowden et al. (1990b), Wisconsin B (0.13–0.188 keV) and C (0.16–0.284 keV) bands match the peak emitting energies of a $\sim$ 0.1 keV plasma and are largely (but not completely) unaffected by the hotter emission from the CGM when taking the band ratio as a proxy of LHB temperature. However, it was completed by 10 sounding rocket flights in $\sim$ 8 years, sampling various parts of a solar cycle. We note that the analysis was done before the realisation that the SWCX process could contaminate the SXRB. Thus, how much of the B/C band ratio genuinely traced the LHB emission is unclear. ROSAT R1 (0.11–0.284 keV) and R2 (0.14–0.284 keV) bands have similar energy coverage to the B and C bands and are similarly sensitive to the LHB temperature. Subtraction of the SWCX (comparing Fig. 11a of Snowden et al. (1997) and Fig. 3 of Liu et al. (2017)) and background absorbed emission (see Sect. 3.5.1) can significantly change the profile of the R2/R1 band ratio. The dipole gradient Snowden et al. (2000) found could be plagued by SWCX as RASS was conducted near solar maximum.

Despite only covering the western Galactic hemisphere, it is a positive sign that our LHB temperature profile shows compatible morphology to the Liu et al. (2017)'s map, but with adequate significance to suggest a gradient. However, the spherical harmonic models we presented are a partial view without information from the eastern Galactic hemisphere. The low-order spherical harmonics would almost certainly change significantly should this information become available, as they are most sensitive to features spanning large angular scales by definition. Nevertheless, we suspect the change is unlikely to reconcile our model with Snowden et al. (1990b, 2000)'s dipole as there is only a very weak sign of longitudinal temperature dependence from the eROSITA data.

Temperature anti-correlation with absorption column density

The left panel of Fig. 3.16 shows the distribution of $\log_{10}(N_{\rm H}/{\rm cm}^{-2})$ inferred from our spectral fitting.

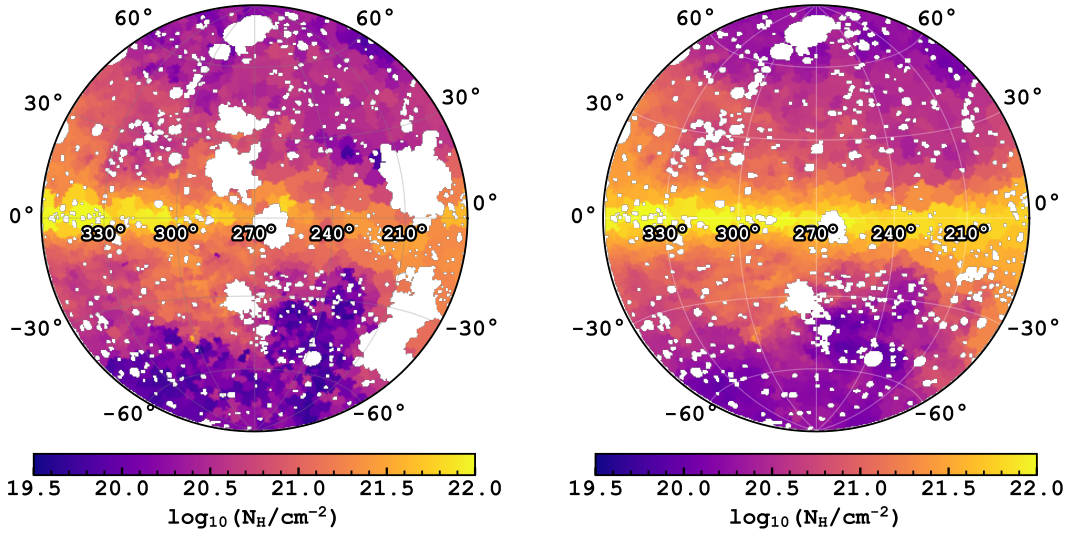

Figure 3.16: Comparison of fitted $N_{\rm H}$ and independent estimate of $N_{\rm H}$ from H I and dust measurements. *Left*: Fitted $N_{\rm H}$. *Right*: Estimate of $N_{\rm H}$ combining neutral hydrogen information from HI4PI (HI4PI Collaboration et al., 2016) and $E(B-V)$ information derived from Planck radiance map (Planck Collaboration et al., 2014).

Neglecting the Galactic plane, where both our and HI4PI $N_{\rm H}$ measurements are not particularly accurate due to modelling simplification and self-absorption, the two $N_{\rm H}$ maps possess almost identical morphology, with the X-ray absorption inferring a lower $N_{\rm H}$ at high Galactic latitudes. By comparing the $kT_{\rm LHB}$ maps in Fig. 3.8 and Fig. 3.10 with the $N_{\rm H}$ maps, one can immediately notice

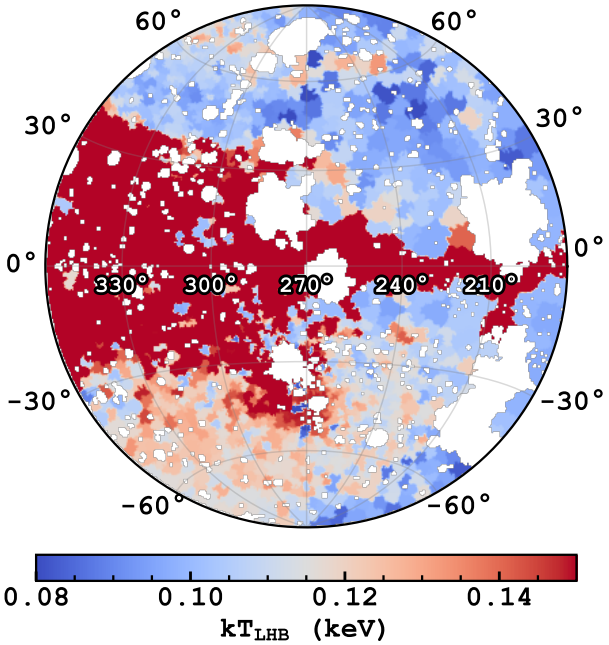

Figure 3.17: Map of $kT_{\rm LHB}$ upon fixing the $N_{\rm H}$ to the HI4PI $N_{\rm H}$. The colour scaling conforms to Fig. 3.8 to highlight the high latitude temperature dichotomy.

the anti-correlation between the $kT_{\rm LHB}$ and $N_{\rm H}$, especially in the southern Galactic hemisphere. The hottest regions of the LHB above $b < -30^\circ$ are where the $N_{\rm H}$ are the lowest. Interestingly, as is described in more detail in Sect. 3.5.2, the hottest regions correspond to the largest $\rm EM_{LHB}$.

Given the morphological similarity of the southern hot patch and the low $N_{\rm H}$ region and the observation that the X-ray absorption column density there is consistently lower than the HI4PI measurement, we suspected the cause of the hot patch was the result of our inaccuracies in fitting the $N_{\rm H}$, biasing $kT_{\rm LHB}$ in the process. Therefore, we reran the spectral modelling of all contour bins and imposed the condition that the $N_{\rm H}$ must be fixed at the HI4PI values.

We show the resulting map on $kT_{\rm LHB}$ in Fig. 3.17. The $kT_{\rm LHB}$ gradient remains, with similar amplitude and direction. The anti-correlation with $N_{\rm H}$ remains clear. Not surprisingly, the quality of the spectral fits became increasingly worse towards the Galactic plane, as the assumption of using total $N_{\rm H}$ alone the line-of-sight becomes questionable. The result of this test indicates the LHB temperature gradient is unlikely to be caused by our $N_{\rm H}$ determination, and in addition, leaving $N_{\rm H}$ free during spectral fitting was appropriate and necessary.

Speculations on the source of temperature gradient

The mechanism that sets up this temperature gradient is unclear. Still, it is not completely unexpected. Schulreich et al. (2023) demonstrate in a sophisticated numerical study that sequential supernova explosions could have created the LHB, with some possibly exploding in the last ~ 1–$2\,$Myr. In their simulation, the LHB temperature is not uniform in the present day; instead, it shows a large-scale gradient that could span approximately an order of magnitude. Therefore, the scenario of recent off-centre supernova explosions can, in principle, explain our measured temperature contrast. However, their simulated temperature gradient direction differs from our measurement. They back-traced the trajectories of the stellar populations, which most likely hosted massive stars that expanded the LB using *Gaia* EDR3 data. Further, they predicted the massive stars' explosion times and positions by considering the initial mass function and stellar isochrones. They used these informed explosion sites and times as input parameters of

their simulation; thus, the simulation's gradient direction is not arbitrary. Judging from their Fig. 4, the simulated temperature gradient is primarily along the Galactic centre-anticentre line, in contrast to our measurement in the north-south direction. Whilst the uncertainty of the stellar traceback does not allow for the explosion sites in the south, shock reflections from the thick LB shell and gas sloshing following any explosions could easily change the direction of the temperature gradient (Pacicco, M. & Schulreich, M., private communication). Pressure gradients in the LHB are washed out following the sound crossing timescale (a few 0.1–1 Myr). Transient shocks within the LHB exist in the simulation of Schulreich et al. (2023). These shocks create hotter and denser plasma layers and can be preferentially picked up in their X-ray emissions as emission measure scales as n^2. The temperature dichotomy we observe could be caused by these shocks in the south. It is likely a matter of fine-tuning the simulations and choosing a correct time stamp to reproduce the current LHB observables so that these shocks appear in the right place and time. Last but not least, the density of the plasma also displays a similar gradient as the temperature in their simulation, which we do not see or have not seen with the current instrumental sensitivity in shadowing experiments (e.g. Yeung et al., 2023) that probed only very few sight lines. Future observations in this direction will be essential to confirm or reject this scenario.

The second possible scenario hinges on more assumptions, including the density of the LHB and magnetic pressure within it do not vary significantly in different directions. Consider a simple static scenario where the LHB is not expanding and is in pressure equilibrium with the surrounding ISM. The temperature gradient, in this case, reflects a pressure gradient set up by the surrounding ISM, where its profile can be traced by the thermal pressure of the LHB, given by

$$\begin{aligned} P_{\rm thermal} &= nkT_{\rm LHB} && (3.8)\\ &= \left(n_e + \sum_A n_A\right) kT_{\rm LHB} && (3.9)\\ &\simeq 1.92 n_e kT_{\rm LHB}, && (3.10) \end{aligned}$$

where n_A is number density of the $A^{\rm th}$ element and $n = 1.92 n_e$ is a common estimation of the total particle density[5] (e.g. Galeazzi et al., 2007; Snowden et al., 2014). The colour bar in the $kT_{\rm LHB}$ map in Fig. 3.10 shows also the resulting thermal pressure, assuming $n_e = 4 \times 10^{-3}\,{\rm cm}^{-3}$ (Yeung et al., 2023). An enhancement of pressure near the Galactic disc can be observed, and the pressure decreases rapidly away from it. It makes intuitive sense that the Galactic disc exerts a larger pressure on the LHB. Indeed, the vertical pressure profile in the Solar neighbourhood is approximately an exponentially decaying function from the midplane, with a scale height of $\sim 500\,{\rm pc}$ (Cox, 2005). The smaller high latitude temperature or pressure gradient could also be explained if the initial surrounding medium was not uniform before the formation of the LHB. This scenario does not necessarily conflict with the off-centre supernova explosions scenario in the simulation of Schulreich et al. (2023) and could both be at work.

3.5.2 Emission measure and extent of the local hot bubble

Fig. 3.13 shows the spatial distribution of the emission measure of the LHB, ${\rm EM_{LHB}}$. In addition to masking known large superbubbles and supernova remnants, we also excluded regions with $\sigma_{\rm EM_{LHB}} < 5 \times 10^{-5}\,{\rm cm}^{-6}\,{\rm pc}$. Regions that make up the latter are usually biased, possibly spectral fits with vanishing LHB components or MCMC chains that did not converge well. Before delving into the correlation or anti-correlation of ${\rm EM_{LHB}}$ with other parameters, it is best to discuss ${\rm EM_{LHB}}$ in the context of the extent of the LHB.

${\rm EM_{LHB}}$ is directly related to the extent of the LHB in a given look direction if one knows the line-of-sight density profile, which is given by the following equation:

$${\rm EM_{LHB}} = \int n_e(l) n_{\rm H}(l) dl. \qquad (3.11)$$

[5]The factor of 1.92 assumes the abundance in Anders & Grevesse (1989). Opting for the abundance of Lodders (2003) (the abundance reference we use for spectral fitting) results in a factor closer to 1.9. The difference is dominated by the difference in Helium abundance: $(n_{\rm He}/n_{\rm H})_{\rm AnGr} = 0.0977$ versus $(n_{\rm He}/n_{\rm H})_{\rm Lodd} = 0.0792$.

By adopting the assumption of a fully ionised solar abundance plasma (see Leahy et al., 2024, for caveats of this assumption), $n_e/n_{\rm H} \simeq 1.2$ and further assuming a constant density profile, we obtained a simple relation between $\mathrm{EM}_{\rm LHB}$ and the extent of the LHB L:

$$\mathrm{EM}_{\rm LHB} = \frac{n_e^2 L}{1.2}. \tag{3.12}$$

One could calibrate n_e under the constant density assumption using sight lines through various molecular clouds on the surface of the LHB. Recent work suggests $n_e \simeq (4 \pm 0.5) \times 10^{-3}\,\mathrm{cm}^{-3}$, moderately independent of the look direction (Yeung et al., 2023), which is the number we adopted in converting $\mathrm{EM}_{\rm LHB}$ to the extent of the LHB. This is smaller than $n_e = (4.68 \pm 0.47) \times 10^{-3}\,\mathrm{cm}^{-3}$ inferred by Snowden et al. (2014), but within the uncertainties. The assumed electron density gives rise to the largest systematic uncertainty in our 3D LHB model. The difference between the two numbers alone entails a 37% difference in estimating the LHB distance.

Figures 3.13 and 3.18 show the structure of the LHB assuming $n_e = 4 \times 10^{-3}\,\mathrm{cm}^{-3}$, in the ZEA projection and a 3D-rendered surface respectively. For the latter, the LHB surface is smoothed and interpolated into the masked regions using radial basis function interpolation (`scipy.interpolate.rbf(*, smooth=0.3)`) implemented in the `Python` package `scipy` (Virtanen et al., 2020).

Despite its irregular shape, the LHB is systematically more extended away from the disk, presumably because the denser medium permeated along the Galactic plane prohibits its expansion. The conventional picture of 1 MK plasma displacing colder ISM phases in the solar neighbourhood first put forward by Sanders et al. (1977) appears to explain our result excellently, especially in the southern Galactic hemisphere. An almost perfect anti-correlation with Galactic $N_{\rm H}$ can be observed in the southern Galactic hemisphere, slightly less so in the northern hemisphere.

For a more comprehensive view of the multiphase ISM in the solar neighbourhood, we also compared our spatial model of the hot phase of the ISM to the local dust maps, inferred primarily from Gaia extinction data by Lallement et al. (2022) and Edenhofer et al. (2024) independently. A sophisticated method was used by Pelgrims et al. (2020) to trace the inner surface of the local bubble (LB) from 3D dust maps, involving identifying inflexion points in the differential extinction radial profiles and an iterative refining process. In our analysis, we took a simpler approach by identifying the LB extent at which the integration of dust maps reaches a column density of $N_{\rm H} = 10^{20}\,\mathrm{cm}^{-2}$, where the optical depth is approximately unity at 0.2 keV. Both the extinction cubes of Lallement et al. (2022) and Edenhofer et al. (2024) were converted from A_V to $N_{\rm H}$ cubes using the conversion $N_{\rm H} = 2.21 \times 10^{21} A_V$ (Güver & Özel, 2009). The extent of the LB inferred from these two cubes is shown in Fig. 3.19.

We could see excellent agreement in a few areas (see the finding chart in Fig. 3.7):
1) in the general direction of the Loop I superbubble or the eROSITA bubbles, both the LHB plasma and dust cubes show distances in the order of 100 pc. The LHB emission appears to be absorption-bounded.
2) The LHB is much more extended in the low $N_{\rm H}$ regions in the southern Galactic hemisphere.
3) Around $240^\circ \lesssim l \lesssim 270^\circ$ on the Galactic plane ($\sim \beta$ Canis Majoris interstellar tunnel (Gry et al., 1985; Welsh, 1991)), one could match the larger extent of the LHB well with the dust maps, both in position and morphology, especially when compared with Edenhofer et al. (2024).
4) In the northern Galactic polar cap ($l \gtrsim 60^\circ$), the LHB is more extended when there is low $N_{\rm H}$.
5) Towards the constellation Centaurus at $(l, b) \simeq (315^\circ, 25^\circ)$, one can see a hint of an extended tunnel, possibly connecting to the Loop I superbubble. This feature can also be seen when integrating the Edenhofer et al. (2024)'s cube in the right panel of Fig. 3.19.
6) On the other hand, we could see in the region of $(180^\circ \lesssim l \lesssim 240^\circ,\ 15^\circ \lesssim b \lesssim 45^\circ)$, little absorbing material is present within 400 pc, yet the LHB does not extend as freely as in regions towards the LoopI/eROSITA bubbles and the Galactic poles. This could be a hint that the hot plasma is not completely volume-filling, or its density is lower in this general direction, or the dust wall of the LB in this direction is very low in density. Indeed, a peak of low-density dust at ~ 150 pc could be present there as found by the recent work by O'Neill et al. (2024). We elaborate on the interstellar tunnels in Sect. 3.5.6.

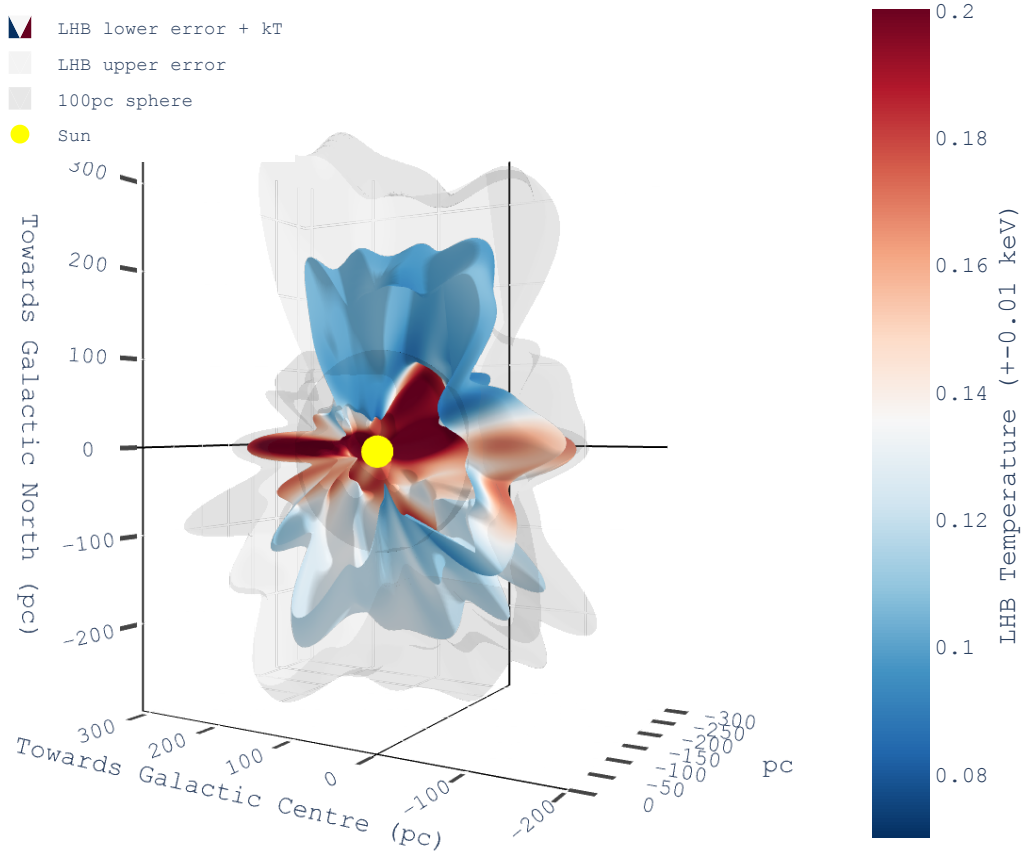

Figure 3.18: Three-dimensional structure of the LHB in the western Galactic hemisphere assuming a constant density of $4 \times 10^{-3}\,\mathrm{cm}^{-3}$. The inner (opaque, coloured) and the outer (grey, translucent) surfaces show the $\pm 1\,\sigma$ uncertainty bounds of the distance under the constant n_e assumption. We note that the two surfaces only reflect the uncertainty in the spectral fitting but not in n_e. We note that kT_{LHB} is also colour-coded on the inner surface. A sphere of 100 pc radius is shown around the Sun (yellow) as a ruler. An interactive version of this figure, including the comparison with dust maps (not shown) can be accessed from the accompanying website (Sect. 3.7).

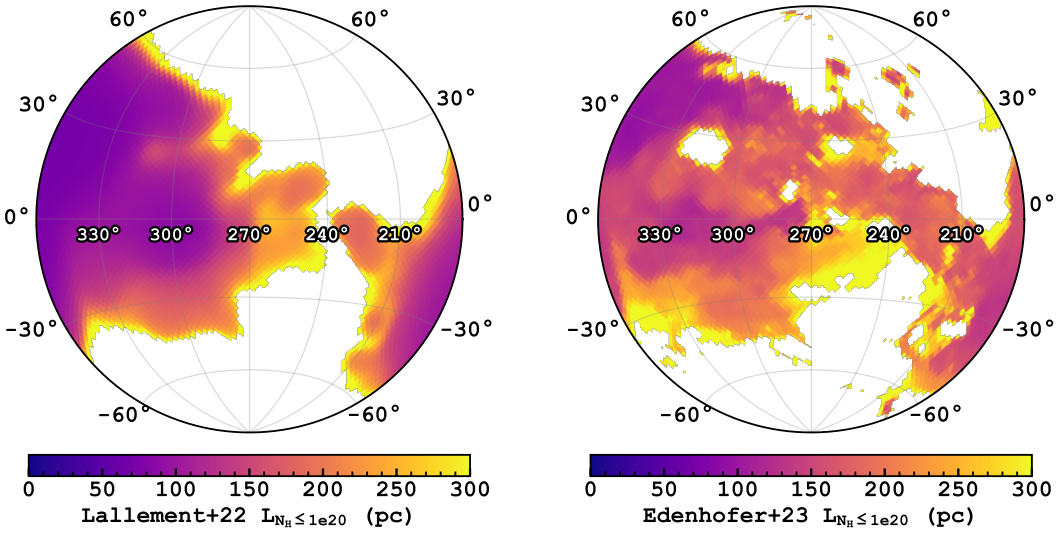

Figure 3.19: Distance at which the integration of $N_{\rm H}$ reaches $10^{20}\,{\rm cm}^{-2}$ in the Lallement et al. (2022) (*left*) and Edenhofer et al. (2024) (*right*) dust cubes, as proxies of the extent of the local bubble. The empty regions in the map indicate that the integration does not reach $N_{\rm H} \geqslant 10^{20}\,{\rm cm}^{-2}$ before 400 pc.

The anti-correlation of $\mathrm{EM_{LHB}}$ and dust can also be appreciated by looking at slices of 3D dust cubes. Fig. 3.20 shows the shape of the LHB shell overlaid on the $y = 0$ slice in the Edenhofer et al. (2024) dust cube. The extent of the LHB matches the onset of extinction extremely well, filling gaps of low dust density.

Liu et al. (2017) produced the latest X-ray LHB model before our work. Consulting their EM map and great-circle cuts (their Figs. 6 and 7), one can see despite the difference in methodology (spectral-fitting versus band-ratio) and instrument, the inferred EM and shape of the LHB are remarkably similar. Nevertheless, we have identified some areas that are interestingly different:
i) at $l \sim 240^\circ$ we found a more distinct transition in LHB extent between the Galactic plane ($b \sim 0$, region of the β Canis-Majoris tunnel) and a large-scale protrusion in the southern Galactic hemisphere ($b \lesssim -30^\circ$) than Liu et al. (2017) .
ii) The aforementioned channel around (l,b)=(315°, 25°) did not appear in the Liu et al. (2017)'s EM map. It was because that region was categorised as contaminated by the background Loop I superbubble and was excluded from the analysis. In fact, the appearance of the tunnel was seen in the ROSAT R1+R2 band map even after the SWCX subtraction (Liu et al., 2017, their Fig. 2).

3.5.3 Degeneracy between the local hot bubble and the Milky Way's circum-galactic medium components

This Section discusses the degeneracy between the LHB and CGM components and our mitigation methods. We begin by laying out the observations that demonstrate this degeneracy. In summary, this led us to incorporate ROSAT R1 and R2 bands into our analysis, as well as imposing a uniform prior to limit $kT_{\rm LHB} < 0.15\,{\rm keV}$ for regions of low $N_{\rm H}$.

Inspecting the spectral fitting results with only eROSITA data revealed a degeneracy between the LHB and the CGM components in some contour bins. An example of this degeneracy can be seen in Fig. 3.21, where we show the parameter correlations in the spectral fits of Bin476 and Bin1875, located at (l, b)=(257.°9, 59.°6) and (296.°7, 47.°6) respectively. Both regions have $\log\left(N_{\rm H}/{\rm cm}^{-2}\right) \simeq 20.5$ as traced by the HI4PI survey (HI4PI Collaboration et al., 2016) using Eq. (3.5). One can see that the posterior distributions of $kT_{\rm CGM}$ are bimodal in both bins. The lower $kT_{\rm CGM}$ peak is contributed by either partially in Bin476, or completely in Bin1875, by

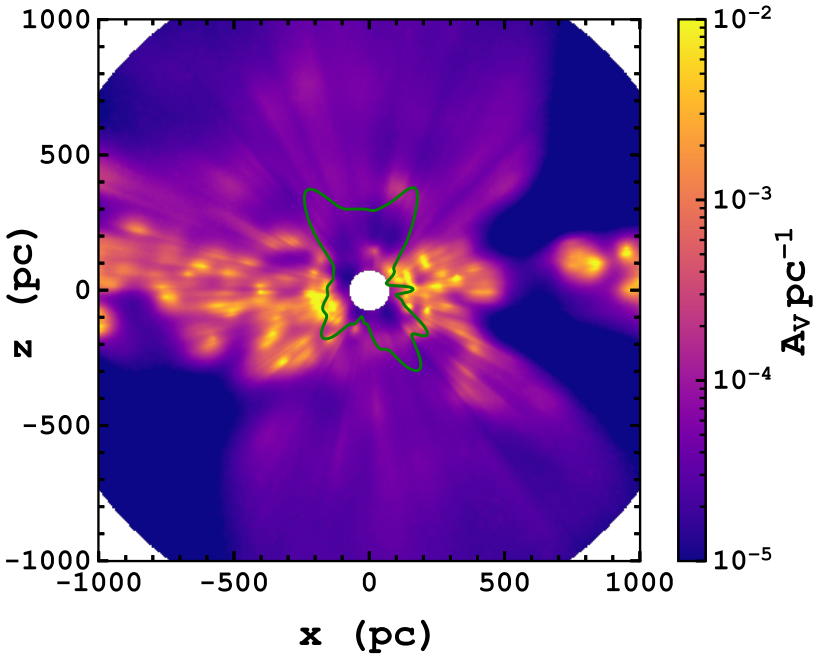

Figure 3.20: A slice of the Edenhofer et al. (2024) cube at the x-z plane overplotted with the silhouette of the LHB.

samples that have $kT_{\rm LHB} > kT_{\rm CGM}$. Similarly, the posterior distributions of $kT_{\rm LHB}$ show either an extended tail in Bin476 or a second peak in Bin1875, at temperatures at least twice that of the main peak. We believe these solutions are unlikely to represent the real picture, but are caused by the similarity of the LHB's and CGM's `apec` models observed at eROSITA's energy resolution. The main differentiating factor of LHB and CGM is the absorption that causes CGM component to drop off at the low energy end. Therefore, one would expect the two to exhibit some levels of degeneracy at regions of low $N_{\rm H}$. To help break the degeneracy, one would ideally go to energies lower than 0.2 keV, but eROSITA's effective area there is small. However, ROSAT maintains a significant effective area until $\sim$ 0.1 keV, and is therefore more sensitive to detect the drop off caused by absorption in the CGM component. The details of how the ROSAT data were used were described in Sect. 3.3. We note that ideally, one should subtract the heliospheric SWCX contributions from the ROSAT R1 and R2 band maps as in Uprety et al. (2016), who reported an all-sky average SWCX contribution of $30 \pm 8\%$ in R1 and $8 \pm 10\%$ in R2. However, given that the average relative uncertainties in R1 and R2 are 37% and 31% in our contour bins and that they only contributed to two spectral bins in the fitting, we believe the bias introduced by neglecting SWCX in ROSAT data is vastly subdominant to the resulting fit parameters of our full spectral analysis. Perhaps a more pertinent question would be whether a pair of data points from ROSAT possesses sufficient capability to resolve the degeneracy between the LHB and CGM components.

The answer is largely affirmative in many contour bins plagued by the degeneracy. For a specific example and a direct comparison, the top panel of Fig. 3.22 shows the corner plot of Bin476 after including the ROSAT data. The high temperature tail in the posterior of $kT_{\rm LHB}$ vanished and samples with $kT_{\rm LHB} > kT_{\rm CGM}$ disappeared. Motivated by the positive results, we incorporated the ROSAT R1 and R2 bands into the spectral analysis.

Nonetheless, cases remained where this was inadequate, especially at low $N_{\rm H}$ regions. For instance, in Bin1875 (lower panel of Fig. 3.22), the degeneracy remained. The posterior distributions remained highly bimodal, albeit a longer MCMC chain was needed to sample the second peak ($kT_{\rm LHB} > kT_{\rm CGM}$). Unfortunately, we could not break this degeneracy using the currently available data. Therefore, we decided to forbid $kT_{\rm LHB}$ to go above 0.15 keV by imposing a uniform

prior between 0.07–0.15 keV on $kT_{\rm LHB}$. Not surprisingly, the resulting posterior distributions no longer show a second peak, as shown in Fig. 3.23. This prior was used in the fitting of all the contour bins where $\log(N_{\rm H}/{\rm cm}^{-2}) < 20.5$. To our knowledge, the LHB temperature has seldomly been measured to be higher than 0.15 keV (e.g. Snowden et al., 1990b, 2000; McCammon et al., 2002; Liu et al., 2017), and conversely, the CGM seldomly below 0.15 keV (e.g. McCammon et al., 2002; Yoshino et al., 2009; Gupta et al., 2021; Bluem et al., 2022; Ponti et al., 2023b), justifying our choice of prior in the low $N_{\rm H}$ regions.

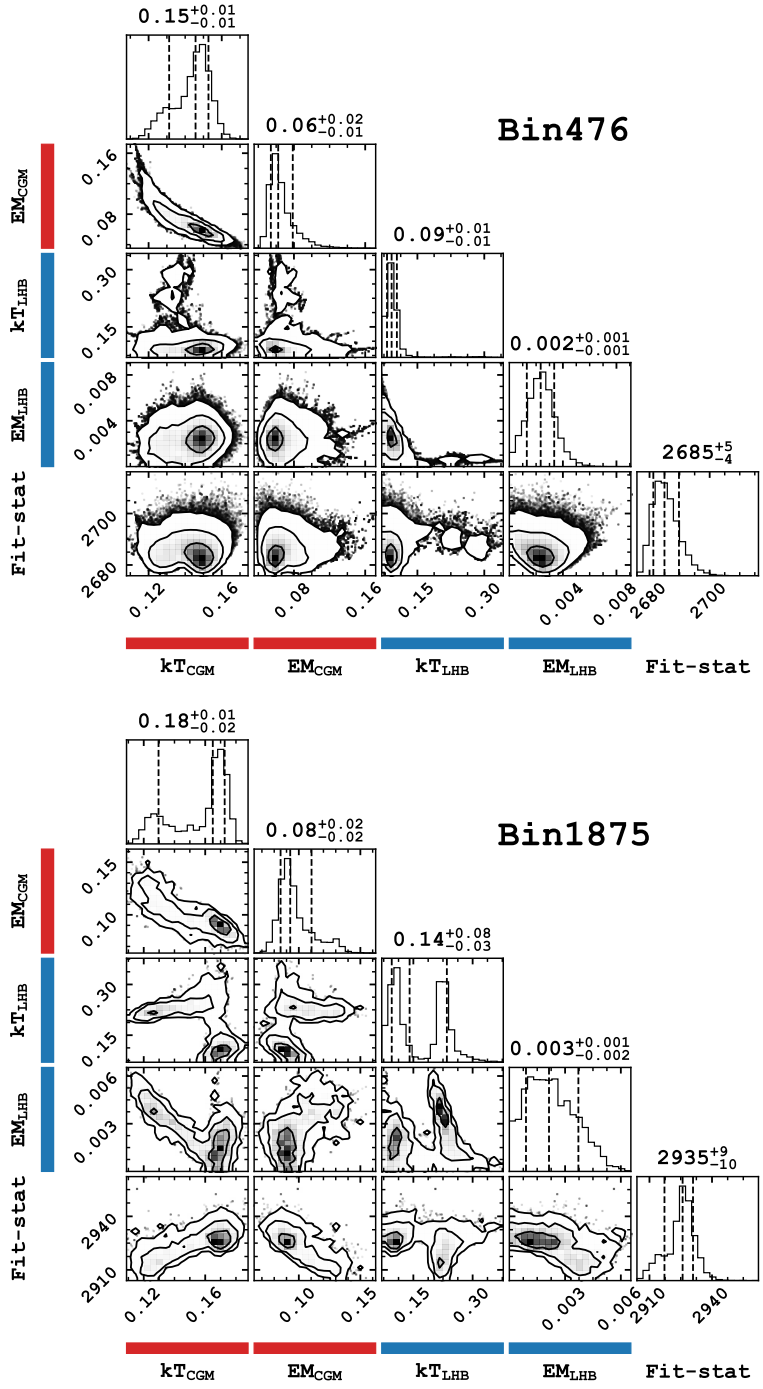

Figure 3.21: Corner plots showing LHB and CGM parameters are degenerate in regions of low $N_{\rm H}$. *Top:* Bin476 at (l, b)=(257°.9, 59°.6). *Bottom:* Bin1875 at (l, b)=(296°.7, 47°.6).

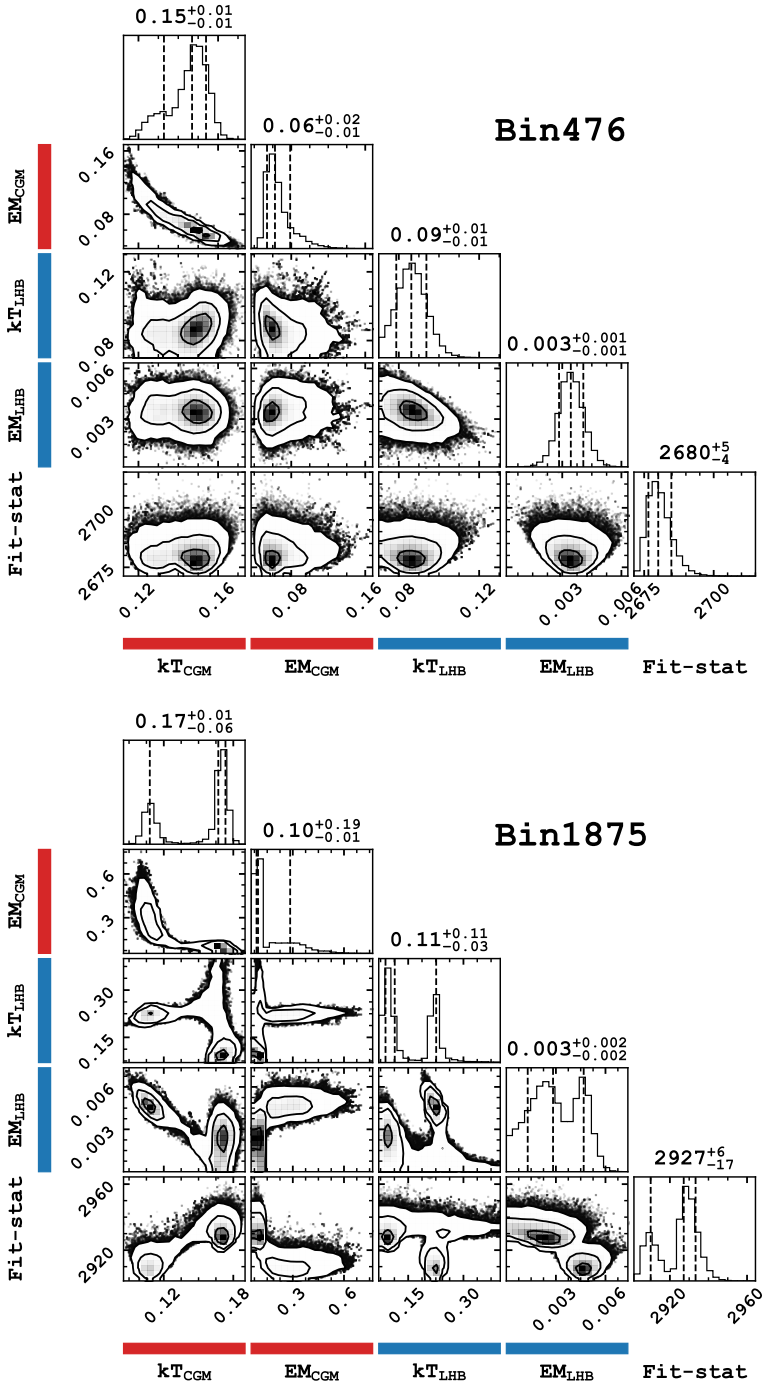

Figure 3.22: The same plots and panel configuration as Fig. 3.21 but with ROSAT R1 and R2 data.

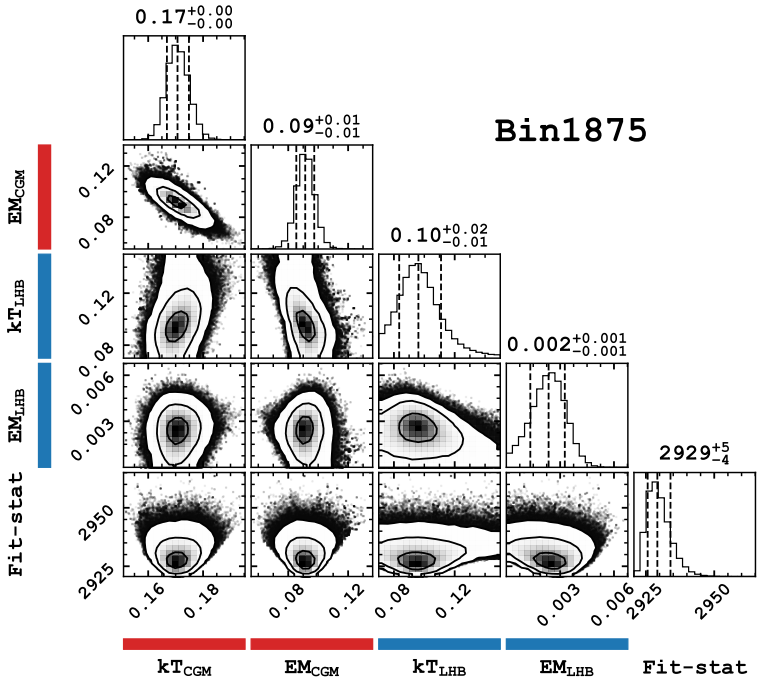

Figure 3.23: Corner plot of Bin1875 after using ROSAT data and imposing a uniform prior on kT_{LHB} below 0.15 keV.

3.5.4 Solar wind charge exchange

The halo orbit of SRG/eROSITA around the Sun-Earth Lagrangian point L2 (Freyberg et al., 2021) avoids much of the magnetospheric SWCX that originates from the interaction of the solar wind ions with neutrals in the Earth's exosphere (Kuntz, 2019). An image of the Earth's exosphere in Ly-α taken from 2348 $R_\oplus$ away shows that it is contained within 94 $R_\oplus$ (Kameda et al., 2017), while SRG never ventured within 175 $R_\oplus$ from the Earth (Freyberg et al., 2021), effectively immune to the magnetospheric SWCX emission since it is always pointing perpendicular to the Sun-Earth-L2 line. Even avoiding the bulk of the exosphere, in principle, SWCX can also occur on the surface of the magnetotail, but we expect its effect to be small since such a thin interaction and emission layer would incur brightness variation in short timescales (minutes to hours), and we do not observe obvious stripes along the ecliptic longitude lines in the soft band in eRASS1 (eROSITA completes scanning a great circle primarily along this direction every four hours).

We further ignored the effect of heliospheric SWCX in our spectral analysis, which can indeed contaminate eROSITA data in general. We verify that this is at least a satisfactory assumption by looking at the $\mathrm{EM_{LHB}}$ map a posteriori. It is well-known that the solar wind density is higher at low heliographic latitudes than at the poles, especially around solar minima (e.g. Porowski et al., 2022). Therefore, unlike pointed observations, eRASS provides a way of estimating the heliospheric SWCX contribution from detecting extra emission preferentially along the ecliptic plane. In Fig. 3.13, we overlaid the ecliptic in black on the $\mathrm{EM_{LHB}}$ map, and the dashed black lines mark the range of $\pm 25^\circ$ within the ecliptic, where the denser, slow solar wind dominates during solar minima (e.g. McComas et al., 1998, 2003). The fact that there is no obvious enhancement within this ecliptic latitude range suggests the heliospheric SWCX contamination in our results is minor. Indeed, as we gradually approached solar maximum, eRASS3 and 4 data clearly show enhancement in this band, but the presentation and the detailed analysis of this effect will be presented in another work (Dennerl et al., in prep).

3.5.5 Energetics and pressure balance within the local hot bubble

We estimated the thermal energy of the LHB as follows:

$$E_{\mathrm{thermal}} = \sum P_{\mathrm{thermal}} \Delta V \tag{3.13}$$

$$= 1.92 n_e \sum k T_{\mathrm{LHB}}(l,b) \Delta V, \tag{3.14}$$

where ΔV is the volume occupied by the LHB plasma within a contour bin. The $\mathrm{EM_{LHB}}$ information is implicitly passed into ΔV in the form of the extent of the LHB. We have incomplete coverage of the sky. Hence, we scaled up our estimation of E_{thermal} to a total of 4π solid angle. Finally, we estimated $E_{\mathrm{thermal}} = 1.3^{+0.9}_{-0.5} \times 10^{51}$ erg, where we have assumed $n_e = 4 \times 10^{-3}\,\mathrm{cm^{-3}}$. This is in the order of the energy released by a supernova explosion. However, one must consider that the LHB's size (radius) is > 100 pc, which is too large for a single explosion. Therefore, the LHB is more likely to have been episodically reheated and expanded by successive supernova explosions and simultaneously radiated its energy away to produce the current energy content.

We presented the thermal pressure map in Fig. 3.10, using $P_{\mathrm{thermal}}/k = nT$. We found the mean pressure of the LHB is $P_{\mathrm{thermal}}/k = 10100^{+1200}_{-1500}\,\mathrm{cm^{-3}\,K}$. These numbers are consistent with pressure measured in the sight line of $(l,b)=(144^\circ,0^\circ)$ by Snowden et al. (2014), hence supporting their finding of the LHB being in pressure equilibrium with the local interstellar clouds (LICs), after accounting for magnetic pressure as measured by *Voyager I* outside of the heliosphere Burlaga & Ness (2014). But we also point out that Snowden et al. (2014)'s sight line lies on the Galactic plane, which we found to have systematically higher thermal pressure. This pressure is also fully consistent with measurements based on X-ray shadowing using eRASS:4 data (Yeung et al., 2023).

Compared with the latest numerical simulation of the LHB by Schulreich et al. (2023), our measured pressure is consistent with their simulated present-day pressure of $10100\,\mathrm{cm^{-3}\,K}$. However, this results from combining their n and T, which are lower and higher by roughly an order of

magnitude compared to our results, respectively. Despite the apparent coincidence, their simulation shows how successive supernova explosions in the Sco-Cen complex can lead to the large-scale temperature gradient within the LHB, as we found in this work (Sect. 3.5.1).

The estimated Galactic midplane total ISM pressure is $P/k \sim (2.8 \pm 0.7) \times 10^4\,\mathrm{cm^{-3}\,K}$, about two to three times the thermal pressure we estimated from the LHB on the plane (Boulares & Cox, 1990; Cox, 2005). As already put forth at the time, one can approximate the cosmic rays, magnetic and dynamical (possibly thermal) pressure as equipartition. This yields a thermal pressure from the ISM about $P_{\mathrm{thermal}}/k \sim 10^4\,\mathrm{cm^{-3}\,K}$, consistent with our measurement. Finally, we would like to highlight that the LHB pressure of $P_{\mathrm{thermal}}/k \sim 10^4\,\mathrm{cm^{-3}\,K}$ is lower than the typical values seen in superbubbles, supernova remnants or wind-blown bubbles (e.g. Oey & García-Segura, 2004; Sasaki et al., 2011; Kavanagh et al., 2012; Sasaki et al., 2022). This may indicate the LHB being open towards higher Galactic latitudes.

3.5.6 Interstellar tunnel network

Cox & Smith (1974) famously postulated supernovae can generate and maintain an interstellar tunnel network in the Galaxy, filled with $\sim 0.1\,\mathrm{keV}$ gas. Mapping the hot phase structure of the LB/LHB in emission has more limitations than mapping the cold phase of the local ISM with stellar extinction or line absorption because one has to assume a model of the emitting components and the absorption they are subject to. This makes inference of the LHB shape on the Galactic plane difficult, as one expects many line-of-sight emitting and absorbing components. Also, extensions and possible connecting tunnels of the LHB that are not aligned with the radial direction are difficult to infer. Nevertheless, as mentioned in Sect. 3.5.2, we found evidence of hot gas filling nearby channels that lack neutral material.

The most convincing evidence of such a channel is the β CMa tunnel ($l \sim 250°, b \sim 0°$), where even the projected morphology of the tunnel in $\mathrm{EM_{LHB}}$ (see Fig. 3.13) is similar to the dust map (especially, the right panel of Fig. 3.19). Historically, ROSAT did not provide enough evidence of the tunnel being filled by hot gas (Welsh & Shelton, 2009, and references therein).[6] However, Dupin & Gry (1998) and Gry & Jenkins (2001) found the intervening absorbing clouds to the stars β CMa and ϵ CMa to show absorptions from high ionisation species such as C IV and Si III, but comparison with the cloud turbulent temperature ($\sim 7000\,\mathrm{K}$) demonstrated that they are likely partially ionised due to photoionisation of the hot stars and/or the interaction with the hot LHB gas in the surrounding. Our observation confirms the presence of the surrounding hot gas in the tunnel. Indeed, both the UV and our soft X-ray observations corroborate the scenario where the warm gas in LICs forms a conductive layer between themselves and the surrounding hot gas (see e.g. Cowie & McKee, 1977; Slavin, 1989). Welsh (1991) suggested this tunnel is connected to the Gum nebula (Gum, 1952), which lies in the same direction at 400 pc (Brandt et al., 1971). The Gum nebula is likely part of a large superbubble GSH 238+00+09 (Heiles, 1998), which the LHB could also connect to.

In addition, we report on a possible channel filled by hot plasma towards the direction ($l \sim 315°$, $b \sim 25°$), in the constellation Centaurus. A zoom-in view of the $\mathrm{EM_{LHB}}$ and dust map tracing the neutral matter in the region is shown in Fig. 3.24. There is an enhancement in $\mathrm{EM_{LHB}}$ in this direction, which anti-correlates with the amount of dust extinction. This implies the presence of extra path length of the LHB plasma, possibly filling the tunnel. It might be another channel connecting to the Loop I superbubble (Egger & Aschenbach, 1995), in addition to the Lupus tunnels first discovered from Na I absorption lines (Welsh et al., 1994; Lallement et al., 2003). The latter are, unfortunately, located on the Galactic plane and, thus, are difficult to identify in our spectral analysis. The Centaurus tunnel region is located on the edge of the eROSITA bubbles, further complicating the spectral fitting. A dedicated spectral analysis, with a tailored spectral extraction region, of this region will likely help disentangle the emission from the Loop I superbubble (its nature or existence has become unclear after the discovery of the eROSITA

[6] Closer inspection of the R12 band count rate map suggests there is indeed a weak enhancement, independent of the subtraction of SWCX (Snowden et al., 1997; Uprety et al., 2016).

bubbles) from the eROSITA bubbles, in terms of spectral properties and distance. This analysis is currently ongoing.

The Antlia supernova remnant (l, b)$\sim$($275^\circ, 15^\circ$) (e.g. Fesen et al., 2021), Monogem Ring (l, b)$\sim$($200^\circ, 8^\circ$) (e.g. Knies et al., 2024) and Orion-Eridanus superbubble (l, b)$\sim$($205^\circ, -30^\circ$) (e.g. Pon et al., 2016) are other nearby bubbles that our data suggest the LHB could be touching or connected to. Monogem Ring is arguably even more interesting because there is a lack of dust (Lallement et al., 2022; Edenhofer et al., 2024) in the line-of-sight up to its distance of $\simeq 300\,\mathrm{pc}$ (Knies et al., 2024, we refer to the closest components in the whole Gemini-Monoceros X-ray enhancement), consistent with the eROSITA spectral analysis of it (Knies et al., 2024). The LHB might be currently merging or about to interact with it.

On the other hand, there is the presence of channels of low N_H that do not seem to be filled with soft X-ray-emitting plasma. The more obvious one is located at (l, b)$\sim$($260^\circ, 29^\circ$), which can be seen in the right panel of Fig. 3.19. The $\mathrm{EM_{LHB}}$ map in Fig. 3.13 does not show an anti-correlated enhancement.

In summary, our data demonstrate that the displacement model in which the LHB plasma fills the LC works well overall. Only a few regions seemingly do not abide by the displacement model.

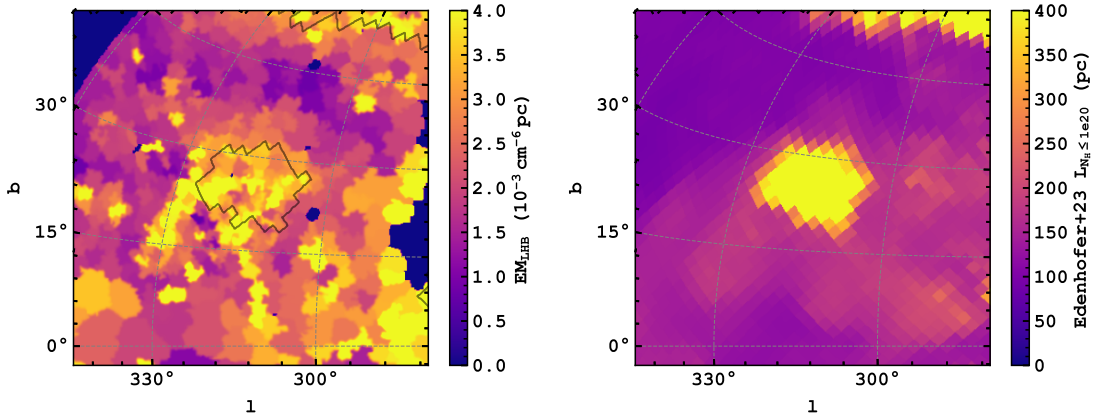

Figure 3.24: Zoom-in of the Centaurus tunnel in the smoothed $\mathrm{EM_{LHB}}$ map (*left*) and dust distance map by integrating the dA_V map up to $10^{20}\,\mathrm{cm^{-2}}$ (*right*) (Edenhofer et al., 2024). The contour line outlining the region where the N_H does not reach $10^{20}\,\mathrm{cm^{-2}}$ in 400 pc is overlaid on the $\mathrm{EM_{LHB}}$ map.

3.5.7 Beyond constant density of the local hot bubble

We have discussed the close anti-correlation between the local dust map and the emission measure of the LHB in Sect. 3.5.2. The dust maps (Fig. 3.19) we compared our LHB shape to were inferred from integrating the N_H up to $10^{20}\,\mathrm{cm^{-2}}$ (an optical depth for a 0.2 keV photon) from our position. An alternative way of locating the shell of the LB is by finding the first peak of the extinction as adopted by Pelgrims et al. (2020) and O'Neill et al. (2024). This might be more physically motivated as the expansion on the LB is expected to create a shell of denser material at its boundary that is not necessarily dense enough to be opaque to soft X-rays.

A comparison of the inferred LB shell from O'Neill et al. (2024) using Edenhofer et al. (2024) data to our constant density LHB model is shown in Fig. 3.25. For this comparison, we adopted their $A'_{0.5}$ peak density distance as the extent of the LB. Their shapes are significantly different, most notably at $b > 60^\circ$, where the apparent enhancement in $\mathrm{EM_{LHB}}$ (hence extent) lacks a counterpart in the LB. Below $b \lesssim 30^\circ$, the LHB and the LB are both more extended but with a fairly different morphology. The clear tunnel in the LB at (l, b) $\simeq$ (250°, -20°) is not shared

by the LHB. There is a reasonable agreement for regions between $-30^\circ \lesssim b \lesssim 60^\circ$, ignoring the various tunnels discussed in Sect. 3.5.6. The simplest reason for the discrepancy between the two maps is the constant density assumption is inaccurate, given $L_{\rm LHB} \propto {\rm EM}_{\rm LHB} n_e^{-2}$, which means the extent of the LHB is more sensitive to n_e than ${\rm EM}_{\rm LHB}$.

One can work conversely, assuming the LB shell is the true extent of the LHB and estimate the electron density of the LHB plasma using Eq. (3.12), as well as its thermal pressure by Eq. (3.10) subsequently. We show the resulting electron density and thermal pressure maps in Fig. 3.26. Clearly, much of the modulation in ${\rm EM}_{\rm LHB}$ is transferred to the variation in density, especially in regions where the LHB extent derived from the constant density assumption differs much from the extent of the LB. This causes the average LHB density at $b > 60^\circ$ to be higher than the rest of the areas by $\sim 40\%$. The extensions towards β CMa (at least the part on the Galactic plane) and Centaurus tunnels mentioned in Sect. 3.5.6 do not have direct counterparts in the LB map, and thus they are taken as high-density regions of the LHB. The thermal pressure map slightly differs from the constant density case shown in Fig. 3.10, where the former displays a weaker north-south gradient because of the higher electron density in the northern polar cap balancing the lower LHB temperature, and it produces a more uniform pressure profile on the largest scale. Indeed, being in pressure equilibrium with its surroundings would be the expectation for an old bubble such as the LHB. From the two maps, the half-sky median electron density and thermal pressure are $n_e = 3.75^{+0.87}_{-0.69} \times 10^{-3}\,{\rm cm}^{-3}$ and $P_{\rm thermal}/k = 10.5^{+3.4}_{-2.5} \times 10^3\,{\rm cm}^{-3}\,{\rm K}$.

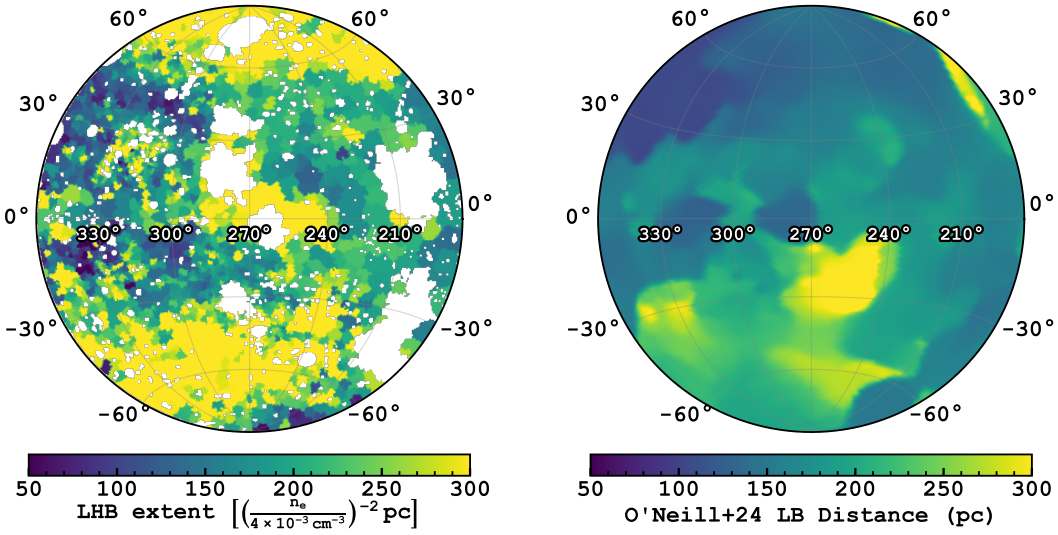

Figure 3.25: Comparison of the local (hot) bubble extent from X-ray and dust. *Left:* Extent of the local hot bubble under the constant $n_e = 4 \times 10^{-3}\,{\rm cm}^{-3}$ assumption. *Right:* Local bubble shell tracing the closest extinction peak inferred by O'Neill et al. (2024). An interactive comparison in 3D can be accessed from the accompanying website (Sect. 3.7).

Assuming the LHB extends up to the first extinction peak is a sound assumption, but it is not without challenges. The hardest part to reconcile is the presence of tunnels that seem independent of the LB shell. We suggest it is unlikely a coincidence that ${\rm EM}_{\rm LHB}$ shows a better anti-correlation to the local dust column density (Fig. 3.19) than the extent of the LB shell, especially when the LB shell peak density is the lowest in these regions (see Fig. 4 in O'Neill et al., 2024). Not accepting it as a coincidence entails hot plasma located beyond the first wall of absorption. They could have the same origin as the LHB or had other heating mechanisms. One possibility is shown by the LB simulation by Schulreich et al. (2023) (third and fourth columns of their Fig. 4), in which pockets of hot plasma could be formed beyond the main LB cavity because of the LHB anisotropic expansion into the inhomogeneous surrounding materials that were already stirred up during the

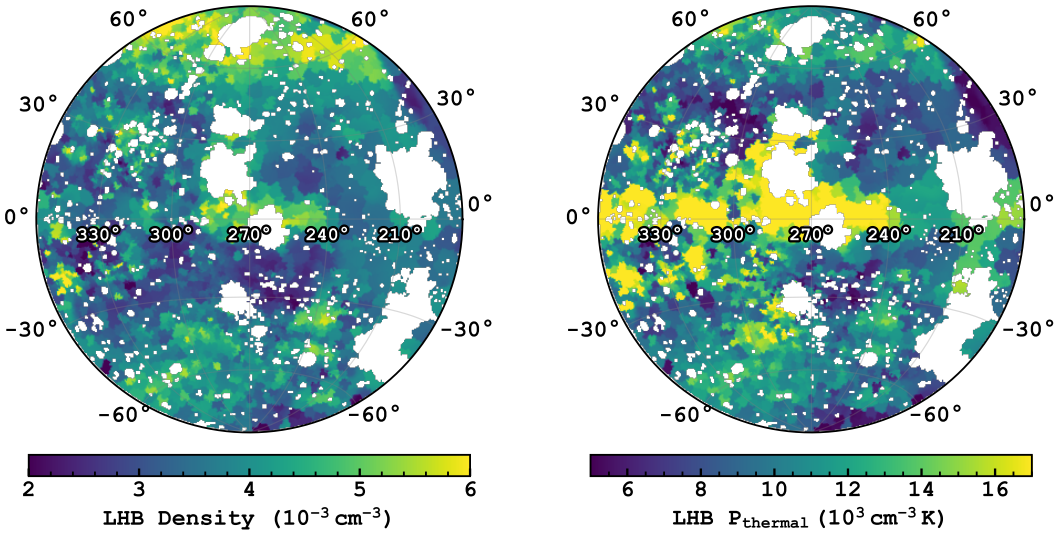

Figure 3.26: Electron density (*left*) and thermal pressure (*right*) of the local hot bubble assuming it extends up to the local bubble shell (O'Neill et al., 2024).

wind-driven phase.

3.5.8 Cosmic X-ray background

Determination of the cosmic X-ray background photon indices

Ponti et al. (2023b) adopts a double-broken power-law model to describe the CXB in the eFEDS field, following the CXB synthesis model by Gilli et al. (2007), which produces a steepening CXB slope $\lesssim 1$ keV from galaxy groups and clusters. The double-broken power-law[7] (`bkn2pow` in `Xspec/PyXspec`) can be written as

$$f(E) = \begin{cases} K(E/\mathrm{keV})^{-1.9} & \text{if } E \leqslant 0.4\,\mathrm{keV} \\ K0.4^{-0.3}(E/\mathrm{keV})^{-1.6} & \text{if } 0.4\,\mathrm{keV} \leqslant E \leqslant 1.2\,\mathrm{keV} \\ K\frac{0.4^{-0.3}}{1.2^{0.15}}(E/\mathrm{keV})^{-1.45} & \text{if } E \geqslant 1.2\,\mathrm{keV}, \end{cases} \tag{3.15}$$

where K is the normalisation of the power-law at 1 keV in the unit of photons s^{-1} cm^{-2} keV^{-1} and the first and second break energies are located at 0.4 and 1.2 keV.

From the spectral fitting of the regions shown in Fig. 3.6, we found that the first break energy at 0.4 keV is redundant as the photon indexes below ($\Gamma_1 = 1.93^{+0.22}_{-0.21}$) and above ($\Gamma_2 = 1.91^{+0.09}_{-0.16}$) this energy are consistent within $1\,\sigma$ when we left all three photon indexes free to vary in the spectral fitting. Therefore, we subsequently replace the double-broken power-law model with a single-broken power-law model, which can be treated as a special case of Eq. (3.15). It has the form

$$f(E) = \begin{cases} K(E/\mathrm{keV})^{\Gamma_1} & \text{if } E \leqslant E_b \\ K(E_b/\mathrm{keV})^{\Gamma_2-\Gamma_1}(E/\mathrm{keV})^{-\Gamma_2} & \text{if } E \geqslant E_b, \end{cases} \tag{3.16}$$

where E_b is the break energy and Γ_1 and Γ_2 are the photon indexes below and above E_b. Another iteration of the spectral fitting with the single-broken power-law model indicates $E_b = 1.19^{-0.26}_{-0.17}$, $\Gamma_1 = 1.81^{+0.24}_{-0.21}$ and $\Gamma_2 = 1.61^{+0.13}_{-0.07}$. This result suggests a change of slope in the CXB at 1.2 keV, below which the slope is possibly steeper from the contributions from active galactic nuclei, galaxy

[7] Three models of CXB were used in Ponti et al. (2023b). We refer to their 'CXB' model here.

groups and galaxy clusters (Hasinger et al., 1993; Smith et al., 2007; Yoshino et al., 2009). Nonetheless, the transition of the CXB slope is only significant on $\sim 1\,\sigma$ level[8] and is not strictly required by the data. Additionally, the uncertainties of the parameters are dominated by the spread from multiple regions instead of the statistical uncertainties within each region. A simple power-law fit yields $\Gamma = 1.68^{+0.08}_{-0.10}$, in good agreement with Γ_2 in the single-broken power-law model. This is steeper than the canonical photon index of 1.4–1.5. Calibration issues could partly cause this, as eROSITA indeed tends to measure cooler cluster temperature than *Chandra* and *XMM-Newton* for massive clusters (Liu et al., 2023; Migkas et al., 2024)[9]. Both treatments of the CXB reproduce the data almost equivalently, with the simple power-law and single-broken power-law resulting in an average C-statistic/dof in the Markov chain Monte Carlo (MCMC) runs of all regions of $3123^{+249}_{-99}/2595$ and $3092^{+228}_{-99}/2588$, respectively. Therefore, we adopted both in our full western Galactic hemisphere analysis and discuss the systematic uncertainties associated with either choice in Sect. 3.5.8. Based on this analysis of the CXB, we froze Γ_1, Γ_2 and E_b to be 1.9, 1.6 and 1.2 keV of the single-broken power-law model, Γ to 1.7 for the simple power-law model as the CXB model in the full spectral analysis.

Normalisation

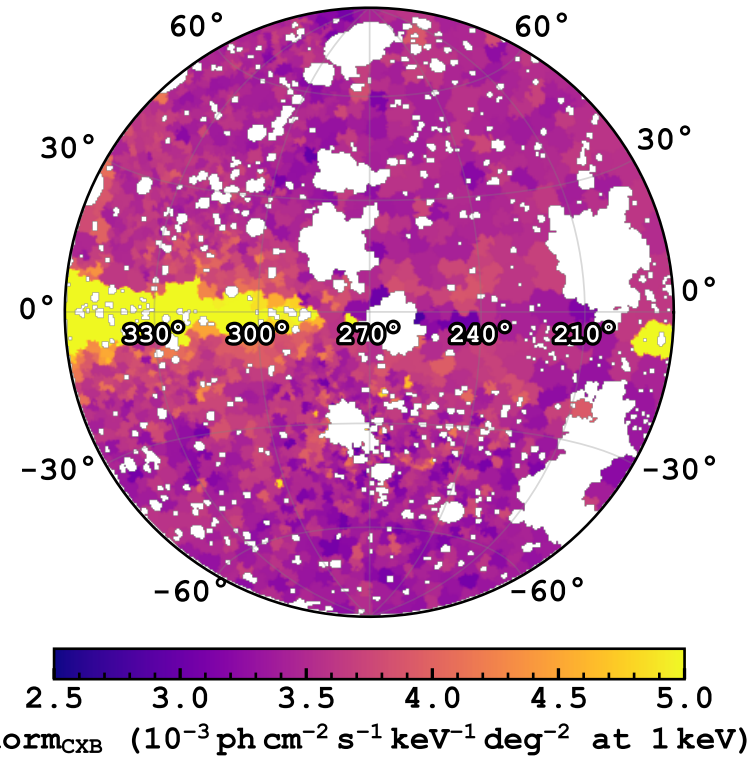

Figure 3.27: Normalisation of the cosmic X-ray background assuming a simple power-law of $\Gamma = 1.7$.

Fig. 3.27 shows the normalisation of the CXB, taken from the simple power-law model of $\Gamma = 1.7$. Ignoring the Galactic plane, the normalisation of the CXB is extremely uniform. At $|b| > 30°$, it has a median of $\mathrm{norm_{CXB}} = 3.54^{+0.24}_{-0.17} \times 10^{-3}$ photons cm^{-2} s^{-1} keV^{-1} deg^{-2} at 1 keV.

[8] Fixing E_b at 1.2 keV would decrease the statistical uncertainties of Γ_1 and Γ_2 to $1.87^{+0.16}_{-0.11}$ and $1.63^{+0.08}_{-0.06}$, respectively.

[9] The currently developing eSASS pipeline processing version `c030` will improve the calibration of the effective area and redistribution matrix above 1 keV.

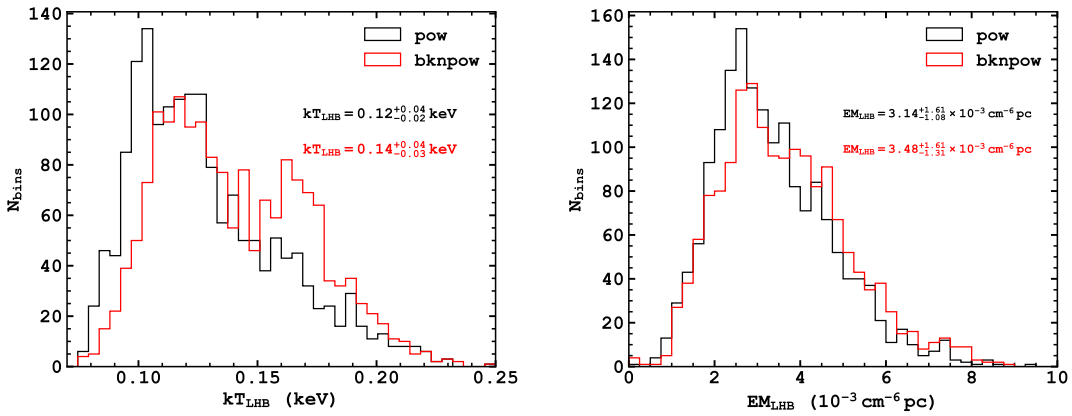

Figure 3.28: Distributions of $kT_{\rm LHB}$ (*left*) and $\rm EM_{LHB}$(*right*) using either a simple power-law (pow) or a broken power-law (bknpow) parametrisation of the CXB.

This means the fluctuation of the CXB is $\lesssim 10\%$, on the angular scales of $\sim 1.^{\circ}5$–4° that we probe set by the contour binning scheme. The enhancement on the Galactic plane is likely due to the Galactic ridge emission.

Our main finding on the CXB is that eROSITA observes a steeper photon index than the conventional value of 1.45 (Cappelluti et al., 2017) (Sect. 3.5.8). It might be due to calibration issues (Migkas et al., 2024) or caused by the steepening of the CXB slope at soft energies. A newer processing version of eROSITA data will potentially mitigate or resolve the calibration issue. Given the steeper slope of Γ ∼1.6–1.7, the normalisation we found is also slightly higher compared to *Chandra* ($(3.32 \pm 0.05) \times 10^{-3}$ photons cm^{-2} s^{-1} keV^{-1} deg^{-2}, Cappelluti et al. (2017)). In addition, the uniformity of the CXB demonstrates the robustness of our spectral fitting to differentiate multiple sky components.

Systematic uncertainties associated with the choice of cosmic X-ray background model

As described in Sect. 3.5.8, the power-law and the broken power-law model could reproduce the diffuse X-ray spectra equally well. So far, we have been discussing the results using a CXB described by a simple power-law model. To test the systematic effect caused by the CXB model, we fitted all spectra again in the same way but using a broken-power-law CXB component. We then plotted the 2D maps and inspected the histograms of the other components. We observed that the distributions of most of the components were unaffected except for the LHB.

Fig. 3.28 shows the difference in distributions of $kT_{\rm LHB}$ and $\rm EM_{LHB}$ by using the two CXB models for regions above $|b| > 10^{\circ}$. The broken power-law model appears to raise the temperature of the LHB systematically by 0.02 keV in terms of the median. On the other hand, the impact of such temperature change on the EM is small ($\sim 0.3 \times 10^{-3}$ cm^{-6} pc) compared to the width of the $\rm EM_{LHB}$ distribution ($\sim 1.5 \times 10^{-3}$ cm^{-6} pc). Inspection of the spectra suggests this is the result of the intricate balancing at the softest end of the spectra (~ 0.2 keV). By increasing the temperature slightly, the LHB could lower its flux density at this energy to accommodate the steepening slope of the CXB.

Fig. 3.29 demonstrates this is indeed a systematic effect by showing the ubiquitous under-subtraction in the residual map made from subtracting the LHB temperature map determined by the simple power-law model from that of the broken power-law model. The broken power-law model consistently predicts a higher LHB temperature than the simple power-law model, and the difference is more enhanced towards the Galactic plane. We computed the median differences below and above $|b| = 30^{\circ}$. For $|b| > 30^{\circ}$, the median difference between the two CXB models is 0.009 keV,

about the same as the $1\,\sigma$ statistical fitting uncertainty in this region. Between $10^\circ < |b| < 30^\circ$, the median difference rises to 0.029 keV, about 1.5 times the statistical uncertainty in this region. We consider these to be the systematic uncertainties of the absolute values of the temperature of the LHB. However, we emphasise that the temperature gradient reported in Sect. 3.5.1 is still present, as this systematic effect only steers the absolute value of $kT_{\rm LHB}$ in a single direction and is only very weakly dependent on location.

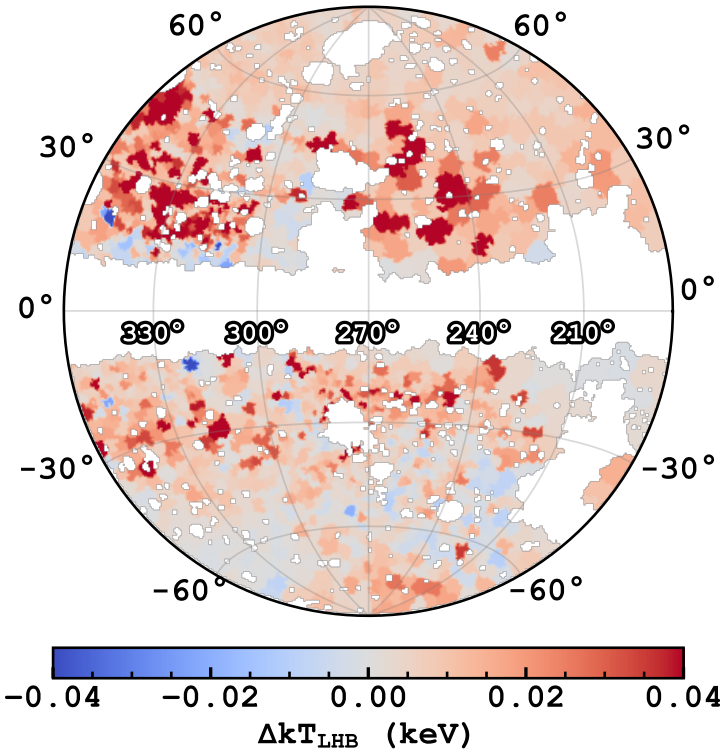

Figure 3.29: Difference in the LHB temperature in assuming a simple power-law CXB model and a broken power-law model, namely, $kT_{\rm LHB,bknpow} - kT_{\rm LHB,pow}$.

3.5.9 Robustness of the spectral fits

The use of `cstat` in evaluating the goodness of fit is possible but not straightforward, as the expected value and the variance of `cstat` depend on the number of counts in each spectral bin (Kaastra, 2017). Instead of the rule-of-thumb $\chi^2/{\rm dof} \sim 1$ indicating a good fit, one needs to compare the fitted `cstat` with the expected value and variance of `cstat` in each spectrum, which is a variable number dependent on counts. Therefore, while the spectral fitting was done using `cstat` (the eROSITA part), we report the $\chi^2/{\rm dof}$ after rebinning each spectrum to have at least 10 counts in each spectral bin using the same model. The rebinning was done following the scheme presented by Kaastra & Bleeker (2016). We present the map of the resulting $\chi^2/{\rm dof}$ values in Fig. 3.30.

We would like to remind the reader that the relatively small and narrow range of $\chi^2/{\rm dof}$ results partly from fitting the spectra up to 5 keV, where the instrumental background dominates with a small CXB contribution. The wide energy range between $\sim$ 2–5 keV can almost always be well-modelled by the dominating, but fixed, FWC model, thus inclined to result in low $\chi^2/{\rm dof}$. However, this energy range has strong constraining power on the subdominant CXB component, which is the only contributing component and was thus included in our spectral fitting.

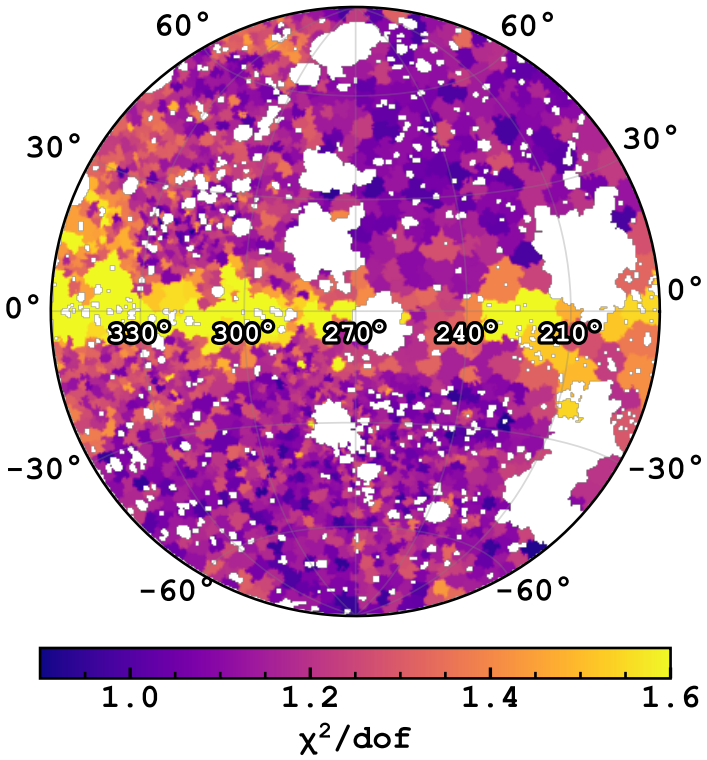

Figure 3.30: Map of reduced-χ^2 (χ^2/dof) after rebinning each spectrum, imposing that each spectral bin receives at least ten counts.

To better understand the robustness of the spectral fits, we show four spectra with increasing values of χ^2/dof in Fig. 3.31 and 3.32, from $\sim$ 1.0–1.7. Fig. 3.31 shows spectra in the range of $1.0 \lesssim \chi^2/\mathrm{dof} \lesssim 1.1$, where no major discrepancies between data and model could be seen. Fig. 3.30 demonstrates these values are typical of spectra away from the Galactic plane and the central part of the Galaxy. On the Galactic plane, poorer spectral fits are expected because of the definite presence of multiple line-of-sight structures, both in emission and absorption, which are not part of our model template. Towards the inner part of the Galaxy ($310^\circ \lesssim l \lesssim 360^\circ$), this scenario exacerbates, and poorer fits begin to be prevalent to even high Galactic latitudes around $-20^\circ \lesssim b \lesssim 30^\circ$. There are many ways to obtain poor fits, but one of the most common ways is the poor reproduction between $\sim$ 0.7–1 keV, where the Fe XVII, Ne IX and Ne X lines dominate. The reproduction is usually imperfect when these lines are bright, especially at the base of the eROSITA bubbles. However, it is currently difficult to distinguish between calibration imperfections and real variations in the astrophysical source. The upcoming pipeline processing version `c030` will address the former slightly in terms of including a more accurate energy resolution in the redistribution matrix.

The robustness of each region's fit and MCMC chain could be inspected by its associated corner plot and steps plot in the choropleth maps on our website (Sect. 3.7).

3.6 Conclusion

In this work, we binned the western Galactic hemisphere into $\sim$ 2000 regions. We extracted their spectra at solar minimum (eRASS1), where the heliospheric SWCX emission was negligible (Dennerl et al. in prep). These spectra were fitted with a model template consisting of the LHB, the Milky Way's CGM, the Galactic corona, the CXB, and, depending on the location,

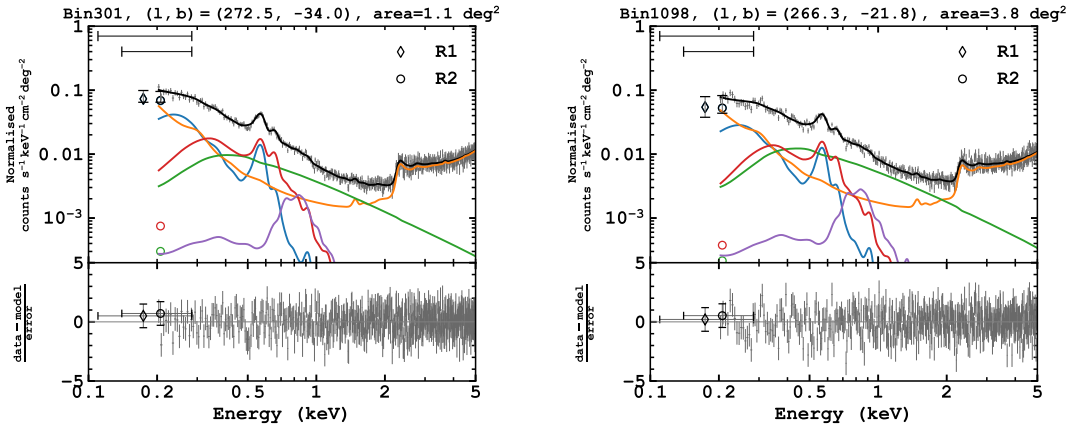

Figure 3.31: Example spectra having $\chi^2/\mathrm{dof} = 0.99$ and 1.10.

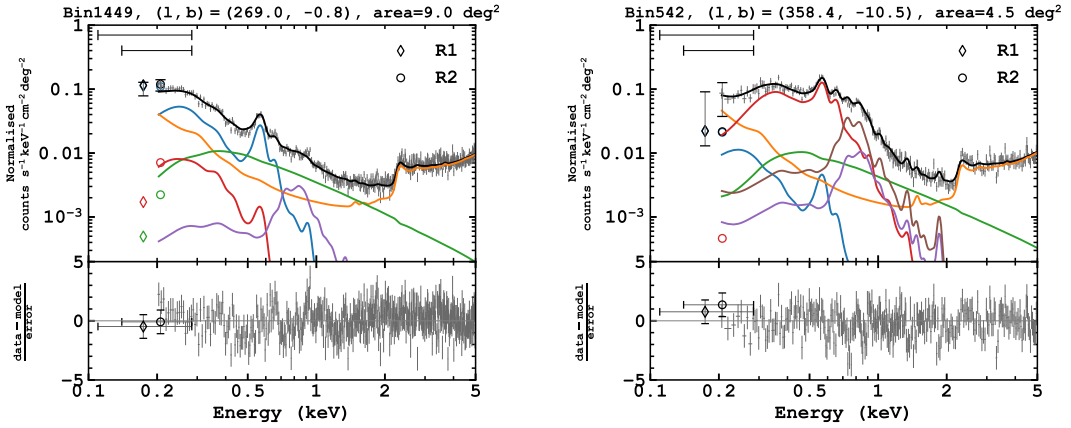

Figure 3.32: Example spectra having χ^2/dof of 1.50 and 1.70, respectively. They are commonly found near the Galactic plane, towards the inner part of the Galaxy and the base of the eROSITA bubbles. The models usually cannot predict the spectrum between ~ 0.7–1 keV well.

the eROSITA bubbles. This resulted in maps of the parameters, primarily the temperature and emission measure maps for the thermal plasma. We focused on the results regarding the LHB. We summarise our main findings below:

- We found the median temperature of the LHB to be $0.111^{+0.018}_{-0.015}$ keV. Much of the spread comes from the approximately north-south gradient above Galactic latitudes of 30°, with the south being hotter (121.8 ± 0.6 eV) than the north (100.8 ± 0.5 eV). Venturing closer to the Galactic plane, there seems to be an increase in LHB temperature, especially at $l \gtrsim 270°$. The origin of the temperature gradient is unclear, but it could be set up by more recent supernova explosions within the LHB. The enhancement in temperature towards the Galactic plane could be due to the enhanced thermal pressure needed in the Galactic plane for the LHB to maintain pressure equilibrium with the surroundings.
- The emission measure of the LHB is higher towards high latitudes in both hemispheres. It entails that the LHB is more extended towards high latitudes, assuming a constant electron density. The emission measure is also spatially anti-correlated with the local dust column density, consistent with the displacement model put forth by Sanders et al. (1977). We produced a 3D model of the LHB in the western Galactic hemisphere.
- We found two tunnels with a low local column density that appear to be filled by hot plasma. One is the well-known β CMa tunnel, and the other is towards (l,b)∼(315°, 25°), in the constellation Centaurus. This hints at the possibility of a widespread tunnel network connecting regions filled by the hot phase of the ISM.
- Both a simple and broken power law could fit the cosmic X-ray background well, but with a steeper slope ($\Gamma \simeq 1.6$–1.7 above 1.2 keV) than the conventional value ($\Gamma = 1.45$). Whether this represents a genuine steepening of the CXB slope below ~ 1 keV or is caused by calibration inaccuracies is uncertain. It will likely become clear with a forthcoming new calibration version.

  From this study, it is clear that eROSITA and its all-sky surveys provide a valuable dataset for studying the SXRB. Future papers will follow to discuss other aspects of the SXRB.

3.7 Data availability

The results of the spectral fits can be accessed and visualised as choropleth maps via the website `https://erosita.mpe.mpg.de/dr1/AllSkySurveyData_dr1/DiffuseBkg/` hosted on the eROSITA DR1 server. An interactive version of the 3D model of the LHB (Fig. 3.18) and structures in the solar neighbourhood can also be accessed there, as well as the spherical harmonics models of LHB temperature presented in Sects. 3.5.1 and 3.10. `Xspec` model files are also available through the website for readers interested in particular regions in the western Galactic hemisphere.

3.8 Acknowledgements

MY thanks Mattia Pacicco and Michael Schulreich for their in-depth explanations of their LB simulations during the EAS meeting 2024 in Padova, which has greatly improved the interpretation of the results. MY extends his gratitude to Susanne Friedrich and Harald Baumgartner for their guidance and help in setting up the accompanying website on the eROSITA DR1 server. MY appreciates the helpful discussion on cluster masks and measurement of cluster temperature provided by Ang Liu. MY and MF acknowledge support from the Deutsche Forschungsgemeinschaft through the grant FR 1691/2-1. GP acknowledges funding from the European Research Council (ERC) under the European Union's Horizon 2020 research and innovation programme (grant agreement No 865637). MS acknowledges support from the Deutsche Forschungsgemeinschaft through the grants SA 2131/13-1, SA 2131/14-1, and SA 2131/15-1. This work is based on data from eROSITA, the soft X-ray instrument aboard SRG, a joint Russian-German science mission

supported by the Russian Space Agency (Roskosmos), in the interests of the Russian Academy of Sciences represented by its Space Research Institute (IKI), and the Deutsches Zentrum für Luft- und Raumfahrt (DLR). The SRG spacecraft was built by Lavochkin Association (NPOL) and its subcontractors, and is operated by NPOL with support from the Max Planck Institute for Extraterrestrial Physics (MPE).

The development and construction of the eROSITA X-ray instrument was led by MPE, with contributions from the Dr. Karl Remeis Observatory Bamberg & ECAP (FAU Erlangen-Nuernberg), the University of Hamburg Observatory, the Leibniz Institute for Astrophysics Potsdam (AIP), and the Institute for Astronomy and Astrophysics of the University of Tübingen, with the support of DLR and the Max Planck Society. The Argelander Institute for Astronomy of the University of Bonn and the Ludwig Maximilians Universität Munich also participated in the science preparation for eROSITA.

The eROSITA data shown here were processed using the eSASS/NRTA software system developed by the German eROSITA consortium.

MY thanks the developers of the following software and packages that made this work possible: `numpy` (Harris et al., 2020), `matplotlib` (Hunter, 2007), `astropy` (Astropy Collaboration et al., 2013, 2018, 2022), `PyXspec` (Arnaud, 1996), `HEAsoft` (Nasa High Energy Astrophysics Science Archive Research Center (Heasarc), 2014), `FTOOLS` (Blackburn, 1995), `contbin` (Sanders, 2006), `lmfit` (Newville et al., 2016), `emcee` (Foreman-Mackey et al., 2013), `corner.py` (Foreman-Mackey, 2016), `plotly` (Plotly Technologies Inc., 2015), `folium` (Filipe et al., 2021), `K3D-jupyter` (Trzesiok et al., 2022), `OpenCV` (Bradski, 2000) and `scipy` (Virtanen et al., 2020).

3.9 Appendix A: Test for non-equilibrium ionisation

Non-equilibrium ionisation (NEI) can happen in the LHB if there were recent rapid heating or cooling events. Electrons respond quickly to temperature change via collisions, but ionisation and recombination of the ions lag behind (e.g. see a review by Breitschwerdt & de Avillez, 2021). As a result, the line intensities under the assumption of collisional ionisation equilibrium (CIE) do not reflect the real temperature of the gas. If a recent supernova exploded within the LHB, parts or all of LHB could be under-ionised due to rapid shock-heating. On the other hand, if the LHB spawned from a dense cloud, it could undergo rapid adiabatic cooling when it bursts out of the cloud, resulting in an over-ionised plasma (Breitschwerdt & Schmutzler, 1994). Henley et al. (2007) investigated both scenarios using a combination of *XMM-Newton*/EPIC-MOS and ROSAT/PSPC data and concluded the data could not distinguish between CIE and under-ionised plasma but disfavoured the over-ionised scenario.

We used a simple test to evaluate whether our data (eRASS1+ROSAT R12) are sensitive to the signature of NEI. We chose the same regions that were used to determine the spectral shape of the CXB (Fig. 3.6) for this analysis. They have a high S/N (400) in the soft band. This minimises the statistical uncertainty and boosts any potential signatures of NEI. We refitted the spectra by replacing the CIE LHB model (`apec`) with a NEI LHB model (`nei`).

We summarise the fitting results in Table 3.1. Six of the seven regions have the fitted density-weighted ionisation timescale $\tau > 10^{12}\,\mathrm{cm^{-3}\,s}$. At $\tau > 10^{12}\,\mathrm{cm^{-3}\,s}$, Smith & Hughes (2010) showed that 90% of carbon and oxygen ions (which dominate the observed LHB emission) would reach CIE for plasma at $\sim 0.1\,\mathrm{keV}$. The one exception is the region centred at (l, b)=$(241°, 45°)$, which returns $\tau = (5.6^{+0.8}_{-0.7}) \times 10^{11}\,\mathrm{cm^{-3}\,s}$, suggesting a small under-ionisation. Fig. 3.33 compares the CIE and NEI models in this region. From the residual spectra, one can see the improvement below $\sim 0.5\,\mathrm{keV}$. Nevertheless, because the NEI models of most regions reduce to the CIE case even at a high S/N of 400, we conclude our data can be sufficiently explained by CIE and keep this assumption throughout our analysis in the main text.

Table 3.1: Fitted LHB parameters of the seven high-SN spectra under the NEI and CIE assumptions. All but one region show an ionisation timescale of $\tau > 10^{12}\,\mathrm{cm^{-3}\,s}$, essentially reducing to the CIE case.

		NEI			CIE	
l (°)	b (°)	kT_{LHB} (keV)	τ_{LHB} ($10^{12}\,\mathrm{cm^{-3}\,s}$)	$\mathrm{EM_{LHB}}$ ($10^{-3}\,\mathrm{cm^{-6}\,pc}$)	kT_{LHB} (keV)	$\mathrm{EM_{LHB}}$ ($10^{-3}\,\mathrm{cm^{-6}\,pc}$)
228	−72	0.120 ± 0.002	25^{+16}_{-17}	$3.41^{+0.14}_{-0.13}$	0.115 ± 0.002	$3.09^{+0.15}_{-0.14}$
202	−61	$0.114^{+0.003}_{-0.002}$	30^{+13}_{-19}	$3.11^{+0.12}_{-0.16}$	$0.112^{+0.002}_{-0.003}$	$2.84^{+0.13}_{-0.12}$
229	−48	0.119 ± 0.003	26 ± 15	$4.34^{+0.27}_{-0.37}$	0.121 ± 0.002	$4.05^{+0.27}_{-0.18}$
205	39	0.103 ± 0.002	23^{+19}_{-17}	$3.48^{+0.14}_{-0.13}$	0.098 ± 0.002	$3.19^{+0.14}_{-0.17}$
241	45	0.116 ± 0.003	$0.55^{+0.08}_{-0.07}$	$3.12^{+0.12}_{-0.11}$	$0.097^{+0.003}_{-0.002}$	$2.96^{+0.18}_{-0.17}$
208	66	0.104 ± 0.002	25 ± 16	$5.63^{+0.19}_{-0.21}$	0.098 ± 0.002	$5.41^{+0.26}_{-0.25}$
258	67	$0.104^{+0.003}_{-0.002}$	17^{+22}_{-16}	$4.72^{+0.18}_{-0.17}$	0.097 ± 0.002	$4.43^{+0.21}_{-0.20}$

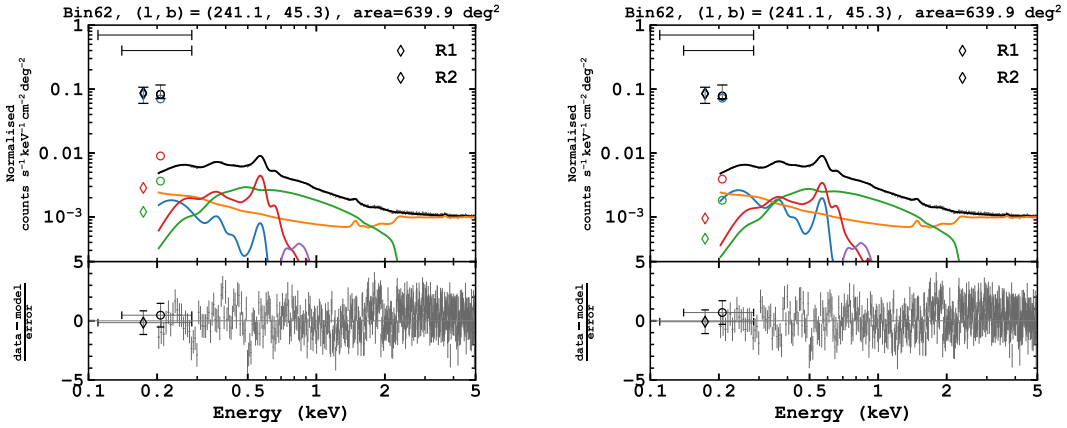

Figure 3.33: Comparison of spectral fits assuming the LHB in CIE (*left*) and NEI (*right*) of the region showing a potential NEI signature. The residual highlights the improvement below 0.5 keV.

3.10 Appendix B: Posterior distributions of the dipole and $l_{\mathrm{max}} = 6$ models of local hot bubble temperature

The best-fit parameters of the dipole model in Fig. 3.14 are presented in Table 3.2. The z-axis points towards the Galactic north pole in our convention, and the x-axis points towards the Galactic centre. Two equivalent representations are presented: the complex a_{lm} coefficients and the dipole vector. In the complex representation, each multipole gives $2l+1$ free parameters; Each $a_{l|m|}$ contributes to two, one for the real part and one for the imaginary part, except from a_{l0} coefficients, which do not have a complex part for real-valued functions.

For the dipole, it can be shown that a_{10} and a_{11} are related to the dipole vector by the following equations:

$$\begin{cases} A_1 = a_{10}\sqrt{\dfrac{3}{4\pi}}\cos\theta_{\mathrm{max}} - 2\sqrt{\dfrac{3}{8\pi}}\sin\theta_{\mathrm{max}} f, & (3.17) \\ \tan\theta_{\mathrm{max}} = -\dfrac{\sqrt{2}}{a_{10}} f & (3.18) \\ \tan\phi_{\mathrm{max}} = -\dfrac{\mathrm{Im}\{a_{11}\}}{\mathrm{Re}\{a_{11}\}}, & (3.19) \end{cases}$$

where $f = \mathrm{Re}\{a_{11}\}\cos\phi_{\mathrm{max}} - \mathrm{Im}\{a_{11}\}\sin\phi_{\mathrm{max}}$, A is the amplitude of the dipole and (θ_{max}, ϕ_{max};

Table 3.2: Best-fit parameters of the dipole ($l_{\max} = 1$) model of $kT_{\rm LHB}$. The resulting temperature model is in units of keV.

Complex	
a_{00}	0.368 ± 0.002
a_{10}	-0.027 ± 0.001
$\mathrm{Re}\{a_{11}\}^{(i)}$	0.014 ± 0.001
$\mathrm{Im}\{a_{11}\}^{(i)}$	-0.036 ± 0.002
Dipole vector	
${A_0}^{(ii)}$	0.104 ± 0.001
${A_1}^{(ii)}$	0.030 ± 0.001
$\phi_{\max}$	$291\overset{\circ}{.}1 \pm 1\overset{\circ}{.}8$
$\theta_{\max}$	$116\overset{\circ}{.}5^{+1\overset{\circ}{.}5}_{-1\overset{\circ}{.}6}$

Notes.
(i) $\mathrm{Re}\{a\}$ and $\mathrm{Im}\{a\}$ refer to the real and imaginary parts of the complex coefficient a.
(ii) A_l has the unit of keV and can be interpreted as the amplitude of the corresponding multipole.

colatitude and azimuth in spherical coordinates) is the direction where this amplitude is obtained.

The posterior distributions of the dipole are shown in Fig. 3.34 both in complex and dipole vector representations.

We list the best-fit parameters of the $l_{\max} = 6$ spherical harmonics model (Fig. 3.15) in Table 3.3.

3.11 Appendix C: Latitudinal profiles of local hot bubble temperature

Figure 3.35 shows the $kT_{\rm LHB}$ data in another light by dividing the western Galactic hemisphere into 15°-wide longitudinal stripes and shows $kT_{\rm LHB}$ as a function of latitude. This presentation has the advantage of enabling visual inspection of the uncertainty associated with individual contour bins and their comparison with the large-scale gradient. Lines of the monopole (orange), dipole (red) and $l_{\max} = 6$ (blue) models are overlaid in addition. With the help of the best-fit monopole model line, it is apparent that $kT_{\rm LHB}$ is higher in the southern hemisphere than in the north. The dipole model can capture the primary latitudinal gradient, especially in the south, but fails to follow the data closely above $b > 30°$. While the model complexity can increase to accommodate the temperature variation on a smaller scale, we note the presence of a temperature gradient in LHB is clear. The scatter is large in the region ($270° \lesssim l \lesssim 300°$,$-40° \lesssim b \lesssim -10°$), which partially covers the Large Magellanic Cloud but cannot be fully attributed to it. The relatively large scatter below $10° < b < 30°$ and $l > 300°$ is caused by the lower $\mathrm{EM}_{\rm LHB}$ in this direction, resulting in higher uncertainties in the determination of $kT_{\rm LHB}$.

3.12 Appendix D: Local hot bubble temperature dichotomy seen from high S/N spectra

Section 3.5.1 demonstrated the north-south dichotomy of the LHB temperature, mainly by the systematic temperature offset between the hemispheres. However, this offset is difficult to appreciate purely by looking at individual spectra of S/N $\simeq$ 80 because the temperature difference of 0.02 keV is only approximately twice the typical fitting uncertainty, as shown in Fig. 3.9.

To highlight the spectral difference, we took two examples of high-S/N spectra (S/N = 400), one from each hemisphere. Figure 3.36 shows the spectrum in the south. The difference in the left and right panels lies only with the model: the left panel has the $kT_{\rm LHB}$ kept at the northern value,

while all model parameters were allowed to vary in the right panel. Figure 3.37 shows the reverse: showing the northern spectrum and keeping the southern temperature of the LHB in the left panel. The comparisons demonstrate the incompatibility of the spectrum from either hemisphere with the LHB temperature measured from the opposite hemisphere. This lends further support for a real LHB temperature dichotomy in the hemispheres.

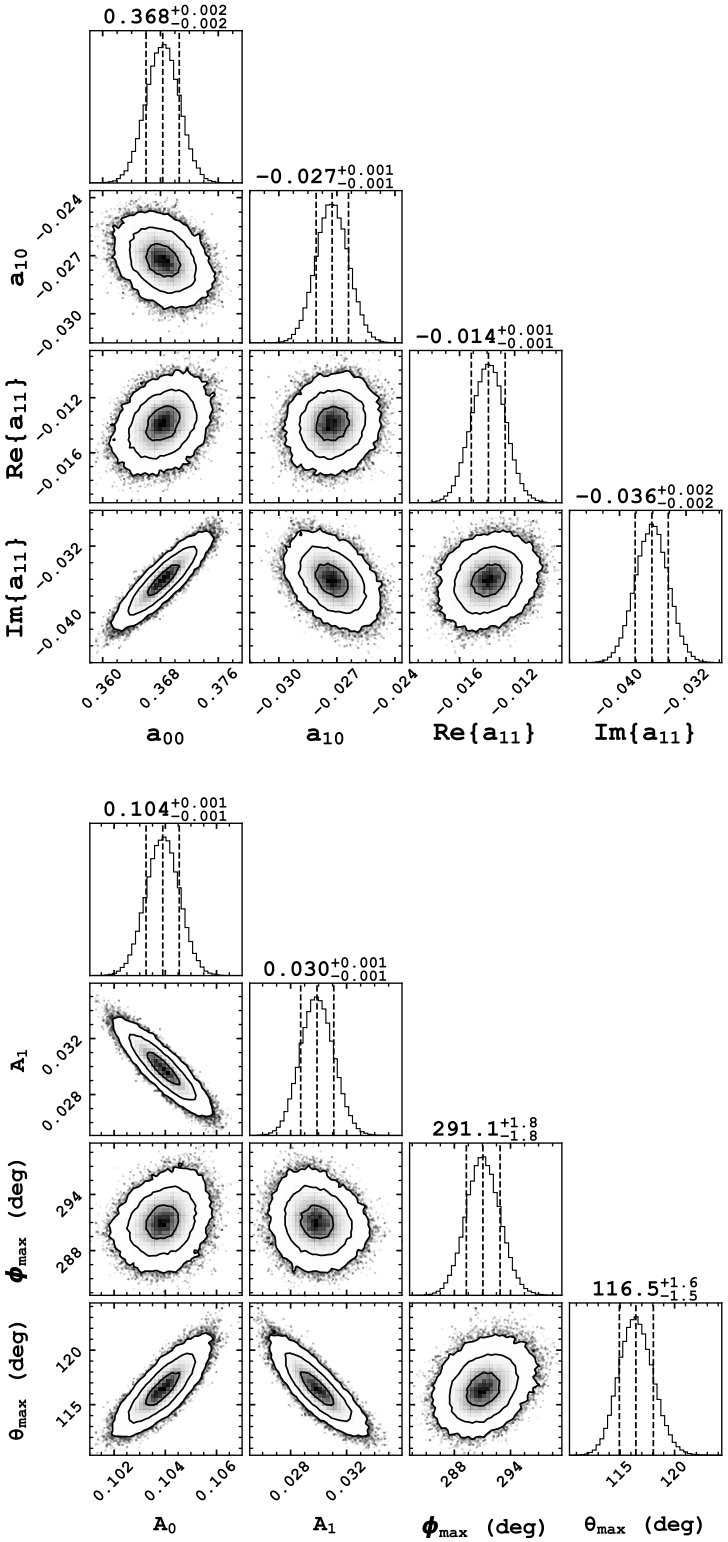

Figure 3.34: Posterior distributions of the dipole ($l_{\max} = 1$) model in complex (*top*) and multipole vector (*bottom*) representations. The contours show the 1, 2, and 3 σ uncertainties.

Table 3.3: Best-fit parameters of the $l_{\max} = 6$ model of $kT_{\rm LHB}$. The resulting temperature model is in units of keV.

Coefficient	Value
a_{00}	6.165 ± 8.591
a_{10}	-2.583 ± 0.730
$\mathrm{Re}\{a_{11}\}$	-1.425 ± 0.983
$\mathrm{Im}\{a_{11}\}$	5.622 ± 8.654
a_{20}	-3.707 ± 5.337
$\mathrm{Re}\{a_{21}\}$	-0.452 ± 0.112
$\mathrm{Im}\{a_{21}\}$	-2.798 ± 0.785
$\mathrm{Re}\{a_{22}\}$	-3.858 ± 6.466
$\mathrm{Im}\{a_{22}\}$	-2.161 ± 1.484
a_{30}	2.327 ± 0.624
$\mathrm{Re}\{a_{31}\}$	0.556 ± 0.346
$\mathrm{Im}\{a_{31}\}$	-1.990 ± 2.931
$\mathrm{Re}\{a_{32}\}$	2.067 ± 0.566
$\mathrm{Im}\{a_{32}\}$	-0.690 ± 0.165
$\mathrm{Re}\{a_{33}\}$	1.952 ± 1.294
$\mathrm{Im}\{a_{33}\}$	-1.798 ± 3.709
a_{40}	0.884 ± 1.186
$\mathrm{Re}\{a_{41}\}$	0.213 ± 0.051
$\mathrm{Im}\{a_{41}\}$	1.300 ± 0.332
$\mathrm{Re}\{a_{42}\}$	0.775 ± 1.232
$\mathrm{Im}\{a_{42}\}$	0.510 ± 0.299
$\mathrm{Re}\{a_{43}\}$	0.564 ± 0.130
$\mathrm{Im}\{a_{43}\}$	1.099 ± 0.292
$\mathrm{Re}\{a_{44}\}$	0.476 ± 1.594
$\mathrm{Im}\{a_{44}\}$	1.177 ± 0.752
a_{50}	-0.520 ± 0.122
$\mathrm{Re}\{a_{51}\}$	-0.091 ± 0.044
$\mathrm{Im}\{a_{51}\}$	0.242 ± 0.341
$\mathrm{Re}\{a_{52}\}$	-0.480 ± 0.116
$\mathrm{Im}\{a_{52}\}$	0.164 ± 0.038
$\mathrm{Re}\{a_{53}\}$	-0.254 ± 0.135
$\mathrm{Im}\{a_{53}\}$	0.178 ± 0.357
$\mathrm{Re}\{a_{54}\}$	-0.389 ± 0.103
$\mathrm{Im}\{a_{54}\}$	0.290 ± 0.062
$\mathrm{Re}\{a_{55}\}$	-0.475 ± 0.283
$\mathrm{Im}\{a_{55}\}$	-0.008 ± 0.473
a_{60}	-0.049 ± 0.054
$\mathrm{Re}\{a_{61}\}$	-0.019 ± 0.005
$\mathrm{Im}\{a_{61}\}$	-0.119 ± 0.024
$\mathrm{Re}\{a_{62}\}$	-0.032 ± 0.054
$\mathrm{Im}\{a_{62}\}$	-0.035 ± 0.015
$\mathrm{Re}\{a_{63}\}$	-0.053 ± 0.012
$\mathrm{Im}\{a_{63}\}$	-0.104 ± 0.022
$\mathrm{Re}\{a_{64}\}$	-0.010 ± 0.056
$\mathrm{Im}\{a_{64}\}$	-0.069 ± 0.030
$\mathrm{Re}\{a_{65}\}$	-0.079 ± 0.015
$\mathrm{Im}\{a_{65}\}$	-0.082 ± 0.021
$\mathrm{Re}\{a_{66}\}$	0.040 ± 0.078
$\mathrm{Im}\{a_{66}\}$	-0.098 ± 0.057

Notes.
$\mathrm{Re}\{a_{lm}\}$ and $\mathrm{Im}\{a_{lm}\}$ refer to the real and imaginary parts of the complex coefficient a_{lm}.

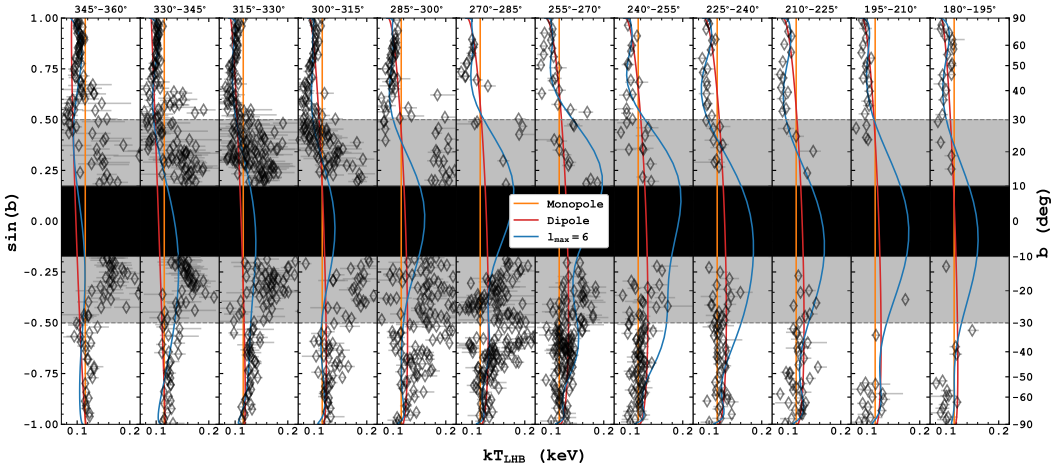

Figure 3.35: Latitudinal profiles of $kT_{\rm LHB}$ with their $1\,\sigma$ error bars in all longitudinal stripes of 15° width in the western Galactic hemisphere. The vertical orange, red and blue lines show the corresponding monopole, dipole and $l_{\rm max} = 6$ models, respectively. The black region indicates the Galactic plane region, which we masked for the temperature gradient analysis. Regions plotted on the white background indicate where the dipole model was fitted ($|b| > 30^\circ$). The $l_{\rm max}$ model was fitted with the inclusion of data from the shaded region ($|b| > 10^\circ$).

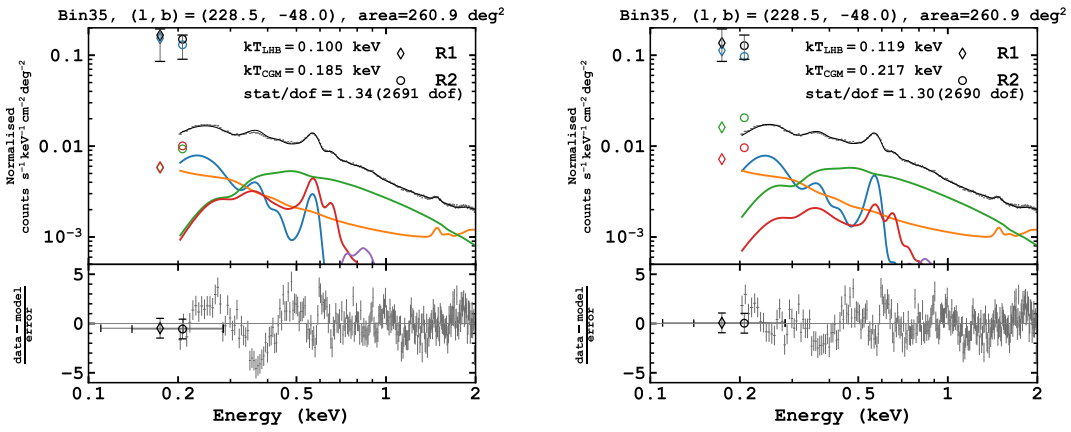

Figure 3.36: North-south temperature dichotomy shown by a high S/N spectra in the south. *Left:* Spectrum in the southern hemisphere fitted while keeping $kT_{\rm LHB}$ fixed at the northern value ($kT_{\rm LHB} = 0.10\,$keV). *Right:* Same as on the left but all the parameters were allowed to vary while fitting.

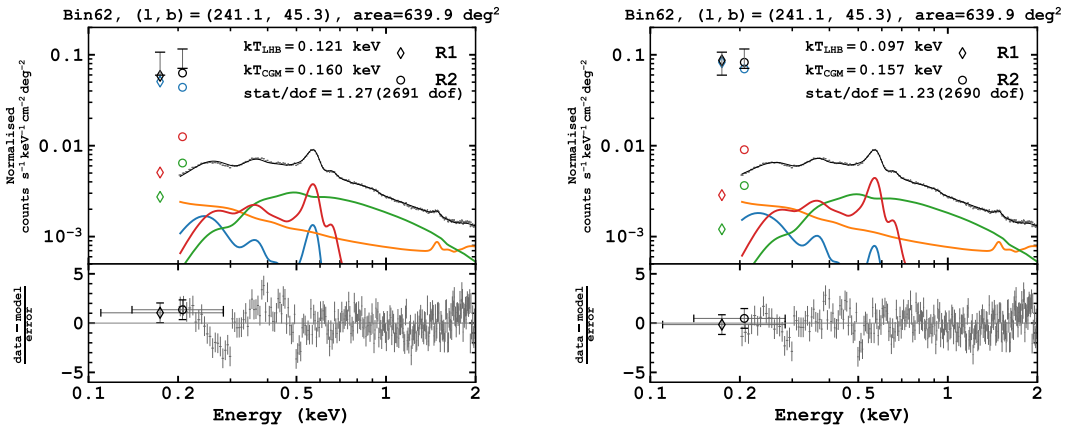

Figure 3.37: Similar to Fig. 3.36, but showing a high S/N spectra in the north. *Left:* Spectrum in the northern hemisphere fitted while keeping $kT_{\rm LHB}$ fixed at the southern value ($kT_{\rm LHB}$ = 0.12 keV). *Right:* Same as on the left, but all the parameters were allowed to vary while fitting.

Chapter 4

eROSITA bubbles

This chapter is based on the article titled 'The SRG/eROSITA diffuse soft X-ray background II. morphology and spectra of the eROSITA bubbles', to be submitted to Astronomy & Astrophysics.

4.1 Abstract

Context. The eROSITA bubbles (eRObub) were discovered in 2020 in the first eROSITA All-Sky Survey (eRASS1), and are among the most extended structures visible in the X-ray sky.
Aims. Using eROSITA all-sky emission maps and spatially resolved spectra, we aim to infer the three-dimensional structure and measure the hot gas properties of the eRObub.
Methods. We fit the morphology with a parametrised geometrical model describing a blast wave propagating in an idealised Galactic halo from the centre. In the spectral analysis, we fit spectra binned to constant S/N and higher S/N spectra from customised regions to examine the gas properties in more detail.
Results. Our geometrical model suggests the horizontal size of both eRObub is well-constrained (semi-minor axis $\sim 6\,\mathrm{kpc}$), but their vertical extent is uncertain, as the observed X-ray emission is almost insensitive to the existence and location of a bubble cap. Additionally, a tilt ($\sim 30^\circ$) towards $l \sim 220^\circ$ is needed to reproduce the silhouette of the northern eRObub, whereas the southern bubble requires little tilt. We spectrally confirm an apparent cool shell at $kT \sim 0.2\,\mathrm{keV}$ surrounding the northern eRObub, likely in collisional ionisation equilibrium. We characterise the plasma in the eRObub interior by two emission components with relatively uniform temperatures: a hotter component at $kT = 0.56^{+0.04}_{-0.02}\,\mathrm{keV}$, and a colder one at $kT = 0.25 \pm 0.03\,\mathrm{keV}$. The emission measure of both components increases towards lower latitudes, with about four times higher values for the colder component. Our spectra suggest sub-solar abundances ($Z = 0.2 \pm 0.1\,Z_\odot$), consistent with expectations for the Galactic halo, while we find no conclusive evidence for α-enhancement. In contrast, the NPS exhibits higher abundances ($Z > 0.5\,Z_\odot$), which, at face value, disfavours a common origin. We found no noticeable difference in X-ray emission in regions overlapping with the Fermi bubbles.

4.2 Introduction

One of the most impactful early discoveries of the *SRG*/eROSITA telescope (Merloni et al., 2012; Predehl et al., 2021; Sunyaev et al., 2021) was that of the two giant X-ray emitting shells visible in its all-sky map, subsequently dubbed the eROSITA bubbles (eRObub) (Predehl et al., 2020). These structures appear to be approximately symmetric about the Galactic centre (GC), with each bubble extending over around $80^\circ \times 80^\circ$ in the sky, and emitting most prominently at energies in the range 0.6–1.0 keV (Predehl et al., 2020). The eRObub bear strong similarity to structures seen at other wavelengths. Most prominently, this includes the Fermi bubbles (FB), nonthermally

emitting symmetric γ-ray structures visible around 1 GeV (Su et al., 2010; Ackermann et al., 2014), extending over $55^\circ \times 45^\circ$, located 'inside' the eRObub in projection. Furthermore, polarised radio and microwave emissions are visible coincident with the North Polar Spur (NPS) (Hanbury Brown et al., 1960; Egger & Aschenbach, 1995; Crocker et al., 2015), an X-ray bright arc which appears to mark the whole eastern edge and extend to the north-western side of the eRObub.

The morphology of the eRObub suggests a vertical extent on scales comparable to the entire Galaxy, assuming their symmetry about the GC, which indicates an energy budget $\sim 10^{56}$ erg necessary for their inflation (Kataoka et al., 2018; Predehl et al., 2020). The necessary power ($P \sim 10^{41}$–$10^{43}\,\mathrm{erg\,s^{-1}}$) is typically assumed to have been generated by one of two possible sources: first, a short-term ($\sim 10^5$ yr) outburst or jet activity of the GC black hole close to its Eddington luminosity several 10^6 yr ago may reproduce the observed morphology well (Yang et al., 2022). In this scenario, the jet drove a shock into the Milky Way circumgalactic medium (CGM), heating the swept-up material to X-ray-emitting temperatures, producing a shell akin to the eRObub. The outflow, along with its leptonic cosmic-ray content (Ackermann et al., 2014), is compressed by the reverse shock and separated from the shocked CGM by a contact discontinuity (Predehl et al., 2020). The inverse-Compton emission from the confined outflow is responsible for the gamma-ray bright FB. Alternatively, the bubbles could be fuelled by past nuclear starburst activity in our Galaxy (e.g., Nguyen & Thompson, 2022), which would lead to large energy input from stellar winds and supernovae. Collimation by the pressure of the surrounding medium would produce bi-conical or bubble-like outflows on timescales similar to the former scenario. Scenarios involving energy injections from tidal-disruption events have also been proposed (Cheng et al., 2011; Scheffler et al., 2025).

Even though the bipolar morphology of both eRObub and FB likely indicates a physical extent on Galactic scales, other evidence suggests that the NPS could be located very nearby (~ 100 pc), most recently based on multiwavelength polarisation information (Panopoulou et al., 2021). Even though such a low distance seems to be contradicted by X-ray absorption measurements (Lallement et al., 2016) and by a lack of radio dispersion (Koljonen et al., 2024) toward the NPS, the question regarding the location of the individual features persists. This concerns, in particular, whether all features are intrinsically physically connected or only superimposed along the line of sight. In order to address this question, a measurement of the physical parameters of the hot gas in multiple locations in the eRObub would be crucial to test for their internal consistency.

Much like the matter of the distance, many of the physical properties of the eRObub have only been probed in pencil-beam observations using a variety of instruments and approaches. For instance, the collisionally heated X-ray emitting plasma appears to have a typical temperature of 0.3 keV (Kataoka et al., 2013, 2015; Ursino et al., 2016), even though temperature substructure, non-equilibrium ionisation (NEI), or multiple emitting components may complicate the matter (Yamamoto et al., 2022; Gupta et al., 2023), as is also evidenced by a putative cool shell observed in eROSITA line ratio maps (Zheng et al., 2024b). The metal abundance and α-enrichment in the bubbles could hold the key to distinguishing the origin of the bubbles (Inoue et al., 2015). The hot gas metallicity has often been assumed to be subsolar at $\sim 0.2\,Z_\odot$ (e.g. Kataoka et al., 2015) in the spirit of a shock-heated CGM. However, this contrasts with findings of enhanced relative abundances of neon and magnesium (Ursino et al., 2016; Gupta et al., 2023), which may be interpreted as a signature of a stellar origin of the bubbles. Finally, it is unclear whether there is any discernible X-ray signature of the compressed outflow predicted inside the FB (Yang et al., 2022), apart from a tentative edge detection in ROSAT band ratios (Su et al., 2010).

This work is the second in a series of papers on the diffuse soft X-ray background observed by eROSITA, with the previous work focusing on the properties of the local hot bubble (LHB) (Yeung et al., 2024). The target of this paper is the quantitative study of the physical properties of the eRObub, obtained via the analysis of their X-ray morphology and the spatially resolved spectroscopy of the diffuse X-ray emission in the first all-sky survey of *SRG*/eROSITA (eRASS1). The main questions we study include the three-dimensional geometry giving rise to the observed morphology of the bubbles, the physical mechanisms contributing to the detected X-ray emission, the temperature and density of the emitting material, and the relative abundances of light α-elements and iron. Based on these properties, we quantify the energetics and shock velocities

needed to inflate the bubbles, discuss how the NPS, the FB, and the putative cool shell fit into the global picture of the bubbles in terms of distance and brightness, and test previous findings of non-solar abundance ratios in the context of different scenarios for the bubbles. Our paper is structured as follows: we describe the underlying data in Sect. 4.3, and present our geometric and spectral analyses in Sects. 4.4 and 4.5, respectively. In Sect. 4.6, we discuss our findings in the context of the physical properties of the eRObub, and we summarise our results in Sect. 4.7.

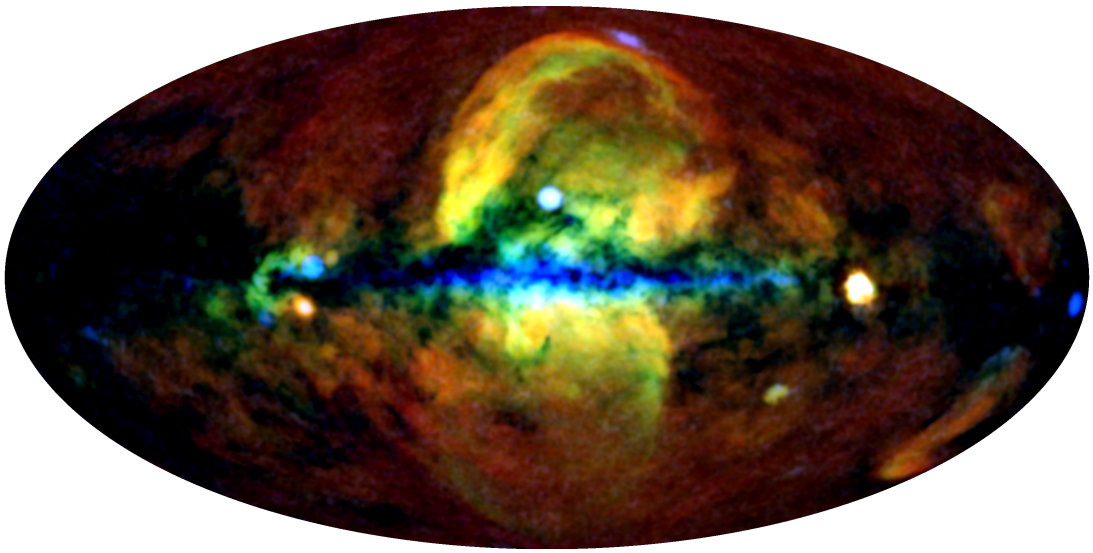

Figure 4.1: Multi-band view of eROSITA bubbles in the 0.3–0.6, 0.6–1.0, 1.0–2.3 keV bands (as in Predehl et al., 2020), after point source removal. The individual bands were smoothed with a Gaussian kernel of 0°.5 and are displayed on a logarithmic scale.

4.3 Data

This section outlines the data products used for the analysis described in this paper. Since our work focuses on morphological and spectral analysis of the X-ray emission of the eRObub, our primary data products are based on the eROSITA All-Sky survey data.

4.3.1 eROSITA Imaging data

In order to gain a full impression of the morphology of the eRObub, including its potential asymmetries, it is necessary to use an all-sky X-ray map reflecting its diffuse X-ray emission. Details on this reconstruction are given in Sect. 4.8. However, briefly, we used the eRASS1 broad-band half-sky maps (Zheng et al., 2024a) to calibrate an all-sky emission map in different energy bands, reconstructed from the eROBub discovery paper (Predehl et al., 2020). The maps in the different energy bands were then cleaned of point-like sources to isolate the diffuse emission component for subsequent analysis, which is displayed in Fig. 4.1. We would like to emphasise that all all-sky maps shown in this work are based entirely on publicly available resources.

4.3.2 Spectroscopic data

This work builds on the methods and results of the half-sky spectral analysis conducted by Yeung et al. (2024), which decomposed the spectra of diffuse X-ray emission across the sky into its individual components, namely emissions from the LHB, CGM, the extragalactic X-ray background (CXB), and the eRObub. For this analysis, the eRASS1 data of the western Galactic hemisphere

were used. In addition, regions around bright compact sources (see Merloni et al., 2024) were excluded from spectral extraction regions. While a deeper data set would be available with multiple cumulative eRASSs, using only the first survey has the advantage of negligible heliospheric charge exchange emission (Ponti et al., 2023b; Yeung et al., 2023), reducing the number of necessary model components. In order to break the temperature degeneracy of the LHB and CGM components, the eRASS1 data were supplemented with photometry derived from the ROSAT all-sky survey (Snowden et al., 1997; Yeung et al., 2024).

4.4 Understanding the bubble morphology

In this Section, we describe our efforts to reproduce the X-ray shape and brightness profile of the eRObub to infer their possible three-dimensional geometry. To achieve this, we construct a physically motivated but analytically describable geometrical model of the emission. Similar work was recently performed by Liu et al. (2024), with the main difference that their work focused exclusively on the bubble borders derived from radio and X-ray data, but not on the emission filling the bubbles.

4.4.1 Morphological model

Geometry

While the general shape of the bubbles can be approximately reproduced with two thick spherical shells symmetric about the Galactic plane (Predehl et al., 2020), such models have shortcomings from a physical point of view: first, using two spherical shells implies two separate centres for the two bubbles, above and below the Galactic plane, respectively. This configuration is likely unrealistic, given that the origin of both bubbles is most likely related and located in the Galactic plane. Second, instead of a constant-density shell with finite thickness, one likely expects a continuous density increase up to the outer radius of the bubbles, if they are truly caused by a shock expanding into the CGM. The situation is similar to what is observed for X-ray bright shells of supernova remnants (SNRs) (e.g., Heiles, 1964; Cox & Anderson, 1982).

The general idea of our model is that of a shell caused by a bipolar point explosion in the GC, which takes the shape of a prolate ellipsoid with semi-major and semi-minor axes a and b, where the larger extent is approximately perpendicular to the Galactic plane. As apparent in the X-ray image (see Fig. 4.20 in Sect. 4.8), the bubbles appear to be slightly tilted with respect to the normal on the Galactic plane, hence we allow for a rotation of the ellipsoid, meaning its semi-major axis direction is given by a polar and an azimuthal angle (θ and ϕ), viewed from the GC. This yields the following expression for the coordinates of an ellipsoidal shell:

$$1 = \left(\frac{x'}{b}\right)^2 + \left(\frac{y'}{b}\right)^2 + \left(\frac{z'}{a}\right)^2 \text{, where} \tag{4.1}$$

$$\begin{pmatrix} x' \\ y' \\ z' \end{pmatrix} = \begin{pmatrix} \cos\theta\cos\phi & \cos\theta\sin\phi & -\sin\theta \\ -\sin\phi & \cos\phi & 0 \\ \sin\theta\cos\phi & \sin\theta\sin\phi & \cos\theta \end{pmatrix} \begin{pmatrix} x \\ y \\ z \end{pmatrix}. \tag{4.2}$$

Here we have used a right-handed Galactocentric reference system, with the origin at the GC and the Sun located at $(x, y, z)_\odot = (-8.18, 0, 0)\,\mathrm{kpc}$ (assuming the Sun lies on the Galactic disk and the geometric distance to Sgr A* taken from GRAVITY Collaboration et al., 2019), and the y-axis increasing toward the east at the GC. The azimuthal angle ϕ of the ellipsoid is defined such that $\phi = 0°$ ($\theta > 0$) corresponds to the northern (southern) bubble tilted away from (toward) the Sun, and $\phi = 90°$ implies a tilt toward the east (west).

Realistically, the assumed shock wave forming the bubble could likely not expand freely, but its expansion was impeded by the surrounding medium, most significantly in the dense Galactic plane. Therefore, we imposed an equatorial narrowing of the bubble, dependent on the height above the Galactic plane. This 'constricted bubble' was parametrized as a z-dependent reduction

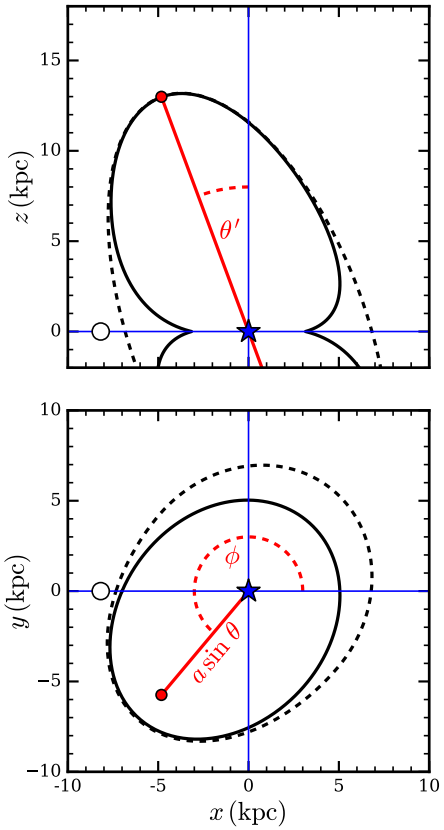

Figure 4.2: Sketch of the geometry of our empirical model of the eROSITA bubbles, with the parameters given in Table 4.1. The top panel shows the side view (from the direction of the positive y-axis) of the northern bubble, with the ellipsoidal shell indicated with the black dashed line, and the constricted ellipsoid with the solid line. The Sun and the GC positions are indicated with a white circle and a blue star, respectively. The red line shows the projection of the ellipsoid major axis, and θ' is the projected tilt angle with $\tan\theta' = \tan\theta\,\cos\phi$. The lower panel shows the corresponding view of the northern bubble silhouette (in the range $z > 0$) from the top, indicating the role of the polar and azimuthal tilt angles θ and ϕ.

of the bubble radius R', with respect to the radius R of the unmodified ellipsoid, with a scale height z_n and a 'waist radius' in the Galactic plane c_n:

$$R'(z) = \left[1 - \frac{b - c_n}{b}\,\exp\left(-\frac{|z|}{z_n}\right)\right] R(z). \tag{4.3}$$

A morphology of two shells centred on the GC naturally emerges, as is visualised in Fig. 4.2. As seen in the eRASS1 all-sky image (Fig. 4.1), the northern eROSITA bubble is tilted toward the west. It also appears to show an increased extent in that direction, as is traced in particular by radio emission (Liu et al., 2024). In contrast, the southern bubble shows little tilt and a smaller horizontal extent. Therefore, separate geometries (i.e., size and orientation) likely have to be used for the northern and southern hemispheres to reproduce the observed bubble shape satisfactorily.

The second ingredient for our model is the assumption of a realistic density profile of the X-ray-bright material within the bubble. Here, we can borrow from simple analytical solutions developed for modelling point explosions (such as SNRs) in the Sedov-Taylor phase (Sedov, 1946; Taylor, 1950). This assumption appears sensible as no strong optical line emission, indicative of radiative cooling, has been observed from the bubbles, thus far. However, a key difference is that for SNRs, an infinitely strong shock can usually be assumed (when $\mathcal{M} \gtrsim 5$), as the shock

velocity strongly exceeds the ambient sound speed ($\approx 15\sqrt{T/10^4\,\mathrm{K}}\,\mathrm{km\,s^{-1}}$), which is far from the truth for the eRObub. Instead, the shock is likely only weakly supersonic (e.g., $\mathcal{M} \approx 1.5$, Predehl et al., 2020), due to the large sound speed in the hot Galactic halo. The Rankine-Hugoniot jump conditions yield the following density increase χ_s behind a nonrelativistic shock:

$$\chi_s := \frac{n_2}{n_1} = \frac{4\mathcal{M}^2}{\mathcal{M}^2 + 3}, \tag{4.4}$$

which implies $\chi_s \sim 1.5 - 2.0$, meaning the gas is compressed much less than in an SNR where $\chi_s = 4$. The analytic solutions by Cox & Anderson (1982) for the density profile of a Sedov-Taylor blast wave allow for the inclusion of χ_s (or equivalently $\mathcal{M}$) as a free parameter, and show that lower Mach number shocks exhibit a much shallower density profile. Ideally, this implies that the apparent thickness of the X-ray bright shell can be used as a tracer of the shock Mach number, motivating our usage of their solutions to model the location-dependent gas density inside the bubbles. For its evaluations, the radius of the narrowed ellipsoidal shell R' measured from the GC was used as the forward shock radius to evaluate the radial density profile $\chi(r/R')$ in each direction (Eq. 16 in Cox & Anderson, 1982). Note that, even if the scenario of a point explosion at the GC does not correspond to the true origin of the bubbles, the main point of our assumption is to 'populate' the geometric shape of the bubbles with a plausible density profile, whose exact shape (i.e. shell thickness) can be regulated by a free parameter, the Mach number.

A further ingredient for our model is that the density of the CGM, with which the shock wave interacts, is not uniform but likely strongly decreasing with Galactocentric radius, meaning that emission at low Galactic latitudes is expected to be strongly brightened. To include this effect, we used the density model combining a spherical halo and a disk component derived by Locatelli et al. (2024b), to estimate the 'ambient' density of the CGM:

$$\begin{aligned} n_1(x,y,z) &= C\,\left(x^2+y^2+z^2+r_0^2\right)^{-3/4} \\ &+ n_0\,\exp\left(-\frac{\sqrt{x^2+y^2}}{\rho_h} - \frac{|z|}{z_h}\right) \end{aligned} \tag{4.5}$$

where $C = 4.6\times10^{-2}\,\mathrm{cm^{-3}\,kpc^{3/2}}$, $n_0 = 3.2\times10^{-2}\,\mathrm{cm^{-3}}$, the disk scale height $z_h = 1.1\,\mathrm{kpc}$ and radius $\rho_h = 6.2\,\mathrm{kpc}$, and the halo core size chosen to be $r_0 = 3\,\mathrm{kpc}$. The blast wave profile $\chi(r)$ along a given direction from the GC can then be multiplied by this value to obtain the post-shock density $n_2 = \chi n_1$. This naturally produces a higher density of emitting material in regions close to the Galactic disk, reproducing the larger brightness observed at low latitudes.

After initial tests of our model, we found a considerable improvement compared to the all-sky image when allowing for a direction-dependent modulation in the density profile of the CGM with which the blast wave interacts. We parametrised this using a quadrupolar relative modulation in density, parametrised as

$$n_2 = \left(1 + (f_\mathrm{quad} - 1)\cos^2\psi\right)\,\chi\,n_1. \tag{4.6}$$

Here, n_1, n_2, and χ are as defined above, and ψ describes the great-circle distance between the direction of a particular position (x,y,z) seen from the GC, and the direction of the quadrupole $(\theta_\mathrm{quad}, \phi_\mathrm{quad})$. This direction and the relative quadrupole amplitude f_quad were included in our fit as free parameters, and including this component in the model allowed us to reproduce much better 'one-sided' morphological features, such as the NPS.

Evaluation and fitting

In order to reproduce the observed X-ray image, we used an image grid corresponding to that of the half-sky maps by Zheng et al. (2024a), rebinned by a factor of two, yielding a pixel size of 6′. Along a given line of sight (l,b), the Galactocentric coordinates of a point at a distance s from the observer are given by:

$$\begin{pmatrix} x \\ y \\ z \end{pmatrix} = \begin{pmatrix} -8.18\,\mathrm{kpc} \\ 0 \\ 0 \end{pmatrix} + s \begin{pmatrix} \cos b\cos l \\ \cos b \sin l \\ \sin b \end{pmatrix}. \tag{4.7}$$

For the line of sight corresponding to each pixel, we numerically determined the points of intersection $s_{\min}$ and $s_{\max}$ with our geometric model of a constricted ellipsoidal shell. The final expression for the emission measure, which directly controls the relative X-ray brightness of the bubbles, is then proportional to the integrated square of the post-shock density along each line of sight:

$$\mathrm{EM} = \int_{s_{\min}}^{s_{\max}} n_2(s)^2 \, \mathrm{d}s. \tag{4.8}$$

In order to quantitatively compare our model to the all-sky data, a few further steps were necessary. First, we related the observed count rate to this model emission measure as $R_i = A_i \Lambda \, \mathrm{EM}_i$. Here, $\Lambda = 284.3 \, \mathrm{ct\,s^{-1}\,deg^{-2}\,cm^6\,pc^{-1}}$ is the expected count rate per emission measure in the 0.6–1.0 keV band, for a 0.3 keV plasma with abundances of $0.2\,Z_\odot$ (see Sect. 4.5.2). The factor A_i is a free parameter, acting as a model normalisation, and can be understood as the squared ratio of true density to model density. Second, to avoid overpredicting the X-ray emission at low Galactic latitudes, we estimated the absorbing column density N_H from the HI4PI map of H I emission (HI4PI Collaboration et al., 2016). Using the Tübingen-Boulder absorption model (Wilms et al., 2000) acting on a 0.3 keV plasma represented by an `apec` model (Smith et al., 2001), we estimated the transparency of this absorbing layer (i.e., the fraction of unabsorbed photons) in the 0.6–1.0 keV band. By multiplying this location-dependent fraction f_A with our model count rate from above, we obtained a proxy for the detected X-ray emission from the eRObub, which can be compared to the observed half-sky map.

We found that background emission from the Galactic plane, cosmic X-ray background, and instrumental background needed to be explicitly included in our model for the fit to be able to trace the actual bubble morphology. Practically, this implied a purely empirical background count rate parametrised as

$$R_B(l,b) = B_U + B_A \, f_A(l,b) \, \exp\left(-\frac{l^2}{2\rho_l^2} - \frac{b^2}{2\rho_b^2}\right), \tag{4.9}$$

where B_U reflects a spatially constant and unabsorbed background, and B_A traces the absorbed emission from the Galactic plane, with a characteristic angular extent ρ_l within the plane, and ρ_b perpendicular to it.[1] The overall model for the count rate can then be written as

$$R(l,b) = R_B(l,b) + \Lambda \begin{cases} A_N \, \mathrm{EM}(l,b|a_N,b_N,\theta_N,\phi_N,\mathcal{M}_N) \text{ for } b \geqslant 0, \\ A_S \, \mathrm{EM}(l,b|a_S,b_S,\theta_S,\phi_S,\mathcal{M}_S) \text{ for } b < 0. \end{cases} \tag{4.10}$$

Finally, we compared our model prediction to the all-sky count rate measurements with the following Gaussian likelihood:

$$\mathcal{L} = -\frac{1}{2} \sum_{l,b} \left\{ \log\left[\sigma^2(l,b) + s^2 R^2(l,b)\right] + \frac{\left[F(l,b) - R(l,b)\right]^2}{\sigma^2(l,b) + s^2 R^2(l,b)} \right\}, \tag{4.11}$$

where F and σ are the measured count rates and their statistical errors, R represents the total model predictions, meaning the combination of bubble and background components, and the sum runs over all pixels in the modelling region (see Sect. 4.9). Finally, s is a free parameter introduced to trace systematic scatter around the model emission. This systematic scatter is necessary since our simplistic model clearly cannot capture the complexity necessary to reproduce the observed 'clumpy' morphology of the bubbles. Therefore, local over- and underpredictions of our model are expected. Given its complicated and high-dimensional character, a statistical sample from this likelihood was drawn using the Markov chain Monte Carlo sampler `emcee` (Foreman-Mackey et al., 2013) to constrain the parameters.

[1] Note that l is defined here to be in the range $[-180°, 180°]$.

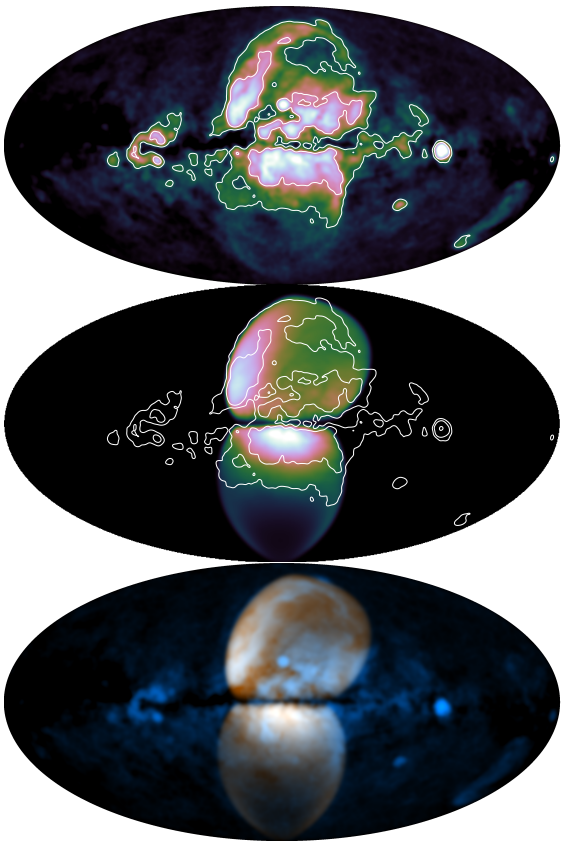

Figure 4.3: Comparison of observed and modelled emission from the eRObub. The top panel shows the observed all-sky diffuse X-ray emission in the 0.6–1.0 keV band, smoothed with a 1° Gaussian kernel. The middle panel shows the predicted X-ray emission from our geometric model of the bubbles (without background components). The overlaid contours trace the observed morphology of the emission. The bottom panel shows an overlay of the two images, with orange reflecting our model, and cyan the observed emission.

4.4.2 Comparison to observed morphology

The best-fit model from our analysis is compared to the smoothed all-sky data in Fig. 4.3, with a more quantitative comparison to the fitted data provided in Fig. 4.21. The corresponding physical parameters are given in Table 4.1, and Fig. 4.22 illustrates degeneracies between the different parameters describing the bubble geometry. Several interesting insights can be gained from inspecting the morphological aspects driving our best-fit model, even though we caution against overinterpreting the quantitative values of our fit parameters, as our model is clearly not sufficiently complex to reproduce the emission from the eRObub fully.

Some of the geometrical parameters describing our best-fit model immediately stand out, such as the contrast between a vertical extent of $a_N = 16.2 \pm 1.5\,\mathrm{kpc}$ in the north (indicated by the red line in Fig. 4.2), and $a_S > 70\,\mathrm{kpc}$ in the south. Our fit prefers such different sizes because of the relatively strong brightness difference at high latitudes, with the northern bubble being significantly brighter than the southern one, which can be reproduced by an origin of the emission in the south at larger distances, meaning in a lower-density environment. In addition, the southern bubble edge appears to reach somewhat larger Galactic latitudes than the north, reaching almost down to $b = -90°$, requiring either a significant tilt in our direction or a considerable vertical extent. The horizontal extent of the two bubbles is constrained comparatively reliably and to quite similar values at semi-minor axes of $b_N = 5.6^{+0.2}_{-0.5}\,\mathrm{kpc}$ and $b_S = 5.7^{+0.3}_{-0.6}\,\mathrm{kpc}$. These values

Table 4.1: Parameters of the bubble model displayed in Figs. 4.3 and 4.21.

Parameter	Value	Parameter	Value
$\log A_N$	$-2.65^{+0.19}_{-0.13}$	z_n	$2.4^{+0.5}_{-1.5}$
$\log a_N$	$1.21^{+0.04}_{-0.04}$	c_n	$3.3^{+0.2}_{-1.6}$
$\log b_N$	$0.748^{+0.017}_{-0.040}$	$\log B_U$	$0.585^{+0.007}_{-0.004}$
θ_N	$27.7^{+2.1}_{-1.7}$	$\log B_A$	$0.934^{+0.028}_{-0.028}$
ϕ_N	221^{+6}_{-5}	ρ_b	$17.4^{+0.5}_{-0.7}$
$\log \mathcal{M}_N$	$0.222^{+0.012}_{-0.011}$	ρ_l	$38.2^{+1.6}_{-1.4}$
$\log A_S$	$-2.31^{+0.15}_{-0.12}$	θ_{quad}	$35.8^{+2.3}_{-1.1}$
$\log a_S$	$1.94^{+0.04}_{-0.07}$	ϕ_{quad}	$355.2^{+1.1}_{-1.2}$
$\log b_S$	$0.75^{+0.02}_{-0.05}$	$\log f_{\mathrm{quad}}$	$0.90^{+0.07}_{-0.11}$
θ_S	7^{+5}_{-2}	s	$0.2431^{+0.0022}_{-0.0023}$
ϕ_S	359^{+4}_{-7}		
$\log \mathcal{M}_S$	$0.55^{+0.22}_{-0.12}$		

Notes.
The value and orientation of the bubble semi-axes for the northern and southern bubbles are described by a, b, θ, and ϕ, whereas the equatorial constriction is parametrised by the scale height z_n (see description in the text).

are somewhat smaller than the spherical shell radius of 7 kpc originally estimated by Predehl et al. (2020). The more recent estimates by Liu et al. (2024) give horizontal radii around 9 kpc for the north, in combination with a strong tilt away from us, and around 6 kpc for the south, in good agreement with our fit. Further, we note that the fitted 'waist' radius of the bubbles $c_n = 3.3^{+0.2}_{-1.6}$ kpc indicates a significant extent of the emitting gas within the Galactic plane. However, this depends on the geometric model used, since extrapolation into a highly absorbed region is required.

Regarding the measured bubble orientation angles θ and ϕ, it appears convincing that the northern bubble is tilted westward (negative y-direction) quite significantly. The tilt is evident in its morphology in the all-sky X-ray image (Fig. 4.3) and might also be traced by counterparts in polarised radio emission (Liu et al., 2024). The quite significant tilt in our direction implied by $(\theta_N, \phi_N) \sim (28^\circ, 220^\circ)$ is connected to a rather compact bubble geometry needing to reach $b \sim +80^\circ$, but dependent on our assumptions for the radial emission profile. On the other hand, the southern bubble appears rather weakly tilted, especially in the east-west direction, at $\theta_S \lesssim 10^\circ$, $\phi_S \sim 0^\circ$. Hence, it seems likely that the two bubbles exhibit different physical sizes and their semi-major axes are not co-aligned. This finding may, however, not be surprising, even in the case of shells driven by outbursts in the GC: the simulations by Pillepich et al. (2021) show that Milky-Way-like galaxies in cosmological simulations exhibit quite chaotic bubble-like structures that need not be limited to a single bubble pair, and are frequently very asymmetric. Our fit implies that both bubbles are tilted towards the Sun. While this may be a random effect, one would also expect to find this behaviour for a conical geometry, in which the nearby portion of the base of the X-ray emitting gas would dominate the emission, and give rise to shell-like structures in projection only (Bland-Hawthorn & Cohen, 2003).

To further illustrate the above points, we demonstrate the model degeneracies introduced by projection effects in Fig. 4.4. This figure displays the three-dimensional geometry of our best-fit model, in comparison with two vastly different bubble geometries, with vertical extents ranging between 7 and 100 kpc, and tilt angles up to $\theta = 60^\circ$. Despite their striking intrinsic differences, all models produce apparent bubbles of very similar sizes and shapes to the observed ones, with the main difference lying in the emission profile within the bubble. The main reason for this inability

to constrain the bubbles' true vertical extent and inclination is our location in the Galactic disk, potentially quite close to the edge of the bubbles. Our location prohibits us from obtaining a proper 'side view' as we could for any other edge-on galaxy, and we are dominated by the 'base' of the bubbles close to the Galactic plane. Crucially, the emission attributed to the 'top' of the bubbles is expected to be extremely faint due to the low densities, so the observed X-ray emission depends little on its location, or even the existence of a closed shell (Bland-Hawthorn & Cohen, 2003). Hence, what we observe as a shell in projection depends strongly on the horizontal bubble extent, but very little on its true vertical size. To summarise, the vertical extent and bubble orientation towards/away from us exhibit strong degeneracies, while the horizontal extent, inside and above the Galactic plane, and east/west orientation, drive the observed emission, and can be treated as more reliable.

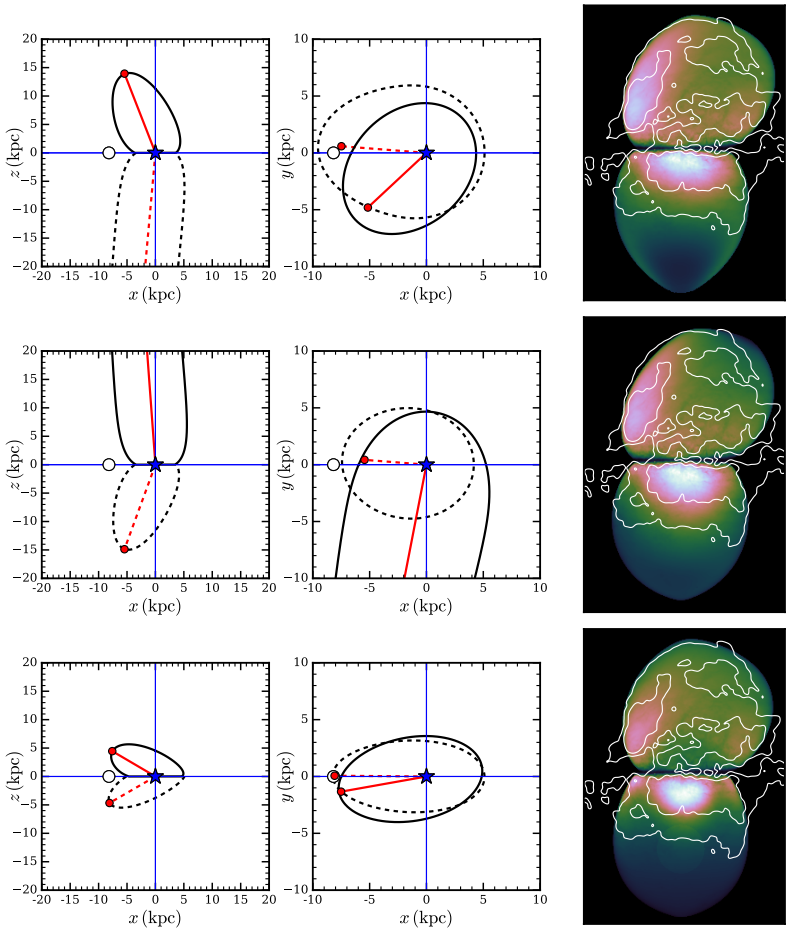

Figure 4.4: Visualisation of the impact of projection effects on the bubble morphology. The left and centre panels show the cross-section of the northern (solid line) and southern (dashed line) bubble shell from the side (along the y-axis), and from the top (z-axis). The right panels show the resulting very similar morphologies. The top row corresponds to our best-fit model (Fig. 4.3), whereas the other two rows show geometrically different models resulting in very similar bubble shapes.

Apart from the geometrical shape, our model also qualitatively reproduces a few of the key features in the emission profiles of the bubbles (See Fig. 4.3). For instance, our model very well reproduces the very X-ray bright region in the latitude range $-20^\circ \leqslant b \leqslant -5^\circ$. Similarly, the northeastern edge of the bubbles is strongly brightened, so it qualitatively reproduces the NPS. Both of these features are likely due to the quadrupolar density enhancement in the direction

$(\theta_{\rm quad}, \phi_{\rm quad}) \approx (36^\circ, 355^\circ)$ allowed by our model. Hence, the prominent X-ray morphology of the NPS alone is not necessarily an argument for a physical separation of the NPS from the bubbles, as density inhomogeneities in the CGM could provide a viable alternative scenario. Similarly, we note a subtle difference in the amplitude scaling factors of the two bubbles, with best-fit values of $A_S/A_N = 2.2 \pm 0.2$, implying that the southern bubble emits more flux per *model* emission measure (Eq. 4.8) than the northern bubble. If true, this may indicate intrinsically higher CGM densities in the south, by around 50%, which one could attribute to material released during past tidal interactions between the Milky Way and the Magellanic Clouds (e.g., Besla et al., 2010; Lucchini et al., 2021).

Finally, our fit produces a significantly higher typical Mach number $\mathcal{M}$ for the shock in the south than in the north. While these numbers are only valid in the case of a point explosion at a single point in time, this difference can be attributed to the different radial emission profiles in the two directions. A higher Mach number produces a sharper density decline behind the shock, meaning a thinner emitting shell in X-rays. Hence, the thicker appearance of the shell in the north (in particular at the NPS) likely drives the lower Mach number there, whereas the opposite is true for the southern bubble, which generally appears more limb-brightened.

4.5 Spectral analysis

We divide the spectral analysis into two parts. The first part (Sect. 4.5.1) uses smaller regions (5–10 $\deg^2$), only imposing a constant S/N criterion in extracting spectra. This approach provides a general view of the spectral properties as a function of location. The second part (Sect. 4.5.2) builds upon the first, with much larger regions defined on special areas and background to accumulate the maximum photon statistics. Spectra such as these provide the greatest chance to measure abundances and identify processes beyond or in addition to the simplest thermal emission.

4.5.1 Global fits to constant S/N regions

Our spectral analysis of the eRObub begins with the methodology described in Yeung et al. (2024), where they divide the western Galactic hemisphere into constant S/N (~ 80; each region subtends $\sim$ 5–10 $\deg^2$ in sky area) bins and fit the spectra by a spectral template consisting of the LHB, CGM, CXB and galactic corona (COR) components. In particular, within the eRObub region, they impose an additional collisional ionisation equilibrium (CIE) component describing the emission from the eRObub. The boundary of the bubbles is chosen such that the change in surface brightness of the 0.2–0.6 keV band is the steepest, outside of which the surface brightness falls back to the background level. We show only regions within the boundary. ROSAT R1 and R2 band fluxes are included in the fitting, further constraining the LHB and CGM emissions. The other spectral components receive Gaussian priors based on the fitting results outside the eRObub of similar Galactic latitudes. We show an example of such a spectrum and its best-fit model in Fig. 4.5.

The elemental abundance of the eRObub is fixed to the solar photospheric values reported in Lodders (2003). The temperature and emission measure (EM) of the eRObub is mainly constrained by the O VIII, Fe XVII and Ne IX,X emission lines. We show the temperature and EM spatial distributions of the eRObub component in Fig. 4.6.

The temperature is largely uniform within the eRObub, at $\sim$0.3 keV, except for the cool shell outlined by the dashed polygons in Fig. 4.6. Ignoring cases reaching the maximum allowed by the colour bar (0.4 keV) for now, most regions span only a narrow range of temperature around 0.3 keV, in contrast to the clear increasing trend in the EM towards the Galactic disk. A closer look at the two parameters as a function of latitudes in Fig. 4.7 reveals a slight gradient in the temperature from $\sim$ 0.25 keV at high latitudes, to $\sim$ 0.3 keV towards the disk. The EM profile shows an order-of-magnitude increase from high to low latitudes, with the NPS producing a prominent enhancement at $60^\circ \lesssim b \lesssim 80^\circ$. The FB regions generally exhibit a higher EM in the northern bubble compared

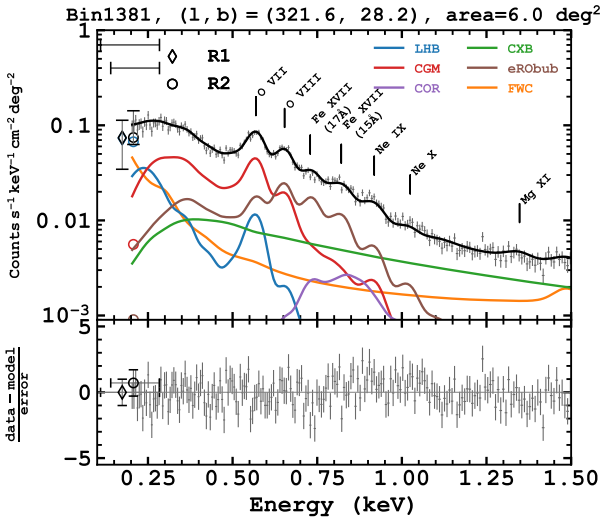

Figure 4.5: Example spectrum within the eROSITA bubbles. The spectrum's most prominent emission lines and contributing components are labelled. The two horizontal error bars at the top left corner indicate the bandwidths of the ROSAT R1 and R2 bands.

to those outside, but their decay slope with latitudes is entirely consistent with each other. The slight difference in EM in the FB is not seen in the southern bubble.

The bulk of the eRObub emission has a temperature consistent with the values reported in Kataoka et al. (2013, 2015), who studied a collection of *Suzaku* and *Swift* pointings across the FB, despite emissions from the CGM and eRObub being modelled by a single CIE component in their work. We demonstrate that the presence of a ~ 0.3 keV plasma is not limited only to the FB (dotted regions in Fig. 4.6) but is a general observation of the eRObub. The simplest explanation of such a temperature jump is the presence of a weak shock, following the Rankine-Hugoniot jump conditions (Kataoka et al., 2013). This general observation is the primary motivation of our geometrical model in Sect. 4.4. On the other hand, our measurement of a higher temperature within the eRObub compared to the CGM is in contrast to the recent report by Gupta et al. (2023), who claim the eRObub are characterised by denser, but not hotter gas, relative to the CGM ($\sim$ 0.15–0.2 keV) by analysing archival *Suzaku* data.

We inspected the regions apparently pinned at the highest temperature of 0.4 keV allowed by the colour bar in the left panel of Fig. 4.6. In fact, they are pinned at 0.7 keV, which is the highest allowed temperature in the fitting. In this case, the eRObub component has the same spectral shape as the COR component (CIE model fixed at 0.7 keV, at solar abundance). We interpret this as a marginal detection of the eRObub component in these regions, as the sum of the enhanced CGM and COR EM can already encapsulate the additional emissions without needing an additional component of distinct temperature. A similar situation also applies to the southern eROSITA bubble at high latitudes, where the eRObub component approaches that of the CGM. These regions can also be identified as regions with much less EM than their immediate neighbours due to their degeneracies with CGM and COR. We will show that the eRObub are spectrally detected even at these regions using bigger spectral extraction regions in Sect. 4.5.2.

One intriguing observation on the eRObub is the presence of an apparent cooler shell at $\sim$0.2 keV about $\sim 10^\circ$ in projected thickness surrounding the northern eRObub throughout the edge, apparently enclosing hotter plasma of 0.3 keV in the interior. The cool shell extends from the top of the northern bubble to $b \sim -40^\circ$ in the southern bubble along the edge. The precise location of this jump could be better traced by the O VIII/O VII ratio map presented in Zheng et al. (2024b). The change in temperature in this shell is not clearly accompanied by a change in

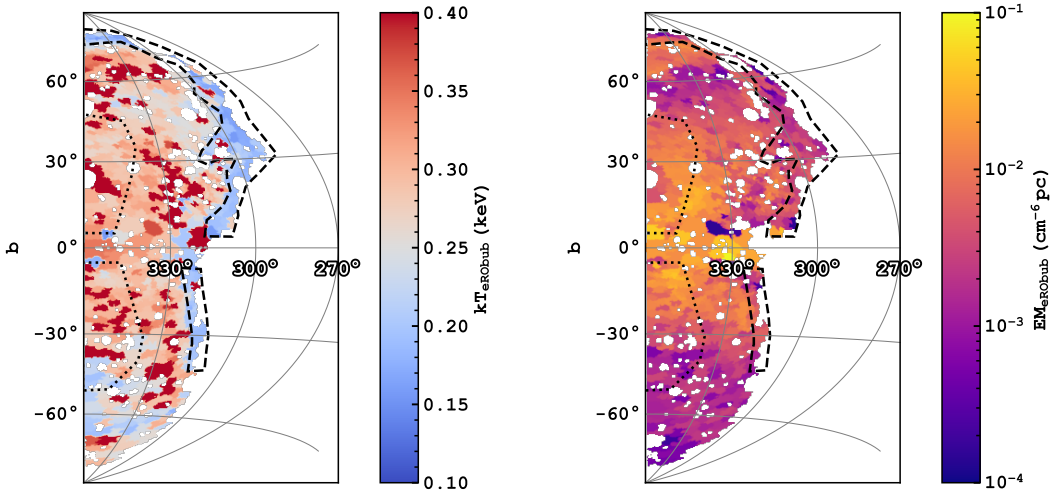

Figure 4.6: Temperature (*left*) and emission measure profile (*right*) of the eROSITA bubbles under the Solar abundance assumption. Dashed lines indicate the region of the cool shell, and the dotted lines demarcate the FB as defined in Ackermann et al. (2014).

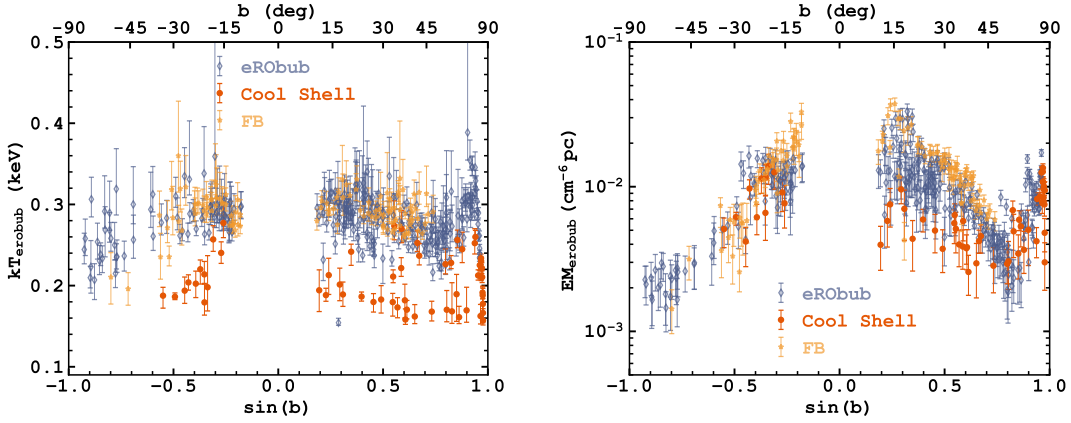

Figure 4.7: Latitudinal profiles of kT_{eRObub} (*left*) and $\mathrm{EM}_{\mathrm{eRObub}}$ (*right*) within the eROSITA bubbles (eRObub) using the constant S/N regions. The spectral bins are divided into three groups: eRObub spectra outside (blue) and inside (yellow) of the Fermi bubbles, and within the cool shell (orange). The boundaries of the Fermi bubbles and the cool shell are shown respectively by the dotted and dashed polygons in Fig. 4.6. Spectral bins within $\pm 10^{\circ}$ from the Galactic plane or having eRObub temperature pinned at 0.7 keV, or bins that have large uncertainties (σ_{kT}/kT or $\sigma_{\mathrm{EM}}/\mathrm{EM} > 0.4$), are ignored. At the North Polar Spur (NPS; $60^{\circ} \lesssim b \lesssim 80^{\circ}$), the temperature decreases from low ($kT \sim 0.3$ keV) to high latitudes ($kT \sim 0.15$ keV), while the EM remains fairly constant throughout. We note that our demarcation of the cool shell cuts through the NPS.

EM from the interior. The left panel of Fig. 4.7 highlights the temperature dichotomy where the regions within the cool shell consistently show a temperature $\lesssim 0.2\,\mathrm{keV}$. While still significant, the cool shell in the north seems to exhibit a slightly lower EM than that of the bubble interior at $b \lesssim 45^\circ$, by approximately a factor of 2. On the other hand, the EM in the southern cool shell is entirely consistent with that in the southern bubble.

The presence of the cool shell makes the choice of the eRObub boundary ambiguous — one can define different boundaries following either the temperature or the EM. This ambiguity is a point already made on the NPS by Churazov et al. (2024) in the eastern Galactic hemisphere. Indeed, the extension of the NPS into the western Galactic hemisphere also shows a gradient in temperature despite the similar EM, with the inner edge being slightly hotter (Figs. 4.6 and 4.7).

4.5.2 Spectra from large regions

Our spectral analysis initially began with small regions ($\sim$ 5–10 deg^2) defined in Yeung et al. (2024), using a constant S/N criterion in the 0.2–0.6 keV band. However, it soon became apparent that within each small region, the S/N ($\sim$ 80) was sometimes insufficient to break the degeneracy between temperatures of the CGM, eRObub and COR, their EMs and the elemental abundance of the eRObub. The degeneracy led to non-negligible fluctuations in the eRObub parameters even in closely neighbouring regions. While one could get insights from the parameters in a statistical way, we found this to be unsatisfying. Instead, defining larger, targeted spectral extraction regions could dissect the eRObub into distinct and representative features while providing a higher S/N for spectral fitting at a price that the region definition is somewhat subjective. We also note here that while using all data from all five eRASSs would increase the S/N, the solar wind charge exchange emission has been shown to increase monotonically with solar cycle and cannot be ignored in later eRASSs, unlike in eRASS1 (Ponti et al., 2023b; Yeung et al., 2023). A more robust spectral fitting setup considering the time domain is needed to extract reliable information from the spectra, which we leave to future work.

Extraction regions

Figure 4.8 presents our large extraction regions in relation to the eRASS1 0.6–1.0 keV surface brightness map (Zheng et al., 2024a). We defined the extraction regions, which can be divided into four groups: background, cool shell, eRObub interior and FB. An important point is to assign each 'source' spectrum a background region within the same latitude range. This helped obtain good fits, probably because the soft X-ray background (SXRB) has a larger gradient along the latitudes than the longitudes. Regions (reg) 0, 4, 8, 12, 16, 18, 22, 26, 29 are background regions that should represent the general background level at each latitude range. Reg 3, 7, 21, 25, 28 and 32 capture much of the cool shell, drawn primarily following the cool shell contour in Fig. 4.6 and O VIII/O VII line-ratio map in Zheng et al. (2024b). Reg 2 covers the remaining part of the NPS, which is bright and shows a higher line ratio than the cool shell. Reg 5, 9, 19, 23, 28 and 30 are the FB regions within the outline specified in Ackermann et al. (2014). The remaining regions are within the eRObub interior. All the regions were confined to a specific latitudinal range, such that within each latitude interval, it is possible to obtain a comparison of the four spectral groups.

We extracted the spectra from these regions in a very similar way to the smaller regions (Sect. 4.5.1) described in Yeung et al. (2024). One point to reiterate here is that sources in the eRASS1 source catalogue (Merloni et al., 2024) with fluxes $F_{0.5-2.0\,\mathrm{keV}} > 10^{-12}\,\mathrm{erg\,s^{-1}\,cm^{-2}}$ were masked to ensure an almost uniform CXB slope and normalisation in all regions. This threshold modifies the CXB photon index to 1.7, tested in a large fraction of the western Galactic hemisphere away from the Galactic plane. We also used the latest `c030` eSASS pipeline configuration, which had multiple improvements compared to the previous `c020` configuration, including correction for the $\sim$ 5% 'missing flux' problem. (Merloni et al., 2024).

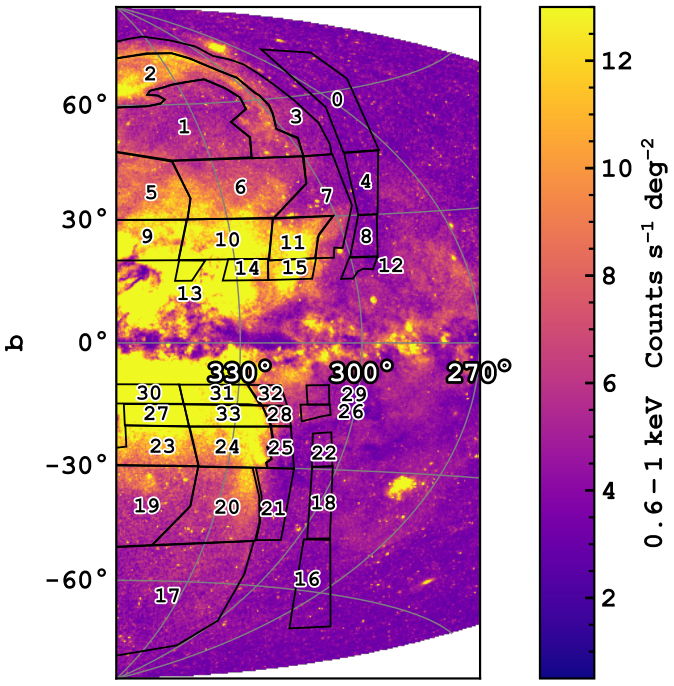

Figure 4.8: eRASS1 surface brightness map in the 0.6–1.0 keV band, overlaid with the outlines and numbering of our large spectral extraction regions. Reg 0, 4, 8, 12, 16, 18, 22, 26 and 29 are the background regions.

Evidence of a temperature transition within the Bubbles

The spectra of the eRObub are fairly complex. This complexity can be appreciated even without any spectral fitting, but by overlaying spectra of large regions within the bubbles. The overlays are shown separately for selected regions within the northern and southern eRObub in Fig. 4.9, folded with the response in surface brightness units. The dominant emission lines are labelled. Much of the difference in the spectral shape redwards of ~ 0.5 keV is mainly driven by the difference in foreground absorption. Qualitatively, the eRObub regions (including the NPS and the FB) are enhanced in Fe XVII, Ne IX and Ne X lines compared to the background regions. These lines alone are strong evidence of a temperature jump in the eRObub compared to the background. The O VIII Lyα line is also enhanced in most regions within the eRObub. However, it is difficult at this stage to draw any conclusions as the absorption column density also modifies the O VIII/O VII ratio.

We draw attention to the cool shell region in the north (reg 3). Despite its higher EM compared to the background, its Fe and Ne emission lines are weaker than in other regions in a relative sense, suggestive of its cooler temperature. Instead, it shows a similar O VIII/O VII ratio compared to the background (reg 0), potentially indicating a similar temperature as the CGM, keeping in mind that absorption could alter this ratio. In the opposite hemisphere, the cool shell region (reg 25) is much less pronounced when compared to the background (reg 22), only showing a slight enhancement in the 0.6–1.0 keV range, which could easily be the difference from the unresolved stellar contribution or the ISM. We found a stronger cool shell signature at lower latitudes ($-20^\circ \lesssim l \lesssim -15^\circ$; reg 32 versus reg 29, not shown); however, we could not rule out that it is caused by the steep rise expected from the stellar contribution or the ISM towards the Galactic plane.

We did not find evidence of the FB regions having an additional nonthermal component,

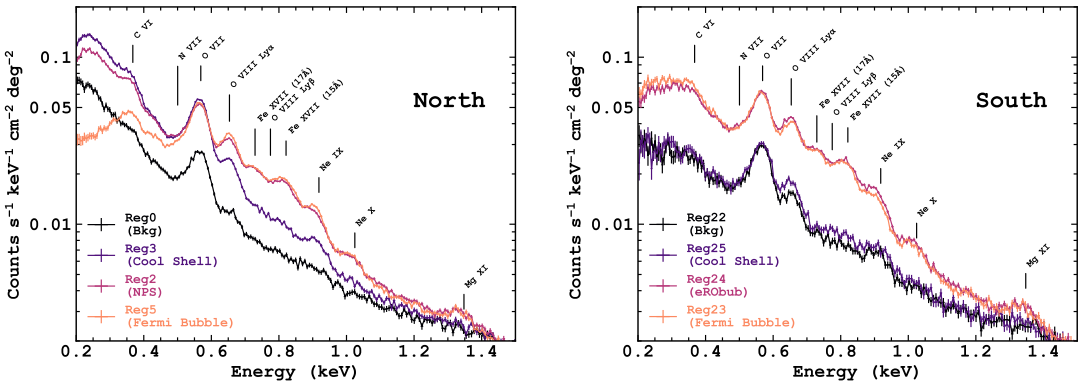

Figure 4.9: Overlay of selected spectra from the northern (*left*) and the southern (*right*) regions. The variations on the redward of the O VII line are mainly driven by differences in foreground absorption.

compared to the rest of the bubbles. This is most obvious when comparing reg 24 (eROsub) and reg 23 (FB) in the south. Their spectra are almost identical, featuring similarly enhanced Fe XVII and Ne XI,X lines. This also applies to the north: the NPS and the FB exhibit similar spectra, even though reg 5 (FB) appears to show stronger Fe and Ne than reg 2 (NPS) in Fig. 4.9. In Fig. 4.10, we show that this line enhancement is well within the variations shown by the regions within the eROsub but outside of the FB. The spectrum of reg 9 (low-b FB) looks significantly different from other spectra away from the Fe XVII and the Ne IX,X lines ($E \lesssim 0.7\,\mathrm{keV}$ and $E \gtrsim 1\,\mathrm{keV}$). The difference in the soft part is caused by a significantly higher N_H, while we found the hard part could be accommodated by a higher eROsub EM in spectral fitting (Sect. 4.5.2, Tables 4.3 and 4.4), without the need for an additional powerlaw component.

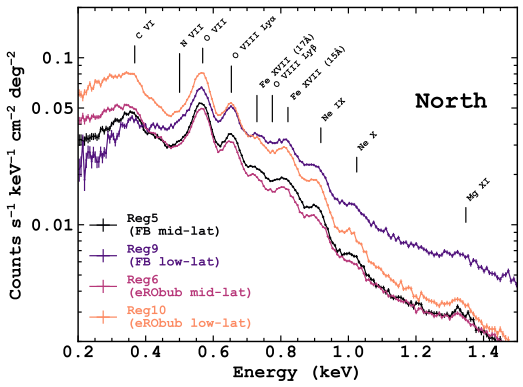

Figure 4.10: Comparison of northern eROSITA and Fermi bubble spectra, separated by two Galactic latitude ranges. Reg 9 is more absorbed and has higher eROsub EM than the other three regions (Tables 4.3 and 4.4). Hence, its spectral shape only resembles the other three near the Fe XVII and Ne IX,X lines.

Preparation for spectral fitting

The error bars in the spectra from the large regions are extremely small, as shown in Fig. 4.9, thanks to the excellent photon statistics we obtained from large sky areas. The better statistics also raise the calibration accuracy we require. In fact, we discovered systematic residuals

around emission lines, hinting at slightly inaccurate energy resolution in the ground-calibrated RMF utilised by the standard pipeline. Therefore, we used an improved response matrix file (RMF) and ancillary response file (ARF) to fit each region, which are calibrated from the SNR 1E 0102-72.3, using the IACHEC model (Plucinsky et al., 2017). A finer input energy grid in the RMF was also needed to properly fold the model spectra into observed space to avoid numerical systematics when discretising a model spectrum from 1024 input energy bins into 1024 observed channels. We found that a factor of four increase in the density of the input energy grid (4096 bins into 1024 observed channels) can effectively eliminate this problem. In practice, we extracted one spectrum, one ARF from each region from the eSASS task `srctool` in the standard `c030` pipeline, then interpolated the extracted ARF into a finer grid, compatible with the new RMF. In addition to a finer energy grid, the improved ARF features improvements on the filter transmission calibration due to possibly more carbon and less aluminium in the optical blocking filters than the specification. This correction was applied together with the interpolation step.

We used `SPEX` version 3.08.1 (Kaastra et al., 1996; de Plaa et al., 2020) to analyse spectra from the large regions. We found `SPEX cie` model in version 3.08.1 seems to reproduce our spectra better than a few versions of `AtomDB/apec` (Smith et al., 2001). We will return to this point in Sect. 4.5.2. The spectra from individual telescope modules (TM) with on-chip filters (TM1, 2, 3, 6 and 6) were summed (abbreviated as TM8) before fitting. All valid patterns (singles, doubles, triples and quadruples) were selected to boost photon statistics. An important aspect when modelling X-ray diffuse emission is the non-X-ray background, which can be isolated by the data taken when the filter wheel was in the `CLOSED` (FWC) position (Freyberg et al., 2021; Yeung et al., 2023). We now use a complete set of FWC data accumulated since eROSITA's launch to create an empirical instrumental background model, and in the `c030` pipeline configuration for self-consistency with the data. The empirical model for the FWC data is created from a known list of fluorescence lines and a continuum described by a 24-order spline. For all regions, the FWC model is fixed in spectral shape, but is allowed to vary in normalisation to fit the 5–9 keV part of the spectrum, where the X-ray background is negligible. The FWC model normalisation factor was then fixed in subsequent analysis.

Like the smaller regions, ROSAT R1 and R2 band fluxes were used in addition to eROSITA data to constrain the models below 0.3 keV.

Background models

We defined a series of background regions sampling the respective latitude ranges of the eRObub regions (see Fig. 4.8). We modelled the emissions from the background regions as the sum of the LHB, CGM, CXB and stellar contribution, where all the components except for the LHB are absorbed by a single or two layers of neutral ISM in solar abundance modelled by the `hot` model in `SPEX`, with temperature fixed at 10^{-3} eV. We began fitting the background regions assuming a single absorption layer, and only switched to a two-layer model if strong residuals persisted below ~ 0.5 keV (in 3 regions at $|b| < 30^{\circ}$). In the two-layer model, the CXB component is absorbed by the full column of Galactic $N_{\rm H}$, while the other absorption component is applied to the CGM and the stellar contribution, and the $N_{\rm H}$ is constrained to be lower than the total Galactic $N_{\rm H}$.

The LHB and CGM components were modelled by the `cie` model, the former with abundance fixed to solar, while the CGM can have variable abundance for C, O, Ne and Fe; other elements heavier than He are coupled with the O abundance. H and He are fixed to solar.

The CXB component was described by a simple power-law model, where the photon index and the normalisation were fixed at 1.7, identical to the smaller, constant S/N regions (Sect. 4.5.1).

Compared to the smaller regions discussed in Sect. 4.5.1, the major change was replacing the COR component with a stellar component. This change is based on the recent report by Ponti et al. (2025), who claim low mass stars with spectral type F to M dominate the emissions from the 0.7 keV COR component. They present a strong correlation between the MW's projected stellar mass profile and the COR component's EM profile. Utilising the strong correlation, they compute the ratio of these two quantities, which can be understood physically as the average X-ray luminosity per solar mass. They show this specific luminosity is consistent with the measurements

from the 10 pc volume-complete sample of low mass stars, hence associating the 0.7 keV component with coronal emissions from low mass stars.

In this work, we assume their interpretation is correct and reverse the process: we took the best-fit model to the stacked X-ray spectrum of the 10 pc low mass star sample (Zheng et al., 2025), assuming this is reasonably representative of the average X-ray emissions from stars in the MW, and scaled this model according to the MW stellar mass model (Hunter et al., 2024) to yield an estimated spectral component from unresolved stars in each large region. Zheng et al. (2025) extract stacked spectra separately for FGK and M stars, and we followed Ponti et al. (2025) to scale the two spectral type groups following the initial mass function by Kirkpatrick et al. (2024) (FGK=47% and M=53% in mass). With this relative mass fraction, we then scaled the combined FGKM stars model ($L_*(E)/M_\odot$; in luminosity per solar mass of FGKM stars) with the 3-dimensional MW stellar mass model ($\rho_{\rm MW}(\vec{r})$), while considering the inverse-square drop-off in flux. More precisely, our model stellar spectrum can be written as

$$F_*(E) = \frac{L_*(E)}{M_\odot} \int \frac{\rho_{\rm MW}(\vec{r})}{4\pi r^2} {\rm d}V \tag{4.12}$$

$$= \frac{L_*(E)}{M_\odot} \int \frac{\rho_{\rm MW}(\vec{r})}{4\pi r^2} r^2 {\rm d}r{\rm d}\Omega \tag{4.13}$$

$$= \frac{L_*(E)\Omega}{M_\odot} \int \frac{\rho_{\rm MW}(\vec{r})}{4\pi} {\rm d}r, \tag{4.14}$$

where Ω is the solid angle of the region. One caveat is that the MW stellar mass model also contains stars with spectral type earlier than F. However, we simplify the situation by computing the integral assuming FGKM stars contribute to all stellar mass. There is no free parameter from the stellar component, as the spectral shape is determined by Zheng et al. (2025) and its normalisation is determined by the MW mass model Hunter et al. (2024).

We show an example spectrum and model of a background region in each hemisphere in Fig. 4.11. The underlying components described above are plotted, with the corresponding model parameters listed in Table 4.2. We obtained excellent fits to all background regions, as shown by their reduced-χ^2 (χ^2/dof) consistently exhibiting values close to 1. Most parameters are within the expectations from the X-ray background spectral analysis in Yeung et al. (2024). The mean LHB and CGM temperatures, $kT_{\rm LHB} = 82 \pm 6$ eV and $kT_{\rm CGM} = 163^{+7}_{-6}$ eV, are slightly lower compared to Yeung et al. (2024), driven by the replacement of the 0.7 keV COR component with the stellar component which has coronal emissions described by multiple CIE temperatures, most notably at ~ 0.3 keV. The CXB normalisation tends to increase gently towards the Galatic plane likely caused by an increased number of sources near the Galactic plane that contribute to the power-law, as the reference value at 1 keV of $3.54^{+0.24}_{-0.17} \times 10^{-3}$ ph s^{-1} cm^{-2} keV^{-1} deg^{-2} is measured from cleaner extragalactic sky at high latitudes $|b| > 30^\circ$ (Yeung et al., 2024).

The best-fit temperatures of the LHB and CGM and elemental abundances of the CGM were taken and fixed to fit the spectra within the eRObub of the same latitude range. This helps to limit the number of free parameters in the fits when the focus is on the eRObub. However, we allow the normalisations (or EM) of the LHB, CGM and CXB to vary during the fits. The only exception to this general procedure was reg 7 and 11, where we found that relaxing the CGM temperature and abundance was the only way to obtain good fits.

Single CIE model and cool shell

We proceeded to fit the regions within the eRObub using an additional CIE component. We found that assuming all metals follow a single ratio to solar abundance is too rigid. After extensive testing, we converged on leaving O, Fe and Ne (also C in one case) abundance free, while other elements heavier than He had abundance coupled to the O abundance. The eRObub CIE component was subjected to the same absorption column density as the CGM and stars components.

We could get reasonable fits to some regions with the single CIE model, most notably for regions located in the cool shell (reg 3, 7, 15, 21, 25, 28 and 32). The best-fit parameters and

Table 4.2: Parameters of the background regions.

Background region	l (°)	b (°)	$kT_{\rm LHB}$ (eV)	$\rm EM_{LHB}$ ($10^{-3}\,\rm cm^{-6}\,pc$)	$kT_{\rm CGM}$ (eV)	$\rm EM_{CGM}$ ($10^{-2}\,\rm cm^{-6}\,pc$)
0	267	58	$88.2^{+4.0}_{-3.9}$	$4.169^{+0.231}_{-0.319}$	$147.3^{+1.6}_{-1.0}$	$6.912^{+0.554}_{-0.536}$
4	286	38	$82.1^{+8.1}_{-6.2}$	$2.557^{+0.726}_{-0.726}$	$155.1^{+1.5}_{-1.4}$	$2.368^{+0.532}_{-0.529}$
8	294	25	$72.9^{+9.6}_{-7.1}$	$2.176^{+0.794}_{-0.732}$	$162.5^{+1.5}_{-1.4}$	$3.693^{+0.514}_{-0.501}$
12	299	18	$126.3^{+31.4}_{-28.9}$	$1.068^{+0.747}_{-0.212}$	$171.8^{+2.5}_{-2.6}$	$7.919^{+1.012}_{-1.130}$
16	283	−57	$87.3^{+4.9}_{-0.2}$	$5.855^{+0.234}_{-0.477}$	$162.8^{+2.3}_{-1.2}$	$3.514^{+0.305}_{-0.305}$
18	299	−38	$86.6^{+10.6}_{-2.4}$	$4.184^{+0.399}_{-0.971}$	$169.2^{+2.2}_{-1.0}$	$1.448^{+0.295}_{-0.742}$
22	305	−26	$80.0^{+9.7}_{-6.7}$	$2.432^{+0.810}_{-0.756}$	$163.2^{+1.5}_{-1.5}$	$6.231^{+0.658}_{-0.636}$
26	310	−16	$77.1^{+13.1}_{-8.3}$	$2.264^{+0.980}_{-0.881}$	$169.5^{+1.5}_{-1.5}$	$8.540^{+0.855}_{-0.817}$
29	310	−12	$75.1^{+5.3}_{-4.3}$	$2.989^{+0.628}_{-0.592}$	$171.0^{+1.7}_{-1.6}$	$8.554^{+0.887}_{-0.853}$

Background region	$Z_{\rm C}$ ($Z_{\rm C,\odot}$)	$Z_{\rm O}$ ($Z_{\rm O,\odot}$)	$Z_{\rm Ne}$ ($Z_{\rm Ne,\odot}$)	$Z_{\rm Fe}$ ($Z_{\rm Fe,\odot}$)	$\rm CXB_{norm}$ ($10^{-3}\,\rm ph\,s^{-1}\,cm^{-2}\,deg^{-2}$)
0	$0.17^{+0.02}_{-0.02}$	$0.09^{+0.01}_{-0.01}$	$0.20^{+0.03}_{-0.02}$	$0.09^{+0.02}_{-0.01}$	$3.720^{+0.025}_{-0.025}$
4	$0.64^{+0.22}_{-0.14}$	$0.31^{+0.09}_{-0.06}$	$0.44^{+0.14}_{-0.10}$	$0.11^{+0.04}_{-0.03}$	$3.528^{+0.032}_{-0.032}$
8	$0.49^{+0.13}_{-0.10}$	$0.20^{+0.03}_{-0.03}$	$0.32^{+0.07}_{-0.05}$	$0.09^{+0.02}_{-0.02}$	$3.708^{+0.040}_{-0.040}$
12	$0.27^{+0.11}_{-0.08}$	$0.11^{+0.02}_{-0.02}$	$0.20^{+0.03}_{-0.03}$	$0.05^{+0.01}_{-0.02}$	$4.175^{+0.283}_{-0.257}$
16	$0.15^{+0.03}_{-0.03}$	$0.12^{+0.01}_{-0.01}$	$0.19^{+0.02}_{-0.02}$	$0.07^{+0.01}_{-0.01}$	$3.629^{+0.019}_{-0.018}$
18	$0.97^{+0.98}_{-0.22}$	$0.54^{+0.52}_{-0.08}$	$1.00^{+0.95}_{-0.17}$	$0.23^{+0.15}_{-0.04}$	$3.412^{+0.029}_{-0.029}$
22	$0.26^{+0.08}_{-0.06}$	$0.14^{+0.02}_{-0.01}$	$0.32^{+0.05}_{-0.04}$	$0.07^{+0.01}_{-0.01}$	$3.936^{+0.044}_{-0.044}$
26	$0.26^{+0.07}_{-0.06}$	$0.14^{+0.02}_{-0.01}$	$0.21^{+0.03}_{-0.03}$	$0.06^{+0.01}_{-0.01}$	$3.938^{+0.060}_{-0.059}$
29	$0.19^{+0.08}_{-0.06}$	$0.12^{+0.01}_{-0.01}$	$0.21^{+0.03}_{-0.03}$	$0.05^{+0.01}_{-0.01}$	$4.189^{+0.061}_{-0.061}$

Background region	$\log\left(\frac{N_{\rm H,CXB}}{\rm cm^{-2}}\right)$	$\log\left(\frac{N_{\rm H,CGM}}{\rm cm^{-2}}\right)^{(a)}$	χ^2/dof	dof$^{(b)}$	eROBub region$^{(c)}$	Sky area ($\rm deg^2$)	$\rm Stars_{norm}$ ($10^3\,M_\odot\,\rm cm^{-2}$)
0	$20.571^{+0.023}_{-0.025}$	...	1.04	175	1, 2, 3	240.78	6.88
4	$20.479^{+0.031}_{-0.033}$	...	1.04	175	5, 6, 7	98.78	4.15
8	$20.613^{+0.032}_{-0.032}$	...	1.07	175	9, 10, 11	57.63	3.84
12	$21.440^{+0.081}_{-0.095}$	$20.745^{+0.120}_{-0.045}$	1.06	174	13, 14, 15	28.37	2.65
16	$20.387^{+0.031}_{-0.023}$	...	1.08	175	17	171.48	5.29
18	$20.632^{+0.024}_{-0.048}$	...	1.22	175	19, 20, 21	90.99	4.38
22	$20.754^{+0.031}_{-0.030}$	...	0.92	175	23, 24, 25	39.09	2.94
26	$20.715^{+0.029}_{-0.028}$	...	0.98	175	27, 28, 33	23.33	2.96
29	$20.836^{+0.033}_{-0.031}$	...	1.22	175	30, 31, 32	25.39	4.30

Notes.
(a) A non-empty entry means a two-layer absorption model was adopted, one for the CXB, and another for the CGM and stars. This column shows the column density of the latter.
(b) Degrees of freedom.
(c) The eROBub regions that the background best-fit parameters were applied to.

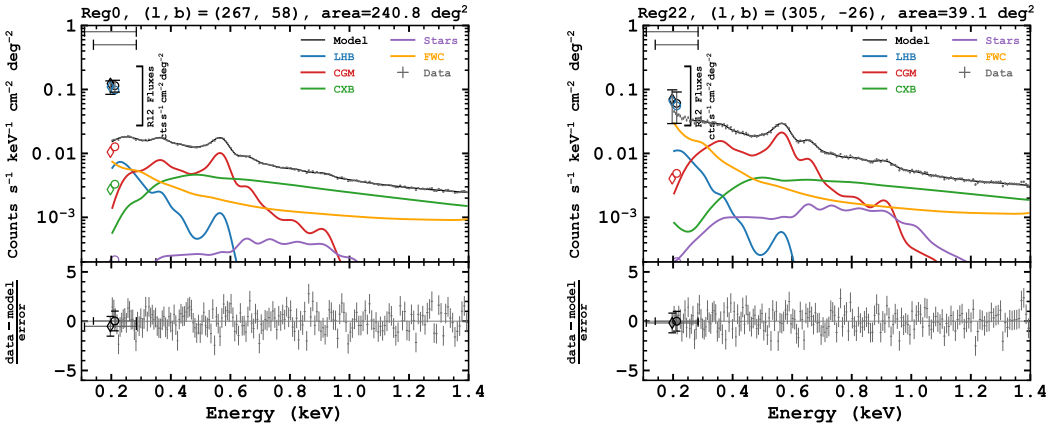

Figure 4.11: Example of the spectra, models and residuals of the two background regions (north: reg 0; south: reg 22), overlaid with the underlying model components. The two horizontal error bars at the top left corner of each panel indicate the bandwidth of the R1 and R2 bands.

fit statistics are listed in Table 4.3 and 4.4. Figure 4.12 shows two example spectra of the cool shell. Region 3 is where the cool shell is the brightest and easily identifiable from the eRASS1 RGB map in Predehl et al. (2020). Interestingly, we found that the optimisation preferred a model almost identical to the background (reg 0) (without an additional eRObub CIE component), with the only difference being the doubling of CGM EM. It seems unphysical to attribute this to a sudden increase in Galactic halo emission. Therefore, after accounting for the difference in sky area, we then fixed the CGM EM and abundance in reg 3 to that of the background, and allowed the eRObub component to account for the additional emissions. Indeed, the resulting cool shell temperature ($kT = 0.178 \pm 0.001$ keV) is similar to, yet slightly hotter than, the CGM temperature of the local background ($kT = 0.147 \pm 0.001$ keV). We obtained a new temperature because the elemental abundances were allowed to vary. On the other hand, the southern cool shell regions (reg 21, 25, 28, 32) possess an eRObub component much fainter than the north, at least an order of magnitude lower in terms of EM. This is the level comparable to the estimated unresolved stellar contribution. Given the uncertainty in predicting the stellar contribution in the SXRB from extrapolating from the volume-complete 10 pc sample, as well as the unknown contribution from the ISM, currently, there is inadequate evidence that the cool shell is present in the southern eRObub.

Besides the cool shell, our simplest assumption of a one-temperature plasma in the eRObub does not fit the spectra well. As we inspect the fits further within the eRObub, there seems to be a persistent type of residual around the two main Fe XVII Lα peaks at $\sim$17 Å ($\sim$0.8 keV) and $\sim$15 Å ($\sim$0.7 keV). We show an example of this residual in the left panel of Fig. 4.13. Elemental or ionic abundances do not affect the line ratio of these two lines, as these are transitions to the ground state from the same ion. We summarise the main transitions contributing to these two peaks in Table 4.5 under the entry of the Fe XVII ion.

We investigated multiple causes for the anomalous Fe XVII 15 Å/17 Å line ratio, including charge exchange, presence of an ionised absorber, and resonance scattering. We found none of these causes to be completely convincing. Therefore, we leave these investigations to Sect. 4.10.1 and 4.10.2 for the interested readers. Instead, we found the most helpful way to resolve the anomalous line ratio was by invoking a second temperature component. However, though unlikely, we cannot rule out the possibility of the anomalous line ratio being caused by the uncertainties in plasma codes, as we shall demonstrate in more detail in Sect. 4.5.2.

Table 4.3: Parameters of regions within the eRObub. Continued in Table 4.4.

Reg	l (°)	b (°)	$\mathrm{EM_{LHB}}$ (10^{-3} cm^{-6} pc)	$kT_{\mathrm{CGM}}{}^{(a)}$ (eV)	$\mathrm{EM_{CGM}}$ (10^{-2} cm^{-6} pc)	$Z_{\mathrm{C,CGM}}{}^{(a)}$ ($Z_{\mathrm{C},\odot}$)	$Z_{\mathrm{O,CGM}}{}^{(a)}$ ($Z_{\mathrm{O},\odot}$)
1	335	54	$3.588^{+0.251}_{-0.330}$	147.3	$9.393^{+0.838}_{-0.152}$	0.167	0.089
2	341	69	$4.241^{+0.058}_{-0.083}$	147.3	$10.537^{+0.359}_{-0.047}$	0.167	0.089
3	291	55	$5.992^{+0.273}_{-0.279}$	147.3	6.912	0.167	0.089
5	350	37	$1.551^{+0.093}_{-0.095}$	155.1	$4.533^{+0.103}_{-0.128}$	0.644	0.314
6	324	38	$2.351^{+0.099}_{-0.099}$	155.1	$3.041^{+0.177}_{-0.193}$	0.644	0.314
7	300	35	$1.794^{+0.650}_{-0.365}$	$127.9^{+10.8}_{-25.5}$	$15.455^{+8.042}_{-1.678}$	$0.129^{+0.044}_{-0.089}$	$0.085^{+0.018}_{-0.055}$
9	352	26	$2.907^{+0.659}_{-1.178}$	162.5	$1.480^{+0.052}_{-1.480}$	0.489	0.205
10	331	25	$5.212^{+0.190}_{-0.131}$	162.5	$1.568^{+0.029}_{-0.479}$	0.489	0.205
11	314	24	$5.703^{+0.649}_{-0.170}$	$146.4^{+2.6}_{-13.0}$	$23.816^{+9.550}_{-1.128}$	$0.138^{+0.014}_{-0.005}$	$0.069^{+0.007}_{-0.057}$
13	342	18	$2.017^{+0.160}_{-0.178}$	171.8	$35.798^{+1.310}_{-3.865}$	0.269	0.106
14	327	18	$2.475^{+0.188}_{-0.188}$	171.8	$27.475^{+0.355}_{-2.165}$	0.269	0.106
15	315	18	$3.009^{+0.157}_{-0.167}$	171.8	$24.157^{+0.311}_{-0.311}$	0.269	0.106
17	336	−64	$6.444^{+0.174}_{-0.180}$	162.8	$3.659^{+0.128}_{-0.132}$	0.154	0.125
19	351	−40	$4.396^{+0.189}_{-0.226}$	169.2	$1.265^{+0.108}_{-0.133}$	0.966	0.539
20	327	−40	$4.225^{+0.192}_{-0.199}$	169.2	$0.830^{+0.021}_{-0.042}$	0.966	0.539
21$^{(f)}$	313	−40	$3.835^{+0.118}_{-0.196}$	169.2	$0.816^{+0.037}_{-0.032}$	0.966	0.539
23	348	−25	$3.526^{+0.279}_{-0.292}$	163.2	$8.816^{+0.417}_{-0.455}$	0.263	0.140
24	331	−25	$3.812^{+0.217}_{-0.218}$	163.2	$8.599^{+0.554}_{-0.463}$	0.263	0.140
25$^{(f)}$	317	−25	$2.048^{+0.229}_{-0.241}$	163.2	$5.761^{+0.256}_{-0.200}$	0.263	0.140
27	350	−17	$4.277^{+0.483}_{-0.496}$	169.5	$15.135^{+0.367}_{-0.804}$	0.261	0.135
28	332	−17	$6.107^{+0.490}_{-0.501}$	169.5	$9.379^{+0.573}_{-0.418}$	0.261	0.135
30	352	−12	$2.590^{+0.312}_{-0.325}$	171.0	$24.966^{+1.341}_{-2.990}$	0.188	0.117
31	334	−12	$3.908^{+0.697}_{-1.642}$	171.0	$22.411^{+1.056}_{-22.411}$	0.188	0.117
32$^{(f)}$	322	−12	$2.339^{+0.337}_{-0.565}$	171.0	$11.430^{+0.904}_{-2.549}$	0.188	0.117
33	319	−17	$2.930^{+0.311}_{-0.315}$	169.5	$16.762^{+0.543}_{-0.628}$	0.261	0.135

Reg	$\mathrm{CXB_{norm}}$ (10^{-3} ph s^{-1} cm^{-2} deg^{-2})	$\log\left(\frac{N_{\mathrm{H,CXB}}}{\mathrm{cm^{-2}}}\right)^{(b)}$	$\log\left(\frac{N_{\mathrm{H,CGM}}}{\mathrm{cm^{-2}}}\right)$	kT_{eRObub1} (keV)	$\mathrm{EM_{eRObub1}}$ (10^{-2} cm^{-6} pc)	$kT_{\mathrm{eRObub2}}{}^{(d)}$ (keV)	$\mathrm{EM_{eRObub2}}{}^{(d)}$ (10^{-3} cm^{-6} pc)
1	$3.612^{+0.135}_{-0.040}$	20.581	$20.489^{+0.021}_{-0.020}$	$0.241^{+0.034}_{-0.005}$	$0.329^{+0.039}_{-0.180}$	$0.603^{+0.046}_{-0.037}$	$1.611^{+0.212}_{-1.474}$
2	$3.546^{+0.020}_{-0.042}$	$20.429^{+0.000}_{-0.004}$	$^{(c)}20.429^{+0.000}_{-0.004}$	$0.251^{+0.002}_{-0.001}$	$0.832^{+0.040}_{-0.210}$	$0.565^{+0.007}_{-0.011}$	$2.697^{+0.190}_{-0.731}$
3	$3.729^{+0.021}_{-0.021}$	20.419	$20.381^{+0.015}_{-0.015}$	$0.178^{+0.001}_{-0.001}$	$3.823^{+0.277}_{-0.275}$	...	...
5	$2.946^{+0.072}_{-0.073}$	21.073	$20.743^{+0.006}_{-0.006}$	$0.279^{+0.010}_{-0.011}$	$3.255^{+0.239}_{-0.204}$	$0.595^{+0.022}_{-0.020}$	$8.297^{+1.218}_{-1.078}$
6	$3.571^{+0.056}_{-0.065}$	20.947	$20.616^{+0.006}_{-0.006}$	$0.238^{+0.009}_{-0.008}$	$4.767^{+0.502}_{-0.465}$	$0.647^{+0.029}_{-0.032}$	$6.122^{+0.734}_{-0.611}$
7	$4.171^{+0.087}_{-0.039}$	20.876	$20.605^{+0.102}_{-0.032}$	$0.206^{+0.038}_{-0.027}$	$1.006^{+2.785}_{-0.827}$	...	...
9	$9.025^{+1.164}_{-0.620}$	21.290	$20.908^{+0.031}_{-0.048}$	$0.227^{+0.003}_{-0.042}$	$10.336^{+11.779}_{-0.075}$	$0.543^{+0.094}_{-0.082}$	$28.170^{+8.507}_{-11.512}$
10	$3.425^{+0.228}_{-0.104}$	21.057	$20.629^{+0.016}_{-0.006}$	$0.227^{+0.002}_{-0.021}$	$10.094^{+3.182}_{-0.150}$	$0.549^{+0.030}_{-0.024}$	$16.672^{+2.372}_{-2.113}$
11	$3.955^{+0.092}_{-0.047}$	20.843	$20.550^{+0.009}_{-0.009}$	$0.213^{+0.001}_{-0.024}$	$1.602^{+2.857}_{-0.163}$	$0.526^{+0.010}_{-0.022}$	$5.000^{+1.170}_{-2.105}$
13	$3.172^{+0.265}_{-0.202}$	21.151	$20.882^{+0.008}_{-0.010}$	$0.290^{+0.013}_{-0.036}$	$1.136^{+3.494}_{-0.676}$	$0.585^{+0.050}_{-0.066}$	$2.125^{+6.392}_{-1.523}$
14	$3.833^{+0.320}_{-0.148}$	21.024	$20.620^{+0.007}_{-0.007}$	$0.318^{+0.020}_{-0.086}$	$2.564^{+0.497}_{-1.413}$	$0.546^{+0.317}_{-0.153}$	$3.947^{+17.881}_{-3.115}$
15	$3.620^{+0.089}_{-0.084}$	21.013	$20.639^{+0.007}_{-0.007}$	$0.349^{+0.003}_{-0.005}$	$1.676^{+0.372}_{-0.372}$	...	...
17	$3.577^{+0.064}_{-0.129}$	$20.267^{+0.017}_{-0.017}$	$^{(c)}20.267^{+0.017}_{-0.017}$	$0.270^{+0.044}_{-0.033}$	$0.287^{+0.098}_{-0.103}$	$0.594^{+0.040}_{-0.045}$	$3.512^{+2.361}_{-1.151}$
19	$3.251^{+0.094}_{-0.129}$	20.574	$20.379^{+0.021}_{-0.024}$	$0.206^{+0.023}_{-0.010}$	$2.912^{+0.696}_{-0.784}$	$0.590^{+0.027}_{-0.023}$	$9.137^{+2.349}_{-1.591}$
20	$3.112^{+0.112}_{-0.102}$	20.583	$20.220^{+0.025}_{-0.027}$	$0.284^{+0.027}_{-0.031}$	$1.014^{+0.229}_{-0.168}$	$0.562^{+0.020}_{-0.012}$	$14.555^{+2.004}_{-2.157}$
21$^{(f)}$	$3.629^{+0.026}_{-0.043}$	20.845	$20.482^{+0.016}_{-0.025}$	$0.227^{+0.023}_{-0.013}$	$1.502^{+0.247}_{-0.320}$	...	...
23	$3.549^{+0.099}_{-0.102}$	20.818	$20.529^{+0.012}_{-0.012}$	$0.265^{+0.017}_{-0.013}$	$2.109^{+0.451}_{-0.342}$	$0.514^{+0.016}_{-0.017}$	$7.702^{+1.651}_{-1.585}$
24	$3.374^{+0.091}_{-0.093}$	20.900	$20.596^{+0.009}_{-0.010}$	$0.260^{+0.017}_{-0.010}$	$2.563^{+0.447}_{-0.409}$	$0.554^{+0.022}_{-0.017}$	$9.003^{+1.619}_{-1.974}$
25$^{(f)}$	$3.988^{+0.167}_{-0.090}$	$21.152^{+0.161}_{-0.055}$	$20.691^{+0.034}_{-0.022}$	$0.343^{+0.010}_{-0.040}$	$0.069^{+0.793}_{-0.053}$	...	...
27	$3.348^{+0.149}_{-0.151}$	20.915	$20.537^{+0.012}_{-0.013}$	$0.289^{+0.011}_{-0.022}$	$2.966^{+0.541}_{-0.350}$	$0.574^{+0.046}_{-0.047}$	$6.973^{+3.629}_{-1.797}$
28$^{(f)}$	$3.944^{+0.111}_{-0.249}$	21.004	$20.597^{+0.023}_{-0.024}$	$0.307^{+0.077}_{-0.047}$	$0.158^{+0.475}_{-0.136}$	...	...
30	$3.568^{+0.196}_{-0.241}$	21.172	$20.774^{+0.007}_{-0.009}$	$0.255^{+0.017}_{-0.023}$	$5.117^{+2.687}_{-1.087}$	$0.550^{+0.031}_{-0.036}$	$13.391^{+4.471}_{-3.369}$
31	$3.622^{+1.101}_{-0.782}$	21.246	$20.825^{+0.045}_{-0.035}$	$0.230^{+0.012}_{-0.049}$	$11.458^{+22.841}_{-1.102}$	$0.579^{+0.124}_{-0.278}$	$13.688^{+12.766}_{-10.740}$
32$^{(f)}$	$4.654^{+0.744}_{-0.114}$	21.244	$20.748^{+0.026}_{-0.016}$	$0.261^{+0.075}_{-0.084}$	$0.239^{+12.498}_{-0.200}$	...	...
33	$3.427^{+0.131}_{-0.152}$	20.989	$20.615^{+0.008}_{-0.008}$	$0.260^{+0.018}_{-0.015}$	$4.842^{+0.906}_{-0.675}$	$0.559^{+0.028}_{-0.024}$	$11.984^{+2.175}_{-2.161}$

Notes.

kT_{LHB} is taken from the corresponding background regions listed in Table 4.2.

(a) Parameters with uncertainties are free while those without uncertainties are fixed at the best-fit value in the corresponding background region (Table 4.2).

(b) If reported without uncertainties, the column density is the total Galactic value. It is fixed during fitting and applied only on the CXB.

(c) Linked with $\log\left(\frac{N_{\mathrm{H,CXB}}}{\mathrm{cm^{-2}}}\right)$.

(d) If empty, the eRObub is modelled as a single temperature plasma.

Table 4.4: Table 4.3 continued.

Reg	$Z_{\rm C,eRObub}{}^{(e)}$ ($Z_{\rm C,\odot}$)	$Z_{\rm O,eRObub}$ ($Z_{\rm O,\odot}$)	$Z_{\rm Ne,eRObub}{}^{(e)}$ ($Z_{\rm Ne,\odot}$)	$Z_{\rm Fe,eRObub}{}^{(e)}$ ($Z_{\rm Fe,\odot}$)	χ^2/dof	dof	Sky area ($\rm deg^2$)	$\rm Stars_{norm}$ ($10^3\,M_\odot\,cm^{-2}$)
1	0.708	$0.708^{+9.292}_{-0.067}$	$0.659^{+4.802}_{-0.079}$	$0.341^{+5.023}_{-0.032}$	1.48	174	484.7	17.29
2	0.652	$0.652^{+0.220}_{-0.064}$	$0.814^{+0.099}_{-0.078}$	$0.445^{+0.009}_{-0.051}$	1.59	174	369.9	11.49
3	$0.569^{+0.070}_{-0.061}$	$0.181^{+0.015}_{-0.013}$	$0.390^{+0.035}_{-0.032}$	$0.127^{+0.012}_{-0.011}$	1.23	176	263.7	7.78
5	0.191	$0.191^{+0.016}_{-0.016}$	$0.209^{+0.012}_{-0.012}$	$0.125^{+0.006}_{-0.006}$	1.73	174	251.5	14.37
6	0.114	$0.114^{+0.008}_{-0.006}$	$0.151^{+0.010}_{-0.009}$	$0.100^{+0.004}_{-0.004}$	2.51	174	387.9	20.01
7	0.583	$0.583^{+9.417}_{-0.254}$	$0.481^{+8.147}_{-0.078}$	$0.259^{+4.929}_{-0.084}$	1.40	173	221.1	11.94
9	0.095	$0.095^{+0.042}_{-0.013}$	$0.175^{+0.126}_{-0.018}$	$0.089^{+0.028}_{-0.007}$	1.71	174	161.6	15.89
10	0.093	$0.093^{+0.005}_{-0.005}$	$0.175^{+0.030}_{-0.008}$	$0.104^{+0.007}_{-0.003}$	3.03	174	206.8	18.87
11	0.313	$0.313^{+0.002}_{-0.019}$	$0.289^{+0.009}_{-0.030}$	$0.142^{+0.002}_{-0.013}$	1.79	172	121.3	9.42
13	1.528	$1.528^{+8.472}_{-1.148}$	$1.643^{+8.357}_{-0.986}$	$1.208^{+6.757}_{-0.506}$	1.27	174	25.8	4.16
14	0.204	$0.204^{+0.042}_{-0.089}$	$0.278^{+0.174}_{-0.076}$	$0.134^{+0.029}_{-0.046}$	1.51	174	52.8	7.31
15	0.418	$0.418^{+0.119}_{-0.077}$	$0.400^{+0.130}_{-0.083}$	$0.164^{+0.050}_{-0.032}$	1.70	176	53.8	6.43
17	0.280	$0.280^{+0.082}_{-0.050}$	$0.174^{+0.059}_{-0.052}$	$0.095^{+0.028}_{-0.030}$	1.85	174	669.8	22.14
19	0.061	$0.061^{+0.009}_{-0.007}$	$0.068^{+0.027}_{-0.026}$	$0.068^{+0.008}_{-0.009}$	1.58	174	313.5	18.14
20	0.128	$0.128^{+0.010}_{-0.012}$	$0.087^{+0.018}_{-0.015}$	$0.083^{+0.007}_{-0.006}$	1.41	174	322.5	16.75
$21^{(f)}$	0.046	$0.046^{+0.008}_{-0.010}$	0.046	0.046	0.99	178	118.0	6.12
23	0.255	$0.255^{+0.050}_{-0.037}$	$0.238^{+0.032}_{-0.026}$	$0.202^{+0.026}_{-0.021}$	1.51	174	168.0	17.07
24	0.272	$0.272^{+0.054}_{-0.037}$	$0.305^{+0.034}_{-0.027}$	$0.185^{+0.026}_{-0.019}$	1.43	174	177.9	16.88
$25^{(f)}$	2.805	$2.805^{+7.195}_{-1.356}$	$1.253^{+5.492}_{-1.151}$	$0.437^{+1.848}_{-0.393}$	0.95	175	53.7	4.49
27	0.331	$0.331^{+0.052}_{-0.062}$	$0.367^{+0.055}_{-0.045}$	$0.273^{+0.039}_{-0.041}$	1.15	174	78.8	13.70
$28^{(f)}$	1.319	$1.319^{+8.681}_{-1.007}$	$1.730^{+8.270}_{-1.440}$	$0.560^{+2.133}_{-0.470}$	1.06	176	26.5	3.52
30	0.234	$0.234^{+0.057}_{-0.061}$	$0.274^{+0.043}_{-0.031}$	$0.200^{+0.036}_{-0.037}$	1.47	174	75.7	24.23
31	0.069	$0.069^{+0.008}_{-0.018}$	$0.145^{+0.078}_{-0.030}$	$0.079^{+0.018}_{-0.020}$	2.44	174	82.7	21.09
$32^{(f)}$	0.701	$0.701^{+6.028}_{-0.664}$	$0.866^{+9.134}_{-0.820}$	$0.409^{+1.023}_{-0.271}$	0.90	175	34.9	7.17
33	0.121	$0.121^{+0.018}_{-0.015}$	$0.208^{+0.018}_{-0.015}$	$0.121^{+0.010}_{-0.008}$	1.46	174	99.8	15.30

Notes.
(e) Linked with $Z_{\rm O,eRObub}$ if reported without uncertainties.
(f) Southern cool shell regions. The detection of the eRObub component is weak, which can be seen from the $\rm EM_{eRObub1}$ column as well as the poor constraints in the elemental abundance columns.

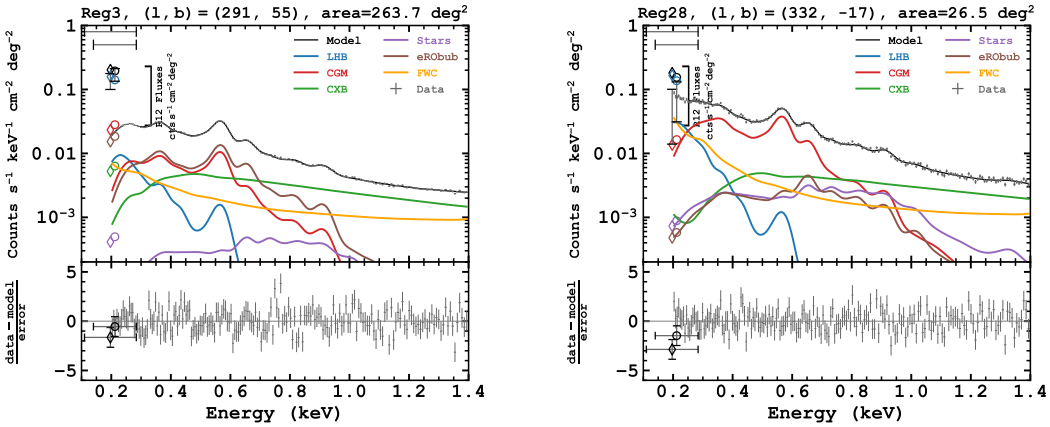

Figure 4.12: Example spectra from the cool shell region, showing reg 3 (*left*) in the north and reg 28 (*right*) in the south.

Table 4.5: List of resonance lines considered. Wavelengths are taken from the CHIANTI atomic database v10 (Dere et al., 1997; Del Zanna et al., 2021) and oscillator strengths f are taken from the NIST database (Kramida et al., 2024, and references therein).

Ions	Lower level	Upper level	Wavelength (Å)	Energy (eV)	f
Ne IX	$1s^2\,{}^1S_0$	$1s2p\,{}^1P_1$	13.45	922	7.2×10^{-1}
Fe XVII	$2s^22p^6\,{}^1S_0$	$2s^22p^5 3d\,{}^1P_1$	15.01	826	2.3
		${}^3D_1$	15.26	812	6.3×10^{-1}
		${}^3P_1$	15.45	802	9.7×10^{-3}
		$2s^22p^5 3s\,{}^3P_1$	16.77	739	1.1×10^{-1}
		${}^1P_1$	17.05	727	1.2×10^{-1}
		${}^3P_2$	17.10	725	4.4×10^{-8}
O VIII (Lyβ)	$1s\,{}^2S_{1/2}$	$3p\,{}^2P_{3/2}$	16.01	775	5.3×10^{-2}
		${}^2P_{1/2}$	16.01	775	2.6×10^{-2}
O VIII (Lyα)		$2p\,{}^2P_{3/2}$	18.97	654	2.8×10^{-1}
		${}^2P_{1/2}$	18.97	653	1.4×10^{-1}
O VII	$1s^2\,{}^1S_0$	$1s2p\,{}^1P_1$	21.60	574	6.9×10^{-1}

Two-temperature CIE Model

Invoking an additional CIE component with freely varying temperature and EM generally improved the fits within the eROsub. The second CIE component has abundance and absorption, which are always linked with the first to limit the number of free parameters. We listed the best-fit parameters with the two-temperature model in Table 4.3 and 4.4. Fig. 4.13 compares single and two-temperature fits to the eROsub spectrum in reg 27. The latter perform significantly better in reproducing the Fe XVII 15 Å/17 Å ratio as well as a better fit to the Ne IX,X lines. The improvement brought by the extra temperature component is significant in all eROsub interior regions.

A general trend emerged from this exercise: both temperature components have consistent temperatures throughout the eROsub, as shown in Fig. 4.14. No significant temperature gradient is observed after discarding regions in the southern cool shell because of the inconclusive detection of eROsub. The low (eROsub1) and high (eROsub2) temperature components have median temperatures of $kT_{\rm low} = 0.26 \pm 0.03$ keV and $kT_{\rm high} = 0.56^{+0.04}_{-0.02}$ keV (uncertainties reflecting the

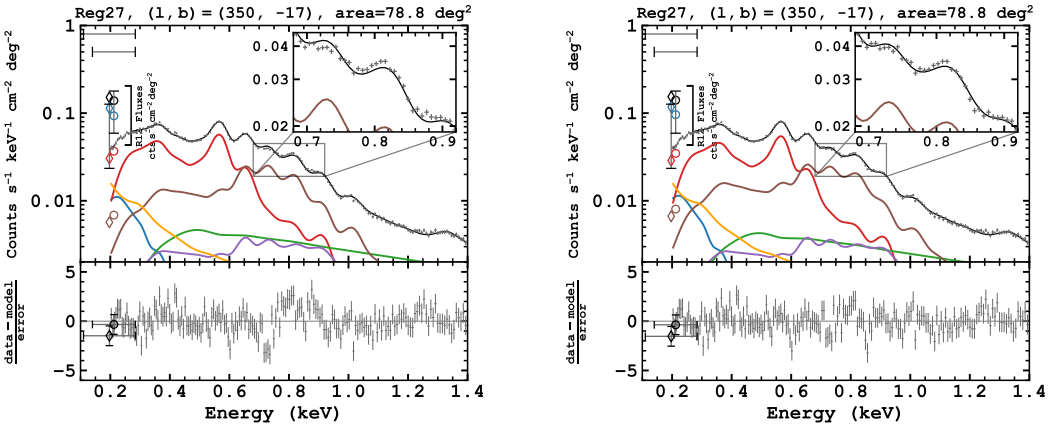

Figure 4.13: Example comparison of single and two-temperature models of the eRObub in reg 27 with insets showing the residuals near the Fe XVII L shell transitions. The line colours follow the legends in Fig. 4.11 and 4.12. *Left:* Single temperature model (χ^2/dof = 1.49; 176 dof). The dominant residual is around the 0.7–0.8 keV range around the Fe XVII L shell transitions (Table 4.5). The data exhibits a higher Fe XVII 15 Å/17 Å ratio than the prediction from the one-temperature model. This is a general observation in most regions within the eRObub, excluding the cool shell. *Right:* Two-temperature model (χ^2/dof = 1.15; 174 dof). The model reproduces the data better, especially the Fe XVII lines. In this particular region, the F-test yields a statistic of 27.5 with a p-value in the order of 10^{-11}, suggesting a highly significant improvement in using a two-temperature model to describe the eRObub.

16$^{\text{th}}$ and 84$^{\text{th}}$ percentiles in the population, not accounting for the statistical uncertainties of each fit), respectively. The low temperature component dominates the flux, with EM $\sim 4^{+3}_{-2}$ times larger than the hot component on average. The EM of both temperature components increases towards the Galactic plane, more sharply for the low temperature component than the high. The EM modulates approximately one order of magnitude from high to low latitudes. The EM shown in Fig. 4.14 is higher than the EM in the constant S/N regions in Fig. 4.7 because the latter's abundance was kept at solar. Because the abundances were fitted in the large regions, and the data generally preferred subsolar values, the EM had to be enhanced to maintain the same surface brightness level.

The data prefer subsolar abundance, with oxygen abundance (linked with all other elements except Fe and Ne) generally lying within 0.1–0.3 solar. As shown by Fig. 4.15, the oxygen abundance does not exhibit a clear trend with latitude. Ne and Fe are marginally consistent with the O abundance. One might notice some indications of supersolar abundance for Ne and subsolar abundance for Fe; however, the scatter between the regions is relatively large. Given there are also uncertainties originating from the choice of abundance tables, which could differ from a few to 20% regarding Ne/O ratio (e.g. Anders & Grevesse, 1989; Asplund et al., 2009; Lodders et al., 2009), there is inadequate evidence to suggest the eRObub has a non-solar Ne/O or Fe/O ratio.

The NPS (reg 2) is a special case in terms of abundance, where O, Fe and Ne abundances are enhanced compared to other eRObub regions. Having a higher abundance echoes the idea from Zhang et al. (2024) and Churazov et al. (2024), who pointed out that the NPS could originate from the active star-forming regions, which would naturally produce metal-enriched hot gas that rises to the halo due to buoyancy. To test if the data indeed prefer a high abundance, we refitted the NPS region, this time with the O and all other metals fixed at 0.2 $Z_\odot$ except for Ne and Fe, which is the mean value within the eRObub. The new χ^2/dof is 1.94, which is worse than the χ^2/dof of the model with O abundance free (1.59). Statistically, the free-O abundance model is strongly preferred as shown by the F-test with a p-value in the order of 10^{-9}. We show the

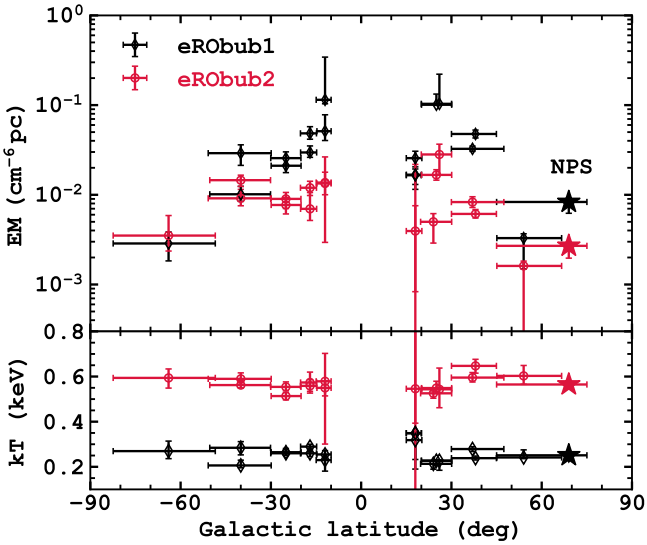

Figure 4.14: Latitudinal profiles of $kT_{\rm eRObub}$ and $\rm EM_{eRObub}$ within the eRObub using the large extraction regions. The cool shell and background regions are not shown in the figure.

model comparison in Sect. 4.11. However, we have reservations about whether the evidence is as strong as the statistics suggest, mainly because we cannot pinpoint a telltale feature from the fits that separates the two scenarios that is as apparent as, for instance, the Fe XVII 15 Å/17 Å ratio. Nevertheless, one could indeed see degradation in the fit quality around 0.35 keV and between 1.0–1.4 keV; these could be remedied by having enhanced N and Mg abundance individually, corroborating an enhanced elemental abundance. The fundamental problem of this uncertainty lies with the inadequate spectral resolution of eROSITA to clearly differentiate the continuum and line emissions. It is worth mentioning that an abundance of $\sim 0.5\,Z_\odot$ is not dissimilar to the previous observations and analyses on the east part of the NPS (Willingale et al., 2003; Miller et al., 2008; Gu et al., 2016b).

Plasma codes

While we presented evidence of two-temperature plasma in the interior of eRObub, it is instructive to compare the level of uncertainties surrounding the model spectra predicted by plasma codes with the level of our residuals. We tested the two most commonly used plasma codes, `AtomDB/apec` (Smith et al., 2001; Foster et al., 2012) and `SPEX` (Kaastra et al., 1996; de Plaa et al., 2020), in their latest releases v3.1.2 and v3.08.1, respectively. In addition, we also included an older `AtomDB/apec` release, v3.0.9, as it was used to fit the constant S/N regions in Sect. 4.5.1. The comparison is shown in Fig. 4.16. Abundances were set to solar using the Lodders et al. (2009) values, which are common in both codes. The comparison was done using the spectral fitting programme `SPEX`, and the `AtomDB/apec` models were imported as user-defined models computed using `PyAtomDB` (Foster & Heuer, 2020). We folded the model spectra with the eROSITA response and effective area and introduced a typical Galactic absorption of $\log N_{\rm H} = 20.5$. Three discrete temperatures (0.2, 0.3 and 0.4 keV) around the expected eRObub temperature were tested, showing noticeable differences between the three implementations within 0.7–0.9 keV.

The `SPEX` model predicts higher emissions than the other two `apec` versions, most notably between 0.7–1.3 keV. The difference is the most pronounced at the Fe XVII 15Å peak, where `SPEX` consistently predicts a higher peak regardless of temperature. It is worth noting that `SPEX` produces a Fe XVII 15 Å/17 Å ratio that is closer to the data. This is the reason why we chose to use the `SPEX cie` model to fit the large regions. The residual at these energies would be worse if `apec` is chosen. The line ratios of the two Fe peaks predicted by the three models are summarised in

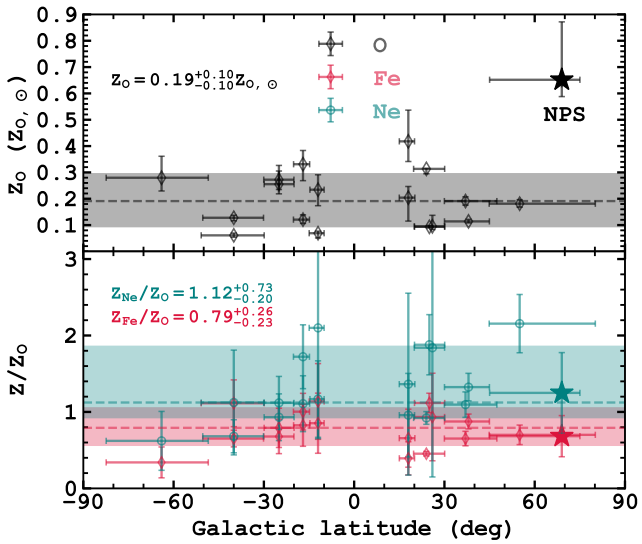

Figure 4.15: Latitudinal profile of O, Fe and Ne abundances. Ne and Fe abundances are shown with respect to O in the lower panel. The unit of the y-axis in the lower panel means the ratio Z_x/Z_O to the ratio in our assumed abundance table from Lodders (2003) (which is ≈ 0.15 in number fraction), but not the absolute number fraction of Fe or Ne to O. We removed regions with poor abundance constraints ($\Delta Z/Z > 0.5$).

Table 4.6: Narrowband ratio E_2/E_1 taken from Fig. 4.16, where $E_1 \in [0.70, 0.77]$ keV (Fe XVII 17 Å peak) and $E_2 \in [0.77, 0.87]$ keV (Fe XVII 15 Å peak). The ratio was computed after dividing the flux by the width of the narrowband.

kT (keV)	SPEX 3.08.1	apec 3.1.2	apec 3.0.9
0.2	0.784	0.694	0.686
0.3	0.804	0.732	0.714
0.4	0.859	0.777	0.757

Table 4.6. It shows that about a ∼10% difference in the Fe XVII 15 Å/17 Å ratio can be expected from using different plasma codes, regardless of the temperature of the plasma within the relevant range.

It is instructive to compare the variation in Fe XVII 15 Å/17 Å ratio introduced by the choice of plasma codes with the amplitudes of residuals we observe from fitting with the single temperature model in the eRObub regions (excluding the cool shell regions, which were well fitted by a single temperature model). The latter was computed by first taking the data-to-model ratios within the two bands (15 Å band: $E \in [0.77, 0.87]$ keV, 17 Å band: $E \in [0.70, 0.77]$ keV, see Fig. 4.16), then dividing the data-to-model ratios of the two bands to quantify how much the data line ratio differ from the model line ratio. A positive line ratio deviation means that the data Fe XVII 15 Å/17 Å ratio is higher than the model prediction, which is indeed the case for all except one region as shown in Table 4.7. However, quantitatively, the mostly positive deviation is in all cases less than ∼10%, which is less than the variations introduced by the choice of plasma codes. Of course, this does not change the fact that we were already using the SPEX model, which produces the highest Fe XVII 15 Å/17 Å ratio in the three plasma codes tested, and still failed to explain the enhanced Fe XVII 15 Å/17 Å ratio in the data. While it is possible that the two-temperature model or the alternative explanations explored in Sect. 4.10.1 and 4.10.2 for the enhanced Fe XVII 15 Å/17 Å ratio could become irrelevant with updated plasma codes with a raised Fe line ratio, recent laboratory measurements in fact suggest a lower $3d/3s$ intensity ratio

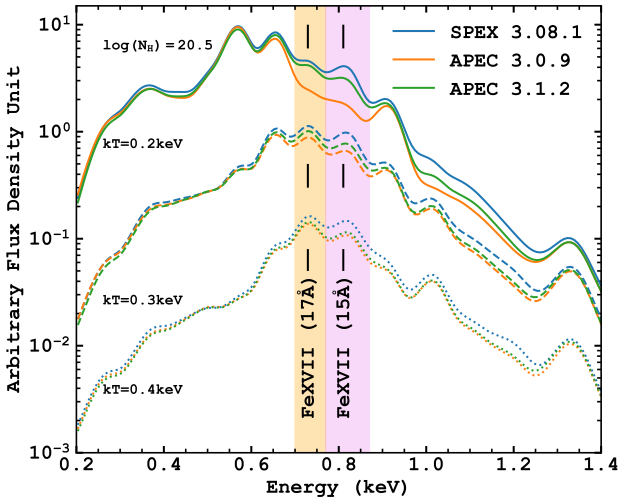

Figure 4.16: Comparison of the spectral shape of CIE models created by different plasma codes, subjected to a typical Galactic absorption column density of $\log(N_{\rm H}/{\rm cm}^{-2}) = 20.5$, and folded with the eROSITA response and effective area. The two main Fe XVII L shell peaks are labelled. The prediction of their line ratio differs significantly. `SPEX` produces the closest line ratio shown by the data. The definitions of the Fe XVII 15 Å (violet) and 17Å (orange) narrow bands are also shown.

(see transitions in Table 4.5), indicating an even lower Fe XVII 15 Å/17 Å compared to theoretical predictions (Shah et al., 2019).

4.6 Discussion

4.6.1 Temperature structure

From the spectral analysis, a relatively clear picture has emerged. The eRObub is generally characterised by two temperature components, one at ~ 0.25 keV and another at ~ 0.55 keV, which are uniform across hemispheres. The elemental abundance of the eRObub gas is also consistent with the expectation of shock-heated halo gas between $Z = 0.1$–$0.3\,Z_\odot$, not immediately obvious of metal enrichment from the star formation activities towards the inner part of the Galaxy. The exceptions to this general picture are the presence of the NPS and the cool shell. The northern eRObub is surrounded by a shell, seemingly having a temperature slightly cooler than the low-temperature eRObub component in projection. The hot component is not present in the cool shell. In terms of its surface brightness, the NPS is an anomaly in the northern eRObub that does not follow the latitudinal decay trend exhibited by other eRObub regions. Our spectral analysis suggests that a higher elemental abundance primarily causes its brightness without an obvious jump in EM.

Intrinsic multi-temperature gas

A two-temperature or even a multi-temperature structure is not intrinsically surprising, as repeated shock heating, continuous cooling or turbulent mixing of plasmas could naturally produce a multi-temperature structure (e.g. Lancaster et al., 2021; Wang et al., 2021). A spread in plasma temperature has been commonly found in the outflow or halo of nearby edge-on disc galaxies (e.g. Strickland et al., 2004; Ranalli et al., 2008). We did test a lognormal temperature distribution

Table 4.7: Data-to-model ratios in the Fe XVII 15 Å and Fe XVII 17 Å bands, and the resulting deviation in the Fe XVII 15 Å/17Å line ratio. The single temperature model is used. The regions listed are the regions where a two-temperature model was needed.

Region	Ratio 15Å	Ratio 17Å	Line-ratio offset (%)
1	1.013	0.989	2.4
2	1.012	0.988	2.4
5	1.022	0.984	3.8
6	1.032	0.972	6.2
9	1.025	0.976	5.0
10	1.045	0.961	8.7
13	1.038	0.973	6.7
14	1.020	0.984	3.6
17	1.006	0.997	0.9
19	1.007	0.991	1.7
20	0.999	1.004	-0.5
23	1.015	0.979	3.8
24	1.014	0.987	2.7
27	1.031	0.971	6.1
30	1.035	0.963	7.5
31	1.029	0.965	6.6

to model the eRObub in the early stage of the spectral analysis. There were two reasons for not pursuing this further. The first one was that the lognormal distribution could not produce a Fe XVII 15 Å/17 Å ratio as high as the data, while not worsening the fit elsewhere. The second reason was that it is computationally expensive to fit, as a lognormal temperature distribution, in essence, is a sum of dozens of individual CIE components, which is calculated on-the-fly in `SPEX`.

Our temperature measurement is broadly consistent with previous findings by Kataoka et al. (2013, 2015) who measured a relatively uniform temperature of ~ 0.3 keV throughout the FB. In addition, we were able to show that this is also the property of gas outside of the FB but inside of the eRObub, even though a two-temperature fit would benefit all regions within the eRObub. The hotter component in our model is usually a few times lower in EM and only distinguishable from the large regions with sufficient S/N. When we were analysing the smaller, lower S/N regions, the hot component was not adequately noticeable. The constancy of the temperature of both components within the bubbles is somewhat puzzling, which may reflect the fact that the X-ray emissions primarily trace the shell region of the eRObub due to the sharply increasing density there (e.g. Weaver et al., 1977; Cox & Anderson, 1982). While we have to factor in the LHB and CGM component that had free normalisations during the spectral fitting, so we were not sensitive to the presence of gas having a temperature lower than 0.15 keV, eROSITA should be sensitive to gas at $kT \sim 1$–2 keV. The absence of such a phase appears on face value to argue against an AGN-burst scenario where the gas is expected to be heated to a few 10^7 K (e.g. Yang et al., 2022, but see the multiple caveats listed within). Our measurement also disfavours a scenario where the FB and eRObub were formed by two AGN jet episodes (Zhang et al., 2025), as a temperature jump would be expected at the boundary of the FB.

Efficient post-shock radiative cooling?

A natural explanation for the cool shell could be that it consists of dense material, which has significantly cooled due to the emitted radiation. Such processes are observed in stellar wind bubbles and old SNRs, where radiative cooling leads to efficient energy loss and the formation of thin dense shells (Raymond, 1979). However, it seems unlikely that radiative cooling at the low ambient densities of the Milky Way CGM is sufficiently efficient to significantly lower the temperature of ~ 0.3 keV gas within a few Myr (cooling time $\gtrsim$ Hubble time for $n = 10^{-4}\,\mathrm{cm}^{-3}$

and $Z = 0.3\,Z_\odot$; Sutherland & Dopita, 1993). An alternative mechanism for producing a cool shell could be cooling due to adiabatic expansion. If the ambient density of the CGM decreases relatively rapidly (i.e., over a small timescale compared to the bubble age), as could be conceivable for a shock moving away from the Galactic plane into the halo, the plasma temperature would be expected to decrease, ideally as $T \propto n^{2/3}$ (Yamaguchi et al., 2018).

As pointed out by Zheng et al. (2024b), the apparent cool shell could also be explained by a projection effect, with the cold portion of the shell at high latitudes being located rather nearby, interacting with higher density material. In this scenario, the hotter gas inside the bubbles is located at larger distances from the Galactic plane and projected at lower apparent radii to the spherical geometry of the bubbles.

Non-equilibrium ionisation in the cool shell?

An alternative explanation for the apparent cool shell could be an inadequate method for temperature determination. This may be the case, particularly if the hot plasma is not in CIE. A simple estimate of the relevant ionisation timescale, quantifying the number of collisions experienced by an average ion, is given by the product of an approximate age of the bubbles and the typical halo density $n_e t \sim 5 \times 10^{-4}\,\mathrm{cm^{-3}} \times 2 \times 10^7\,\mathrm{yr} \approx 3 \times 10^{11}\mathrm{cm^{-3}\,s}$ (see below), indicating a slightly underionised plasma. Tentative evidence for NEI along a sight line towards the NPS has, in fact, been presented by Yamamoto et al. (2022). An underionised plasma is characterised by a preferential occupation of lower ionisation states, compared to the CIE expectation for a given plasma temperature, which would mimic a lower temperature when fitted with a CIE model, and leave clear signatures in an oxygen line ratio map (Zheng et al., 2024b). Hence, the observed cool shell may in fact be a shell of underionised plasma behind the forward shock, which has experienced shock heating sufficiently recently to not have fully equilibrated. Even though this scenario bears a strong resemblance to processes observed in young SNRs (e.g. Borkowski et al., 2001), a fundamental difference is that the observed shock strength in the eRObub is much lower due to the interaction with tenuous hot CGM, implying less drastic differences between pre- and post-shock temperatures. Hence, the effect of NEI on the observed spectrum is likely different from that observed in SNRs.

To test this scenario, we replaced the CIE eRObub model with the `neij` model in `SPEX` for the cool shell spectrum (reg 3). The `neij` model describes the subsequent plasma emission following a sudden temperature change. The initial guess of the ionisation parameter (u) was $10^{11}\,\mathrm{cm^{-3}\,s}$. We reset the C, O, Ne and Fe abundances to $0.2\,Z_\odot$ and the $\mathrm{EM_{eRObub}}$ to approximately match the overall normalisation of the spectrum. The pre-shock temperature was fixed to that of the CGM, while the post-shock temperature was left free with an initial guess of 0.5 keV. It was obvious from several trials from different sequences of parameter thawing that the best-fit was always achieved for a large ionisation timescale ($u \gtrsim 10^{12}\,\mathrm{cm^{-3}\,s}$). At $u > 10^{12}\,\mathrm{cm^{-3}\,s}$ with a temperature in the order of 10^6–10^7 K, a vast majority of ions would have reached CIE (Smith & Hughes, 2010). Therefore, the NEI model simply returns to a CIE model. This result already indicates the cool shell is unlikely to be in NEI. To foster a more quantitative comparison, we fixed $u = 3 \times 10^{11}\,\mathrm{cm^{-3}\,s}$, as we argued to be a reasonable estimate given the approximate bubble age and CGM density, to force at least a moderate NEI signature and see how other parameters would adjust and accommodate this change. The best-fit model performed slightly worse than the CIE case ($\chi^2/\mathrm{dof} = 1.27$ versus 1.23 in the CIE case), but fundamentally, the resulting NEI and CIE had very similar spectral shape. This was because the post-shock temperature had decreased accordingly ($kT_\mathrm{post} = 0.19$ keV) to suppress the NEI signature. We therefore rule out the NEI scenario for the cool shell despite its intrinsic attractiveness.

Low temperature foreground component?

Another possibility for the cool shell is that it is not a physical part of the eRObub but a foreground structure to the eRObub. The most popular candidate would be the Loop I superbubble, visible in cold gas, whose relevance has been jeopardised after discovering the (southern) eRObub (Predehl

et al., 2020). Naturally, the Loop I superbubble would express itself in the cool shell and as a general foreground to the eRObub. Then the cool shell is the region where the Loop I superbubble does not overlap with the background eRObub in projection. The EM profile in Fig. 4.6 of the eRObub EM could become more symmetric about the Galactic plane if the Loop I contribution is subtracted out. However, admittedly, such an asymmetry is less evident from the large region, likely because abundance effects have introduced scatter in the EM.

Egger & Aschenbach (1995) identified and linked the observation of a local ring-like structure in H I (Dickey & Lockman, 1990) with simulation results from Yoshioka & Ikeuchi (1990), where Yoshioka & Ikeuchi (1990) showed that the formation of a dense ring or wall between two spherical shock waves is possible if both have reached the radiative stage. This observation led Egger & Aschenbach (1995) to conclude the existence of the Loop I superbubble, and its current interaction with the LHB.

While the main proposal of Egger & Aschenbach (1995) is to invoke the Loop I superbubble as the origin of the NPS, which remains a topic of great debate, we draw attention to a tentative observation which provides further evidence to the existence of a dust wall and hence the existence of the Loop I superbubble, revealed by a state-of-the-art 3-dimensional dust map inferred from Gaia stellar extinction (Edenhofer et al., 2024). Figure 4.17 shows the column density between a radial distance of 100 to 150 pc from us, where we converted the A_V pc^{-1} information in Edenhofer et al. (2024) to the unit of N_H pc^{-1} using $N_\mathrm{H} = 2.21 \times 10^{21}\, A_V$ by Güver & Özel (2009). We point out a prominent curved edge highlighted by orange arrows in the figure, located at a distance of 100–150 pc. The edge appears to mark the end of a dense wall, which further supports the scenario proposed by Egger & Aschenbach (1995) if they are real features but not artefacts in the inversion. In addition, Yeung et al. (2024) found that the LHB has a higher EM towards the direction of Centaurus, potentially caused by a tunnel of hot gas linking the Loop I superbubble with the LHB. This tunnel can be seen in the dust map as a hole with little N_H, located just within the northern dust edge as labelled in Fig. 4.17. One possibility for the cool shell (red outline in Fig. 4.17) is that the Loop I superbubble is more extended in projection than the extent of the dust edge/wall and the Galactic outflow in the background, hence producing a shell-like structure in front of the eRObub. A foreground component also would help to reconcile the somewhat higher EM in the northern bubble as seen in Fig. 4.6, when a uniform abundance is assumed everywhere.

A sketch of the possible scenario is illustrated in Fig. 4.18, which shows a slice of the 3D dust extinction map on the plane of $l = 320°$ (Edenhofer et al., 2024). It shows a wall of dense materials that is commonly referred to as the wall of the LHB. At about $b \sim 30°$ is the location of the Centaurus tunnel, which is a gap in the LHB wall that is potentially connected to the Loop I superbubble. One can see that the wall is inclined towards the LHB at higher latitudes, with the end marked by the dust edge in white at $b \sim 60°$. At longitude $l = 320°$, the cool shell is located at $b \sim 70°$. As the cool shell is a clear enhancement in the X-ray, the boundary of the Loop I superbubble should be sharp there. In the extreme case that the Loop I superbubble contributes solely to the cool shell, we can estimate its density and pressure from the fitted temperature and EM. If we assume the line-of-sight distance through the cool shell is $\sim$ 200 pc (400 pc) and the EM from the cool shell region is $\approx 4 \times 10^{-2}$ cm^{-6} pc (reg 3 in Table 4.3), the density of the cool shell would be $n_e \approx 1.4 \times 10^{-2}$ cm^{-3} (10^{-2} cm^{-3}). The corresponding thermal pressure is $P/k \sim 3 \times 10^4$ cm^{-3} K (2×10^4 cm^{-3} K), over-pressured with respect to the LHB (Puspitarini et al., 2014; Snowden et al., 2014; Yeung et al., 2024) and is probably still expanding. This estimate is in between the LHB and the Orion-Eridanus superbubble also in the solar neighbourhood ($n_e \sim 10^{-2}$ cm^{-3} and $P/k \sim 5 \times 10^4$ cm^{-3} K; Guo et al. 1995; Joubaud et al. 2019). However, the fitted abundance of the cool shell is consistent with other eRObub regions, which is lower than one would expect for a superbubble originating from a cascade of supernova explosions in the Sco-Cen OB association (Egger, 1998), casting doubt on this scenario.

Shadowing experiments of clouds beyond the Loop I superbubble, yet in front of the eRObub, are perfect targets to decompose the emissions from the two, given there are identifiable differences in their spectral shapes. Two such prime targets are molecular clouds CG 12 and Dobashi 6193. Both are sufficiently distant at about 650–700 pc (Reipurth & Bragg, 2021; Yeung & Freyberg, 2024), which is likely beyond the Loop I superbubble. They shadow the eRObub at about $b \sim 20°$,

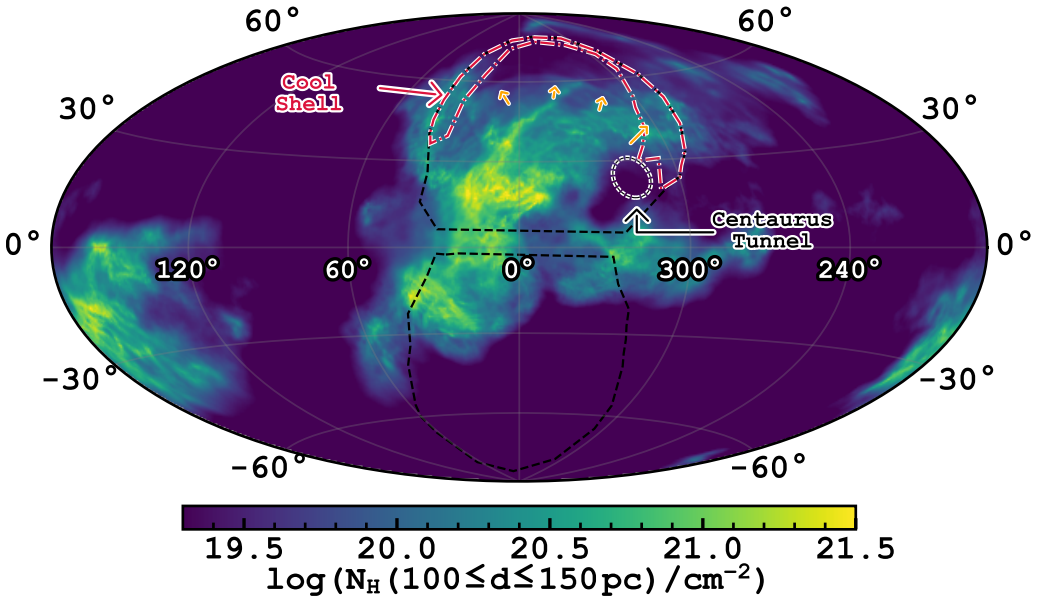

Figure 4.17: Column density map integrated between 100–150 pc inferred from Gaia stellar extinction (Edenhofer et al., 2024). The dust edge is highlighted by orange arrows, which may mark the end of the LHB-Loop I supberbubble interface. The cool shell could be a part of the Loop I superbubble that is not overlapping with the background outflow. We also indicate the location of the Centaurus tunnel, which appears to be a channel between the LHB and the Loop I superbubble that lies within the extent of this interface (Yeung et al., 2024). The overall silhouette of the eRObub is shown by the black dashed lines.

at the western base of the eRObub. One could quantitatively measure or rule out the X-ray emission from the Loop I superbubble with X-ray observations towards these targets.

4.6.2 Shock speed and energetics

Our spectroscopic analysis confirms previous works which found a typical gas temperature $\sim$ 0.3 keV inside the eRObub (Kataoka et al., 2013, 2018; Ursino et al., 2016), as we find a dominating component that has a characteristic temperature distribution in the range $kT = 0.26 \pm 0.03$ keV. This is around a factor $\sim$ 1.6 higher than the temperature of the CGM of $\simeq$ 0.16 keV measured in the background regions, with which the eRObub interact. Following the Rankine-Hugoniot jump conditions implies a very weak shock with a Mach number $\mathcal{M} \sim 1.6$, driven into the CGM. In Sect. 4.4, we showed that this Mach number would also be consistent with observed bubble morphology in the north, whereas the emission appears more limb-brightened in the south, pointing toward a higher Mach number. For the corresponding CGM sound speed $c_s \approx 200$ km/s, $\mathcal{M} \sim 1.6$ implies a shock velocity $v \approx 330$ km/s, inflating the eRObub. Furthermore, this implies a relative increase in pressure by a factor 3.0 at the shock front.

The eRObub predominantly emit in the 0.2–1.5 keV band. To estimate the energetics of the eRObub within this band, we summed the fluxes from both the low and high temperature components of our large regions (Table 4.8). They totalled $\sim 4 \times 10^{-8}$ erg s^{-1} cm^{-2}. The flux from the low-temperature component of the northern eRObub is twice that of the southern one. In contrast, the hemispheric difference is small for the hot component. We remind the reader that the region coverage of the eRObub is not complete at low latitudes to avoid confusion from complex line-of-sight structures during spectral fitting (coverage: north: $l \gtrsim 15°$; south: $l \lesssim -10°$), so this is likely an under-estimation of the fluxes from the full eRObub. For comparison, our geometrical model

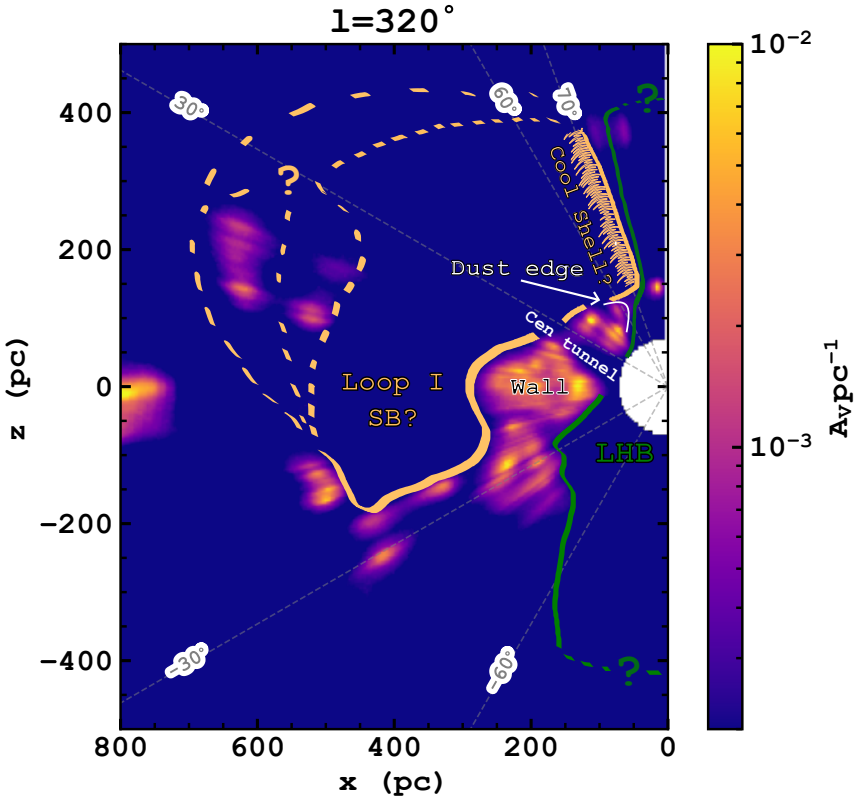

Figure 4.18: Illustration of the possible scenario of the cool shell as a part of the Loop I superbubble. The extinction map is taken from Edenhofer et al. (2024). The approximate outlines of the LHB and the Loop I superbubble are drawn, most uncertain at high latitudes and on the backside of the Loop I superbubble. If the cool shell is indeed foreground, its strong enhancement against the background means the boundary of the Loop I superbubble is well-defined at this latitude ($b \approx 70°$) and is probably still expanding.

reported in Table 4.1 produces integrated (absorption-corrected) count rates of $2.8 \times 10^4\,\mathrm{ct\,s^{-1}}$ and $2.3 \times 10^4\,\mathrm{ct\,s^{-1}}$ for the northern and southern bubbles, respectively. Assuming emission from a $kT = 0.3\,\mathrm{keV}$ plasma, this suggests a slightly larger total flux of $\sim 6.8 \times 10^{-8}\,\mathrm{erg\,s^{-1}\,cm^{-2}}$ in the 0.2–1.5 keV band, as expected.

To estimate the luminosity of the bubbles, we computed a spatially varying 'effective distance' for the emission by evaluating our geometric model:

$$d_{\mathrm{eff}}^2 = \frac{\int n(s)^2 s^2\,\mathrm{d}s}{\int n(s)^2\,\mathrm{d}s}, \tag{4.15}$$

which corresponds to an emission-weighted mean squared distance to the bubbles, along the line of sight. When averaged over the two respective hemispheres, the geometrical model has effective distances of $d_{\mathrm{eff}} = 6.4\,\mathrm{kpc}$ and $d_{\mathrm{eff}} = 10.9\,\mathrm{kpc}$ for the northern and southern bubbles. Assuming the fluxes determined in our spectral fits, this yields luminosities of $1.2 \times 10^{38}\,\mathrm{erg\,s^{-1}}$ and $2.2 \times 10^{38}\,\mathrm{erg\,s^{-1}}$, respectively. For comparison, the fluxes of our geometrical model imply $1.8 \times 10^{38}\,\mathrm{erg\,s^{-1}}$ and $4.3 \times 10^{38}\,\mathrm{erg\,s^{-1}}$. Our luminosity estimates are slightly lower than the estimation by Predehl et al. (2020), mostly driven by a lower effective distance to the northern bubble in our model, but not a difference in flux or surface brightness.

Nonetheless, assuming our vertical extent of 16 kpc of the northern bubble and the current shock speed of $330\,\mathrm{km\,s^{-1}}$, we recover an age of the eRObub to be $\sim 20\,\mathrm{Myr}$, as in Predehl et al.

Table 4.8: Breakdown of the total flux from the eRObub, by hemispheres and temperature components (Sect. 4.5.2)

Total flux (0.2–1.5 keV) (10^{-9} erg s^{-1} cm^{-2})		
Component	cool (0.26 keV)	hot (0.56 keV)
North	18.4	5.5
South	9.0	6.2

Notes.
Fluxes within the $-10° < b < 15°$ were not taken into account as they were not covered by the spectral extraction regions.

(2020). Nonetheless, this computation is highly uncertain, as both the true bubble geometry and shock wave trajectory need to be assumed, and it only indicates a rough estimate of the characteristic age of the bubbles. Due to the strongly asymmetric morphology of the eRObub in an inhomogeneous ambient medium, we refrained from using any spherically symmetric model (e.g. Sedov-Taylor) to constrain the energy which inflated the bubbles. Instead, we rescaled our best-fit model of the X-ray emitting density profiles for the two bubbles using their normalisations (i.e., $\propto A_i^{1/2}$), and integrated over the bubble volume to obtain a census of the entire hot gas mass. We obtained average densities of $\bar{n}_N = 9.3 \times 10^{-4}\,\mathrm{cm}^{-3}$ and $\bar{n}_S = 2.8 \times 10^{-4}\,\mathrm{cm}^{-3}$ for the two hemispheres (with the difference mainly due to the larger volume attributed to the southern bubble), and an integrated hot gas mass of $7.4 \times 10^7\,M_\odot$. Assuming our average temperature of $kT = 0.26\,\mathrm{keV}$, this yields a total thermal energy of $9.2 \times 10^{55}\,\mathrm{erg}$, recovering a total energy in a similar range as Predehl et al. (2020), despite vastly different assumed geometries.

4.6.3 Origin of the eRObub

Our results, including energetics, temperature, and abundances of the X-ray emitting gas, could inform models of the formation of the eRObub and FB, invoking past star formation or AGN activity. Most prominently, our analysis measures a sub-solar composition of the emitting material of $\sim 0.2\,Z_\odot$, which is not dissimilar to the expected CGM abundance. We could not confirm the observation of $\mathrm{Ne/O} = 2.1 \pm 0.2\,\mathrm{Ne}_\odot/\mathrm{O}_\odot$ along selected sight lines by Gupta et al. (2023) as the scatter in our measurement ($\mathrm{Ne/O} = 1.12^{+0.73}_{-0.20}\,\mathrm{Ne}_\odot/\mathrm{O}_\odot$) is large. However, we note the tendency of such enhancement in the northern hemisphere (Fig. 4.15). On the other hand, we saw an indication of Fe depletion with respect to O.

Generally, Ne overabundance in the eRObub would be unexpected in an AGN outburst model. However, it would also not be trivial to ascribe such behaviour to a fuelling of the bubbles by star formation (cf. Gupta et al., 2023). Generally, the stellar winds and core-collapse supernovae associated with star formation bursts are expected to produce large quantities of light α-elements, including O, Ne, and Mg, and smaller amounts of Fe-group elements (Sukhbold et al., 2016), as might be visible in our average ratio of $\mathrm{Fe/O} = 0.79^{+0.26}_{-0.23}\,\mathrm{Fe}_\odot/\mathrm{O}_\odot$. However, relative enhancements in the production of Ne to O compared to the solar composition are typically not predicted for stellar nucleosynthesis for any mass in the range $9 - 120\,M\odot$ (Sukhbold et al., 2016). Therefore, we believe further theoretical modelling is necessary before quantitatively interpreting the relative abundances in the X-ray bright plasma in the eRObub in favour of a particular physical origin.

As shown above, their X-ray morphology and temperature imply an energy around $10^{56}\,\mathrm{erg}$ necessary for inflating the bubbles, which requires a mechanism with an average power of $P \gtrsim 1.5 \times 10^{41}\,\mathrm{erg\,s}^{-1}$ to produce the bubbles within an age around $2 \times 10^7\,\mathrm{yr}$. Such an energy output is certainly feasible for an AGN outburst (e.g., Yang et al., 2022), even over much shorter time spans, as the Eddington luminosity of the Milky Way black hole is $L_\mathrm{Edd} \approx 5 \times 10^{44}\,\mathrm{erg\,s}^{-1}$. Achieving the required power from a star formation burst requires energy input corresponding to around one supernova per century, or a total of 10^5 supernovae during the lifetime of the

bubbles. While these numbers are in principle feasible for a nuclear starburst (Sarkar et al., 2015; Nguyen & Thompson, 2022), such a large supernova rate would imply significant elevated gamma-ray emission from the GC at the radioactive decay energy of ^{26}Al, which is in contrast with the observed distribution (Diehl et al., 2006; Su et al., 2010). Furthermore, such a high supernova rate appears to be contradicted by the relatively low star formation rate of $0.1\,M_\odot\,\mathrm{yr}^{-1}$ measured for the GC (Barnes et al., 2017), which implies a supernova rate around $1\,\mathrm{kyr}^{-1}$ when assuming a Kroupa initial mass function (Kroupa, 2001) and a minimum exploding mass of $8\,M_\odot$. A possible alternative scenario invoking star-formation fuelling is that of a conical Galactic wind originating in star-forming regions, which produces a bubble-like morphology only in projection (Zhang et al., 2024; Churazov et al., 2024). This scenario would both reduce the total energy of the hot gas and increase its likely lifetime, reducing the required power output sufficiently to allow fuelling by the observed star formation activity in the Galaxy.

Generally, a shortcoming of an AGN outburst model is that a short, strong energy injection predicts much higher present-day temperatures (or equivalently oxygen line ratios) than observed in X-ray data (Sarkar et al., 2023). In particular, the multi-keV plasma behind the forward shock predicted by Yang et al. (2022) does not appear to be observed in eROSITA spectra of any portion of the bubbles. This problem would likely be avoided by a model invoking long-term, low-power fuelling of the bubbles, such as through star formation (Sarkar et al., 2015, 2017; Nguyen & Thompson, 2022; Zhang et al., 2024), as the involved temperatures would be expected to be much lower.

A further interesting puzzle piece is given by the orientation of the bubbles. While the FB appear to be relatively orthogonal to the Galactic plane (Ackermann et al., 2014), the eRObub appear to be somewhat tilted, as the northern and southern orientation angles appear to be offset from each other in the east-west direction (see Sect. 4.4). A hypothetical AGN jet can, in principle, have an arbitrary orientation with respect to the Galactic plane, and thus a tilted bubble morphology appears unsurprising. However, one may expect a nuclear starburst to produce a perpendicular structure, particularly in the presence of collimation through dense surrounding gas in the Galactic disk. However, as shown by Nguyen & Thompson (2022), a non-uniform distribution of stellar mass within the nuclear region may be capable of producing similarly tilted morphologies as observed. Furthermore, the apparent 'tilt' of both bubbles towards the Sun may also be interpreted as a signature of a conical star-formation-driven outflow (Zhang et al., 2024; Churazov et al., 2024) producing a bubble morphology in projection.

A final important aspect to consider is the presence of leptonic cosmic rays, in the form of the FB, on the inside of the eRObub. Such a morphology appears to be well reproduced in simulations of an energetic short-term jet activity from Sgr A*, in which energetic cosmic rays are injected at the base of the jet, and are advected with the hydrodynamic flow (Yang et al., 2022). Thermal X-ray emission from CGM gas shocked and heated by the jet forms the eRObub, which is separated by a contact discontinuity from the decelerated outflow in which the leptonic cosmic rays produce radio and GeV γ-ray emission via synchrotron and inverse Compton processes. In contrast, in the model of starburst powering, it is not intuitively explained why the most energetic cosmic rays would be located behind the reverse shock (i.e. in the FB), rather than the forward shock, corresponding to the eRObub. A multiwavelength morphology similar to the observed one would require cosmic rays to be accelerated in the nuclear region, rather than at the shock front expanding into the CGM.

While an origin close to the GC is required if one assumes that the eRObub and the FB are physically connected, it is worth reminding that the two structures need not to share a common origin. Although a significant portion of the eRObub emission is likely from the inner Galaxy, the active star-forming ring at a Galactocentric distance of 3–5 kpc has been shown to be powerful enough to easily drive galactic winds to a vertical distance of 10 kpc (Zhang et al., 2024). Magnetic ridges observed in radio polarised intensity maps also appear to trace the silhouette of the eRObub closely. The fact that these magnetic ridges seemingly originate from the locations of high star formation rates in the star-forming ring seems to lend credibility to this model. It is also unclear whether the edge of the eRObub is a forward shock front or just a contact discontinuity. The fact that we found the NEI signature to be unimportant in interpreting the eRObub spectra may point

to the latter, as proposed by Churazov et al. (2024) who suggested the NPS (or more generally for different parts of the eRObub) could be raised to a high vertical distance due to the buoyancy of hot gas stemming from active star-forming regions. Our measurement of an enhanced elemental abundance of the NPS compared to the other parts of the eRObub agrees with this scenario for the NPS. However, an alternative explanation might be required for the rest of the eRObub.

4.7 Summary

This work presents a detailed analysis of the physical properties of the gigantic X-ray emitting eROSITA bubbles, based on the first *SRG*/eROSITA All-Sky Survey dataset. On the one hand, this analysis included the comparison of the observed all-sky emission map with geometrical models, which was complemented by a detailed modelling of spatially resolved X-ray spectra.

In our morphological analysis, we constructed an empirical geometrical model of the eRObub, consisting of two half-ellipsoids with flexible orientation, filled with three-dimensional hot-gas densities following the profile of a blast wave originating from the GC, and propagating in an idealised CGM halo. We demonstrated that such a model can reasonably reproduce the eRASS1 count rate map (Predehl et al., 2020). By fitting our geometrical model in projection to the observed emission map, we found that the eRASS1 data provide a good handle on the horizontal extent of the eRObub ($\sim 6\,\mathrm{kpc}$). However, limited by our vantage point within the Galactic plane and the low density in the outer CGM, the eRASS1 is almost insensitive to the vertical extent of the eRObub. Our model requires a significant tilt of the northern bubble towards the west and the Sun ($(\theta, \phi) \approx (30^\circ, 220^\circ)$) in order to reproduce the protruded contour of the eRObub in the west. In contrast, the southern bubble only appears to exhibit a weak tilt towards the Sun, indicating a significant north-south geometrical asymmetry. The fact that our model prefers an orientation of both bubbles in our direction might be seen as evidence for an outflow that in reality is conical and originating at $\sim 3\,\mathrm{kpc}$ from the GC, and need not exhibit a closed shell-like morphology.

Under the assumption of our blast-wave density profile, the shell thickness is a tracer of the shock Mach number, which would indicate a faster shock in the southern bubble, whereas the outflow appears only weakly supersonic in the north ($\mathcal{M} \sim 1.5$). Furthermore, if the observed brightness variations are taken to trace the ambient CGM density, significant deviations from a simple azimuthally symmetric density profile are required, for instance, to reproduce the bright NPS.

Using the spectra extracted from constant S/N regions with sky area $\sim$5–10 deg^2 throughout the eRObub in the western Galactic hemisphere, we produced temperature and EM maps of the eRObub by modelling it as a CIE plasma in addition to the conventional SXRB components. Overall, the eRObub temperature is consistent with $\sim 0.3\,\mathrm{keV}$ gas with EM increasing towards the Galactic plane. The maps also confirm an apparent shell of cooler gas surrounding the northern bubble that is as bright as the eRObub interior, which is unexpected in a simple forward shock picture for the eRObub. However, significant scatter remains in the temperature and EM measurements, hinting at hidden spectral features that a simple single temperature assumption cannot fully explain.

In light of the limitation brought by S/N, we subsequently defined customised larger regions to boost S/N and isolate interesting features such as the FB and NPS, while accounting for the latitudinal variations in the background. Even without fitting, it was immediately apparent from the enhanced Fe XVII, Ne IX,X and Mg XI lines that the temperature is significantly enhanced above the CGM temperature. However, the FB regions do not exhibit a noticeable difference in X-ray spectral signature, such as evidence of nonthermal emission, compared to the eRObub regions outside.

The improved S/N from the large regions allowed us to determine the abundances of oxygen, iron, and neon. Despite the greater number of degrees of freedom, a single temperature model could not fit most regions satisfactorily, except for the cool shell, which was characterised by temperatures of 0.18–0.21 keV. The greatest difficulty in matching the observed spectra arose from the Fe XVII L shell lines between $\sim$0.70–0.85 keV that consistently showed an enhanced $3d/3s$ (or

15 Å/17 Å) line ratio. We showed that, while predictions differ slightly across popular plasma codes `SPEX` and `AtomDB/apec`, none can reproduce the observed ratio using a single temperature component, indicating the need for a second temperature component to resolve the discrepancy. We found alternative explanations for a boosted Fe XVII 15 Å/17 Å ratio, involving resonant scattering, charge exchange, or an ionised absorber, less convincing than a two-temperature model. The low- and high-temperature components exhibit remarkable constancy across latitudes, at 0.26 ± 0.03 keV and $0.56^{+0.04}_{-0.02}$ keV respectively, with the cooler component on average exhibiting $\sim$ 4 times more EM. The presence of two temperatures could indicate a wider distribution of gas temperatures in the outflow, quite commonly found in X-ray observations of nearby edge-on galaxies.

The cool shell could be formed by rapid radiative cooling following the passing of a forward shock forming the eRObub, as seen in some old SNRs. This scenario is challenged by the low ambient density in the outer halo, casting doubt on the efficiency of radiative cooling in this case. In principle, NEI effects could also be important, especially in low-density environments after shock heating, implying underionisation in the cool shell, which may mimic a lower temperature plasma in CIE. However, we found no evidence of NEI when fitting the corresponding model to the observed cool shell spectra, indicating that the cool shell gas has likely reached equilibrium.

The cool shell does not require a two-temperature model to fit and has a temperature similar to the low-temperature component within the eRObub, raising the possibility that the low-temperature component is at least partially contributed by a foreground structure that does not entirely overlap with the Galactic outflow in the background. The natural candidate is the Loop I superbubble. We identified a prominent dust edge within 100–150 pc from us in the recent three-dimensional dust map (Edenhofer et al., 2024), marking the end of a wall of dust at high latitude ($b \approx 60°$), that could be compressed by the interaction of the Loop I superbubble and the LHB – echoing the original idea by Egger & Aschenbach (1995). Future shadowing observations of molecular clouds beyond the distance of the Loop I superbubble can quantify or eliminate the foreground contribution of the eRObub.

The eRObub spectra favour a subsolar elemental abundance similar to the CGM ($\sim 0.2\,Z_\odot$), consistent with a structure that extends to large vertical distance. However, our data provide tentative evidence of light α-enhancement compared to iron, which would be suggestive of a star-formation driven scenario involving metal enrichment through core-collapse supernovae. However, the evidence of metal enrichment seems strongest towards the NPS, in which our fitting showed a statistically significant increase in abundances compared to the rest of the eRObub. This could indicate a separate origin for the NPS from the eRObub, for instance, stemming from active star-forming regions on the Galactic disc.

4.8 Appendix A: Reconstruction of a smoothed eRASS1 all-sky map

A three-colour all-sky map based on eRASS1 was published in image form in the eROSITA bubble discovery paper (Predehl et al., 2020)[2], but were not released in a directly machine-readable format. Since the eROSITA all-sky maps strongly outperform the imaging quality of all previous X-ray all-sky surveys, it is worthwhile to reconstruct the eRASS1 map on a quantitative scale. In order to achieve this, we mapped the individual images in the RGB channels (0.3–0.6 keV, 0.6–1.0 keV, 1.0–2.3 keV) of Predehl et al. (2020) from their Hammer-Aitoff projection onto the coordinate system of the published eRASS1 half-sky broad-band maps (Zheng et al., 2024a)[3]. These half-sky maps were then smoothed to mimic the processing performed on the available image (Predehl et al., 2020), and used to recalibrate the all-sky emission from arbitrary image units back into physical count rates. Since the eRObub appear most prominently in the intermediate energy band

[2]See also https://www.mpe.mpg.de/7461761/news20200619

[3]These half-sky maps are publicly available at https://erosita.mpe.mpg.de/dr1/AllSkySurveyData_dr1/HalfSkyMaps_dr1/

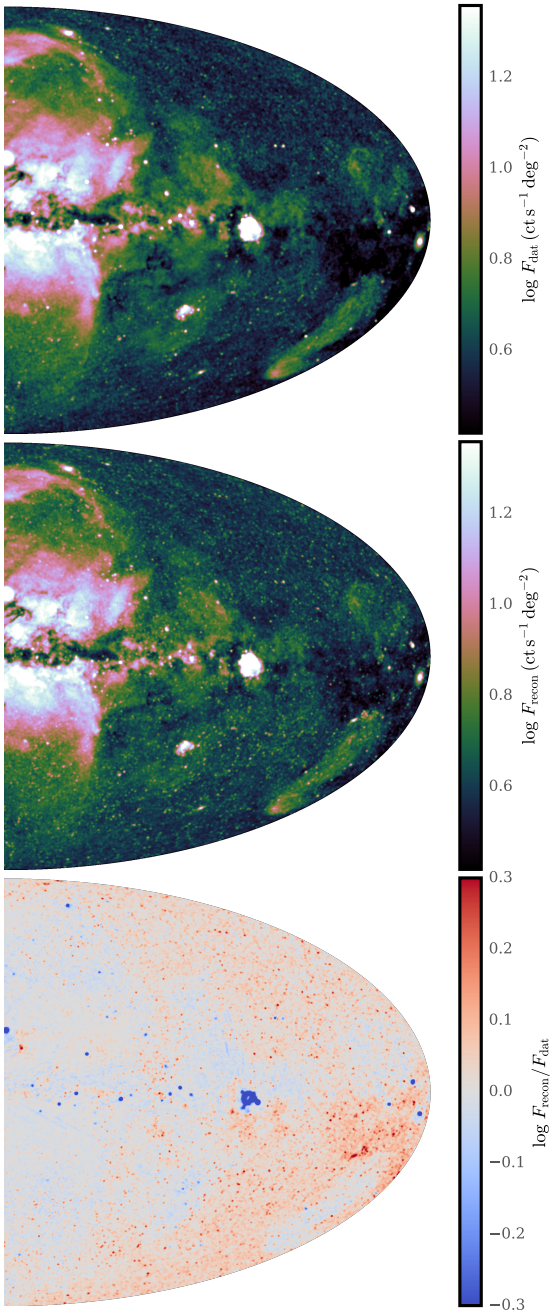

Figure 4.19: Calibration of reconstructed all-sky map. The top panel shows the publicly available eRASS1 0.6–1.0 keV all-sky image (Zheng et al., 2024a; Merloni et al., 2024), and the middle panel shows our best attempt at recalibrating the all-sky eRASS1 image (Predehl et al., 2020) on a quantitative scale. The bottom panel shows the ratio of the two, with areas appearing in blue/red having under-/overestimated reconstructed fluxes. The average deviation is $\Delta \log F_{\rm recon}/F_{\rm dat} \approx 7.7 \times 10^{-2}$, corresponding to relative deviations around 20%. All maps were smoothed with a Gaussian kernel of 15′ for display purposes.

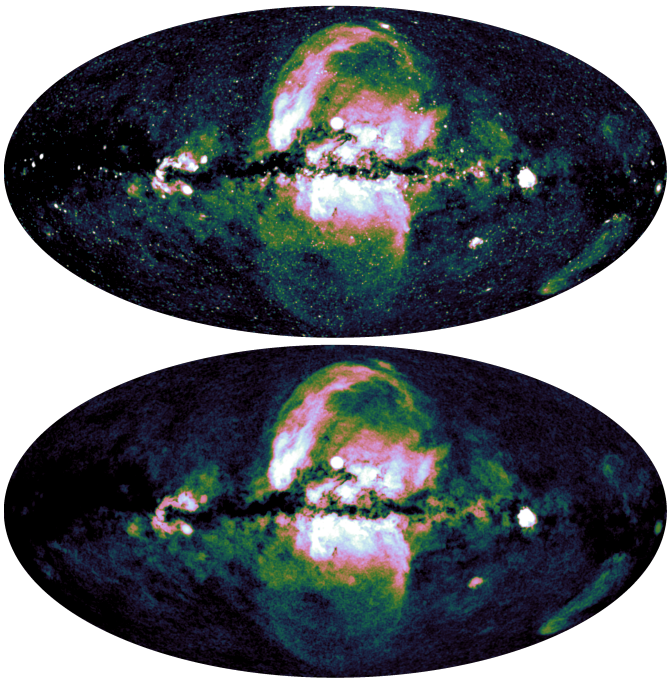

Figure 4.20: Masking of point and point-like source in the eRASS1 all-sky map. The top and bottom panels show the eRASS1 all-sky image (Zheng et al., 2024a; Merloni et al., 2024) in the 0.6–1.0 keV band, before and after our masking of point sources, respectively. Both maps were smoothed with a Gaussian kernel of 15′ for display purposes.

0.6–1.0 keV (Predehl et al., 2020), this energy band was the primary focus of our reconstruction. To achieve this, we sorted the all-sky image into narrow bins of increasing image value, and for each bin, we computed the corresponding median count rate in the overlapping area in the available half-sky image in the same band. The resulting nonlinear relation between image values and corresponding physical units was then used to place the all-sky map on a physical scale of count rate per unit area.

This process of reconstruction is illustrated in Fig. 4.19. While the reconstructed map is visually almost indistinguishable from the half-sky map, quantitative offsets are present. On the one hand, these are caused by the saturation of the all-sky image around the brightest sources. However, a relative excess can also be seen in the reconstruction of faint regions, which can likely be attributed to the removal of the emission from detected point sources in Zheng et al. (2024a), lowering the apparent flux in the areas without much diffuse emission. These shortcomings have little impact on our results, since we are interested only in large-scale structures ($\gtrsim 1^\circ$) with significant diffuse emission. Furthermore, we refrain from interpreting any quantitative flux scales in our analysis, since we are primarily interested in the geometry of the bubbles and relative flux differences. The large spatial scales of our analysis target also imply that little improvement would be expected from including additional eRASSs, which would only lower statistical fluctuations, while systematics are our main source of uncertainty.

The resulting recalibrated map (top panel in Fig. 4.20) contains numerous bright extended objects with much smaller angular sizes than the target of our analysis, the eRObub. These objects, which include Galactic SNRs, galaxy clusters, and misclassified emission around bright point sources (Merloni et al., 2024), are treated as contaminants for our morphological analysis. In order to remove these, we followed a pragmatic approach similar to Predehl et al. (2020), in which we successively convolved the half-sky map with Gaussian filters of scales increasing from 15′ to 1.°5. After each step, the input image was compared to the convolved one, and pixels were

masked which exceeded the smoothed image by a fixed threshold. The 'holes' left by the masked pixels were filled by the local value of the respective smoothed image. In this way, the majority of X-ray emitting structures with scales $\ll 1^\circ$ were excluded from our analysis. In Fig. 4.20, we show our resulting cleaned map with bright point and point-like sources removed (see Fig. 4.1 for an RGB representation). As can be seen, our approach is very effective at removing compact sources with typical extents $\ll 1^\circ$ from the map. However, intrinsically highly extended features, such as the Vela SNR, the Large Magellanic Cloud, the Virgo galaxy cluster, or bright straylight around Sco X-1, persisted in the map and had to be masked manually before fitting.

4.9 Appendix B: Supplementary information on morphological fits

This section provides further quantitative details on the morphological fit of the eRObub performed in Sect. 4.4. Figure 4.21 displays a quantitative comparison of the observed count rate, with the posterior prediction, and associated uncertainty of our modelling, as well as the deviations of the data from the best fit (taking into account systematic scatter). This demonstrates much more complex structures in the real eRObub than our model can produce. Strong deviations are clearly present around the eastern base of the northern bubble, where absorption appears strongly underestimated, as well as along the NPS, which in reality is even thicker than predicted for a mildly supersonic shock wave shell. Furthermore, the western edge of the southern bubble and the Lotus Petal Cloud (Liu et al., 2024) show excess observed emission.

In Fig. 4.22, we illustrate the multidimensional constraints on the model parameters of the two bubbles derived with MCMC. These plots showcase the bimodality of certain parameter constraints, for instance, the semi-minor axes ($b_{N,S}$) of the two ellipsoids, with potential peaks at 5.0 and 5.8 kpc. Furthermore, parameter degeneracies are observed, such as between the northern bubble vertical size a_N and its tilt θ_N, which are dictated mostly by the Galactic latitude of the northern bubble edge. The same effect leads the vertical size of the southern bubble to be entirely unconstrained above a lower limit, as the top of the bubble has effectively no influence on the fit. Overall, these exercises reemphasise that, while the general discussion of the eRObub morphologies (Sect. 4.4) may be illuminating, the presented tools are little more than toy models designed to separate projection effects from intrinsic morphology, and are incapable of tracing the physical complexity of the actual phenomenon known as the eRObub.

4.10 Appendix C: Alternative explanations to the enhanced Fe XVII 15 Å/17 Å line ratio

We considered two alternative scenarios, resonance scattering and charge exchange combined with ionised gas absorption, in producing the enhanced Fe XVII 15 Å/17 Å line ratio in addition to the two-temperature plasma model. Despite the arguably more interesting physics involved, we found they were not as convincing as the two-temperature model.

For Sects. 4.10.1 and 4.10.2, the spectral extraction regions were defined slightly differently from the main text as illustrated by Fig. 4.23. Reg 0 and 10 in Fig. 4.23 are the background regions for the analyses below.

4.10.1 Appendix C.1: Resonance scattering

One possible mechanism to produce an enhanced Fe XVII 15 Å/17 Å ratio is by resonance scattering (RS). Fe XVII λλ 15.01, 15.26 Å lines have higher oscillator strengths compared to the Fe XVII λλ 16.77, 17.05 Å lines (see Table 4.5), thus the former can become optically thick more easily compared to the latter (Gilfanov et al., 1987). This effect has been observed in cores of galaxy clusters from the evidence that the Fe XVII 15 Å lines are being suppressed due to the non-negligible optical depth (e.g. Xu et al., 2002; Sanders & Fabian, 2006; Werner et al., 2009, see also a review from

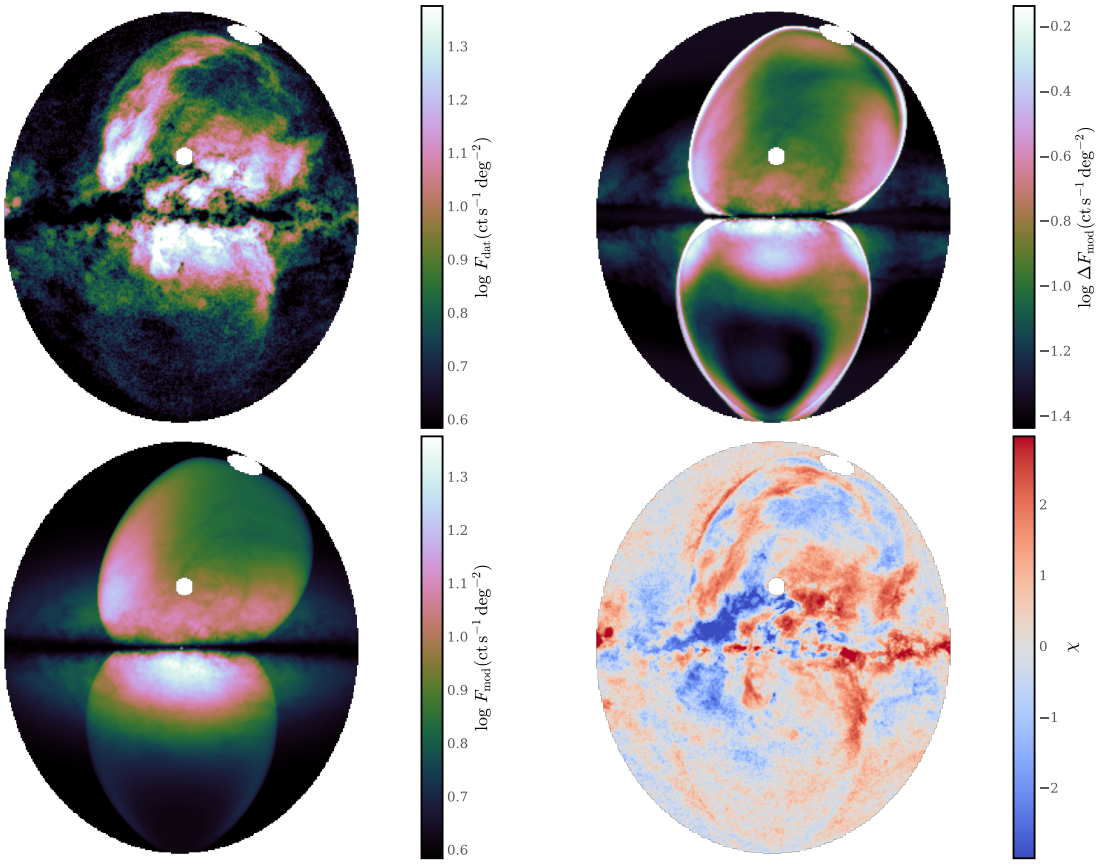

Figure 4.21: Visualisation of the 'best fit' of the bubble morphology. The top left panel shows the fitted data, the compact-source-masked 0.6–1.0 keV count rate image of the region surrounding the eRObub. The lower left shows the corresponding morphological fit, meaning the median of the posterior at a given location. The upper right shows the corresponding error, i.e., the posterior uncertainty. Finally, the lower right shows the normalised deviation from the best fit χ, taking into account both the fitted systematic scatter s and the model uncertainty.

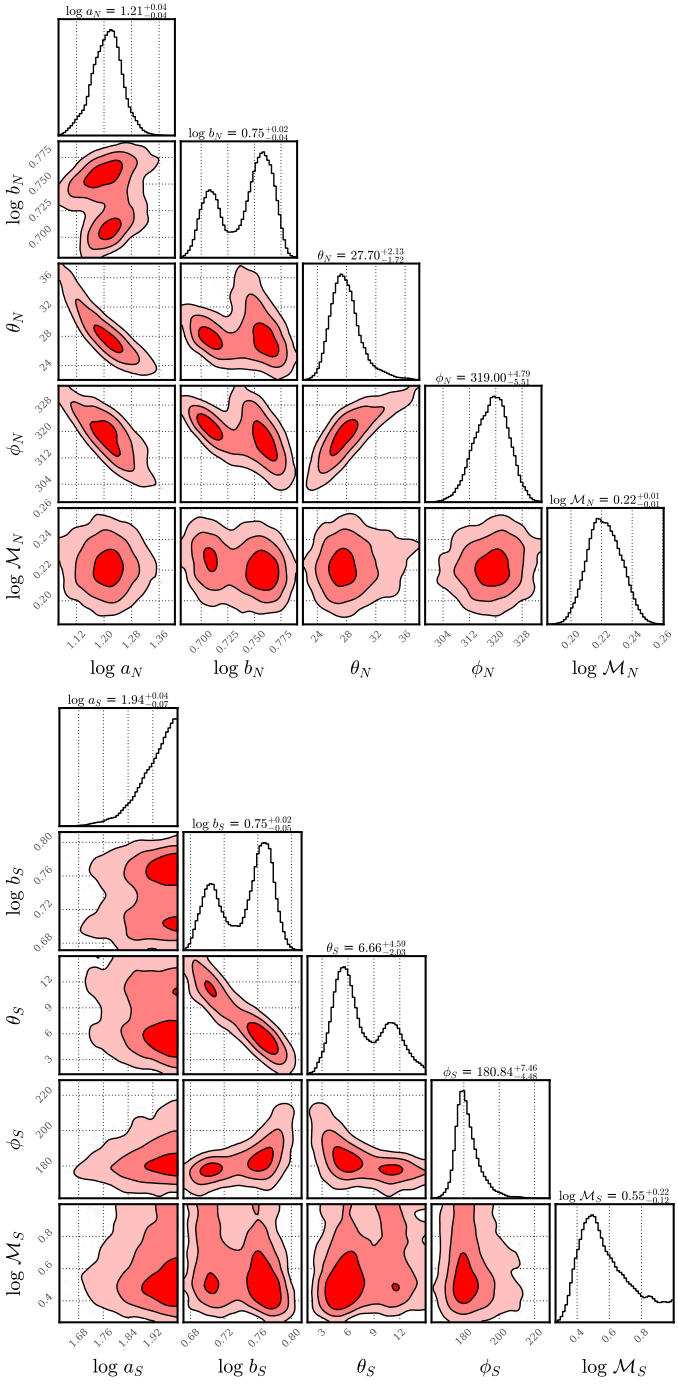

Figure 4.22: Geometrical parameter degeneracies. The top and bottom panels show the constraints on the parameters describing our geometrical model of the northern and southern bubbles, respectively. In each corner plot, the diagonal plots show the marginal probabilities, and the off-diagonal plots the joint probabilities (marking $1, 2, 3\,\sigma$ contours), of bubble size (a_i, b_i), orientation (θ_i, ϕ_i), and shock Mach number ($\mathcal{M}_i$).

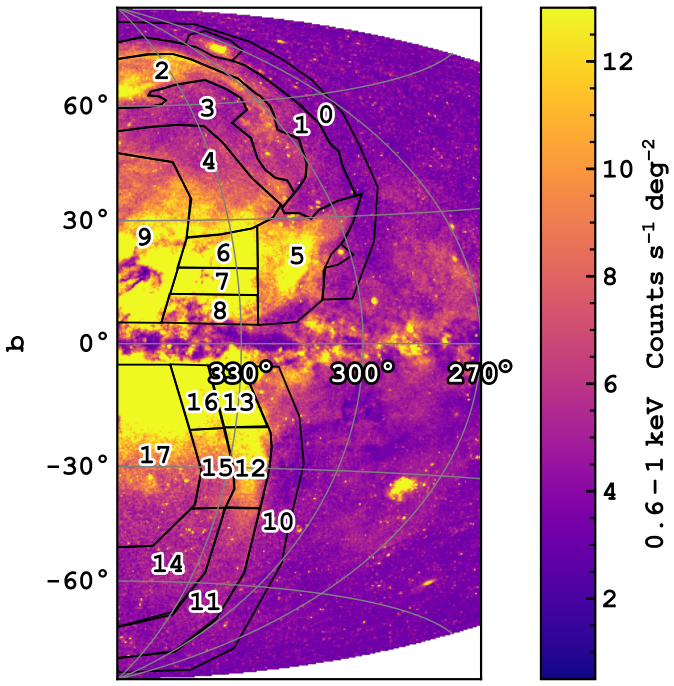

Figure 4.23: Region definition for Sect. 4.10.1 and 4.10.2.

Churazov et al. (2010)). In fact, in the simplest case of a gaseous sphere in hydrostatic equilibrium, usually appropriate for galaxy clusters or elliptical galaxies, the expectation from RS is that the photons of the strong resonance lines will diffuse out from the core, suppressing the line intensity towards the core while enhancing it at the outskirts. If RS is responsible for the anomalous line ratio, our data suggest a scenario where the Fe XVII 15Å photons are scattered into the line of sight, analogous to cluster outskirts.

We added the list of resonance lines in Table 4.5 in addition to the single temperature models to test the RS scenario further. The listed resonance lines with oscillator strength $f > 10^{-2}$ were added as Gaussian lines of free normalisations, with line centres fixed at the listed wavelengths and a fixed width of FWHM=5 eV (negligible compared to eROSITA spectra resolution of FWHM∼60 eV (Predehl et al., 2021), but numerically beneficial during fitting). The RS lines were also subjected to the same absorption column density as other background components. We show an example comparison of a single temperature model and the model with additional RS lines in Fig. 4.24.

With the additional resonance lines, the anomalous Fe XVII 15 Å/17 Å ratio is remedied, by the help an enhanced Fe XVII 15 Å line and almost no additional Fe XVII 17 Å contribution by RS. The best-fit parameters (and upper limits of resonance lines if intensity is consistent with 0) are shown in Table 4.9. It is common for the low-latitude regions to show enhanced O VIII Lyα and Ne IX line in the RS component. eROSITA's CCD detectors do not have adequate spectral resolution to resolve and identify the individual resonance lines. However, if we look into the best-fit parameters for indications, the Fe XVII λ 15.26 Å line is stronger than the Fe XVII λ 15.01 Å line despite the lower f, not following the expectation from RS exactly. The cause of this not difficult to see from the residuals from the single temperature model (upper panel of Fig. 4.24) that the residual peaks almost exactly at 0.80 keV (15.5 Å), centred closer to the Fe XVII 15 Å lines that have smaller f. This is an argument against the RS hypothesis, and the main reason why it is not our preferred

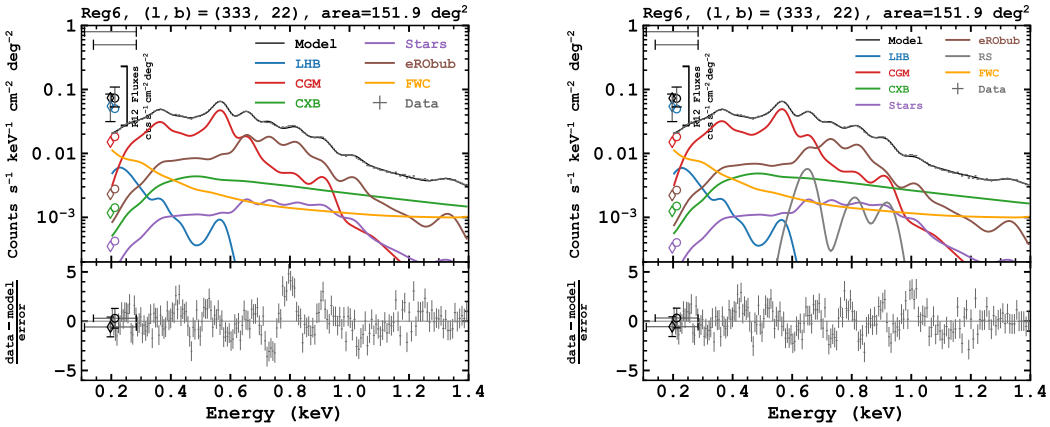

Figure 4.24: Comparison of the one temperature model with the model with additional RS lines in Reg 6 defined in Fig. 4.23.

solution to the anomalous Fe line ratio. Nonetheless, the 0.80 keV under-subtraction could also be caused by a contribution from the closely spaced O VIII Lyβ below 0.8 keV, complicating the line identification under eROSITA ∼60 eV spectral resolution.

The main source of resonance photons could be from the hot ISM in the Galactic plane, or coronal emissions from stars, but it is less likely to be from the eRObub itself. It is because if the eRObub is the main source, the situation is likely similar to RS in SNRs, where the denser gas at the shell has higher optical depth and scatters the photons away from the line of sight (Kaastra & Mewe, 1995; Amano et al., 2020; Li et al., 2024). This would create a suppressed Fe XVII 15 Å/17 Å ratio, contrary to our observation. Of course, the discussion above implicitly assumed a shell-like density profile, which may not necessarily apply to the eRObub. On the other hand, a more realistic model strongly depends on the geometry and densities of the hot gas, which we do not have enough observational constraints on, unlike galaxy clusters or elliptical galaxies, where one can assume spherical symmetry. More detailed work involving, for instance, Monte Carlo simulations, is helpful in quantifying the effect of RS in non-spherical geometries. Nonetheless, suppose the source of resonance photons is either the hot ISM or coronal emission from stars in the MW, then they should be, on zeroth order, distributed in a way following the disk-like MW potential. Even without the spherical symmetry of galaxy clusters, it is still natural to expect RS to cause a diffusion of resonance photons from the disk towards higher vertical distances and be scattered into our line-of-sight.

4.10.2 Appendix C.2: Charge exchange and ionised absorber

Gu et al. (2016b) suggests charge exchange (CX) and the presence of an ionised absorber yields a statistically significant improvement on the spectral fits of the *Suzaku*/XIS and *XMM-Newton*/EPIC data of the NPS. The evidence of CX mainly relies on the observation of line centroid shift of the O VII Heα triplet towards the forbidden line, which is evident in the *Suzaku*/XIS data, but less so in the *XMM-Newton*/EPIC data. The need for an ionised absorber originates from the anomalously high O VIII Lyβ/Lyα ratio.

From the eROSITA spectra, it is not obvious that there is a systematic shift in the O VII Heα centroid redwards to the forbidden line under the assumption of CIE plasma. We suspect the shift Gu et al. (2016b) observed could be caused by small calibration imperfections in the *Suzaku*/XIS at ∼ 0.5 keV, where similar residual can be seen when the standard calibration source SNR 1E 0102.2-7219 is fitted with the IACHEC model (Plucinsky et al., 2017). Otherwise, the *XMM-Newton*/EPIC spectra agree with the CIE assumption reasonably well at O VII Heα, similar to eROSITA spectra. Despite the intrinsic attractiveness of CX in a Galactic outflow scenario,

Table 4.9: Best-fit parameters of the models with additional resonance lines.

Region[††]	EM_{LHB} (10^{-3} cm^{-6} pc)	EM_{CGM} (10^{-2} cm^{-6} pc)	CXB_{norm} (ph s^{-1} cm^{-2} keV^{-1} deg^{-2})	kT_{eRObub} (keV)	EM_{eRObub} (10^{-2} cm^{-6} pc)	$Z_{O,eRObub}$ ($Z_{O,\odot}$)	$Z_{Ne,eRObub}$ ($Z_{Ne,\odot}$)
2	$4.28^{+0.12}_{-0.13}$	$5.66^{+0.04}_{-0.04}$	$4.05^{+0.11}_{-0.39}$	$0.370^{+0.008}_{-0.006}$	$1.24^{+0.17}_{-0.21}$	$0.20^{+0.03}_{-0.16}$	$0.20^{+0.03}_{-0.16}$
3	$3.68^{+0.11}_{-0.11}$	$4.45^{+0.04}_{-0.04}$	$3.65^{+0.03}_{-0.03}$	$0.368^{+0.005}_{-0.005}$	$1.64^{+0.05}_{-0.05}$	$0.05^{+0.00}_{-0.00}$	$0.05^{+0.00}_{-0.00}$
4*	$2.34^{+0.06}_{-0.06}$	$6.88^{+0.04}_{-0.06}$	$3.54^{+0.03}_{-0.03}$	$0.374^{+0.003}_{-0.003}$	$2.07^{+0.09}_{-0.09}$	$0.11^{+0.01}_{-0.01}$	$0.11^{+0.01}_{-0.01}$
5*	$3.15^{+0.07}_{-0.07}$	$11.17^{+0.05}_{-0.05}$	$3.81^{+0.02}_{-0.02}$	$0.364^{+0.004}_{-0.003}$	$2.22^{+0.05}_{-0.05}$	$0.05^{+0.00}_{-0.00}$	$0.05^{+0.00}_{-0.00}$
6*	$2.18^{+0.11}_{-0.11}$	$13.98^{+0.12}_{-0.12}$	$3.38^{+0.08}_{-0.07}$	$0.378^{+0.004}_{-0.006}$	$4.21^{+0.23}_{-0.23}$	$0.14^{+0.01}_{-0.01}$	$0.14^{+0.01}_{-0.01}$
7*	$2.75^{+0.11}_{-0.11}$	$18.81^{+0.18}_{-0.18}$	$3.41^{+0.11}_{-0.10}$	$0.379^{+0.005}_{-0.005}$	$6.86^{+0.33}_{-0.33}$	$0.10^{+0.01}_{-0.01}$	$0.10^{+0.01}_{-0.01}$
8	$1.99^{+0.05}_{-0.05}$	$5.68^{+1.89}_{-1.12}$	$4.43^{+0.03}_{-1.57}$	$0.227^{+0.081}_{-0.018}$	$4.10^{+0.70}_{-3.73}$	$0.20^{+0.00}_{-0.15}$	$0.20^{+0.00}_{-0.15}$
9	$1.78^{+0.21}_{-0.22}$	$9.98^{+0.36}_{-0.71}$	$4.07^{+0.18}_{-0.43}$	$0.375^{+0.004}_{-0.010}$	$2.12^{+0.13}_{-0.81}$	$0.22^{+0.16}_{-0.09}$	$0.22^{+0.16}_{-0.09}$
11	$3.72^{+0.18}_{-0.35}$	$2.26^{+0.03}_{-0.18}$	$3.43^{+0.06}_{-0.11}$	$0.550^{+0.027}_{-0.037}$	$0.79^{+0.15}_{-0.08}$	$0.06^{+0.01}_{-0.01}$	$0.06^{+0.01}_{-0.01}$
12*	$2.16^{+0.13}_{-0.14}$	$6.13^{+0.07}_{-0.07}$	$2.77^{+0.09}_{-0.09}$	$0.499^{+0.008}_{-0.009}$	$2.86^{+0.17}_{-0.16}$	$0.09^{+0.01}_{-0.01}$	$0.09^{+0.01}_{-0.01}$
13*	$2.25^{+0.10}_{-0.10}$	$13.98^{+0.12}_{-0.12}$	$3.91^{+0.06}_{-0.06}$	$0.365^{+0.003}_{-0.003}$	$6.26^{+0.16}_{-0.16}$	$0.05^{+0.00}_{-0.00}$	$0.05^{+0.00}_{-0.00}$
14	$5.13^{+0.17}_{-0.19}$	$2.42^{+0.03}_{-0.94}$	$3.63^{+0.21}_{-0.04}$	$0.510^{+0.027}_{-0.192}$	$0.58^{+0.76}_{-0.04}$	$0.05^{+0.00}_{-0.00}$	$0.05^{+0.00}_{-0.00}$
15	$2.28^{+0.17}_{-0.17}$	$4.40^{+0.07}_{-0.07}$	$3.06^{+0.10}_{-0.10}$	$0.500^{+0.014}_{-0.014}$	$1.98^{+0.18}_{-0.17}$	$0.09^{+0.01}_{-0.01}$	$0.09^{+0.01}_{-0.01}$
16*	$1.09^{+0.20}_{-0.25}$	$13.62^{+0.23}_{-0.49}$	$4.20^{+0.17}_{-0.25}$	$0.360^{+0.017}_{-0.007}$	$5.21^{+0.53}_{-0.75}$	$0.07^{+0.01}_{-0.02}$	$0.07^{+0.01}_{-0.02}$
17*	$3.11^{+0.09}_{-0.07}$	$7.60^{+0.04}_{-0.05}$	$3.90^{+0.03}_{-0.04}$	$0.370^{+0.002}_{-0.002}$	$2.61^{+0.16}_{-0.08}$	$0.11^{+0.00}_{-0.01}$	$0.11^{+0.00}_{-0.01}$

Region[††]	$Z_{Mg,eRObub}$ ($Z_{Mg,\odot}$)	$Z_{Fe,eRObub}$ ($Z_{Fe,\odot}$)	$\log\left(\frac{N_H}{cm^{-2}}\right)$	$I_{Ne\,IX}$ (10^{33} ph s^{-1} deg^{-2})	$I_{Fe\,XVII\,\lambda\,15.01\,Å}$ (10^{33} ph s^{-1} deg^{-2})	$I_{Fe\,XVII\,\lambda\,15.26\,Å}$ (10^{33} ph s^{-1} deg^{-2})	$I_{O\,VIII\,Ly\beta}$ (10^{33} ph s^{-1} deg^{-2})
2	$0.20^{+0.03}_{-0.16}$	$0.20^{+0.03}_{-0.16}$	$20.441^{+0.008}_{-0.008}$	$10.22^{+0.64}_{-0.62}$	$6.22^{+3.68}_{-3.84}$	$4.86^{+4.22}_{-3.97}$	< 2.21
3	$0.05^{+0.00}_{-0.00}$	$0.05^{+0.00}_{-0.00}$	$20.462^{+0.008}_{-0.008}$	$3.26^{+0.55}_{-0.56}$	$6.30^{+0.84}_{-3.45}$	< 2.61	< 2.61
4*	$0.11^{+0.01}_{-0.01}$	$0.11^{+0.01}_{-0.01}$	$20.642^{+0.004}_{-0.004}$	$9.33^{+0.57}_{-0.56}$	< 1.80	$15.29^{+0.98}_{-0.98}$	< 1.80
5*	$0.05^{+0.00}_{-0.00}$	$0.05^{+0.00}_{-0.00}$	$20.646^{+0.003}_{-0.003}$	$11.56^{+0.58}_{-0.58}$	< 1.96	$14.60^{+0.99}_{-0.99}$	< 1.96
6*	$0.14^{+0.01}_{-0.01}$	$0.14^{+0.01}_{-0.01}$	$20.707^{+0.005}_{-0.005}$	$24.83^{+1.64}_{-1.72}$	< 6.13	$27.47^{+2.60}_{-2.63}$	< 6.13
7*	$0.10^{+0.01}_{-0.01}$	$0.10^{+0.01}_{-0.01}$	$20.831^{+0.004}_{-0.004}$	$44.34^{+2.13}_{-2.28}$	< 7.16	$45.89^{+3.57}_{-3.56}$	< 7.16
8	$0.20^{+0.00}_{-0.15}$	$0.20^{+0.00}_{-0.15}$	$21.055^{+0.046}_{-0.023}$	$42.80^{+1.53}_{-15.82}$	< 87.35	$54.03^{+2.20}_{-49.36}$	< 56.80
9	$0.22^{+0.16}_{-0.09}$	$0.22^{+0.16}_{-0.09}$	$20.903^{+0.016}_{-0.017}$	$26.47^{+4.02}_{-4.91}$	$28.31^{+1.41}_{-28.31}$	< 40.85	< 4.24
11	$0.06^{+0.01}_{-0.01}$	$0.06^{+0.01}_{-0.01}$	$20.116^{+0.024}_{-0.085}$	< 2.33	$1.26^{+1.31}_{-1.26}$	< 2.33	< 2.33
12*	$0.09^{+0.01}_{-0.01}$	$0.09^{+0.01}_{-0.01}$	$20.535^{+0.009}_{-0.009}$	$11.65^{+1.59}_{-1.56}$	< 5.34	$3.74^{+2.53}_{-3.01}$	< 5.34
13*	$0.05^{+0.00}_{-0.00}$	$0.05^{+0.00}_{-0.00}$	$20.748^{+0.004}_{-0.004}$	$21.23^{+1.60}_{-1.52}$	< 6.85	$31.71^{+2.89}_{-7.19}$	< 6.85
14	$0.05^{+0.00}_{-0.00}$	$0.05^{+0.00}_{-0.00}$	$20.157^{+0.078}_{-0.137}$	< 5.68	$1.42^{+4.18}_{-1.42}$	< 2.15	< 2.15
15	$0.09^{+0.01}_{-0.01}$	$0.09^{+0.01}_{-0.01}$	$20.471^{+0.014}_{-0.014}$	$3.52^{+1.61}_{-1.72}$	< 5.96	$3.75^{+2.86}_{-3.75}$	< 5.96
16*	$0.07^{+0.01}_{-0.02}$	$0.07^{+0.01}_{-0.02}$	$20.820^{+0.011}_{-0.015}$	$7.72^{+5.74}_{-4.07}$	< 9.43	$39.33^{+12.75}_{-13.90}$	< 6.93
17*	$0.11^{+0.00}_{-0.01}$	$0.11^{+0.00}_{-0.01}$	$20.591^{+0.006}_{-0.004}$	$5.82^{+0.70}_{-0.73}$	< 4.35	$23.27^{+1.33}_{-5.16}$	< 1.29

Region[††]	$I_{Fe\,XVII\,\lambda\,16.77\,Å}$ (10^{33} ph s^{-1} deg^{-2})	$I_{Fe\,XVII\,\lambda\,17.05\,Å}$ (10^{33} ph s^{-1} deg^{-2})	$I_{O\,VIII\,Ly\alpha}$ (10^{33} ph s^{-1} deg^{-2})	$I_{O\,VII}$ (10^{33} ph s^{-1} deg^{-2})	χ^2/dof[†]	Sky Area (deg^2)
2	< 2.21	$7.12^{+1.97}_{-2.11}$	$42.68^{+1.68}_{-1.65}$	< 2.21	1.84	421.59
3	< 2.61	$5.90^{+0.98}_{-1.84}$	$20.91^{+1.29}_{-1.28}$	< 2.61	1.42	356.25
4*	< 1.80	$2.79^{+1.04}_{-1.07}$	$49.69^{+1.39}_{-1.42}$	< 2.20	2.15	518.70
5*	< 1.96	$9.16^{+1.06}_{-1.07}$	$81.79^{+1.43}_{-1.34}$	< 1.96	4.65	474.29
6*	< 6.13	$9.53^{+3.09}_{-3.18}$	$112.85^{+3.81}_{-4.07}$	< 6.13	1.60	151.89
7*	< 7.16	$16.15^{+4.19}_{-4.32}$	$194.97^{+5.21}_{-5.41}$	< 7.16	2.23	130.02
8	< 56.82	$2.47^{+2.31}_{-2.47}$	$15.77^{+156.17}_{-2.08}$	< 103.87	4.69	157.79
9	< 4.24	$22.19^{+3.01}_{-20.80}$	$94.78^{+33.43}_{-13.09}$	< 27.76	3.67	579.68
11	< 2.33	$2.01^{+1.57}_{-1.69}$	$2.43^{+3.80}_{-1.27}$	< 12.32	3.03	399.10
12*	< 5.34	$9.84^{+2.38}_{-2.43}$	$56.34^{+2.86}_{-2.94}$	< 5.34	1.60	174.53
13*	< 6.85	$10.52^{+3.36}_{-3.20}$	$25.91^{+4.41}_{-4.31}$	< 6.85	2.95	135.97
14	< 2.15	$1.08^{+1.01}_{-1.08}$	$1.89^{+1.37}_{-1.33}$	< 16.99	1.58	433.18
15	< 5.96	$3.83^{+2.44}_{-2.48}$	$24.60^{+2.92}_{-2.90}$	< 5.96	1.31	156.16
16*	< 6.93	$7.68^{+12.25}_{-7.17}$	< 22.59	< 6.93	2.47	134.38
17*	< 1.29	$3.39^{+2.09}_{-1.48}$	$22.87^{+1.98}_{-1.89}$	< 1.29	2.84	719.29

Notes.
(††) We note that the region definition in the table follows Fig. 4.23, which is not the same as the main text.
(*) Regions where RS is necessary.
(†) dof=167.

where there is an interface of hot ionised plasma and neutral matter for CX to occur, the eROSITA spectra are unable to confirm it.

On the other hand, the observation of the enhanced O VIII Lyβ/Lyα ratio in the NPS is also apparent in the EPIC spectra in Gu et al. (2016b). They proposed the presence of an ionised absorber to explain the ratio enhancement, as the O VIII Lyα line has a higher transition probability than the Lyβ line, hence it would be more strongly absorbed than the Lyβ line and boost the Lyβ/Lyα ratio. We initially suspected an ionised absorber could also explain the anomalous Fe XVII 15 Å/17 Å ratio we observed, due to the close energy proximity of the O VIII Lyβ to the Fe XVII 15 Å lines. However, after extended testing with additional CX and ionised absorber models, it was found not to be the case.

Figure 4.25 demonstrates the lack of substantial improvement after including both CX and ionised absorber (`CX×hot`) in the modelling, especially near 0.8 keV. The CX component was modelled using the `CX` model in `SPEX` (Gu et al., 2016a), where the CX plasma component has abundance coupled to the eRObub. However, the temperature was allowed a small freedom to vary near the eRObub temperature. The ionised absorber was modelled using the `hot` model, but with a variable temperature around 0.17 keV and variable column density. The `CX` model has the merit of producing stronger line blend around 15 Å, but not near 17 Å, hence partially helpful in explaining the anomalous Fe XVII 15 Å/17 Å ratio. However, it never produces a single sharp line at 0.8 keV, hence cannot fully explain the residual. In addition, absorption by an ionised absorber does not only boost the O VIII Lyβ/Lyα ratio, but also decreases the Fe XVII 15 Å resonance lines more strongly than the 17 Å lines due to the stronger oscillator strength, hindering the increase of the Fe XVII 15 Å/17 Å ratio as is required by the data. A closer look and comparison of the spectral fits in Gu et al. (2016b) and ours reveals the residual peaks are located at slightly different energies: the *Suzaku* and *XMM-Newton* spectra in Gu et al. (2016b) have the residual peak closer to the O VIII Lyβ line at 775 eV while the eROSITA spectra are consistently at $\simeq$ 800 eV. Therefore, we concluded that invoking CX and an ionised absorber cannot satisfactorily explain the eROSTIA data.

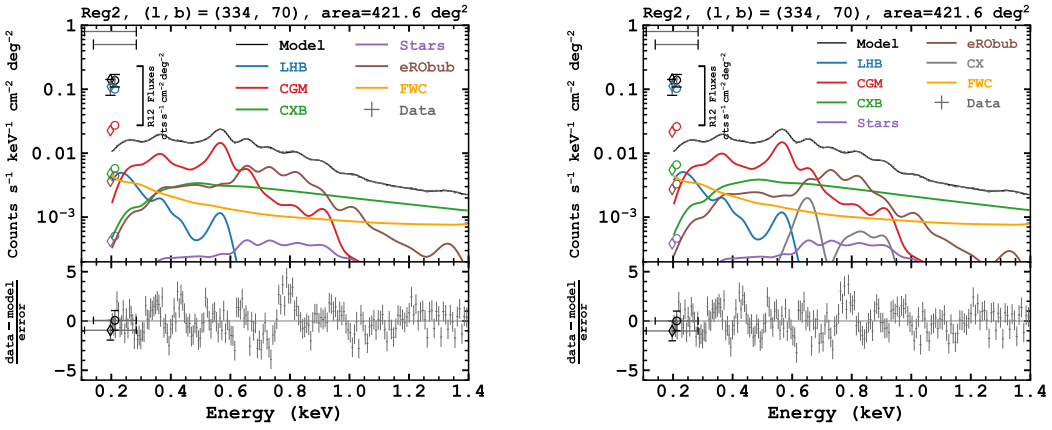

Figure 4.25: Comparison between the baseline model (*top*) and the model including charge exchange (CX) and an ionised absorber (*bottom*) in reg 2 defined in Fig. 4.23, which is the inner part of the NPS extension into the western Galactic hemisphere. The main residual at 0.8 keV remains significant and does not sufficiently suppress the enhanced Fe XVII 15 Å/17 Å ratio.

4.11 NPS abundance comparison

We provide more information on the comparison of the free and fixed (0.2 $Z_\odot$ except Fe and Ne) abundance model on the NPS. The spectral fits are compared in Fig. 4.26. As mentioned in

Sect. 4.5.2, the free oxygen (linked to all other metals except for Fe and Ne) abundance model performs better statistically with a p-value of $\approx 10^{-9}$ than the fixed abundance model in the F-test. Visually, improvements can be seen near the C VI line near 0.36 keV and the Mg XI line near 1.35 keV. Strong residual remains near the C VI line even in the free abundance case (C was linked with O in the fit); a higher C abundance will likely deliver a better fit. The higher O VII line from the eRObub component is caused by a lower temperature ≈ 0.21 keV as opposed ≈ 0.25 keV in the free abundance case. The lowering of the eRObub temperature in the fixed abundance model was compensated for with a lower CGM EM.

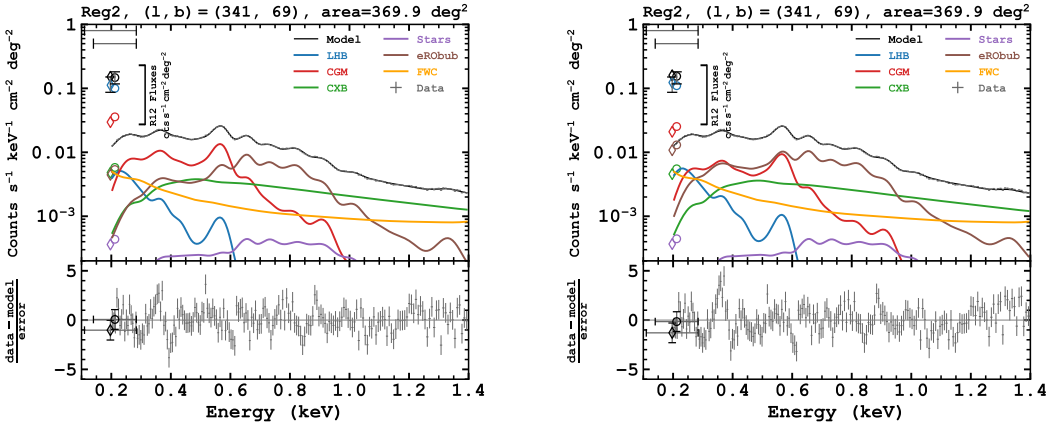

Figure 4.26: Comparison of NPS region fitted by free (*top*) and fixed (*bottom*) abundance. We note that in both cases, Ne and Fe abundances were left free.

Chapter 5

Summary

This thesis harnesses the power of both the X-ray imaging and spectroscopic capability of the eROSITA telescope to study two of the largest projected X-ray structures in the sky: the local hot bubble and the eROSITA bubbles.

5.1 Chapter summary

5.1.1 Chapter 2: X-ray shadowing as a probe to the SWCX and LHB

Chapter 2 combines complementary information from the high angular resolution column density maps of giant molecular clouds on the LHB surface to analyse the temporal change in the foreground emission. The main aim is to separate and quantify the SWCX and the LHB emissions. Prior to eROSITA, the determination of the two was subjected to higher uncertainties caused by a few factors, including mission orbits and pointings intersecting with the Earth's geocorona, solar maximum conditions, and short time sampling. The L2 orbit of eROSITA and the perpendicular scanning direction of eRASSs relative to the Sun removed the geocoronal SWCX contamination. The eRASS survey cadence of 6 months, starting from the solar minimum conditions for more than two years, also ensured a favourable sampling frequency of heliospheric SWCX and a sufficient period to observe the effect from the solar cycle. Our shadowing analysis clearly shows the monotonic increase of heliospheric SWCX contribution with solar activity and pointed to a minimal level of SWCX in eRASS1. The sets the scene for our subsequent choice of using eRASS1 data only for the studies of the LHB and eRObub in Chapter 3 and 4 to minimise the contamination from SWCX. Regarding the LHB, the most significant result is the indication of a temperature difference ($\sim 20\,\mathrm{eV}$) and a seemingly constant ($\lesssim 10\%$) line-of-sight-averaged ($n_e \sim 4\times10^{-3}\,\mathrm{cm}^{-3}$) electron density across hugely different sight lines. We argue that this indicates the LHB indeed extends up to the molecular clouds despite their significantly different distances, as density is a quantity that relates two independent measurements (EM and distance) and is not expected to be a constant without a physical link. Additionally, we demonstrate that the SWCX intensity is a function of ecliptic latitudes, following the expected behaviour of the solar wind, which is more ionised near the ecliptic plane. As an aside, we also carried out an extensive analysis of the eROSITA instrumental background inferred from FWC observations, involving the effects caused by the solar activity cycle and the detector temperature. The spectral models describing the eROSITA instrumental background have benefited and will benefit diffuse emission studies based on eROSITA.

5.1.2 Chpater 3: Half-sky analysis of the LHB

Chapter 3 extends the decomposition of the SXRB beyond specific molecular cloud sight lines to a full half-sky context in the western Galactic hemisphere. We restricted ourselves to only eRASS1 for the sake of SWCX suppression. We focus on the properties of the LHB despite the

fact that spectral decomposition contains more information on the other components, including, for example, the CGM and CXB. Our work produces half-sky maps of the LHB temperature and EM maps. We discovered an unexpected north-south temperature dichotomy, with the south at $kT = 121.8 \pm 0.6$ eV, about 20 eV hotter than the north at $|b| \gtrsim 30°$. Inspired by the recent numerical simulation efforts on the LHB, we suggest that such temperature non-uniformity could be explained as evidence of the most recent supernova explosion(s) in the LHB. However, despite the clear theoretical motivation, the current eRASS1 data do not have adequate evidence to support that the LHB plasma is out of CIE due to recent heating from supernovae. This is possibly linked with the insufficient spectral resolution of CCD detectors. Future spectroscopic missions with spectral resolution in the eV regime, combined with a large grasp, will likely be much more sensitive to any NEI signatures.

Utilising the electron density we calibrated with molecular sight lines in Chapter 2 and assuming a simple constant density assumption, we produce a three-dimensional model of the LHB hot gas. It features large extensions towards the Galactic poles because of the least resistance to its expansion. We found a clear anti-correlation of the LHB EM with cold gas column density in the solar neighbourhood, inferred from *Gaia*-era three-dimensional dust maps. This anti-correlation is in agreement with the classical 'displacement' model, where the hot gas seemingly displaces the colder phases in the ISM. The validity of this model supports the popular theory of the LHB formation in which multiple supernovae exploded and produced shock waves in the ISM to heat the LHB interior to $\sim 10^6$ K. In parallel, the shock waves compressed a shell of dense material, which subsequently collapsed to form the wall of the LB and the associated giant molecular clouds. From the comparison with local dust maps, we found evidence of two prominent 'interstellar tunnels' that are a possible extension of the LHB, connecting the LHB to nearby superbubbles. One of them is a new discovery, towards the constellation Centaurus, possibly linking to the Loop I superbubble. It might be a local example of a more pervasive network of hot ISM sustained by supernova feedback in the Milky Way (Cox & Smith, 1974). We made all the SXRB best-fit parameters in the western Galactic hemisphere public, which would be a good starting point for background estimations in extended source studies.

5.1.3 Chapter 4: Morphology and spectrum of the eRObub

We shift our focus to the eRObub in Chapter 4, in terms of their morphology and spectral properties. We prescribe an empirical geometrical model to the eRObub, assuming a density structure following a Sedov-Taylor blast wave propagating into an idealistic Galactic halo from the Galactic centre. The model parameters, including the vertical and horizontal extents of the bubbles, the tilt and its direction, Mach number, are optimised using the eRASS1 all-sky map in 0.6–1.0 keV band. Such a geometrical prescription could reproduce the projected surface brightness profile satisfactorily. We found a significant tilt ($\sim 30°$) in the direction of $l \sim 220°$ (towards our direction and west) could best reproduce the westward-inclined projected outline of the northern bubble and the appearance of the NPS. Additionally, we concluded that the eRASS1 map provides good constraints on the eRObub's horizontal extent (~ 6 kpc) but not the vertical extent, caused by our location close to the eRObub on the Galactic plane and the intrinsic faintness of the low-density outer halo.

From the spectral fitting of constant S/N regions ($\sim$5–10 deg^2) in the eRObub, we find the eRObub is characterised by a plasma of ~ 0.3 keV, however with a sizeable scatter. A curious feature, with the appearance of a shell made of cooler gas but significantly brighter than the background, is seen surrounding the bulk of the northern eRObub. To further investigate the source of the scatter as well as special regions in the eRObub, such as the FB and the cool shell, we define bespoke large regions to boost the S/N to look for processes beyond a single CIE component in the eRObub spectra. We find that a single temperature CIE component is insufficient to reproduce the high-S/N spectra, most notably around the Fe XVII L shell lines between 0.7–0.85 keV where the data is often marked by an enhanced $3d/3s$ line ratio. We found that the anomalously high line ratio could be remedied by a two-temperature model, as opposed to the other explanations such as resonant scattering, charge exchange and absorption from ionised

gas. The two temperatures (~ 0.25 keV and ~ 0.55 keV) are surprisingly constant across latitudes, despite the increasing EM towards the Galactic plane. On the other hand, the cool shell is well fitted by a single temperature component at ~ 0.2 keV in CIE. It could be a part of a foreground structure such as the Loop I superbubble. Its spectrum does not support the relevance of NEI after the recent passing of a shock. We are able to measure the abundances of mainly O, Fe and Ne in the eRObub thanks to the high S/N. The eRObub plasma appears subsolar ($Z \sim 0.2\,Z_\odot$), consistent with the expectation of a shock heating the Galactic halo, but without significant chemical enrichment from star-formation, despite a small indication of α-enhancement. The NPS is an outlier in terms of abundance, which is significantly higher ($Z > 0.5\,Z_\odot$) than the rest of the eRObub. This could potentially hint at a different origin than the general eRObub, for example, being a hot plume that rises from an active star-forming region (Churazov et al., 2024).

5.2 Outlook

Being within the LHB makes it difficult to measure its shape and extent. While we measured a constant line-of-sight-averaged electron density for the LHB with X-ray shadowing, it is almost certain that the situation is more complicated. For instance, pulsar scintillation measurements clearly show screens of warm plasmas ($\sim 10^4$ K) exist in the LHB (Reardon et al., 2025). In fact, the best tracer of LHB shape is likely not in the X-ray; new measurements from other wavelengths, such as low-frequency radio measurements of Faraday depth (Erceg et al., 2024) or starlight polarisation (Panopoulou et al., 2025), could trace magnetic fields compressed on the LB wall and hold important information on the extent of the LHB. A holistic picture of the LHB requires a model that satisfies constraints from all tracers.

The promise of the X-ray aspect of the LHB could lie with diagnosing plasma conditions other than or beyond CIE. New missions with high spectral resolution will likely deliver new evidence on NEI or photoionisation, which have long been suspected from theoretical predictions (e.g. Breitschwerdt & Schmutzler, 1994) and EUV observations (Jelinsky et al., 1995; Linsky & Redfield, 2021). The He-like ions could provide further insight into the importance of CX in the interface between the hot gas in the interior of the LHB with neutral materials on the bubble wall. Micro-calorimeter appears to be the most likely candidate to deliver this improvement in the near future. In fact, projected to go onto the Chinese Space Station in 2028, DIXE, a non-focusing micro-calorimeter, promises to deliver 6 eV resolution at 0.6 keV with $10^\circ \times 10^\circ$ FoV, will likely deliver a breakthrough on this front (Jin et al., 2024). Further into 2030s, HUBS, a focusing telescope of 1 deg^2 FoV and ~ 500 cm^2 effective area, equipped with a micro-calorimeter of even better spectral resolution (0.8–2 eV) has the potential to probe all the aforementioned physics in great detail (Cui et al., 2020). Much of the discussion here also applies to the plasma conditions in the eRObub. At this spectral resolution, even the simplest line-shift measurement at sub-eV (~ 0.6 eV) resolution corresponds to ~ 300 km s^{-1} velocity resolution. For the eRObub, this promises a direct measurement of the expansion velocity comparable to the current indirect shock speed estimate. In general, component decomposition of the SXRB can benefit greatly from micro-calorimetric data; for instance, one might be able to decompose the CGM component from the rest by observing or assuming a smooth function of the rotation velocity and translating that into a line shift in all the emission lines.

One of the brightest and nearest superbubbles in the X-ray sky is the Orion-Eridanus superbubble. Taking advantage of an external view, revisiting its X-ray properties with eROSITA could lend new insights into our current understanding of the LHB. For instance, one could analyse the emissions near the edge (in fact, several shells have been seen in isolation), which is difficult to probe for the LHB or the relative importance of photoionisation versus collisional ionisation.

X-ray shadowing technique can also be used to constrain the distance and the foreground emissions to the eRObub. I have, in fact, identified two prime targets to this end. They are CG 12 and Dobashi 6193, as shown in Fig. 5.1. CG 12 is well-known to be located at a distance of 670 pc from us (Reipurth & Bragg, 2021). I used *Gaia* extinction data to constrain the distance of Dobashi 6193 to ~ 700 pc (Yeung & Freyberg, 2024). They are sufficiently distant such that

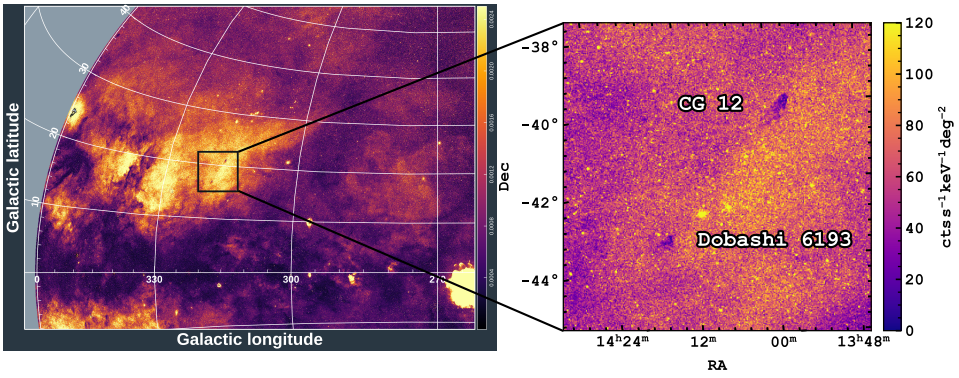

Figure 5.1: eROSITA image and location of CG 12 and Dobashi 6193, casting shadows in the eRObub.

they are likely to lie behind the proposed Loop I superbubble. Spectral analysis of their on- and off-cloud spectra is likely to inform whether the eRObub is absorption-bounded, or has significant foreground emissions that could point to the existence of the Loop I superbubble. My proposals for the two clouds to XMM-Newton and Einstein Probe have been accepted, although the observations have not been taken at the time of writing and are dependent on the final scheduling. Even the observation and analysis of one of the clouds could lend clarity for the distance or foreground of the eRObub.

Appendix A

Selected co-author publications

A selected list of my co-author publications in reverse chronological order is shown below.

1. *The SRG/eROSITA all-sky survey: View of the Fornax galaxy cluster*
   T. H. Reiprich, A. Veronica, F. Pacaud, P. Stöcker, V. Nazaretyan, A. Srivastava, A. Pandya, J. Dietl, J. S. Sanders, *M. C. H. Yeung*, A. Chaturvedi, M. Hilker, B. Seidel, K. Dolag, J. Comparat, V. Ghirardini, M. Kluge, A. Liu, N. Malavasi, X. Zhang, E. Hernández-Martínez
   Astronomy & Astrophysics, accepted (2025)
   I contributed to the characterisation of the non-X-ray background.

2. *The SRG/eROSITA All-Sky Survey: Large-scale view of the Centaurus cluster*
   Angie Veronica, Thomas H. Reiprich, Florian Pacaud, Jeremy S. Sanders, Efrain Gattuzz, *Michael C. H. Yeung*, Esra Bulbul, Vittorio Ghirardini, Ang Liu, Caroline Mannes, Alexander Morelli and Naomi Ota
   Astronomy & Astrophysics, 694, A168 (2024)
   I contributed to the X-ray spectral modelling Section and compared the fitting results to my eRObub work due to Centaurus cluster's location behind the eRObub.

3. *Using SRG/eROSITA to predict soft proton induced ATHENA backgrounds*
   Emanuele Perinati, Michael J. Freyberg, *Michael C. H. Yeung*, Konrad Dennerl, Christian Pommranz, Bastian Heß, Debastian Diehold, Chris Tenzer and Andrea Santangelo
   Experimental Astronomy, 58, 2, 9 (2024)
   I contributed to reducing and providing the FWC and eRASS1 datasets, and estimating the CXB contribution.

4. *eROSITA narrowband maps at the energies of soft X-ray emission lines*
   Xueying Zheng, Gabriele Ponti, Nicola Locatelli, Jeremy Sanders, Andrea Merloni, Werner Becker, Johan Comparat, Konrad Dennerl, Michael Freyberg, Chandreyee Maitra, Manami Sasaki, Andrew Strong and *Michael C. H. Yeung*
   Astronmy & Astophysics, 689, A328 (2024)
   My main contribution is the interpretation of the O VIII/O VII narrowband ratio, in light of the parallel half-sky spectral fitting I was doing (Chapter 3).

5. *Morphological Evidence for the eROSITA Bubbles Being Giant and Distant Structures*
   Teng Liu, Andrea Merloni, Jeremy Sanders, Gabriele Ponti, Andrew Strong, *Michael C. H. Yeung*, Nicola Locatelli, Peter Predehl, Xueying Zheng, Manami Sasaki, Michael Freyberg, Konrad Dennerl, Werner Becker, Kirpal Nandra, Martin Mayer and Johannes Buchner
   Astrophysical Journal Letters, 967, L27 (2024)
   I contributed to the discussion and editing of the article.

6. *On the Evidence for Molecular Outflows in High-redshift Dusty Star-forming Galaxies*
   James Nianias, Jeremy Lim, and *Michael Yeung*

Astrophysical Journal, 963, 19 (2024)
I contributed to initiating the project after discovering that the atmospheric absorption features overlap with molecular outflow signatures of a lens system in the article.

7. *Abundance and temperature of the outer hot circumgalactic medium. The SRG/eROSITA view of the soft X-ray background in the eFEDS field*
G. Ponti, X. Zheng, N. Locatelli, S. Bianchi, Y. Zhang, K. Anastasopoulou, J. Comparat, K. Dennerl, M. Freyberg, F. Haberl, A. Merloni, T. H. Reiprich, M. Salvato, J. Sanders, M. Sasaki, A. Strong and *M. C. H. Yeung*
Astronomy & Astrophysics, 674, A195 (2023)
I contributed to the spectral modelling and the editing of the article.

8. *Characterizing the patchy appearance of the circumgalactic medium and the influence of foreground absorption*
G. Ponti, J. S. Sanders, N. Locatelli, X. Zheng, Y. Zhang, *M. Yeung*, M. Freyberg, K. Dennerl, J. Comparat, A. Merloni, E. Di Teodoro, M. Sasaki and T. H. Reiprich
Astronomy & Astrophysics, 670, A99 (2023)
I contributed to the presented ideas, discussion and editing of the article.

9. *X-ray analysis of JWST's first galaxy cluster lens SMACS J0723.3-7327*
A. Liu, E. Bulbul, M. E. Ramos-Ceja, J. S. Sanders, V. Ghirardini, Y. E. Bahar, *M. Yeung*, E. Gatuzz, M. Freyberg, C. Garrel, X. Zhang, A. Merloni and K. Nandra
Astronomy & Astrophysics, 670, A96 (2023)
I contributed to the characterisation of the non-X-ray background.

Bibliography

Ackermann, M., Albert, A., Atwood, W. B., et al. 2014, ApJ, 793, 64

Alexander, D. M., Bauer, F. E., Brandt, W. N., et al. 2003, AJ, 126, 539

Alves de Oliveira, C., Schneider, N., Merín, B., et al. 2014, A&A, 568, A98

Amano, Y., Uchida, H., Tanaka, T., Gu, L., & Tsuru, T. G. 2020, ApJ, 897, 12

Anders, E. & Grevesse, N. 1989, Geochim. Cosmochim. Acta, 53, 197

André, P., Men'shchikov, A., Bontemps, S., et al. 2010, A&A, 518, L102

Arcangeli, L., Borghi, G., Bräuninger, H., et al. 2017, SPIE Conf. Ser., 10565, 1056558

Arnaud, K. A. 1996, in Astronomical Society of the Pacific Conference Series, Vol. 101, Astronomical Data Analysis Software and Systems V, ed. G. H. Jacoby & J. Barnes, 17

Arnaud, M. & Raymond, J. 1992, ApJ, 398, 394

Asplund, M., Grevesse, N., Sauval, A. J., & Scott, P. 2009, ARA&A, 47, 481

Astropy Collaboration, Price-Whelan, A. M., Lim, P. L., et al. 2022, ApJ, 935, 167

Astropy Collaboration, Price-Whelan, A. M., Sipőcz, B. M., et al. 2018, AJ, 156, 123

Astropy Collaboration, Robitaille, T. P., Tollerud, E. J., et al. 2013, A&A, 558, A33

Barnes, A. T., Longmore, S. N., Battersby, C., et al. 2017, MNRAS, 469, 2263

Beiersdorfer, P., Boyce, K. R., Brown, G. V., et al. 2003, Science, 300, 1558

Bely-Dubau, F., Gabriel, A. H., & Volonte, S. 1979, MNRAS, 189, 801

Berghöfer, T. W. & Breitschwerdt, D. 2002, A&A, 390, 299

Berkhuijsen, E. M. 1972, A&AS, 5, 263

Berkhuijsen, E. M., Haslam, C. G. T., & Salter, C. J. 1971, A&A, 14, 252

Besla, G., Kallivayalil, N., Hernquist, L., et al. 2010, ApJ, 721, L97

Bethe, H. A. & Salpeter, E. E. 1957, Quantum Mechanics of One- and Two-Electron Atoms (Springer-Verlag Berlin Heidelberg)

Blackburn, J. K. 1995, in Astronomical Society of the Pacific Conference Series, Vol. 77, Astronomical Data Analysis Software and Systems IV, ed. R. A. Shaw, H. E. Payne, & J. J. E. Hayes, 367

Bland-Hawthorn, J. & Cohen, M. 2003, ApJ, 582, 246

Bland-Hawthorn, J. & Gerhard, O. 2016, ARA&A, 54, 529

Bluem, J., Kaaret, P., Kuntz, K. D., et al. 2022, ApJ, 936, 72

Bobin, J., Rapin, J., Larue, A., & Starck, J.-L. 2015, Trans. Sig. Proc., 63, 1199–1213

Bochkarev, N. G. 1987, Ap&SS, 138, 229

Borkowski, K. J., Lyerly, W. J., & Reynolds, S. P. 2001, ApJ, 548, 820

Borovsky, J. E. & Valdivia, J. A. 2018, Surv. Geophys., 39, 817

Boulares, A. & Cox, D. P. 1990, ApJ, 365, 544

Bowyer, C. S., Field, G. B., & Mack, J. E. 1968, Nature, 217, 32

Bradski, G. 2000, The OpenCV Library

Brandt, J. C., Stecher, T. P., Crawford, D. L., & Maran, S. P. 1971, ApJ, 163, L99

Brandt, W. N. & Yang, G. 2022, in Handbook of X-ray and Gamma-ray Astrophysics, ed. C. Bambi & A. Sangangelo (Springer Nature), 78

Branduardi-Raymont, G., Bhardwaj, A., Elsner, R. F., et al. 2007, A&A, 463, 761

Bregman, J. N., Anderson, M. E., Miller, M. J., et al. 2018, ApJ, 862, 3

Bregman, J. N. & Lloyd-Davies, E. J. 2007, ApJ, 669, 990

Breitschwerdt, D. 1996, Space Sci. Rev., 78, 173

Breitschwerdt, D. & de Avillez, M. A. 2021, Ap&SS, 366, 94

Breitschwerdt, D., Feige, J., Schulreich, M. M., et al. 2016, Nature, 532, 73

Breitschwerdt, D. & Schmutzler, T. 1994, Nature, 371, 774

Bresnahan, D., Ward-Thompson, D., Kirk, J. M., et al. 2018, A&A, 615, A125

Brown, G. V., Beiersdorfer, P., Chen, H., et al. 2009, J. Phys. Conf. Ser., 163, 012052

Brunner, H., Liu, T., Lamer, G., et al. 2022, A&A, 661, A1

Bulbul, E., Kraft, R., Nulsen, P., et al. 2020, ApJ, 891, 13

Bulbul, E., Liu, A., Kluge, M., et al. 2024, A&A, 685, A106

Burlaga, L. F. & Ness, N. F. 2014, ApJ, 784, 146

Cánovas, H., Cantero, C., Cieza, L., et al. 2019, A&A, 626, A80

Cappelluti, N., Arendt, R., Kashlinsky, A., et al. 2017, ApJ, 847, L11

Carloni Gertosio, R., Bobin, J., & Acero, F. 2023, Signal Process., 202, 108776

Cash, W. 1979, ApJ, 228, 939

Chen, L. W., Fabian, A. C., & Gendreau, K. C. 1997, MNRAS, 285, 449

Cheng, K. S., Chernyshov, D. O., Dogiel, V. A., Ko, C. M., & Ip, W. H. 2011, ApJ, 731, L17

Churazov, E., Khabibullin, I. I., Bykov, A. M., et al. 2024, A&A, 691, L22

Churazov, E., Zhuravleva, I., Sazonov, S., & Sunyaev, R. 2010, Space Sci. Rev., 157, 193

Cowie, L. L. & McKee, C. F. 1977, ApJ, 211, 135

Cox, D. P. 1998, in IAU Colloq. 166: The Local Bubble and Beyond, ed. D. Breitschwerdt, M. J. Freyberg, & J. Truemper, Vol. 506 (Springer-Verlag Berlin Heidelberg), 121–131

Cox, D. P. 2005, ARA&A, 43, 337

Cox, D. P. & Anderson, P. R. 1982, ApJ, 253, 268

Cox, D. P. & Smith, B. W. 1974, ApJ, 189, L105

Cravens, T. E. 1997, Geophys. Res. Lett., 24, 105

Crocker, R. M., Bicknell, G. V., Taylor, A. M., & Carretti, E. 2015, ApJ, 808, 107

Crowder, S. G., Barger, K. A., Brandl, D. E., et al. 2012, ApJ, 758, 143

Cruddace, R., Paresce, F., Bowyer, S., & Lampton, M. 1974, ApJ, 187, 497

Cui, W., Chen, L. B., Gao, B., et al. 2020, J. Low Temp. Phys., 199, 502

Cumbee, R. S., Mullen, P. D., Lyons, D., et al. 2018, ApJ, 852, 7

Das, S., Mathur, S., Gupta, A., Nicastro, F., & Krongold, Y. 2019, ApJ, 887, 257

de Avillez, M. A. & Breitschwerdt, D. 2005, A&A, 436, 585

de Avillez, M. A. & Breitschwerdt, D. 2012, A&A, 539, L1

De Luca, A. & Molendi, S. 2004, A&A, 419, 837

de Plaa, J., Kaastra, J. S., Gu, L., Mao, J., & Raassen, T. 2020, in Astronomical Society of the Pacific Conference Series, Vol. 527, Astronomical Data Analysis Software and Systems XXIX, ed. R. Pizzo, E. R. Deul, J. D. Mol, J. de Plaa, & H. Verkouter, 725

Del Zanna, G., Dere, K. P., Young, P. R., & Landi, E. 2021, ApJ, 909, 38

Dennerl, K. 2010, Space Sci. Rev., 157, 57

Dennerl, K., Englhauser, J., & Trümper, J. 1997, Science, 277, 1625

Dennerl, K., Lisse, C. M., Bhardwaj, A., et al. 2006, A&A, 451, 709

Dere, K. P., Landi, E., Mason, H. E., Monsignori Fossi, B. C., & Young, P. R. 1997, A&AS, 125, 149

Dickey, J. M. & Lockman, F. J. 1990, ARA&A, 28, 215

Diehl, R., Halloin, H., Kretschmer, K., et al. 2006, Nature, 439, 45

Draine, B. T. 2011, Physics of the Interstellar and Intergalactic Medium (Princeton University Press)

Dupin, O. & Gry, C. 1998, A&A, 335, 661

Edenhofer, G., Zucker, C., Frank, P., et al. 2024, A&A, 685, A82

Egger, R. 1998, in IAU Colloquium 166: The Local Bubble and Beyond, ed. D. Breitschwerdt, M. J. Freyberg, & J. Truemper, Vol. 506 (Springer-Verlag Berlin Heidelberg), 287–296

Egger, R. J. & Aschenbach, B. 1995, A&A, 294, L25

Ellis, J., Fields, B. D., & Schramm, D. N. 1996, ApJ, 470, 1227

Erceg, A., Jelić, V., Haverkorn, M., et al. 2024, A&A, 688, A200

Fang, T., Buote, D., Bullock, J., & Ma, R. 2015, ApJS, 217, 21

Fang, T. & Jiang, X. 2014, ApJ, 785, L24

Fesen, R. A., Drechsler, M., Weil, K. E., et al. 2021, ApJ, 920, 90

Filipe, Journois, M., Frank, et al. 2021, python-visualization/folium v0.12.1

Foreman-Mackey, D. 2016, corner.py: Scatterplot matrices in Python

Foreman-Mackey, D., Hogg, D. W., Lang, D., & Goodman, J. 2013, PASP, 125, 306

Foster, A., Cui, X., Dupont, M., Smith, R., & Brickhouse, N. 2020, BAAS, 235, 180.01

Foster, A. R. & Heuer, K. 2020, Atoms, 8, 49

Foster, A. R., Ji, L., Smith, R. K., & Brickhouse, N. S. 2012, ApJ, 756, 128

Fraternali, F., Marasco, A., Armillotta, L., & Marinacci, F. 2015, MNRAS, 447, L70

Freyberg, M. 1994, Untersuchungen der kosmischen und nichtkosmischen Komponenten der Röntgenhintergrundstrahlung mit ROSAT, PhD thesis, Ludwig-Maximilians University of Munich, Germany

Freyberg, M., Perinati, E., Pacaud, F., et al. 2021, SPIE Conf. Ser., 11444, 114441O

Freyberg, M. J. 1998, in IAU Colloq. 166: The Local Bubble and Beyond, ed. D. Breitschwerdt, M. J. Freyberg, & J. Truemper, Vol. 506 (Springer-Verlag Berlin Heidelberg), 113–116

Freyberg, M. J., Budau, B., Burwitz, V., et al. 2012, SPIE Conf. Ser., 8443, 844351

Freyberg, M. J., Müller, T., Perinati, E., et al. 2022, SPIE Conf. Ser., 12181, 1218155

Friedrich, P., Bräuninger, H., Budau, B., et al. 2008, SPIE Conf. Ser., 7011, 70112T

Frisch, P. C., Redfield, S., & Slavin, J. D. 2011, ARA&A, 49, 237

Frisch, P. C. & York, D. G. 1983, ApJ, 271, L59

Fuchs, B., Breitschwerdt, D., de Avillez, M. A., Dettbarn, C., & Flynn, C. 2006, MNRAS, 373, 993

Gabriel, A. H. & Jordan, C. 1969, MNRAS, 145, 241

Galeazzi, M., Chiao, M., Collier, M. R., et al. 2014, Nature, 512, 171

Galeazzi, M., Chiao, M., Collier, M. R., et al. 2011, Exp. Astron., 32, 83

Galeazzi, M., Gupta, A., Covey, K., & Ursino, E. 2007, ApJ, 658, 1081

Galli, P. A. B., Bouy, H., Olivares, J., et al. 2021, A&A, 646, A46

Galli, P. A. B., Bouy, H., Olivares, J., et al. 2020, A&A, 634, A98

Gaunt, J. A. 1930, Phil. Trans. R. Soc. Lond. Ser. A, 229, 163

Gehrels, N. 1986, ApJ, 303, 336

Giacconi, R., Bechtold, J., Branduardi, G., et al. 1979, ApJ, 234, L1

Giacconi, R., Gursky, H., Paolini, F. R., & Rossi, B. B. 1962, Phys. Rev. Lett., 9, 439

Giacconi, R., Zirm, A., Wang, J., et al. 2002, ApJS, 139, 369

Gilfanov, M. R., Syunyaev, R. A., & Churazov, E. M. 1987, Astron. Zh., 13, 3

Gilli, R., Comastri, A., & Hasinger, G. 2007, A&A, 463, 79

Gloeckler, G. & Geiss, J. 2007, Space Sci. Rev., 130, 139

Goodman, J. & Weare, J. 2010, Commun. Appl. Math. Computat. Sci, 5, 65

Gordon, C. & Arnaud, K. 2021, PyXspec: Python interface to XSPEC spectral-fitting program, Astrophysics Source Code Library, record ascl:2101.014

GRAVITY Collaboration, Abuter, R., Amorim, A., et al. 2019, A&A, 625, L10

Gry, C. & Jenkins, E. B. 2001, A&A, 367, 617

Gry, C., York, D. G., & Vidal-Madjar, A. 1985, ApJ, 296, 593

Gu, L., Kaastra, J., & Raassen, A. J. J. 2016a, A&A, 588, A52

Gu, L., Mao, J., Costantini, E., & Kaastra, J. 2016b, A&A, 594, A78

Gu, L., Yamaguchi, H., Foster, A., et al. 2025, PASJ

Gum, C. S. 1952, The Observatory, 72, 151

Guo, Z., Burrows, D. N., Sanders, W. T., Snowden, S. L., & Penprase, B. E. 1995, ApJ, 453, 256

Gupta, A., Kingsbury, J., Mathur, S., et al. 2021, ApJ, 909, 164

Gupta, A., Mathur, S., Kingsbury, J., Das, S., & Krongold, Y. 2023, Nat. Astron., 7, 799

Güver, T. & Özel, F. 2009, MNRAS, 400, 2050

Hanbury Brown, R., Davies, R. D., & Hazard, C. 1960, The Observatory, 80, 191

Hapgood, M. A. 1992, Planet. Space Sci., 40, 711

Harris, C. R., Millman, K. J., van der Walt, S. J., et al. 2020, Nature, 585, 357

Hasinger, G. 2004, Nucl. Phys. B Proc. Suppl., 132, 86

Hasinger, G., Burg, R., Giacconi, R., et al. 1993, A&A, 275, 1

Hasinger, G., Burg, R., Giacconi, R., et al. 1998, A&A, 329, 482

Haslam, C. G. T., Salter, C. J., Stoffel, H., & Wilson, W. E. 1982, A&AS, 47, 1

Haslam, C. G. T., Wilson, W. E., Graham, D. A., & Hunt, G. C. 1974, A&AS, 13, 359

Heiles, C. 1964, ApJ, 140, 470

Heiles, C. 1998, ApJ, 498, 689

Henley, D. B. & Shelton, R. L. 2008, ApJ, 676, 335

Henley, D. B. & Shelton, R. L. 2010, ApJS, 187, 388

Henley, D. B. & Shelton, R. L. 2012, ApJS, 202, 14

Henley, D. B. & Shelton, R. L. 2013, ApJ, 773, 92

Henley, D. B., Shelton, R. L., & Kuntz, K. D. 2007, ApJ, 661, 304

HI4PI Collaboration, Ben Bekhti, N., Flöer, L., et al. 2016, A&A, 594, A116

Hickox, R. C. & Markevitch, M. 2006, ApJ, 645, 95

Hill, A. S., Joung, M. R., Mac Low, M.-M., et al. 2012, ApJ, 750, 104

H.M. Nautical Almanac Office. 1961, Explanatory Supplement to The Astronomical Ephemeris and The American Ephemeris and Nautical Almanac (H.M. Nautical Almanac Office)

Hughes, J. P. & Helfand, D. J. 1985, ApJ, 291, 544

Hunter, G. H., Sormani, M. C., Beckmann, J. P., et al. 2024, A&A, 692, A216

Hunter, J. D. 2007, CiSE, 9, 90

Innes, D. E. & Hartquist, T. W. 1984, MNRAS, 209, 7

Inoue, Y., Nakashima, S., Tahara, M., et al. 2015, PASJ, 67, 56

Janev, R. K. & Winter, H. 1985, Phys. Rep., 117, 265

Jelinsky, P., Vallerga, J. V., & Edelstein, J. 1995, ApJ, 442, 653

Jenkins, E. B. 2009, Space Sci. Rev., 143, 205

Jin, H., Mao, J., Chen, L., et al. 2024, J. Low Temp. Phys., 215, 256

Joubaud, T., Grenier, I. A., Ballet, J., & Soler, J. D. 2019, A&A, 631, A52

Kaaret, P., Koutroumpa, D., Kuntz, K. D., et al. 2020, Nat. Astron., 4, 1072

Kaaret, P., Zajczyk, A., LaRocca, D. M., et al. 2019, ApJ, 884, 162

Kaastra, J. S. 2017, A&A, 605, A51

Kaastra, J. S. & Bleeker, J. A. M. 2016, A&A, 587, A151

Kaastra, J. S. & Jansen, F. A. 1993, A&AS, 97, 873

Kaastra, J. S. & Mewe, R. 1995, A&A, 302, L13

Kaastra, J. S., Mewe, R., & Nieuwenhuijzen, H. 1996, in UV and X-ray Spectroscopy of Astrophysical and Laboratory Plasmas, ed. K. Yamashita & T. Watanabe, 411–414

Kaastra, J. S., Paerels, F. B. S., Durret, F., Schindler, S., & Richter, P. 2008, Space Sci. Rev., 134, 155

Kahn, S. M. 2005, in Saas-Fee Advanced Course 30: High-energy spectroscopic astrophysics, ed. M. Güdel & R. Walter (Springer-Verlag Berlin Heidelberg), 3–81

Kahn, S. M., Behar, E., Kinkhabwala, A., & Savin, D. W. 2002, Phil. Trans. R. Soc. Lond. Ser. A, 360, 1923

Kameda, S., Ikezawa, S., Sato, M., et al. 2017, Geophys. Res. Lett., 44, 11,706

Kataoka, J., Sofue, Y., Inoue, Y., et al. 2018, Galaxies, 6, 27

Kataoka, J., Tahara, M., Totani, T., et al. 2015, ApJ, 807, 77

Kataoka, J., Tahara, M., Totani, T., et al. 2013, ApJ, 779, 57

Kavanagh, P. J., Sasaki, M., & Points, S. D. 2012, A&A, 547, A19

Kirkpatrick, J. D., Marocco, F., Gelino, C. R., et al. 2024, ApJS, 271, 55

Knies, J. R., Sasaki, M., Becker, W., et al. 2024, A&A, 688, A90

Koljonen, K. I. I., Lindseth, S. S., Linares, M., Harding, A. K., & Turchetta, M. 2024, MNRAS, 529, 575

Korschinek, G., Faestermann, T., Knie, K., & Schmidt, C. 1996, Radiocarbon, 68, 38

Koutroumpa, D., Lallement, R., & Kharchenko, V. 2009a, in AIP Conf. Proc., Vol. 1156, The Local Bubble and Beyond II, ed. R. K. Smith, S. L. Snowden, & K. D. Kuntz (AIP Publishing), 62–73

Koutroumpa, D., Lallement, R., Raymond, J. C., & Kharchenko, V. 2009b, ApJ, 696, 1517

Kramida, A., Ralchenko, Y., Reader, J., & NIST ASD Team. 2024, NIST Atomic Spectra Database (version 5.12)

Kroupa, P. 2001, MNRAS, 322, 231

Kuntz, K. D. 2019, A&A Rev., 27, 1

Kuntz, K. D. & Snowden, S. L. 2000, ApJ, 543, 195

Kuntz, K. D. & Snowden, S. L. 2008, A&A, 478, 575

Kushino, A., Ishisaki, Y., Morita, U., et al. 2002, PASJ, 54, 327

Ladjelate, B., André, P., Könyves, V., et al. 2020, A&A, 638, A74

Lallement, R. 2023, C. R. Phys., 23, 1

Lallement, R., Snowden, S., Kuntz, K. D., et al. 2016, A&A, 595, A131

Lallement, R., Vergely, J. L., Babusiaux, C., & Cox, N. L. J. 2022, A&A, 661, A147

Lallement, R., Vergely, J. L., Valette, B., et al. 2014, A&A, 561, A91

Lallement, R., Welsh, B. Y., Vergely, J. L., Crifo, F., & Sfeir, D. 2003, A&A, 411, 447

Lancaster, L., Ostriker, E. C., Kim, J.-G., & Kim, C.-G. 2021, ApJ, 914, 89

Leahy, D. A., Foster, A., & Seitenzahl, I. 2024, AJ, 167, 130

Leroy, J. L. 1999, A&A, 346, 955

Li, Y., Zhang, G.-Y., Chen, Y., Sun, L., & Zhang, S. 2024, ApJ, 967, 99

Liedahl, D. A. 1999, in X-Ray Spectroscopy in Astrophysics: lectures held at the Astrophysical School X in Amsterdam, The Netherlands, September 22 – October 3, 1997, ed. J. van Paradijs & J. A. M. Bleeker, Vol. 520 (Springer-Verlag Berlin Heidelberg), 189

Liedahl, D. A., Osterheld, A. L., & Goldstein, W. H. 1995, ApJ, 438, L115

Linsky, J. L. & Redfield, S. 2021, ApJ, 920, 75

Lisse, C. M., Dennerl, K., Englhauser, J., et al. 1996, Science, 274, 205

Liu, A., Bulbul, E., Ghirardini, V., et al. 2022, A&A, 661, A2

Liu, A., Bulbul, E., Ramos-Ceja, M. E., et al. 2023, A&A, 670, A96

Liu, J., Mao, S., & Wang, Q. D. 2011, MNRAS, 415, L64

Liu, T., Merloni, A., Sanders, J., et al. 2024, ApJ, 967, L27

Liu, W., Chiao, M., Collier, M. R., et al. 2017, ApJ, 834, 33

Locatelli, N., Ponti, G., & Bianchi, S. 2022, A&A, 659, A118

Locatelli, N., Ponti, G., Merloni, A., et al. 2024a, A&A, 688, A85

Locatelli, N., Ponti, G., Zheng, X., et al. 2024b, A&A, 681, A78

Lodders, K. 2003, ApJ, 591, 1220

Lodders, K., Palme, H., & Gail, H. P. 2009, Landolt Börnstein, 4B, 712

Longair, M. S. 1999, in X-Ray Spectroscopy in Astrophysics: lectures held at the Astrophysical School X in Amsterdam, The Netherlands, September 22 – October 3, 1997, ed. J. van Paradijs & J. A. M. Bleeker, Vol. 520 (Springer-Verlag Berlin Heidelberg), 1

Lotz, W. 1967, Z. Phys., 206, 205

Lotz, W. 1968, Z. Phys., 216, 241

Lucchini, S., D'Onghia, E., & Fox, A. J. 2021, ApJ, 921, L36

Lumb, D. H., Warwick, R. S., Page, M., & De Luca, A. 2002, A&A, 389, 93

Luo, B., Brandt, W. N., Xue, Y. Q., et al. 2017, ApJS, 228, 2

Magaudda, E., Stelzer, B., Covey, K. R., et al. 2020, A&A, 638, A20

Maíz-Apellániz, J. 2001, ApJ, 560, L83

Markevitch, M., Bautz, M. W., Biller, B., et al. 2003, ApJ, 583, 70

Matilsky, T., Gursky, H., Kellogg, E., et al. 1973, ApJ, 181, 753

Mazzotta, P., Mazzitelli, G., Colafrancesco, S., & Vittorio, N. 1998, A&AS, 133, 403

McCammon, D., Almy, R., Apodaca, E., et al. 2002, ApJ, 576, 188

McCammon, D. & Sanders, W. T. 1990, ARA&A, 28, 657

McComas, D. J., Bame, S. J., Barraclough, B. L., et al. 1998, Geophys. Res. Lett., 25, 1

McComas, D. J., Elliott, H. A., Schwadron, N. A., et al. 2003, Geophys. Res. Lett., 30, 1517

McKee, C. F. & Ostriker, J. P. 1977, ApJ, 218, 148

Meidinger, N., Andritschke, R., Bornemann, W., et al. 2014, SPIE Conf. Ser., 9144, 91441W

Merloni, A., Lamer, G., Liu, T., et al. 2024, A&A, 682, A34

Merloni, A., Predehl, P., Becker, W., et al. 2012, arXiv e-prints, arXiv:1209.3114

Mewe, R. 1999, in X-Ray Spectroscopy in Astrophysics: lectures held at the Astrophysical School X in Amsterdam, The Netherlands, September 22 – October 3, 1997, ed. J. van Paradijs & J. A. M. Bleeker, Vol. 520 (Springer-Verlag Berlin Heidelberg), 109

Mewe, R., Gronenschild, E. H. B. M., & van den Oord, G. H. J. 1985, A&AS, 62, 197

Mewe, R., Lemen, J. R., & van den Oord, G. H. J. 1986, A&AS, 65, 511

Migkas, K., Kox, D., Schellenberger, G., et al. 2024, A&A, 688, A107

Miller, E. D., Tsunemi Hiroshi, Bautz, M. W., et al. 2008, PASJ, 60, S95

Miller, M. J. & Bregman, J. N. 2013, ApJ, 770, 118

Miller, M. J. & Bregman, J. N. 2015, ApJ, 800, 14

Miller, M. J., Hodges-Kluck, E. J., & Bregman, J. N. 2016, ApJ, 818, 112

Milne, E. A. 1924, Phil. Mag., 47, 209

Mitrani, S., Behar, E., Drake, J. J., et al. 2024, ApJ, 970, 54

Mou, G., Sun, D., Fang, T., et al. 2023, Nat. Commun., 14, 781

Mullen, P. D., Cumbee, R. S., Lyons, D., et al. 2017, ApJ, 844, 7

Mullen, P. D., Cumbee, R. S., Lyons, D., & Stancil, P. C. 2016, ApJS, 224, 31

Nakahira, S., Tsunemi, H., Tomida, H., et al. 2020, PASJ, 72, 17

Nakashima, S., Inoue, Y., Yamasaki, N., et al. 2018, ApJ, 862, 34

Nasa High Energy Astrophysics Science Archive Research Center (Heasarc). 2014, HEAsoft: Unified Release of FTOOLS and XANADU

Neher, H. V. & Anderson, H. R. 1962, J. Geophys. Res., 67, 1309

Newville, M., Stensitzki, T., Allen, D. B., et al. 2016, Lmfit: Non-Linear Least-Square Minimization and Curve-Fitting for Python, Astrophysics Source Code Library, record ascl:1606.014

Nguyen, D. D. & Thompson, T. A. 2022, ApJ, 935, L24

Oey, M. S. & García-Segura, G. 2004, ApJ, 613, 302

O'Neill, T. J., Zucker, C., Goodman, A. A., & Edenhofer, G. 2024, ApJ, 973, 136

Pan, Z., Qu, Z., Bregman, J. N., & Liu, J. 2024, ApJS, 271, 62

Panopoulou, G. V., Dickinson, C., Readhead, A. C. S., Pearson, T. J., & Peel, M. W. 2021, ApJ, 922, 210

Panopoulou, G. V., Markopoulioti, L., Bouzelou, F., et al. 2025, ApJS, 276, 15

Paresce, F. 1984, AJ, 89, 1022

Parker, E. N. 1958, ApJ, 128, 664

Pelgrims, V., Ferrière, K., Boulanger, F., Lallement, R., & Montier, L. 2020, A&A, 636, A17

Perinati, E., Freyberg, M. J., Yeung, M. C. H., et al. 2024, Exp. Astron., 58, 9

Perryman, M. A. C., Lindegren, L., Kovalevsky, J., et al. 1997, A&A, 323, L49

Pfeffermann, E., Briel, U. G., Hippmann, H., et al. 1987, SPIE Conf. Ser., 733, 519

Piccinotti, G., Mushotzky, R. F., Boldt, E. A., et al. 1982, ApJ, 253, 485

Picquenot, A., Acero, F., Bobin, J., et al. 2019, A&A, 627, A139

Picquenot, A., Acero, F., Holland-Ashford, T., Lopez, L. A., & Bobin, J. 2021, A&A, 646, A82

Picquenot, A., Williams, B. J., Acero, F., & Guest, B. T. 2023, A&A, 672, A57

Pillepich, A., Nelson, D., Truong, N., et al. 2021, MNRAS, 508, 4667

Planck Collaboration, Abergel, A., Ade, P. A. R., et al. 2014, A&A, 571, A11

Planck Collaboration, Fermi Collaboration, Ade, P. A. R., et al. 2015, A&A, 582, A31

Plotly Technologies Inc. 2015, Collaborative data science

Plucinsky, P. P., Beardmore, A. P., Foster, A., et al. 2017, A&A, 597, A35

Pommranz, C. M. 2024, Interdisciplinary Applications of Automated Computational Workflows for XMM-Newton Cross-Calibration and Monte Carlo Simulations of eROSITA and a Breast PET Insert, PhD thesis, Eberhard Karls Universität Tübingen

Pon, A., Ochsendorf, B. B., Alves, J., et al. 2016, ApJ, 827, 42

Ponti, G., Sanders, J. S., Locatelli, N., et al. 2023a, A&A, 670, A99

Ponti, G., Yeung, M. C. H., Stel, G., et al. 2025, A&A, submitted

Ponti, G., Zheng, X., Locatelli, N., et al. 2023b, A&A, 674, A195

Porowski, C., Bzowski, M., & Tokumaru, M. 2022, ApJS, 259, 2

Porquet, D. & Dubau, J. 2000, A&AS, 143, 495

Porquet, D., Dubau, J., & Grosso, N. 2010, Space Sci. Rev., 157, 103

Predehl, P., Andritschke, R., Arefiev, V., et al. 2021, A&A, 647, A1

Predehl, P., Sunyaev, R. A., Becker, W., et al. 2020, Nature, 588, 227

Puspitarini, L., Lallement, R., Vergely, J. L., & Snowden, S. L. 2014, A&A, 566, A13

Putman, M. E., Peek, J. E. G., & Joung, M. R. 2012, ARA&A, 50, 491

Qu, Z., Koutroumpa, D., Bregman, J. N., Kuntz, K. D., & Kaaret, P. 2022, ApJ, 930, 21

Ranalli, P., Comastri, A., Origlia, L., & Maiolino, R. 2008, MNRAS, 386, 1464

Rasmussen, A. P., Behar, E., Kahn, S. M., den Herder, J. W., & van der Heyden, K. 2001, A&A, 365, L231

Raymond, J. C. 1979, ApJS, 39, 1

Raymond, J. C. & Smith, B. W. 1977, ApJS, 35, 419

Reardon, D. J., Main, R., Ocker, S. K., et al. 2025, Nat. Astron., 9, 1053

Redfield, S. & Linsky, J. L. 2004, ApJ, 613, 1004

Reipurth, B. & Bragg, J. 2021, RNAAS, 5, 1

Revnivtsev, M., Gilfanov, M., Sunyaev, R., Jahoda, K., & Markwardt, C. 2003, A&A, 411, 329

Ridge, N. A., Di Francesco, J., Kirk, H., et al. 2006, AJ, 131, 2921

Ringuette, R., Koutroumpa, D., Kuntz, K. D., et al. 2021, ApJ, 918, 41

Roberts, S. R. & Wang, Q. D. 2015, MNRAS, 449, 1340

Robertson, I. P., Kuntz, K. D., Collier, M. R., Cravens, T. E., & Snowden, S. L. 2009, in American Institute of Physics Conference Series, Vol. 1156, The Local Bubble and Beyond II, ed. R. K. Smith, S. L. Snowden, & K. D. Kuntz (AIP Publishing), 52–61

Roy, A., André, P., Palmeirim, P., et al. 2014, A&A, 562, A138

Sakai, K., Mitsuda, K., Yamasaki, N. Y., et al. 2012, in AIP Conf. Proc., Vol. 1427, Suzaku 2011: Exploring the X-ray Universe: Suzaku and Beyond, ed. R. Petre, K. Mitsuda, & L. Angelini (AIP Publishing), 342–343

Sanders, J. S. 2006, MNRAS, 371, 829

Sanders, J. S. & Fabian, A. C. 2006, MNRAS, 370, 63

Sanders, W. T., Kraushaar, W. L., Nousek, J. A., & Fried, P. M. 1977, ApJ, 217, L87

Sarkar, K. C. 2024, A&A Rev., 32, 1

Sarkar, K. C., Mondal, S., Sharma, P., & Piran, T. 2023, ApJ, 951, 36

Sarkar, K. C., Nath, B. B., & Sharma, P. 2015, MNRAS, 453, 3827

Sarkar, K. C., Nath, B. B., & Sharma, P. 2017, MNRAS, 467, 3544

Sasaki, M., Breitschwerdt, D., Baumgartner, V., & Haberl, F. 2011, A&A, 528, A136

Sasaki, M., Knies, J., Haberl, F., et al. 2022, A&A, 661, A37

Scheffler, T., Schulreich, M. M., Schurer, D. P. P. R., & Breitschwerdt, D. 2025, A&A, 695, A34

Schmitt, J. H. M. M., Snowden, S. L., Aschenbach, B., et al. 1991, Nature, 349, 583

Schulreich, M. M., Breitschwerdt, D., Feige, J., & Dettbarn, C. 2017, A&A, 604, A81

Schulreich, M. M., Feige, J., & Breitschwerdt, D. 2023, A&A, 680, A39

Schwartz, D. A. 1980, Phys. Scr, 21, 644

Seaton, M. J. 1959, MNRAS, 119, 90

Sedov, L. I. 1946, ZAMM, 10, 241

Sfeir, D. M., Lallement, R., Crifo, F., & Welsh, B. Y. 1999, A&A, 346, 785

Shah, C., Crespo López-Urrutia, J. R., Gu, M. F., et al. 2019, ApJ, 881, 100

Slavin, J. D. 1989, ApJ, 346, 718

Smith, R. K., Bautz, M. W., Edgar, R. J., et al. 2007, PASJ, 59, 141

Smith, R. K., Brickhouse, N. S., Liedahl, D. A., & Raymond, J. C. 2001, ApJ, 556, L91

Smith, R. K., Foster, A. R., & Brickhouse, N. S. 2012, Astron. Nachr., 333, 301

Smith, R. K. & Hughes, J. P. 2010, ApJ, 718, 583

Snowden, S. L., Chiao, M., Collier, M. R., et al. 2014, ApJ, 791, L14

Snowden, S. L., Cox, D. P., McCammon, D., & Sanders, W. T. 1990a, ApJ, 354, 211

Snowden, S. L., Egger, R., Finkbeiner, D. P., Freyberg, M. J., & Plucinsky, P. P. 1998, ApJ, 493, 715

Snowden, S. L., Egger, R., Freyberg, M. J., et al. 1997, ApJ, 485, 125

Snowden, S. L., Freyberg, M. J., Kuntz, K. D., & Sanders, W. T. 2000, ApJS, 128, 171

Snowden, S. L., McCammon, D., Burrows, D. N., & Mendenhall, J. A. 1994, ApJ, 424, 714

Snowden, S. L., McCammon, D., & Verter, F. 1993, ApJ, 409, L21

Snowden, S. L., Mebold, U., Hirth, W., Herbstmeier, U., & Schmitt, J. H. M. 1991, Science, 252, 1529

Snowden, S. L. & Schmitt, J. H. M. M. 1990, Ap&SS, 171, 207

Snowden, S. L., Schmitt, J. H. M. M., & Edwards, B. C. 1990b, ApJ, 364, 118

Sofue, Y. 1973, PASJ, 25, 207

Sofue, Y. 1977, A&A, 60, 327

Sofue, Y. 1994, ApJ, 431, L91

Sofue, Y. 2000, ApJ, 540, 224

Strickland, D. K., Heckman, T. M., Colbert, E. J. M., Hoopes, C. G., & Weaver, K. A. 2004, ApJS, 151, 193

Su, M., Slatyer, T. R., & Finkbeiner, D. P. 2010, ApJ, 724, 1044

Sukhbold, T., Ertl, T., Woosley, S. E., Brown, J. M., & Janka, H. T. 2016, ApJ, 821, 38

Sunyaev, R., Arefiev, V., Babyshkin, V., et al. 2021, A&A, 656, A132

Sutherland, R. S. & Dopita, M. A. 1993, ApJS, 88, 253

Tanaka, Y. & Bleeker, J. A. M. 1977, Space Sci. Rev., 20, 815

Tanaka, Y., Uchida, H., Tanaka, T., et al. 2022, ApJ, 933, 101

Taylor, G. 1950, Proc. R. Soc. Lond. Ser. A., 201, 159

Trzesiok, A., Tgandor, Kostur, M., et al. 2022, K3D-tools/K3D-jupyter: 2.12.0

Uchida, H., Katsuda, S., Tsunemi, H., et al. 2019, ApJ, 871, 234

Ueda, M., Sugiyama, H., Kobayashi, S. B., et al. 2022, PASJ, 74, 1396

Uprety, Y., Chiao, M., Collier, M. R., et al. 2016, ApJ, 829, 83

Ursino, E., Galeazzi, M., & Liu, W. 2016, ApJ, 816, 33

Vecchi, A., Molendi, S., Guainazzi, M., Fiore, F., & Parmar, A. N. 1999, A&A, 349, L73

Verner, D. A., Ferland, G. J., Korista, K. T., & Yakovlev, D. G. 1996, ApJ, 465, 487

Verner, D. A. & Yakovlev, D. G. 1995, A&AS, 109, 125

Virtanen, P., Gommers, R., Oliphant, T. E., et al. 2020, Nat. Methods, 17, 261

Voirin, J., Manara, C. F., & Prusti, T. 2018, A&A, 610, A64

von Steiger, R., Schwadron, N. A., Fisk, L. A., et al. 2000, J. Geophys. Res., 105, 27217

Wang, Q. D. & McCray, R. 1993, ApJ, 409, L37

Wang, Q. D., Zeng, Y., Bogdán, Á., & Ji, L. 2021, MNRAS, 508, 6155

Weaver, R., McCray, R., Castor, J., Shapiro, P., & Moore, R. 1977, ApJ, 218, 377

Weller, C. S. & Meier, R. R. 1974, ApJ, 193, 471

Welsh, B. Y. 1991, ApJ, 373, 556

Welsh, B. Y., Craig, N., Vedder, P. W., & Vallerga, J. V. 1994, ApJ, 437, 638

Welsh, B. Y. & Shelton, R. L. 2009, Ap&SS, 323, 1

Werner, N., Zhuravleva, I., Churazov, E., et al. 2009, MNRAS, 398, 23

White, S. D. M. & Frenk, C. S. 1991, ApJ, 379, 52

Willingale, R., Hands, A. D. P., Warwick, R. S., Snowden, S. L., & Burrows, D. N. 2003, MNRAS, 343, 995

Willingale, R., Starling, R. L. C., Beardmore, A. P., Tanvir, N. R., & O'Brien, P. T. 2013, MNRAS, 431, 394

Wilms, J., Allen, A., & McCray, R. 2000, ApJ, 542, 914

Wolter, H. 1952, Ann. Phys. (Berlin), 445, 94

Wood, B. E., Redfield, S., Linsky, J. L., Müller, H.-R., & Zank, G. P. 2005, ApJS, 159, 118

Wulf, D., Eckart, M. E., Galeazzi, M., et al. 2019, ApJ, 884, 120

Xu, H., Kahn, S. M., Peterson, J. R., et al. 2002, ApJ, 579, 600

Yamaguchi, H., Tanaka, T., Wik, D. R., et al. 2018, ApJ, 868, L35

Yamamoto, M., Kataoka, J., & Sofue, Y. 2022, MNRAS, 512, 2034

Yang, H., Zhang, S., & Ji, L. 2020, ApJ, 894, 22

Yang, H. Y. K., Ruszkowski, M., & Zweibel, E. G. 2022, Nat. Astron., 6, 584

Yao, Y., Nowak, M. A., Wang, Q. D., Schulz, N. S., & Canizares, C. R. 2008, ApJ, 672, L21

Yao, Y. & Wang, Q. D. 2007, ApJ, 666, 242

Yeung, M. C. H. & Freyberg, M. J. 2024, RNAAS, 8, 268

Yeung, M. C. H., Freyberg, M. J., Ponti, G., et al. 2023, A&A, 676, A3

Yeung, M. C. H., Ponti, G., Freyberg, M. J., et al. 2024, A&A, 690, A399

Yoshino, T., Mitsuda, K., Yamasaki, N. Y., et al. 2009, PASJ, 61, 805

Yoshioka, S. & Ikeuchi, S. 1990, ApJ, 360, 352

Zhang, H.-S., Ponti, G., Carretti, E., et al. 2024, Nat. Astron., 8, 1416

Zhang, R., Guo, F., Xie, S., et al. 2025, arXiv e-prints, arXiv:2507.13665

Zheng, X., Ponti, G., Freyberg, M., et al. 2024a, A&A, 681, A77

Zheng, X., Ponti, G., Locatelli, N., et al. 2024b, A&A, 689, A328

Zheng, X., Ponti, G., Stelzer, B., & Dennerl, K. 2025, A&A

Zucker, C., Goodman, A. A., Alves, J., et al. 2022, Nature, 601, 334

Acknowledgements

I am grateful to my supervisor, Michael Freyberg, for his guidance over the last four years. He always has time for me and has only been encouraging of my ideas. I greatly treasure our close master-apprentice relationship and his selfless generosity in sharing his experience and knowledge.

I must also thank Gabriele Ponti, my de facto co-supervisor, who has been an essential part of almost all projects I have had in my PhD. I have thoroughly enjoyed all our discussions, whether dedicated or informal, over lunch, dinner or cross-country car rides.

My thanks extend to my University supervisor, Werner Becker, who agreed to take me as a student and has always been supportive and helpful during my PhD. I also need to thank Manami Sasaki. Without her, eRO-STEP and this position and project would not exist. Their input was invaluable to the progression of my PhD. I am also immensely grateful to Konrad Dennerl, my role model in how to do science. He has always been patient in explaining calibration and charge exchange to me or listening to me rumble about my projects. I want to thank Arne Rau, my mentor, who has ensured my well-being throughout these four years.

I sincerely thank Martin Mayer for his help on the eROSITA bubbles project, the morphology part, and more. Without him, the paper would have taken much longer to finish, if not impossible. I also must thank Andy Strong for trusting me to finish this project.

A warm thank you to Yi Zhang, who has been the perfect office companion for the last four years.

I must thank everyone in the Hot Milk meeting/group not already mentioned above, Jeremy Sanders, Nicola Locatelli, Xueying Zheng, Heshou Zhang, Giovanni Stel, Tong Bao, Elisa Lentini and Samaresh Mondal. They have given me constant feedback in meetings or warmly welcomed me in Merate. I must also thank the eSASS team, especially Miriam Ramos, Ian Stewart and Jeremy Sanders, for their wonderful help with anything about eROSITA data and software.

I sincerely thank Birgit Boller and Harald Baumgartner, whose help in administrative and IT have alleviated much of my daily burden.

My PhD life would be less enjoyable with friends in MPE or eROSTEP, especially David Kaltenbrunner, Aafia Zainab, Jonathan Knies and Jan Kurpas. Outside of the workplace, I need to thank Tommy Lau, David Ngan and Mandy Wong for all the fun times we had testing food around Munich.

My parents have never wavered in their support for my choices, even though some mean a separation of half the globe. For this, I am forever in their debt.

Lastly, though words risk diminishing its worth, I thank Lilian for walking alongside me on this journey.